PRODUCTION AND PROPERTIES OF NON-DEBYE SODIUM LASER PLASMAS

A Thesis Submitted for the Degree of

DOCTOR OF PHILOSOPHY

in the

UNIVERSITY OF LONDON

by

OTTO MAX ALBERT LAMOTTE LANDEN

The Blackett Laboratory
Imperial College of Science and Technology
London SW7

July 1983

I Dedicate this Thesis

to my Parents, Brother

and Pets at Home



LASER SYSTEM

ABSTRACT

High electron density, low temperature plasmas have been produced with a minimum of 1 electron/Debye sphere by high power short pulse laser pumping of dense (10^{16} cm^{-3} to 4 x 10^{17} cm^{-3}) sodium vapor. Two laser wavelengths were used: λ = 5890 Å corresponding to the sodium resonance D line (3s → 3p), and λ = 6854 Å corresponding to two-photon resonant (3s ↠ 3d) three-photon ionization.

The recombining plasmas were diagnosed by time-resolved emission spectroscopy. In both pumping schemes, all atomic lines 3p - ns and 3p - nd for $3 \leq n < 10$ were observed. Their lineshapes revealed a variety of plasma spectroscopic effects including ion and electron collisional broadening, spectral line shifts, the emergence of satellites and of dipole forbidden components 3p - nf,ng for n = 4,5,6, and the merging of spectral lines. All results were compared with existing theory and discrepancies discussed.

Peak electron densities of 2.5 x 10^{16} cm^{-3} were inferred from line-widths after correcting for opacity effects. All states above n = 3 were shown experimentally and theoretically to be in partial Local Thermodynamic Equilibrium with the free electrons. This enabled time-resolved electron temperatures of .2 to .3 eV to be determined from Boltzmann plots of relative line intensities.

Such low temperatures, coupled with other experimental evidence, suggested laser-induced associative ionization involving atoms in the 3p state as the dominant ionization mechanism when pumping the sodium D line in dense vapor. In the multiphoton ionization scheme, laser

effects proved more important as shown by AC Stark shifts of the 3d level, corresponding to peak laser fluxes of 10^8 W cm^{-2}.

The 100 - 200 ns plasma lifetimes observed experimentally could be explained by diffusion and collisional recombination. Electron-neutral atom heat transfer was theoretically shown to be the main plasma energy loss mechanism. Sodium dimer absorption and re-emission, however, prevented further diagnosis of the plasma by laser scattering from free electrons. Hence alternative laser ionization schemes for producing non-Debye plasmas in caesium and xenon, where molecular interference should be substantially diminished, are discussed and preliminary results on caesium are presented.

ACKNOWLEDGEMENTS

I thank Dr. R. J. Winfield for his invaluable assistance during the assembly and maintenance of equipment and during the recording of results. I am also greatly indebted to my supervisor, Dr. J. D. Kilkenny, for many useful suggestions and for experimental guidance. Thanks also go to Professor D. D. Burgess, Dr. R. W. Lee and Dr. D. J. Bond for helpful discussions and explanations. John Westlake is to be thanked for the power supplies for the glass laser amplifiers and Jack Beckwith and Berndt Benker for building dye laser components. I am grateful to Dave Spirit and Dr. M. Nightingale for their co-operation during the absorption experiment and to Mrs. Diana Beydoun for typing this thesis.

I thank the Science and Engineering Research Council for funding this experiment and I am very grateful to my parents for financial and moral support. I also thank Professor M. G. Haines and the Committee of Vice-Chancellors and Principals of the Universities of the United Kingdom for providing a reduction in fees in the form of an Overseas Research Student's Award held during my first 2 years. Finally, I am also grateful for the Research Assistantships offered to me by Professor D. D. Burgess and Dr. J. D. Kilkenny in 1982 and 1983 respectively.

CONTENTS

		Page
ABSTRACT		5
ACKNOWLEDGEMENTS		7
CONTENTS		9
LIST OF FIGURES		15
LIST OF TABLES		19
GLOSSARY OF SYMBOLS		21
UNITS		25
CHAPTER 1	INTRODUCTION	
1.1	Non-Debye Plasmas	27
1.2	Ionization of Gases and Vapors by Radiation	29
1.3	Ionization Mechanisms for Resonance Pumping of Sodium	30
1.4	Ionization Rate in Dense Sodium Vapor	36
1.5	Experimental Considerations	37
1.6	Contents of Chapters	37
1.7	Role of Author	38
CHAPTER 2	EQUIPMENT	
2.1	Introduction	39
2.2.1	Glass Laser	39
2.2.2	Frequency Doubling	40
2.3.1	Dye Oscillator	44
2.3.2	Dye Amplifiers	47
2.3.3.1	Dye Solutions at λ_L = 5890 Å	50
2.3.3.2	Dye Solutions at λ_L = 6854 Å	51

CHAPTER 2 (continued)		Page
2.4	Ovens	53
2.5	Sodium Containment	59
2.6.1	Diagnostic Equipment for Transmission Experiment	62
2.6.2	Diagnostic Equipment for Absorption Experiment	62
2.6.3	Diagnostic Equipment for Fluorescence and Scattering Experiments	62
2.6.4	Diagnostic Equipment for Calibration	63
CHAPTER 3	IONIZATION BY RESONANCE PUMPING (λ_L = 5890 Å)	
3.1	Ionization Scheme	65
3.2	Transmission Experiments	65
3.2.1	Introduction	65
3.2.2	Experimental Details and Results	69
3.2.3	Analysis of Transmission Results	69
3.2.4	Conclusion on Transmission Results	73
3.3	Fluorescence Experiments	74
3.3.1	Introduction	74
3.3.2	Experimental Layout	75
3.3.3	Sodium Vapor Density	76
3.3.3.1	Vapor Pressure Tables	76
3.3.3.2	Dimer Absorption of He - Ne Laser Beam	77
3.3.3.3	Curve of Growth of Resonance Line	78
3.3.4	Fluorescence Results	81
3.4	Electron Density	88
3.4.1	Introduction	88
3.4.2	Line Broadening Mechanisms	88
3.4.2.1	Doppler Effect	89
3.4.2.2	Helium - Sodium Collisions	89

CHAPTER 3 (continued) Page

3.4.2.3	Dimer - Atom Collisions	89
3.4.2.4	Atom - Atom Collisions	90
3.4.2.5	Resonance Broadening	90
3.4.2.6	AC Stark Effect	90
3.4.2.7	Power Broadening	91
3.4.2.8	Instrument Function	92
3.4.2.9	Opacity Effects	92
3.4.2.10	Plasma Broadening	92
3.4.2.11	Summary	94
3.4.3	Radiation Transport	95
3.4.4	N_e versus N(3p) Plot	97
3.4.5	Temporal Histories of N_e and N(3p)	99
3.4.6	Stark Shifts	101
3.4.7	Forbidden Components	103
3.4.8	Satellites	106
3.4.8.1	Molecular Transitions	106
3.4.8.2	Impurity Lines	106
3.4.8.3	Quasi-molecular Satellites	107
3.4.8.4	Plasma Satellites	107
3.4.9	Continuum Depression	112
3.5	Electron Temperature	114
3.5.1	Introduction	114
3.5.2	Experimental Details	117
3.5.3	Boltzmann Plot	117
3.5.4	Validity of LTE	120
3.5.5	Ionization Equilibrium and Plasma Chemistry	122
3.5.6	Temporal History of T_e	125

CHAPTER 3 (continued)		Page
3.6	Ion and Atom Temperatures	128
3.7	Temporal History of N_D	129
3.8	Plasma Dependence on Laser Characteristics	129
3.8.1	Bandwidth	129
3.8.2	Dual Wavelength Pumping (λ_L = 0.59 μm and 0.53 μm)	131
3.8.3	Laser Pulse Length	132
3.9	Ionization Mechanism	133
CHAPTER 4	MULTIPHOTON IONIZATION (λ_L = 6854 Å)	
4.1	Introduction	139
4.2	Ionization Scheme	140
4.3	Experimental Layout	142
4.4	Fluorescence Results	142
4.5	Electron Density	147
4.5.1	Radiation Transport	148
4.5.2	N_e and N(3p) Temporal Histories	148
4.5.3	Stark Shift	151
4.5.4	Forbidden Components and Satellites	151
4.6	Ionization Yield versus Laser Detuning	154
4.6.1	Introduction	154
4.6.2	Atom - Laser Interactions	154
4.6.3	Non-Resonant Multiphoton Ionization	157
4.7	Plasma Inhomogeneity	157
4.8	Electron Temperature	158
4.8.1	Boltzmann Plot	158
4.8.2	T_e Temporal History	158
4.9	Temporal History of N_D	161
4.10	Summary	161

		Page
CHAPTER 5	PROPERTIES OF METAL VAPOR PLASMAS	
5.1	Introduction	163
5.2	Molecular Effects	163
5.2.1	Absorption Spectroscopy	163
5.2.2	Thomson Scattering	166
5.3	Inverse Bremsstrahlung Heating	173
5.4	Plasma Recombination	175
5.5	Plasma Lifetime	178
CHAPTER 6	CONCLUSIONS	179
CHAPTER 7	PRODUCTION OF NON-DEBYE PLASMAS IN OTHER VAPORS	
7.1	Introduction	183
7.2	Multiphoton Ionization of Xenon	183
7.3	Multiphoton Ionization of Caesium	185
REFERENCES	. . . . .	189

LIST OF FIGURES

CHAPTER 1

		Page
1.	Sodium term diagram	31

CHAPTER 2

2.1	Complete experimental layout	41
2.2	Nd:glass oscillator	42
2.3	Frequency doubling efficiencies of KDP and KD*P	45
2.4	Bandwidth of frequency doubled Nd:glass beam	46
2.5	Dye oscillator	49
2.6	First oven and temperature profiles	54
2.7	Dimer absorption spectrum	57
2.8	Second oven	58
2.9	Sodium containment schemes	61

CHAPTER 3

3.1	Sodium term diagram with ionization scheme	67
3.2	Experimental layout for transmission experiment	68
3.3	Sodium D line absorption of laser	71
3.4	Laser transmission at low sodium densities	72
3.5	Laser transmission at high sodium densities	72
3.6	Polaroid picture of spectrum of transmitted light	70
3.7	Curve of growth of blue wing of D2 line	79

CHAPTER 3 (continued)

		Page
3.8	Sodium term diagram with emission lines	80
3.9	3p-3d lineshape: λ_L = 5890 Å	82
3.10	3p-3d Lineshape: λ_L = 5896 Å	82
3.11	3p-5s lineshape	83
3.12	3p-4d lineshape	83
3.13	3p-6s lineshape	84
3.14	3p-5d lineshape	85
3.15	3p-6d lineshape	85
3.16	Temporal history of 3p-4d lineshape	86
3.17	3p-5f and satellites	87
3.18	3p-4f and satellites	87
3.19	Opacity effect on lineshape	92
3.20	Radiation transport model	95
3.21	N(3p) versus N_e plot	98
3.22	Temporal history of N_e	100
3.23	Temporal history of N(3p)	100
3.24	$N_e(t)$ from 3p-4d shift	104
3.25	$N_e(t)$ from I_{3p-5f}/I_{3p-5d}	104
3.26	$N_e(t)$ from I_{3p-4f}/I_{3p-4d}	104
3.27	Plasmon satellites scheme	108
3.28	Microdensitometer traces of high-lying levels	115
3.29	Continuum depression	116
3.30	Boltzmann plot	119
3.31	Autodetachment scheme	124
3.32	Temporal history of T_e at low sodium densities	126
3.33	Temporal history of T_e at high sodium densities	126
3.34	Temporal history of N_D	130

CHAPTER 3 (continued)

		Page
3.35	Associative ionization scheme	135

CHAPTER 4

4.1	Sodium term diagram with ionization scheme	141
4.2	Experimental layout of dye laser	143
4.3	3p-3d lineshape	145
4.4	3p-5s lineshape	145
4.5	3p-4d lineshape	146
4.6	Temporal history of N_e	149
4.7	Temporal history of N(3p)	149
4.8	N_e from 3p-4d shift	152
4.9	N_e from I_{3p-4f}/I_{3p-4d}	152
4.10	3p-4f and satellites	153
4.11	AC Stark shift at high N_e	155
4.12	3p-3d fluorescence versus laser tuning for low and high laser flux	155
4.13	Boltzmann plot	159
4.14	Temporal history of T_e	160
4.15	Temporal history of N_D	160

CHAPTER 5

5.1	Experimental layout for absorption experiment	164
5.2	Polaroid trace of time-resolved laser absorption	165
5.3	3p-4d absorption lineshape	165
5.4	Broad spectrum of scattered laser light (λ_L = 5266 Å)	168

CHAPTER 5 (continued)

		Page
5.5	Spectrum of scattered laser light in the vicinity of λ_L = 5266 Å (with and without plasma)	169
5.6	Dimer term diagram with scattering scheme	170
5.7	Scattered signal at λ = 5266 Å versus sodium density	172
5.8	Peak fractional ionization versus sodium density	177

CHAPTER 7

7.1	Xenon term diagram with ionization scheme	184
7.2	Caesium term diagram with ionization scheme	186

LIST OF TABLES

CHAPTER 1

		Page
1.	Compilation of previous experimental results on resonantly pumped metal vapors	35

CHAPTER 2

2.1	Characteristics of frequency doubling crystals	43
2.2	Distribution of pump energy to dye cells	48
2.3	Dye solutions for λ_L = 5890 Å	50
2.4	Performance of dye laser at λ_L = 5890 Å	51
2.5	Dye solutions tested for λ_L = 6854 Å	52
2.6	Performance of dye laser at λ_L = 6854 Å	53
2.7	Compilation of sodium vapor containment techniques	59

CHAPTER 3

3.1	Previous results from strongly-coupled non-degenerate plasmas	75
3.2	Spectroscopic parameters of observed transitions	93
3.3	Comparison of N_e determined from shifts and widths of emission lineshapes	102
3.4	Spectroscopic parameters of satellites	109

CHAPTER 4

4.1	Reproducibility of plasma density	148

LIST OF SYMBOLS

Roman

A_{ij}	Spontaneous decay rate of level j to level i
B_{ij}	Stimulated emission coefficient between levels i and j
B(T)	Black-body function at temperature T
C_{ij}	Electron collision rate coefficient between levels i and j
D_{jk}	Diffusion coefficient for species j through species k
E_i	Energy of level i above ground-state
E_{ij}	Energy gap between states i and j
E_p	Particle electric field
E_w	Wave electric field
F	Photon flux
I	Laser flux
I_{ij} or I_k	Flux from transition i - j or k
$I(\nu)$, $I(\lambda)$	Spectral flux
I_B	Bleaching flux
K_0	Line center absorption coefficient
N_D	Number of electrons per Debye sphere
N_e	Number density of electrons
N_j	Number density of species j
$N(n\ell)$	Population number density of level $n\ell$
P_j	Pressure of species j
T_e	Electron temperature
T_j	Temperature of species j

U_j	Partition function of species j
W	Electron impact width
W'	Energy flux
d	Electron impact shift
f_{ij}	Oscillator strength between levels i and j
g	Gaunt factor
g_i	Degeneracy of level i
k	Absorption coefficient
ℓ	Path length in vapor
ℓ	Orbital quantum number
n	Principal quantum number
r	Plasma radius
t	Time
v_j	Mean velocity of species j

Greek

Γ	Strong coupling parameter
Δ	Wavelength separation of doublet
Δ_j	Correction or uncertainty in parameter j
$\Delta\lambda$	Half-width half-maximum of lineshape
$\Delta\lambda_{jk}$	Wavelength separation between features j and k
$\Delta\lambda_s$	Plasma induced shift
$\Delta\lambda_W$	Plasma induced width
α	Ion broadening parameter
$\alpha(T_e)$	3-body recombination rate coefficient at temperature T_e

γ	General HWHM of feature
$\delta\omega$, $\delta\lambda$	AC Stark shift
λ_D	Debye length for electrons
λ_L	Laser wavelength
λ_{ij}	Wavelength of transition i - j
λ_0	Line center wavelength
μ_{ij}	Dipole moment between states i and j
ν	Frequency
σ	Cross-section
τ_L	Laser pulse length
τ_{ee}	Electron thermalization time
τ_{ei}	Electron-ion thermalization time
τ_i	Lifetime of state i
τ_{ION}	Time to reach $\sim \frac{2}{3}$ fractional ionization
τ_j	Optical depth of species j
τ_0	Line center optical depth
χ_j	Ionization potential of species j
ω	Radial frequency
ω_{AF}	Radial frequency separation between allowed and forbidden components
ω_p	Plasma frequency

UNITS

Unless otherwise stated, the following units were used:

eV	for energies, temperatures and ionization potentials
Å	for wavelength and wavelength separations
Seconds (s)	for time and laser pulse length
W cm^{-2}	for fluxes
cm^{-3}	for number densities
cm	for lengths
cm^2	for cross-sections

CHAPTER 1

INTRODUCTION

1.1 Non-Debye Plasmas

Inertial confinement fusion relies on compressing a high temperature ($T_e \sim 10$ keV) plasma to supersolid densities ($N_e > 10^{25}$ cm^{-3}) (Nuckolls et al., 1972). Experimental research to date has yielded plasmas with $N_e = 10^{23} - 10^{24}$ cm^{-3} and $T_e = 0.1 - 1$ keV (Ahlstrom, 1982). In such a regime of high N_e and relatively low T_e, the particle and photon transport properties of the plasma constitute a difficult many-body problem (Burgess and Lee, 1982). The mean thermal energy of ions and electrons becomes comparable or even smaller than the mean potential energy due to Coulomb forces between charged particles. The ratio of potential energy to kinetic energy, Γ, is given by (Hansen, 1973):

$$\Gamma_e \equiv \frac{e^2}{4\pi\varepsilon_0 k T_e}\left(\frac{4\pi N_e}{3}\right)^{1/3} \qquad \text{for electrons of number density } N_e \text{ and temperature } T_e$$

$$\Gamma_i \equiv \frac{Z^2 e^2}{4\pi\varepsilon_0 k T_e}\left(\frac{4\pi N_i}{3}\right)^{1/3} \qquad \text{for ions of charge Z, number density } N_i \text{ and temperature } T_i$$

A strongly-coupled plasma is then defined by $\Gamma > 1$, where Γ is a measure of the strength of correlations between particles. The derivation of the Debye shielding distance, λ_D, which assumes $\Gamma << 1$, then becomes inapplicable and this accounts for the term "non-Debye" plasmas.

The transition to non-Debye plasmas is defined here as occurring when the mean ion sphere radius becomes longer than the appropriate Debye length. For electrons:

$$\left(\frac{3}{4\pi N_e} \right)^{1/3} \gtrsim \lambda_D \qquad \text{where} \quad \lambda_D = \sqrt{\frac{\varepsilon_0 k T_E}{N_e e^2}}$$

This can be rewritten as:

$$\frac{4\pi}{3} N_e \lambda_D^3 \equiv N_D = (3\Gamma)^{-3/2} \lesssim 1 \quad \text{where} \quad N_D = \frac{1.7 \times 10^9 \; T_e^{3/2}}{N_e^{1/2}} \qquad (1.1)$$

(T_e in eV, N_e in cm^{-3}). Hence the number of electrons per Debye sphere, N_D, is less than one for non-Debye plasmas if $\Gamma \gtrsim 1/3$. Under these conditions, the concept of shielding of a test particle by a "cloud" of ions and electrons within a Debye length becomes invalid.

One significant change in the "plasma" is in the transport coefficients. The electrical and thermal conductivities of a plasma, dominated by weak distant collisions for Debye plasmas with a maximum impact parameter λ_D (Spitzer and Härm, 1953), become increasingly dependent on strong (90° deflection) collisions and correlations as λ_D approaches the inter-particle separation. A reduction by a factor of four in the electrical conductivity relative to Spitzer's value has been deduced both theoretically (Wilhelm, 1982) and experimentally (Ivanov et al., 1976 and Barolskii et al., 1975) for $N_D = 0.2$. For $N_D = 1$, this discrepancy is a factor of two.

It has been suggested that strong correlations between particles in a plasma should lead to a lattice structure (Hansen, 1973). Hence, as for a crystal, the average charge within the mean interparticle distance of a test ion would be negative. However, analytic

calculation for a one-dimensional plasma (Pozwolski, 1981) and a Monte Carlo simulation of a one-component plasma (Hansen, 1973) suggest N_D has to be less than 0.02 in a singly-charged plasma for the excess density of oppositely charged particles surrounding a test particle to be > 10% of the mean particle density. Similarly, the effect of correlations for $N_D \sim 0.3$ on electron impact broadening of spectral lines was calculated as < 5% in the lineshape regions accessible to accurate diagnostics (Boercker et al., to be published).

Hence, the only "non-Debye effect" likely to be observed experimentally for $N_D \sim 1$, $\Gamma \sim 0.3$ is the applicability of the Debye length as the maximum cutoff impact parameter. This was one of the motivations for producing and diagnosing spectroscopically a weakly non-Debye plasma ($N_D \sim 1$).

1.2 Ionization of Gases and Vapors by Radiation

Ionization of gases by radiation can be classified into two sections: non-resonant and resonant with respect to electronic transitions of the individual atoms. The non-resonant scheme, commonly referred to as optical breakdown of gases, became feasible with the advent of short pulse Q-switched lasers in the 1960s. These lasers yield high fluxes, typically > 10^{10} - 10^{11} W cm^{-2}, which are necessary for complete ionization of gases at several atmospheres (e.g. Lampis and Brown, 1968).

However, much weaker light fluxes are needed for appreciable ionization to occur by resonant ionization. This has been demonstrated experimentally in caesium for example where the radiation flux from discharge tubes resonant with the 6s - 6p transition (see Fig. 7.2) was sufficient to yield electron densities of up to 10^{12} cm^{-3} at tempera-

tures of $\sim$ 2000 K (Witting and Gyftopoulos, 1965; Morgulis et al., 1968 and Yamada and Okuda, 1973).

1.3 Ionization Mechanisms for Resonance Pumping of Sodium

In 1976, McIlrath and Lucatorto observed near complete ionization, within 600 ns, of dense ($N_{Na} \sim 10^{16}$ cm^{-3}) sodium vapor irradiated by a 10^5 W cm^{-2}, 1 μs dye laser beam tuned to the first resonance line 3s - 3p at λ = 5890 Å (see Fig. 1). Since then efficient ionization by resonance radiation has been observed in all alkali and alkaline earth vapors tested (Li: Lucatorto and McIlrath, 1977; Ba: Bachor and Kock, 1981; Sr, Ba, Ca: Skinner, 1980).

In fact, a theoretical model for laser ionization based on resonance saturation (LIBORS) was proposed earlier by Measures in 1970. A computer code was subsequently developed to simulate the experiment described above (Measures and Cardinal, 1981; Measures et al., 1979 and Measures et al., 1981). The details of the ionization scheme as proposed by Measures are as follows.

The laser saturates the 3s - 3p transition in sodium (see Fig. 1) and also provides "seed" electrons by the processes discussed below. These electrons gain kinetic energy by depopulating the 3p level through super-elastic collisions. The "hot" electrons then collisionally ionize electrons in the 3p level or excite them to higher levels from which they can be photoionized. This leads to avalanche ionization where the ionization energy is supplied by the laser continually replenishing the 3p population.

The list of ionization mechanisms is as follows:

(a) Two photons from the 3p level

$$N(3p) + 2h\nu_L \rightarrow Na^+ + e^- \qquad (T_e = 0.73 \text{ eV})$$

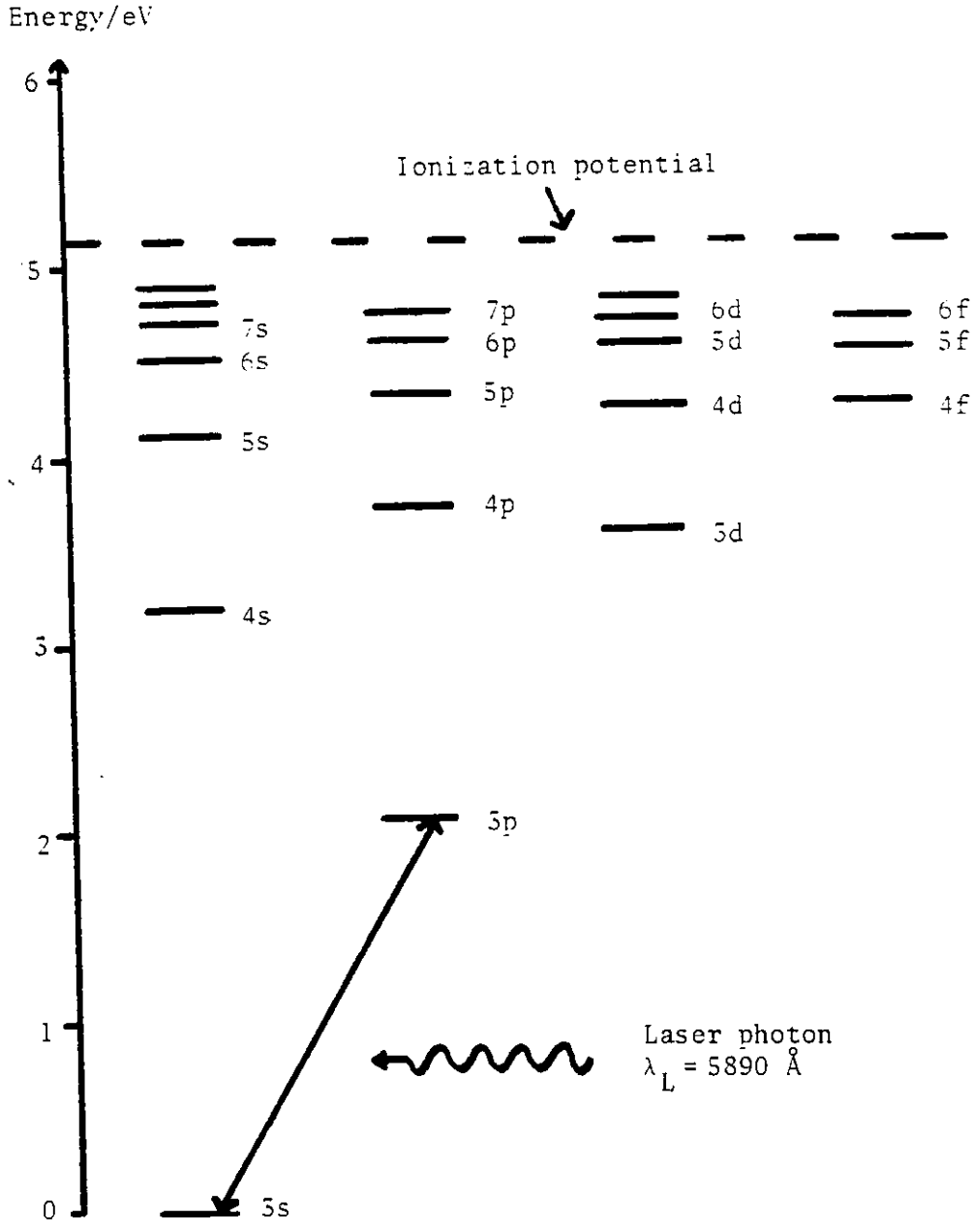


Fig. 1. Sodium term diagram.

For linearly polarized light, Laughlin (1978) and Geltman (1980) agree on:

$$\frac{dN_e}{dt} = 1.5 \times 10^{-12} \; I^2 \; N(3p) \qquad cm^{-3} \; s^{-1}$$

where I is the laser flux in W cm^{-2}, ν_L is the laser frequency and N(3p) the resonance state population density.

(b) Laser-induced collisions

$$N(3p) + N(3p) + h\nu_L \rightarrow N(3s) + Na^+ + e^- \qquad (T_e < 0.7 \text{ eV})$$

The ionization rate for this process has been calculated as (Geltman, 1977):

$$\frac{dN_e}{dt} = 4 \times 10^{-26} \; v_{Na} \; I \; \frac{N(3p)^2}{2!}$$

where v_{Na} is the mean relative velocity of sodium atoms in cm s^{-1}.

(c) Laser-induced Raman scatter and single photon

$$N(3p) + h\nu_L \rightarrow N(n\ell) + h\nu' \qquad (\nu' \neq \nu_L)$$

$$N(n\ell) + h\nu_L \rightarrow Na^+ + e^- \qquad (T_e \sim 0.5 \text{ eV})$$

The total rate for Raman processes to sodium levels $n\ell$ which can be ionized by a single laser photon is (Loudon, 1973):

$$\sum_{n\ell} \frac{dN(n\ell)}{dt} = 3 \times 10^{-4} \; I \; N(3p) \qquad (1.2)$$

The single photon ionization cross-section for these levels $n\ell$ varies between 3×10^{-18} cm^2 and 10^{-17} cm^2 (Aymar et al., 1976), yielding the following ionization rate:

$$\frac{dN_e}{dt} = 3 \times 10^{-18} \; F \; N(n\ell) \equiv 10 \; I \; N(n\ell) \qquad (1.3)$$

where F is the photon flux in cm^{-2} s^{-1}.

In two-stage processes, the rate determining step is the slower

one, which is the Raman process in this case. Hence, by equation (1.2):

$$\frac{dN_e}{dt} \sim 3 \times 10^{-4} \; I \; N(3p)$$

(d) Energy pooling collisions and single photon

Example: $N(3p) + N(3p) \rightarrow N(3s) + N(5s)$

$N(5s) + h\nu_L \rightarrow Na^+ + e^- \qquad (T_e \sim 0.7 \text{ eV})$

The total cross-section for energy pooling collisions between atoms in the 3p state has been recently estimated as 5×10^{-15} cm^2 (Huennekens and Gallagher, 1983). Hence:

$$\sum_{n\ell} \frac{dN(n\ell)}{dt} = 5 \times 10^{-15} \; v_{Na} \frac{N(3p)^2}{2!}$$

$$= \frac{dN_e}{dt}$$

since the single photon process representing the second step is again quicker for $I > 10^7$ W cm^{-2} and $N(3p) < 10^{18}$ cm^{-3}, the parameter region of interest (see section 1.5).

(e) Associative ionization

$N(3p) + N(3p) \rightarrow Na_2^+ + e^- \qquad (T_e < 0.1 \text{ eV})$

This process was first proposed by Freudenberg in 1931, but the most recent cross-section is 5×10^{-17} cm^2 (Huennekens and Gallagher, 1983). Hence:

$$\frac{dN_e}{dt} = 5 \times 10^{-17} \; v_{Na} \frac{N(3p)^2}{2!} \qquad (1.4)$$

(f) Laser-induced associative ionization

$N(3p) + N(3s) \rightarrow Na_2^*$

$Na_2^* + h\nu_L \rightarrow Na_2^+ + e^- \qquad ((T_e < 0.1 \text{ eV})$

In this process, a transient excited dimer state, Na_2^*, is formed.

This can be ionized by a single laser photon (Weiner and Polak-Dingels, 1981). For $I > 10^5$ W cm^{-2}, the geometric cross-section was estimated as 10^{-14} cm^2 (Carré et al., 1981). Hence

$$\frac{dN_e}{dt} = 10^{-14} v_{Na} N(3s) N(3p) \qquad (1.5)$$

(g) Super-elastic collisions followed by collisional ionization

$$N(3p) + e^- \rightarrow N(3s) + e^- + 2.1 \text{ eV}$$

$$e^- + N(3p) \rightarrow Na^+ + e^- + e^-$$

The super-elastic collision rate with the 3p level is given by (Enemark and Gallagher, 1972):

$$\frac{dN(3p)}{dt} = - 10^{-7} N_e N(3p) \qquad (1.6)$$

Since an electron that undergoes two de-excitation collisions will have sufficient kinetic energy (> 4.2 eV) to ionize collisionally a bound electron from the 3p state (ionization potential = 3 eV, see Fig. 1.), the avalanche ionization rate is approximately given by:

$$\frac{dN_e}{dt} = 5 \times 10^{-8} N_e N(3p)$$

$$\sim 5 \times 10^{-8} N_e (N_{Na} - N_e) \text{ if vapor saturated} \qquad (1.7)$$

and $T_e \lesssim 1$ eV.

These various excitation and ionization mechanisms have been proposed by numerous research groups to explain the rapid ionization witnessed. Their experimental conditions and results are listed in Table 1.

However, only three measurements, all spectroscopic, of both N_e and T_e have been performed and published to date for laser ionized metal vapors (Krebs and Schearer, 1982; Skinner, 1980 and Bachor and Kock, 1981) (see Table 1.). The three results suggested that a high

TABLE 1.

EXPERIMENTAL COMPILATION OF RESONANCE PUMPING OF METAL VAPORS

Reference	N_{Na}/cm^{-3}	$I/W\ cm^{-2}$	τ_L/ns	N_e/cm^{-3}	T_e/eV	Proposed Ionization Mechanisms
Salter (1980)	10^{13}-10^{15}	1.4×10^{5} P	300		0.2 ?	
Kumar (1982)	10^{14}-10^{17}	5×10^{4} P	1000			
Krebs (1982)	10^{16}	10^{7} P	4	7×10^{14}	0.08	
Huennekens (1982-83)	10^{14}-10^{16}	10^{4}-10^{5} P	~ 5			Two-photon, associative, energy pooling
Stacewicz (1980,81)	10^{13}-10^{16}	10^{6}-10^{10} P	10		0.9-1.6	Two-photon, associative, LIBORS
Allegrini (1976)	10^{13}-10^{15}	1-5 CW				Energy pooling
Bearman (1978)	10^{13}	10^{2} CW		10^{8}		Associative
de Jong (1979)	10^{9}	0.5 CW				Associative
Kushawaha (1980)	10^{13}	20 CW				Associative
Carré (1981)	10^{12}-10^{15}	3×10^{5} P	1000		2.8	Laser-induced associative & collisional
Weiner (1981)	5×10^{9}	10^{3}-10^{5} P	300 ?			Laser-induced associative & collisional
McIlrath (1976)	10^{16}	10^{6} P	1000	10^{16}		LIBORS
Cardinal (1981)	10^{15}-10^{16}	1.4×10^{6} P	700			LIBORS
Le Gouët (1982)	10^{13}	3 CW				LIBORS
Hellmuth (1981)	?	10^{7} P	4			Three-photon
Bachor (1981)	10^{14}-10^{15}	10^{3} P	1500	10^{15}	0.3-0.4	LIBORS Ba
McIlrath (1977)	6×10^{15}	10^{6} P	300	6×10^{15}		LIBORS Li
Skinner (1980)	10^{15}-4×10^{15}	10^{5}-10^{6} P	300	2×10^{15}	0.3-0.5	LIBORS Sr, Ba, Ca.

KEY: P = pulsed; CW = continuous; τ_L = Laser pulse length.
(All but last three references are for sodium.)

density low temperature plasma approaching the non-Debye limit, $N_D = 1$, could be produced by resonant pumping. Since the majority of published cross-sections for alkali vapors are for sodium (Table 1.), this alkali was chosen for the experiments described in Chapters 3, 4 and 5.

1.4 Ionization Rate in Dense Sodium Vapor

By equation (1.1), the values for N_e and T_e yielding $N_D = 1$ are as follows:

N_e/cm^{-3}	10^{15}	10^{16}	10^{17}	10^{18}
T_e/eV	0.07	0.15	0.33	0.70

Assuming a sodium plasma in thermal equilibrium can be produced satisfying $N_D = 1$, the neutral density N_{Na} would have to be greater than 10^{17} cm^{-3} (e.g. $T_e \sim 0.5$ eV for $\sim 50\%$ ionization at $N_{Na} = 10^{17}$ cm^{-3}) (Drawin and Felenbok, 1965). In addition, if > 10% fractional ionization is desired, the laser flux should then be sufficiently low ($< 10^9$ W cm^{-2}) to prevent inverse bremsstrahlung heating (section 5.3). Under these conditions, laser-induced associative ionization is the dominant "seed" process. However, the exponential ionization growth rate represented by super-elastic collisions and collisional ionization (equation (1.7)) should predominate once a critical electron density N_e^c has been reached, defined by equating expressions (1.5) and (1.7):

$$10^{-14} \, v_{Na} \, N_{Na}^2 = 5 \times 10^{-8} \, N_e^c \, (N_{Na} - N_e^c) \qquad (1.8)$$

where $N_{Na} \sim N(3s) \sim N(3p)$ for a laser saturated vapor. Hence: $N_e^c \sim 10^{-2} \, N_{Na}$ at $T_{OVEN} \sim 800$ K.

The time to reach, say, 95% ionization is then given by the sum of:

(a) The time to reach N_e^c by laser-induced associative ionization, t_1. Using equations (1.5) and (1.8):

$$t_1 = \frac{N_e^c}{10^{-14}\, v_{Na}\, N_{Na}^2} = \frac{2 \times 10^7}{N_{Na}} \qquad (1.9)$$

(b) The time to reach $N_e = 0.95\, N_{Na}$ by electron collisional ionization, t_2. Integrating equation (1.7):

$$t_2 = 2 \times 10^7 \int_{N_e^c}^{0.95\, N_{Na}} \frac{dN_e}{N_e\,(N_{Na} - N_e)}$$

Hence: $$t_2 = \frac{2 \times 10^7}{N_{Na}} \ell n \frac{19\, N_{Na}}{N_e^c}$$

Therefore: $$t_1 + t_2 \sim \frac{2 \times 10^8}{N_{Na}} \text{ s} \qquad (1.10)$$

1.5 Experimental Considerations

For $N_{Na} = 10^{17}$ cm^{-3}, the ionization time and hence minimum laser pulse length necessary should be $\sim$ 2 ns by equation (1.10). The minimum laser energy flux required, W', for complete ionization of a, say, 10 cm length of vapor yielding $N_e \sim 10^{17}$ cm^{-3} and $T_e \sim 0.6$ eV is given by:

$$W' = e\, N_e\, (\chi + \tfrac{3}{2}\, T_e)\, \ell \sim 1 \text{ J cm}^{-2}$$

where χ is the ionization potential of sodium = 5.14 eV and ℓ is the vapor length in cm. This corresponds to a laser flux of 10^8 W cm^{-2} for a 10 ns pulse length.

1.6 Contents of Chapters

Chapter 2 describes the experimental apparatus used for high-power

laser ionization of dense sodium vapor. In Chapter 3, transmission and fluorescence results from the plasma produced by resonant pumping are presented and compared with theory. Fluorescence results for a sodium plasma formed by multiphoton ionization are discussed in Chapter 4 and compared with those of Chapter 3. Several experimentally observed properties of laser-irradiated metal vapor plasmas are analyzed quantitatively in Chapter 5. In Chapter 6, the conclusions of the previous chapters are summarized. Suggestions for future work on xenon and caesium are described and recent results on laser ionization of Cs vapor are presented in Chapter 7.

1.7 Role of Author

The author received considerable technical assistance from Dr. R. J. Winfield and apparatus designed, built and/or tested by other persons is acknowledged in Chapter 2. Unless otherwise stated, the results of Chapters 2 to 7 and their analyses are the work of the author.

CHAPTER 2

EQUIPMENT

2.1 Introduction

The calculations presented in Chapter 1 dictated the following experimental requirements:

(a) A short pulse high power laser which could be tuned to sodium resonances. This is described in sections 2.2 and 2.3.

(b) The production of dense sodium vapor which was both amenable to laser pumping and to viewing of the resultant fluorescence above stray laser light levels. Such sodium containment and heating is discussed in sections 2.4 and 2.5.

(c) Time-resolved spectroscopic measurements of the laser excited sodium vapor. The diagnostic apparatus used is described in section 2.6.

A schematic diagram of the complete experimental layout is shown in Fig. 2.1.

2.2.1 Glass Laser

A commercial Nd-glass laser system manufactured by JK Lasers (System 2000) was used to pump a tunable dye laser. The glass laser consisted of a Q-switched oscillator, a x3 beam expanding telescope and two rod amplifiers, all rods and flashlamps being water-cooled. IV4 Schott phosphate glass was chosen rather than silicate glass as host material due to its intrinsic higher small signal gain (Koechner,

1976) and shorter oscillator pulse length.

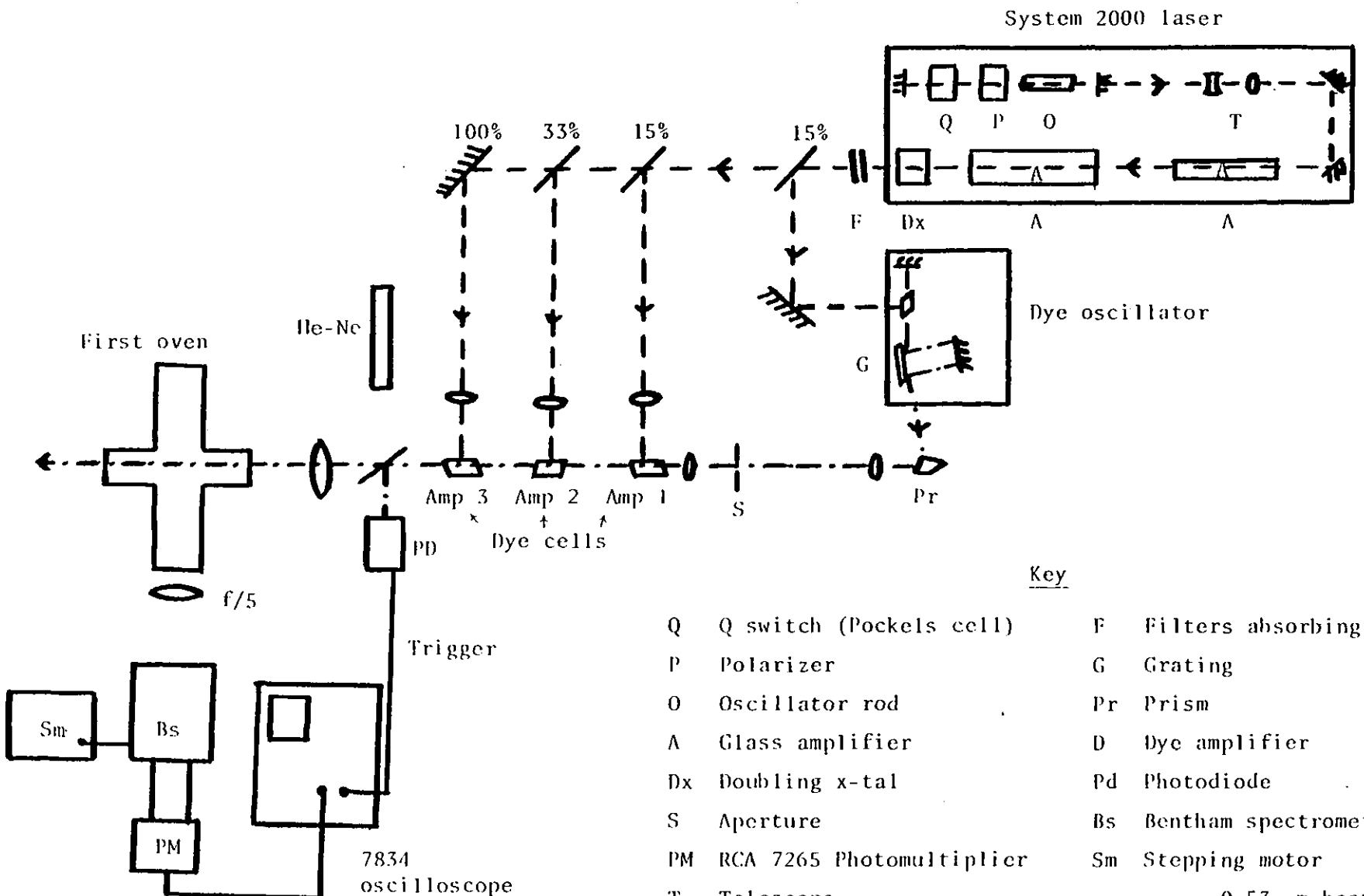
The oscillator rod was 5" long by ¼" diameter. Q-switching was achieved using a polarizer followed by a Pockels cell operating at ¼-wave voltage (Fig. 2.2). A 2.2 mm aperture was used in the oscillator cavity to produce a single transverse mode (TEM_{00}), 0.5 mrad divergence beam at λ = 10532 Å. This proved to be superior to a multimode output as its lower divergence increased the conversion efficiency of the doubling crystals by 50% and provided for a more homogeneous pumped volume in the dye cells. The oscillator could be fired every 2 seconds when realignment was necessary, usually on a monthly basis.

The first and second amplifier rods were 9" by ⅜" and 9" by ⅝" respectively. The second amplifier suffered thermomechanical damage as did the oscillator rod. This seemed to bear out the lower damage thresholds witnessed in phosphate glass lasers compared to the more commonly used silicate glass lasers (Koechner, 1976).

The laser system was then run without further mishap at a maximum of 4J in 45 ns FWHM over 1 cm^2, corresponding to a flux of $\sim$ 100 MW cm^{-2} and below the damage threshold of 10 J cm^{-2} (Koechner, 1976).

2.2.2 Frequency Doubling

Since tunable lasing in the yellow (5890 Å) and red (6854 Å) regions of the spectrum was required, a shorter wavelength for pumping a dye laser system was obtained by frequency doubling the 1 μm beam in non-linear birefringent crystals. A variety of such crystals were available: ADP, CDA, KD*P and KDP, where D* is dideuterium. Each were temperature stabilized to within 0.1°C. Their respective energy conversion efficiencies were then measured using a calorimeter with two HA3 filters placed behind the crystals to absorb > 99.99% of the



Key

Q	Q switch (Pockels cell)	F	Filters absorbing 1.05 μm
P	Polarizer	G	Grating
O	Oscillator rod	Pr	Prism
A	Glass amplifier	D	Dye amplifier
Dx	Doubling x-tal	Pd	Photodiode
S	Aperture	Bs	Bentham spectrometer
PM	RCA 7265 Photomultiplier	Sm	Stepping motor
T	Telescope	— — — —	0.53 μm beam
		— • — • —	0.59 μm dye laser

Fig. 2.1. Complete experimental layout.

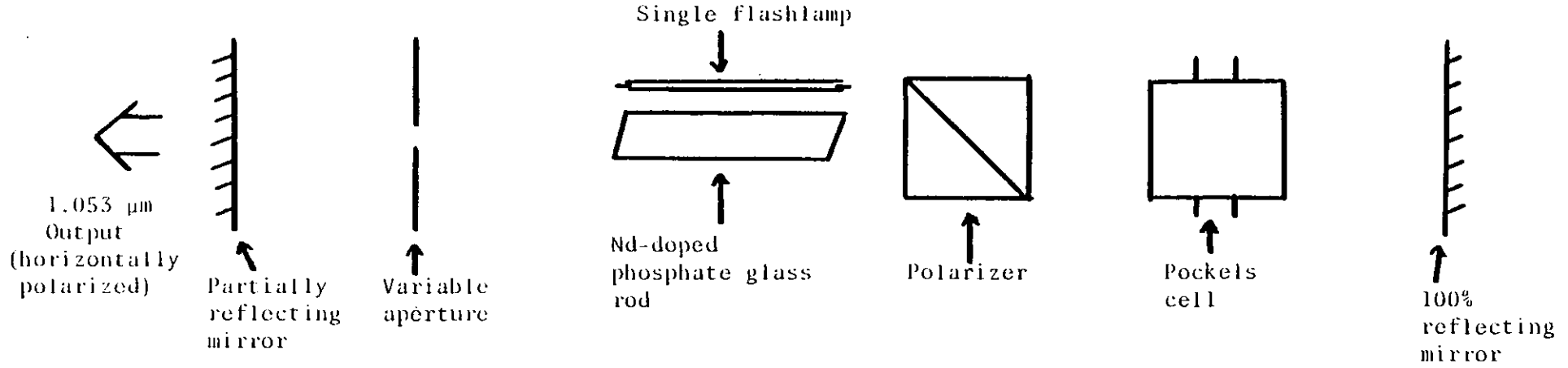


Fig. 2.2. Nd:glass oscillator.

remaining horizontally polarized 1 μm beam. The green beam (λ = 0.53 μm) output in each case was maximized by angle tuning to within 0.1 mrad.

The crystal characteristics and performances are presented in Table 2.1. Type I and Type II refer to the angle between the polarization of the fundamental and second harmonic beams, 90° and 45° respectively. θ is the angle between the incident beam and optic axis of the crystal, in the plane perpendicular to the ordinary axis. $\Delta\theta$ is twice the detuning angle from θ for which the conversion efficiency drops by a factor of two. The power conversion efficiency is for an incident 1 μm flux of 15 MW cm^{-2}.

TABLE 2.1

Doubling Crystal Characteristics

Crystal	Type	T/°C	Length/cm	θ/°	$\Delta\theta$/mrad	Efficiency/%	1μm Absorption/%
CDA	I	30	1.5	90	54	7.2	< 5%
ADP	I	25	3.8	41.4	0.4	7.9	60%
ADP	II	27	3.8	63.5	0.8	7.3	
KD*P	II	30	3.0	53.9	1.1	7.5	< 5%
KDP	I	30	4.0	40.3	0.4	7	20%

The dependence of the power conversion efficiency on the 1 μm incident power flux for KD*P and KDP are presented in Fig. 2.3, along with theoretical predictions (Handbook of Lasers, 1971). The conversion efficiency for KDP fell below theoretical calculations predominantly because the acceptance angle of the crystal, 0.4 mrad, was less than

the beam divergence.

Frequency conversion was accompanied by pulse shortening. The 45 ns FWHM 1 μm beam was converted to a 30 ns FWHM 0.53 μm beam even for the highest 1 μm incident fluxes used, I_ω = 100 MW cm^{-2}, where saturation of frequency doubling would be expected to occur. This pulse length ratio, 0.7, agreed very well with that predicted, $1/\sqrt{2}$, for temporal Gaussian pulses in unsaturated conditions for which $I_{2\omega} \propto (I_\omega)^2$.

The glass laser system could thus deliver 300 mJ in 30 ns over 0.5 cm^2 of 0.53 μm radiation, corresponding to 20 MW cm^{-2}, well below crystal damage thresholds. The doubled Nd-glass laser bandwidth was measured using a 1 m Czerny-Turner Monospek 2000 grating spectrometer with 0.3 Å resolution coupled to an RCA 7265 photomultiplier and 466 Tektronix oscilloscope, yielding a FWHM of 2.5 Å centered at λ = 5266 ± 0.5 Å (Fig. 2.4). Such a bandwidth would certainly be the predominant factor limiting spectral resolution in future laser scattering experiments.

2.3 Dye Laser

2.3.1 Dye Oscillator

The oscillator was based on a Shoshan design (Shoshan et al., 1977) and was built by B. Benker and G. Kolbe (Fig. 2.5). The dye cell consisted of three glass windows glued to three sides of a stainless steel housing. The 0.53 μm beam was passed through a cylindrical lens to form a 200 μm wide horizontal line focus of pumped dye molecules. The cavity consisted of two nominally 100% reflecting mirrors and a grating with 1800 lines/mm. Amplified spontaneous emission (ASE) occurring preferentially along the line focus was then

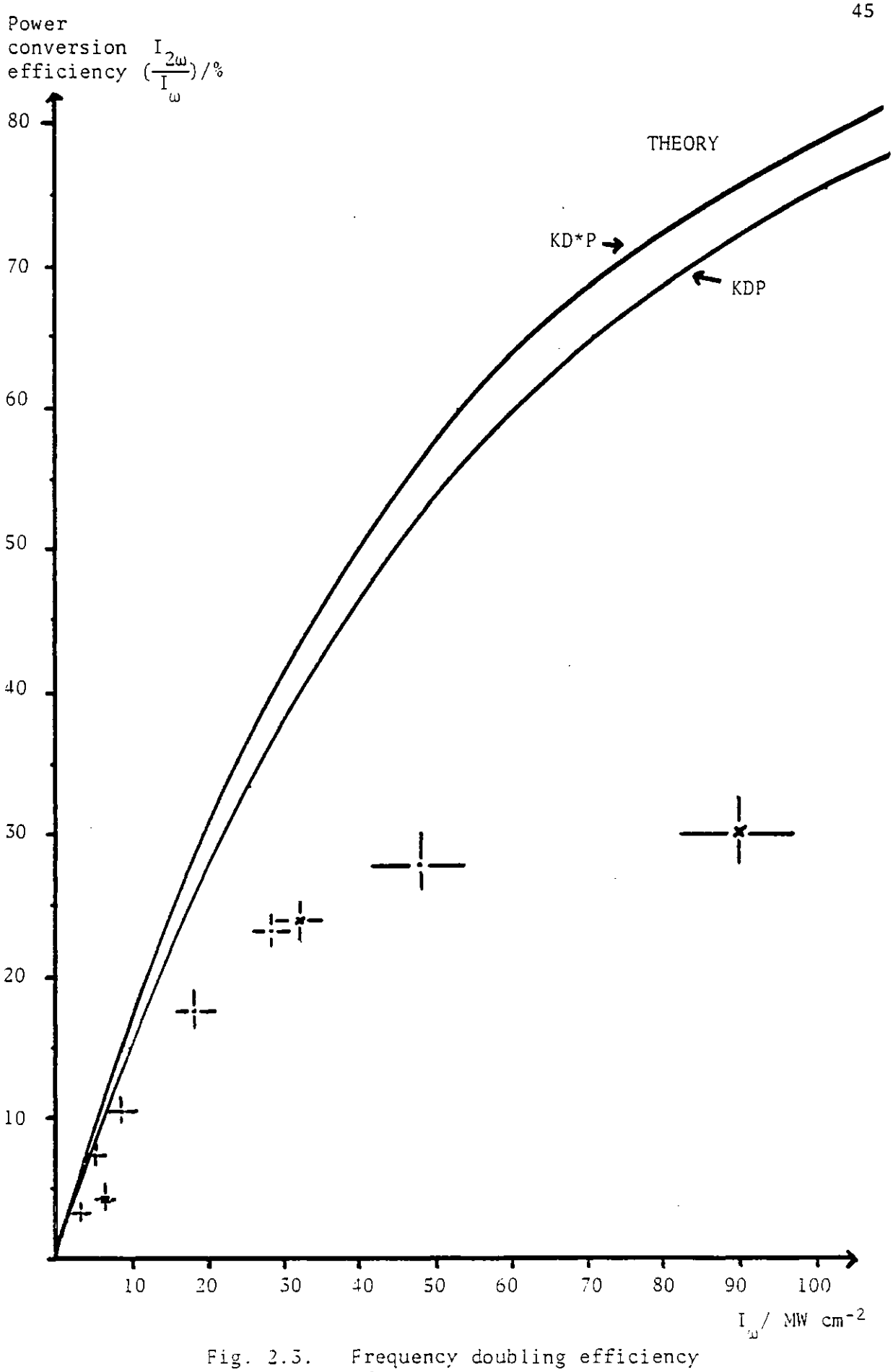


Fig. 2.3. Frequency doubling efficiency of KD*P and KDP crystals.

• KD*P × KDP

(Solid lines represent theory neglecting absorption and reflection losses.)

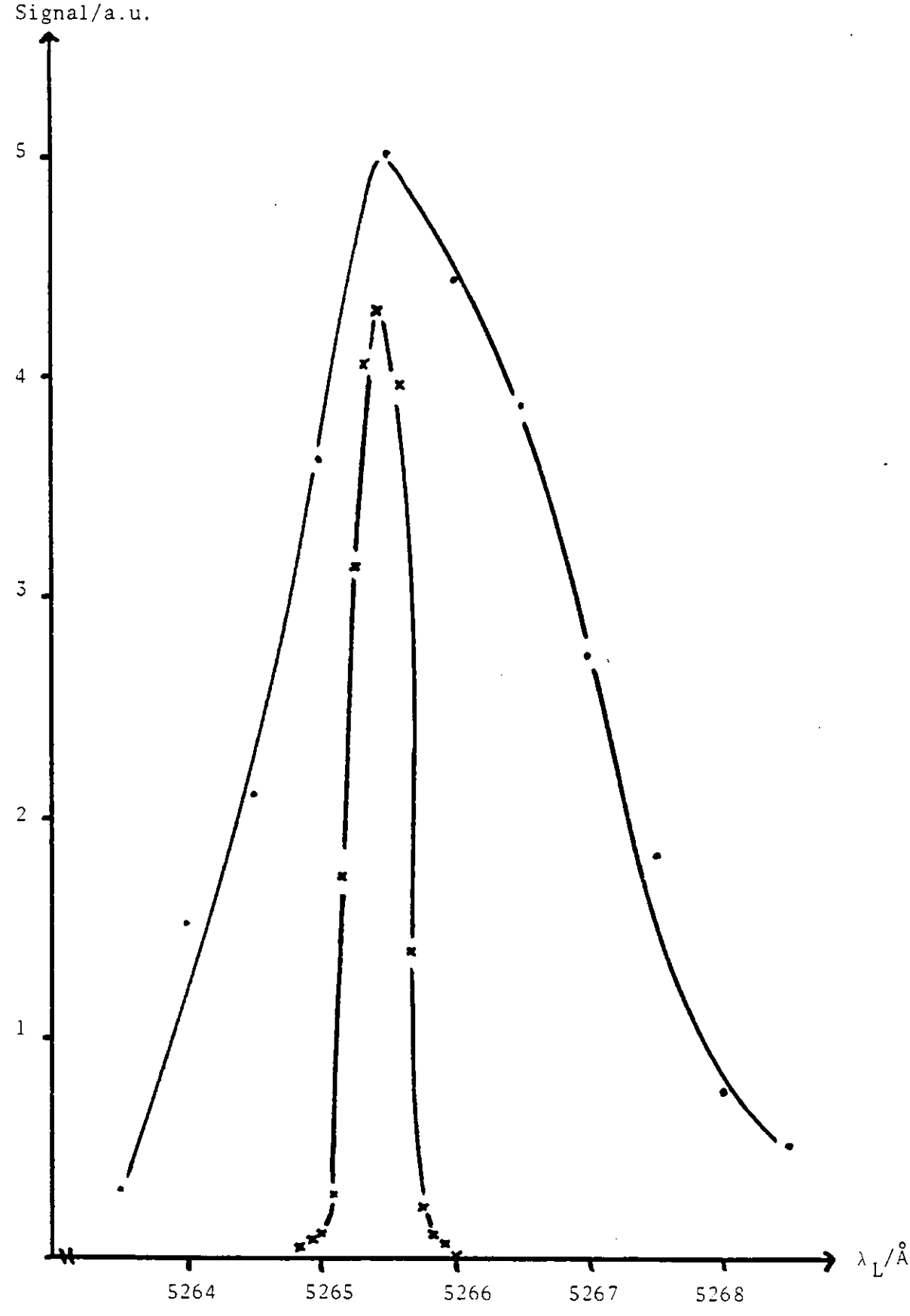


Fig. 2.4. Spectrum of frequency doubled Nd:glass beam. (Crosses represent instrument function of spectrometer.)

spectrally narrowed by using the first order diffraction from the grating as feedback. The output which was the grating reflection comprised a narrow-band (< 30 mÅ), 2 mrad divergence component superimposed upon a several 100 Å wide ASE component. Tuning to within 50 mÅ was achieved by tilting mirror B (Fig. 2.5) about a vertical axis.

The radiation was further spectrally filtered by passage through a constant deviation prism followed by focusing onto a pinhole aperture. This allowed only the tuned wavelength of interest and an estimated 10 to 20 Å on either side to be transmitted for further amplification in a chain of dye cells.

2.3.2 Dye Amplifiers

The amplifier cells were of similar design to the oscillator cell and were between 1.5 to 2 cm in length. Each had translational and rotational adjustment and were pumped transversely. Circulation of the dye solutions was deemed not to be necessary as the pumping rate never exceeded one shot every 20 seconds during an experimental run. The following parameters were all interdependent in choosing the optimal system which maximized the output dye laser power:

(a) Number of dye amplifiers.

(b) Distribution of 0.53 μm pump energy amongst the dye amplifiers.

(c) Optics for transport of the dye laser beam between cells.

(d) Dye types and concentrations.

In practice, two distinct systems were assembled to accommodate for the difference in dye lasing efficiencies at 5890 Å and 6854 Å (see Table 2.2).

TABLE 2.2

Distribution of Pump Energy

FRACTION/% / λ/Å	OSCILLATOR	AMP 1	AMP 2	AMP 3
5890	15 (ND1 Filter)	13	24	48
6854	15	28	57	Not used

With hindsight, two general comments should be made concerning multi-stage transversely pumped dye laser systems.

(a) The sharing of a given amount of pump laser energy amongst several dye cells proved more efficient (a factor of 2 in Rhodamine 6G) than just pumping one cell. This was because a greater fraction of the stored pump energy could be released under maximum efficiency conditions, saturated stimulated emission, by increasing the pump energy for each successive cell to match the increase in incident dye beam intensity. Clearly, such an advantage would be lost for infinitely high small-signal gain systems. However the dye concentrations and hence gain, $< 10\ cm^{-1}$, were kept low in the amplifier cells to reduce depletion of the pump energy by ASE.

(b) The optimum number of stages used was determined by the lasing efficiency of the dye solutions (Table 2.2). The higher the threshold pump energy for fluorescence, the higher the fraction of pump energy necessarily distributed to the first amplifier cell and hence to each successive stage. Thus the final cell(s) would be under-pumped and therefore redundant, the result being fewer stages for less efficient dyes.

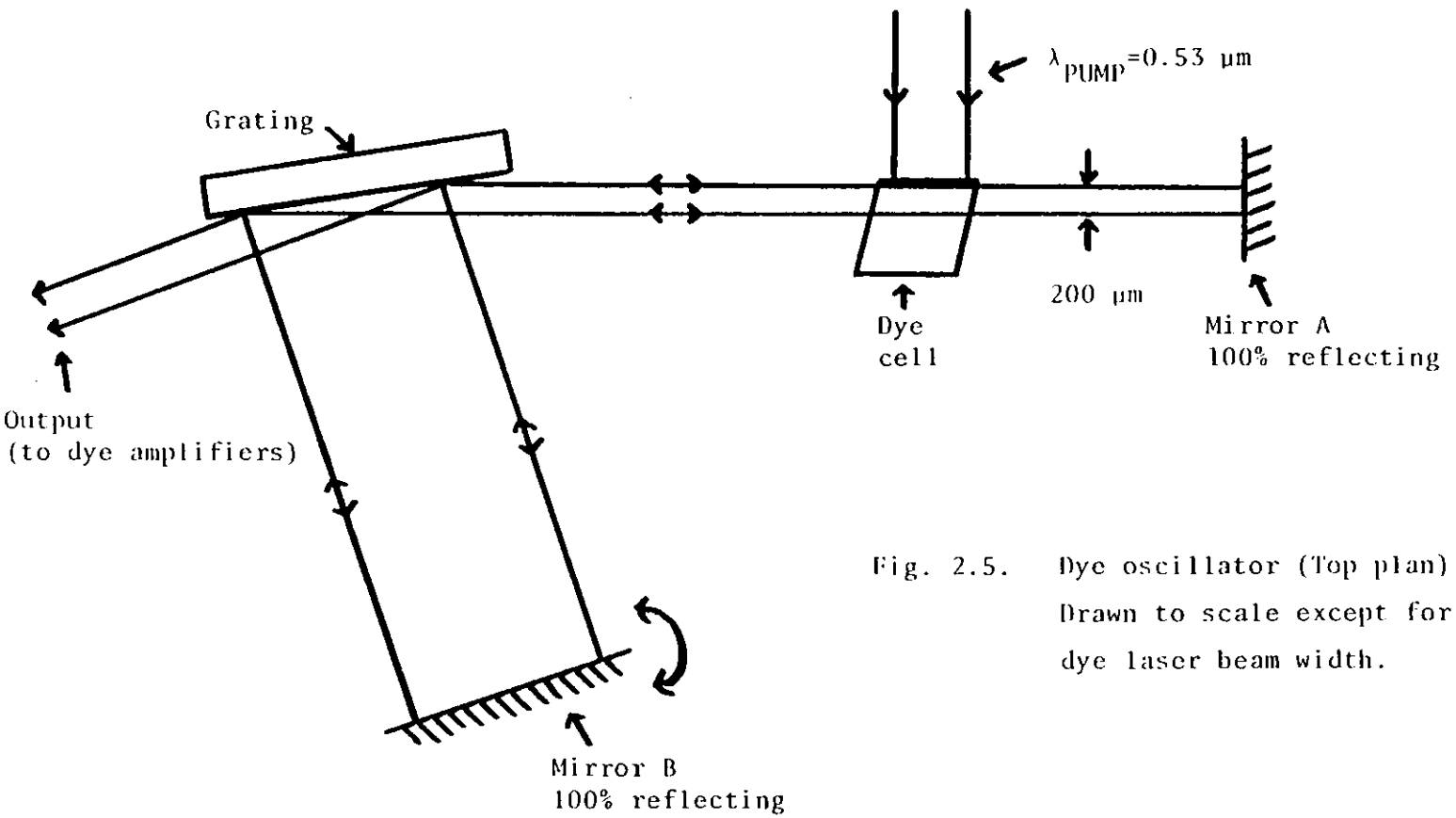


Fig. 2.5. Dye oscillator (Top plan). Drawn to scale except for dye laser beam width.

2.3.3 Dye Solutions

2.3.3.1 λ = 5890 Å. The two clear choices were Rhodamine 6G and Rhodamine B. Only Rhodamine 6G lased in the oscillator cavity, its peak ASE fluorescence being blue shifted, compared to flashlamp pumped systems, to 5700 Å at 1 g/litre in AR methanol. The peak fluorescence of Rhodamine 6G was even further to the blue as expected when diluted to 100 mg/litre in the dye amplifier cells. A gain in efficiency of two was achieved by replacing it with Rhodamine B at similar concentrations in the amplifier cells. The final molar concentrations opted for are listed in Table 2.3.

TABLE 2.3

Dye Solutions for λ = 5890 Å

Cell	Dye	Conc./M
Oscillator	Rhodamine 6G	1.5×10^{-3}
Amp 1	Rhodamine B	2×10^{-4}
Amp 2	"	"
Amp 3	"	"

Each amplifier cell was aligned in turn by measuring its tuned laser output energy, using pyroelectric meters between 0.01 mJ and 10 mJ and using a thermopile joulemeter for 3 mJ and above. Table 2.4 lists the performance of each stage. These amplifier efficiencies were similar to the highest efficiencies reported for other multistage laser

systems (Loth et al., 1975 and Wallenstein et al., 1979). The final maximum reproducible output, not including an estimated 20% ASE component, was 2 MW in 25 ns within 4 mm^2 with a 2 mrad divergence. The bandwidth was measured as < 10 mÅ FWHM using a Fabry-Perot with a free spectral range of 30 mÅ and 5 mÅ resolution. The energy fluctuations from shot-to-shot were 20%. The best laser beam spatial cross-sections achieved were D-shaped due to the flat inner surfaces of the front windows of the cells.

TABLE 2.4

Dye Laser Performance at λ = 5890 Å

Cell	0.53μm Energy/mJ	I/P Dye Energy/mJ	O/P Dye Energy/mJ	Efficiency/%
Oscillator	2	-	0.1	5
Amp 1	16	0.1	1.3	7.5
Amp 2	64	1.3	19	30
Amp 3	120	19	64	40
TOTAL	220	-	64	30

2.3.3.2 λ = 6854 Å. A variety of single dye and two dye (donor-acceptor) solutions were tested in the oscillator and the results shown in Table 2.5. The numbers refer to relative outputs and weak and strong refer to the dye concentrations, typically 0.2 g/ℓ and 1 g/ℓ respectively. If the lasing region of the dye mixture did not encompass λ = 6854 Å, this was noted as "λ too high" or "λ too low" in the Table. Finally, blank boxes represented too great a

TABLE 2.5

Dye Solutions Tested for λ = 6854 Å

TRANSFER DYES		LASING DYES					
		OXAZINE 720		OXAZINE 725		CRESYL VIOLET	
		Weak	Strong	Weak	Strong	Weak	Strong
R6G	Weak	λ too low				λ too low	λ too high
	Strong		3.5	4			
RB	Weak	λ too low			λ too high	λ too low	λ too low
	Strong		6	13			
Cresyl Violet	Weak	λ too low				λ too low	λ too low
	Strong		8	3			
None	-		λ too high		λ too high	λ too low	λ too low

penetration of the pumping beam into the dye for efficient lasing. Hence a mixture of 10^{-3} M Rhodamine B and 2.5 x 10^{-4} M Oxazine 725 in methanol proved to be the most efficient dye at λ = 6854 Å, and this solution was used in all three cells. Rhodamine B was superior to Rhodamine 6G as transfer dye because of the better spectral overlap between the emission bands of Rhodamine B (Berlman, 1971) and the absorption band of Oxazine 725. The optimum concentration ratio of donor to acceptor dye as well as the observed blue shift of Oxazine 725 in a dye mixture were in good agreement with results found elsewhere for Rhodamine-Oxazine mixtures (Reva et al., 1981).

Table 2.6 outlines the peak red laser system performance. A maximum power of 500 KW in 22 ns over 2 mm^2 was achieved. As such,

TABLE 2.6

Dye Laser Performance at λ = 6854 Å

Cell	0.53μm Energy/mJ	1/P Dye Energy/mJ	0/P Dye Energy/mJ	Efficiency/%
Oscillator	60	-	0.5	1
Amp 1	110	0.5	4	3
Amp 2	230	4	13	4
Total	400	-	13	3

it was 80% less efficient than the pure Rhodamine system because of losses incurred during two stage absorption and re-emission of photons and the lower quantum efficiency of Oxazine. It was interesting to note, however, the substantial reduction in ASE output from the oscillator compared to the Rhodamine 6G, attributed to operating closer to threshold lasing levels. The bandwidth was measured as before and estimated at < 10 mÅ and the divergence estimated at 2 mrad.

Both dye laser systems were maintained reproducible over an 18 month period by changing to a new dye solution when the laser output dropped significantly.

2.4 Ovens

The first oven consisted of a stainless steel pipe with 8 ports (Fig. 2.6a), designed by J. Salter. The major axis was fitted with four semi-cylindrical electric heating elements rated at 690 W each. With fire bricks placed around the elements to prevent excessive radiative and convective heat losses (Melton et al., 1980) temperatures

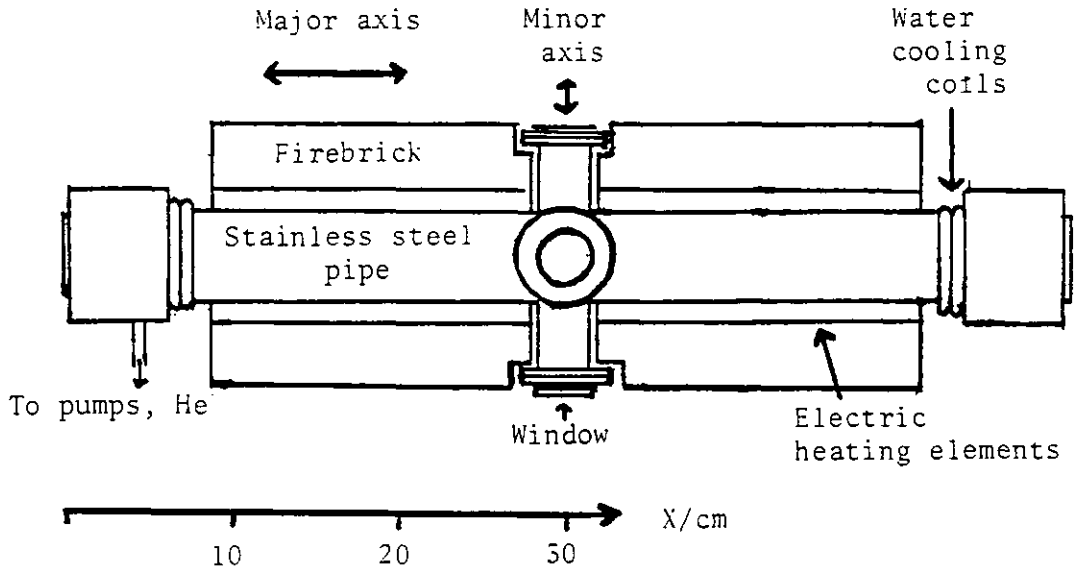


Fig. 2.6a. First oven: cylindrical symmetry about major axis and minor axes.

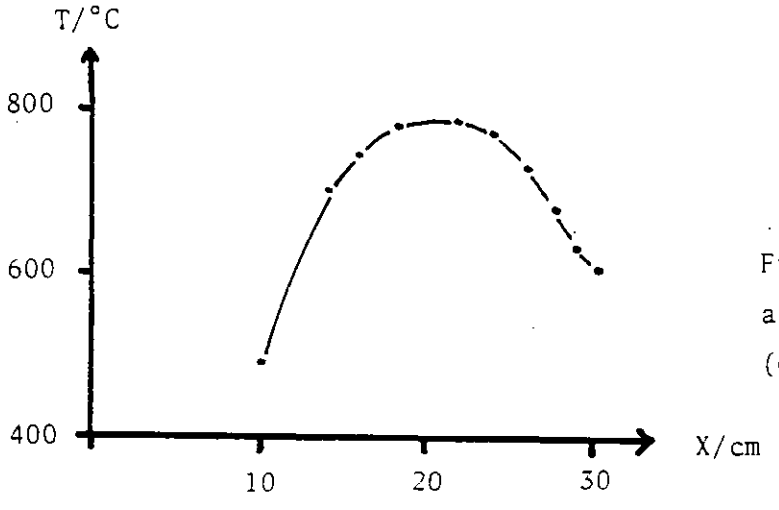


Fig. 2.6b. Temperature profile along major axis without heat-pipe. (Courtesy of Dr. R. J. Winfield)

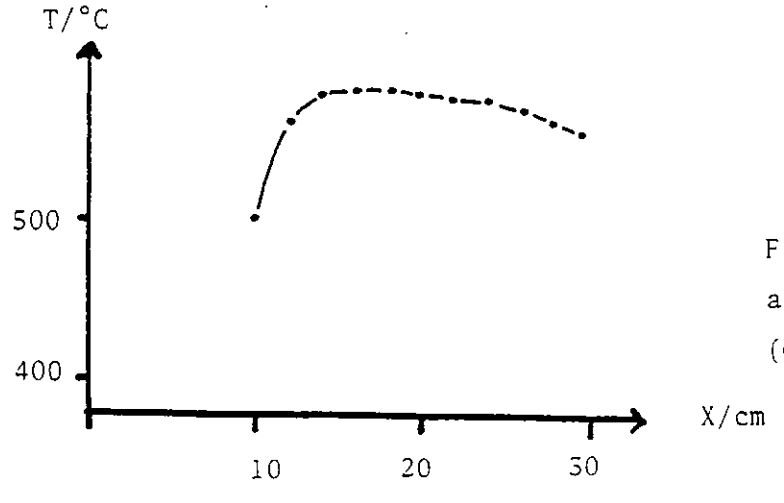


Fig. 2.6c. Temperature profile along major axis with heat-pipe. (Courtesy of Dr. R. J. Winfield)

up to 1000K were achieved corresponding to sodium vapor densities of 10^{18} cm^{-3} (JANAF Tables, 1971). All 8 ports were water cooled at the window ends to prevent the "O" rings providing the vacuum seals from melting.

Approximately 10 g of 99% grade sodium metal was initially placed in the centre region of the pipe. The oven was pumped down to 4 x 10^{-4} Torr and 20 Torr of helium added as buffer gas to protect the windows from sodium attack. A chromed-alumel thermocouple was inserted along the major axis to monitor the vapor temperature and hence density. Figure 2.6b shows the temperature profile along the major axis of the heated oven. For diagnostic purposes, a constant temperature throughout the central region of the oven was desirable. In an effort to remedy this, the oven was changed to heat-pipe operation (Melton et al., 1980) by insertion of a stainless steel gauze with 0.15 mm mesh spacing along the insides of the oven. In a heat-pipe, sodium vapor flowing outwards to the cooler ends of the oven condenses onto the mesh, flows back as a liquid by capillary action to the hottest region and is revaporized. This rapid heat transfer along the oven axis keeps, in theory, the flow zone isothermal. The new temperature profile was indeed flatter as predicted, but still dropped by 30°C at the central region, corresponding to a 60% density drop (Fig. 2.6c).

Unfortunately, as calculated in Chapter 1, there was insufficient laser power to bleach through such a 20 cm column of superdense ($> 3 \times 10^{17}$ cm^{-3}) vapor just to reach the cooler, diagnosable region. It was therefore decided to pump along the minor axis of the oven and view sideways. This plan was defeated by the large dimer (Na_2) density along the major axis of the oven reabsorbing the laser induced

fluorescence. For a sodium density of 10^{18} cm^{-3}, 13% dimers were expected in saturated vapor (JANAF Tables, 1971) with a mean photon absorption cross-section of 10^{-17} cm^2 (de Groot et al., 1975). This represented an unacceptable optical depth of greater than 20.

An absorption spectra using a tungsten lamp and plate spectrograph taken along the minor axis of the oven for $N_{Na} = 10^{17}$ cm^{-3} at the center region showed strong broad-band absorption features corresponding to the sodium D lines and the $A \leftarrow X$ and $B \leftarrow X$ dimer bands (Fig. 2.7). Thus it became apparent that either (a) sodium containment in a small volume within the present oven, or (b) a smaller oven with peak densities at the diagnosable region was necessary to reduce the optical depths seen by both laser and diagnostics. Both alternatives were used. Scheme (a) will be discussed in the next section and was used for the D line pumping experiments.

A plan of the second oven representing scheme (b), designed by R. Winfield and used for multiphoton ionization of sodium, is shown in Fig. 2.8. The oven was machined from a solid block of stainless steel with 6 cylindrical horizontal holes accommodating four 1 KW and two 0.5 KW firebar elements isolated from the oven by 1 mm thick quartz tubes. As for the previous oven, a stainless steel gauze was inserted for heat-pipe operation. The variety of angles subtended between the eight ports provided for viewing of different scattering K vectors in future laser scattering experiments. The optical depth measured at the He-Ne laser wavelength, $\lambda = 6328$ Å, was 0.5 for $N_{Na} = 5 \times 10^{16}$ cm^{-3}, a factor of 20 less than for the first oven. Such optical depths were corrected for in relative line intensity measurements described in section 4.8 and the satisfactory results obtained were proof that this second oven was suitable for diagnostics for

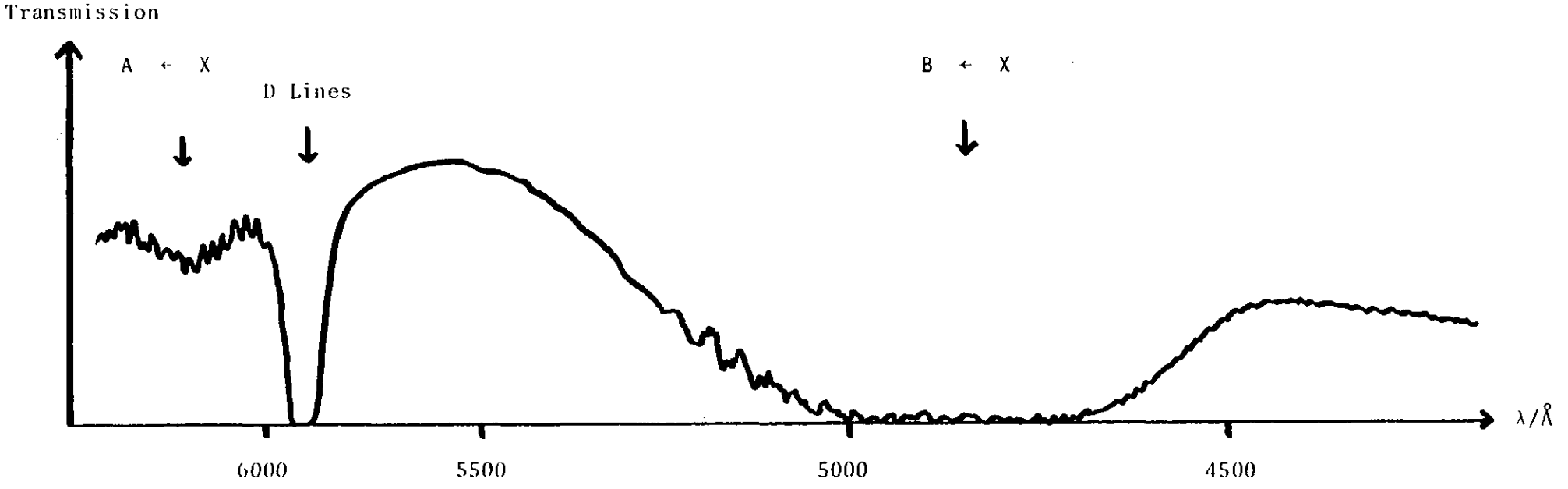


Fig. 2.7. Sodium vapor absorption spectrum: $N_{Na} = 10^{17}$ cm^{-3}.
(Courtesy of Dr. R. J. Winfield)

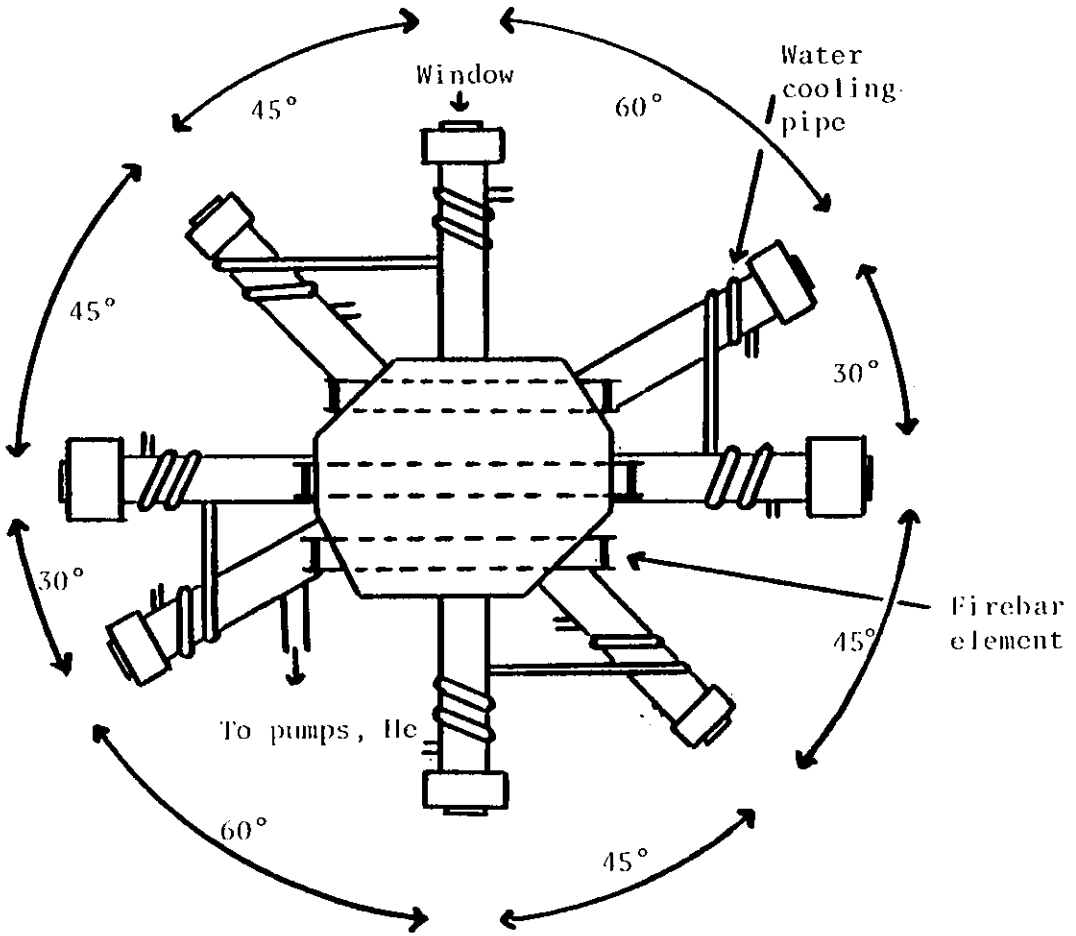


Fig. 2.8. Second oven (top plan).

Scale 4:1

$N_{Na} < 10^{17}$ cm^{-3}.

2.5 Sodium Containment

A variety of transparent materials have been used by different experimental groups to contain hot sodium vapor. The conditions are listed in Table 2.7, all of which are below $N_{Na} = 10^{17} - 10^{18}$ cm^{-3}, the density region desired.

TABLE 2.7

Sodium Vapor Containment

Reference	Material	T_{MAX}/K	N_{Na}/cm^{-3}
Gallagher, 1978	Pyrex	425	10^{11}
Gross, 1975	Pyrex	400	2×10^{10}
Granier, 1980	Alumino-Silicate	570	3×10^{14}
Krasinski, 1980	Corning 1720	620	10^{15}
Carré, 1981	Sapphire	540	10^{14}
Krebs, 1981	Sapphire	670	5×10^{15}
Stacewicz, 1981	Borax on Pyrex	700	10^{16}
Woerdman, 1979	Gehlenite Glass	755	3×10^{16}

Nevertheless, all materials, apart from gehlenite glass which was not commercially available (private communication, Woerdman) were tested at densities superior to 10^{16} cm^{-3}. Pyrex, alkali resistant Schott glass, Corning 1720 alkali resistant glass from Thorn and borax coated quartz all became orange or dark red within ½ hour exposure at

$N_{Na} = 3 \times 10^{16}$ cc^{-1}. Translucent alumina and sapphire, however, suffered only minor surface abrasions and gradual coating by a water soluble soot-like deposit. Therefore, all fluorescence experiments to be described in the next Chapter used either (Figs. 2.9a, b, c):

(a) sapphire windows clamped on to the sides of a miniature stainless steel heat-pipe tube placed along the length of the oven minor axis;

(b) an alumina heat-pipe tube along this same axis, or

(c) a sapphire tube held in a vertical position at the center of the oven, exhibiting 90% transmission at the He-Ne laser wavelength when clean.

Each of these provided a maximum sodium vapor length of 5 mm as viewed by the diagnostic equipment. The last scheme was implemented for the majority of the experiments as it also reduced the vapor length seen by the laser. Before each experimental run, the sapphire tube was washed in water, chromic acid, alcohol and acetone. Approximately 2 cm of sodium metal was then placed in the lower third of the tube, and the tube itself placed vertically in the oven which was pumped down to 4×10^{-4} Torr. The sodium vapor was free to escape through the top of the tube upon heating. Thus, within a month, the main body of the oven had acquired an unacceptably high vapor density and hence optical depth and had to be purged of sodium metal collecting at the oven window ends.

The time-consuming efforts in preparing a clean sodium cell daily, however, proved to be crucial in providing strong enough fluorescence signals for meaningful diagnostics to be carried out.

2.6 Diagnostic Equipment

The specifications of the diagnostic apparatus used for the

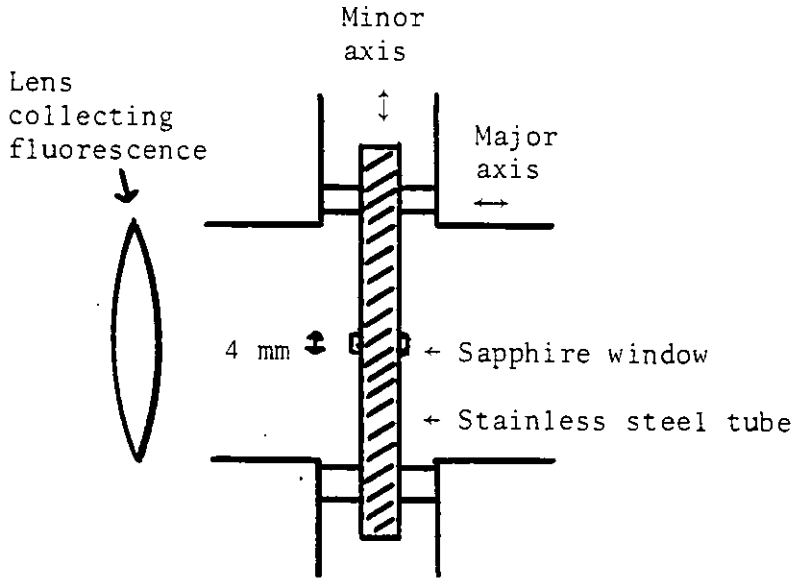


Fig. 2.9a.

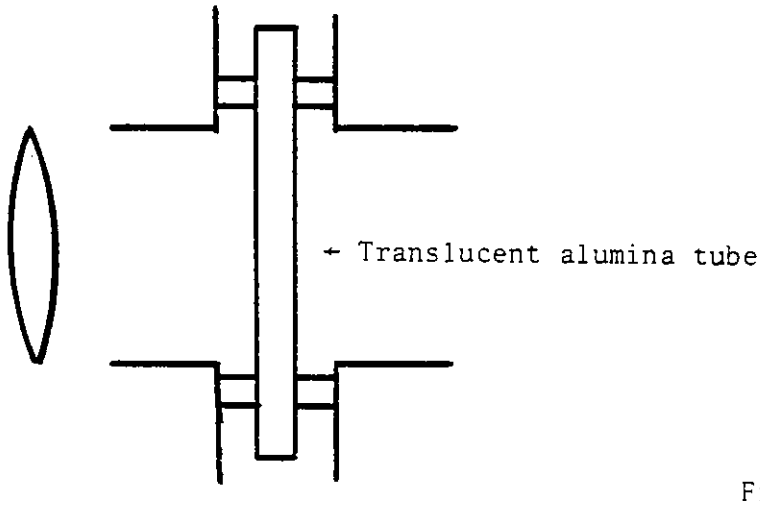


Fig. 2.9b.

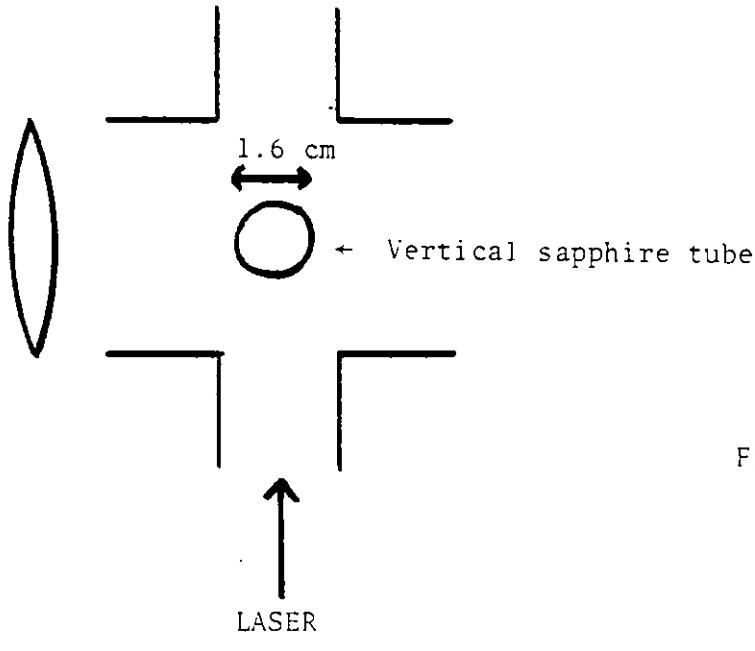


Fig. 2.9c.

Figs. 2.9a, b, c. Sodium containment schemes.

transmission, fluorescence, absorption and scattering experiments are listed in this section. Details of the optics and geometry used in each experiment will be presented in the next three chapters.

2.6.1 Transmission Experiment

Two PIN photodiodes with 1 ns risetimes were used to monitor input and transmitted laser fluxes. A Chelsea Instruments 30 cm spectrometer with camera and 40 Å/mm dispersion was also used.

2.6.2 Absorption Experiment

A tunable, < 10 mÅ bandwidth CW Spectra-Physics Model 380A dye laser was used in conjunction with a Hilger Watts 30 cm spectrometer and IP-28 photomultiplier.

2.6.3 Fluorescence and Scattering Experiments

The fluorescence/scattered signals were focused into a 30 cm f/4.7 Bentham grating spectrometer with a 1200 lines/mm grating and a maximum resolution of 1.5 Å. The spectrally dispersed light was then collected by either:

(a) an RCA 7265 14-dynode chain photomultiplier fitted with an S-20 cathode, operating between 1.2 and 3 kV;

(b) a Hadland Instruments streak camera with S-20 cathode, image intensifier and camera.

The electrical signals from the photomultiplier were recorded on either Tektronix 466 or 7834 oscilloscopes at 100 MHz or 20 MHz bandwidth.

2.6.4 Calibration

Wavelength: Low pressure Phillips Na lamp and prism bench spectrometer

Na Vapor Density: Tungsten lamp

Absolute Fluorescence Intensities: Tungsten Ribbon lamp Type W2GGV22 (calibrated against Standard Lamp by G. Cox (15/5/82)).

CHAPTER 3

IONIZATION BY RESONANCE PUMPING (λ_L = 5890 Å)

3.1 Ionization Scheme

The term diagram for NaI is shown in Fig. 3.1. The 3p state is split by the spin-orbit interaction common to all alkalis. This produces the characteristic sodium D line doublet: D1 ($3s_{\frac{1}{2}}$ - $3p_{\frac{1}{2}}$) at λ = 5896 Å and D2 ($3s_{\frac{1}{2}}$ - $3p_{3/2}$) at λ = 5890 Å.

3.2 Transmission Experiments

3.2.1 Introduction

The aims of this experiment were as follows:

(a) Fine tuning of the laser to the 3s - 3p line centers.

(b) A comparison of laser flux absorbed with sodium vapor density x length product derived from vapor pressure tables. For < 10% fractional ionization, this should be approximately given by equating the laser energy density absorbed, W', to the energy stored in the saturated 3p level and to that lost by spontaneous emission:

$$W' = -\tfrac{3}{4}\,(1 + A_{3s-3p} \times \tau_L)\, N_{Na}\, \ell\, E_{3s-3p} \qquad (3.1)$$

where ℓ is the excited vapor length, A_{3s-3p} the spontaneous decay rate of the 3p level and τ_L the laser pulse length.

The bleaching flux, I_B, necessary to maintain saturation in the absence of electron collisional de-excitation can then be defined as:

$$I_B = \tfrac{3}{4} N_{Na} E_{3s-3p} A_{3s-3p} \ell \qquad (3.2)$$

$$= 2 \times 10^7 \text{ W cm}^{-2}$$

for $N_{Na} = 10^{17}$ cm^{-3}, $E_{3s-3p} = 2.1$ eV, $A_{3s-3p} = 6 \times 10^7$ s^{-1} and ℓ = 10 cm.

(c) A search for near complete ionization of sodium vapor predicted earlier (section 1.4) as occurring when:

$$\tau_{ION} = \frac{2 \times 10^8}{N_{Na}} \qquad \text{(equation (1.10))}$$

Additional laser energy supplied towards ionization should lead to an increase in the slope of an absorption versus increasing sodium density plot. This effect has been reported by Koch et al. (1980) when pumping the 3p - 4d transition in sodium, and discussed in greater detail by Tam and Happer (1977) for dense Cs vapor irradiated by a mW CW dye laser tuned to the $6p_{\frac{1}{2}}$ - $8d_{3/2}$ transition lying $\sim$ 1.5 eV above ground-state. In this latter case, molecular rather than resonance absorption was predominant before significant ($N_e = 3 \times 10^{14}$ cm^{-3}) ionization took place during which a 10-fold increase in the absorption slope was observed. A transition between complete saturation and complete ionization in resonantly pumped sodium vapor would yield a maximum increase in slope of $(\chi + \frac{3}{2}T_e)/E_{3s-3p} \sim 3$. Despite this modest increase, deviations from linear absorption (equation (3.1)) were investigated as possible evidence for ionization.

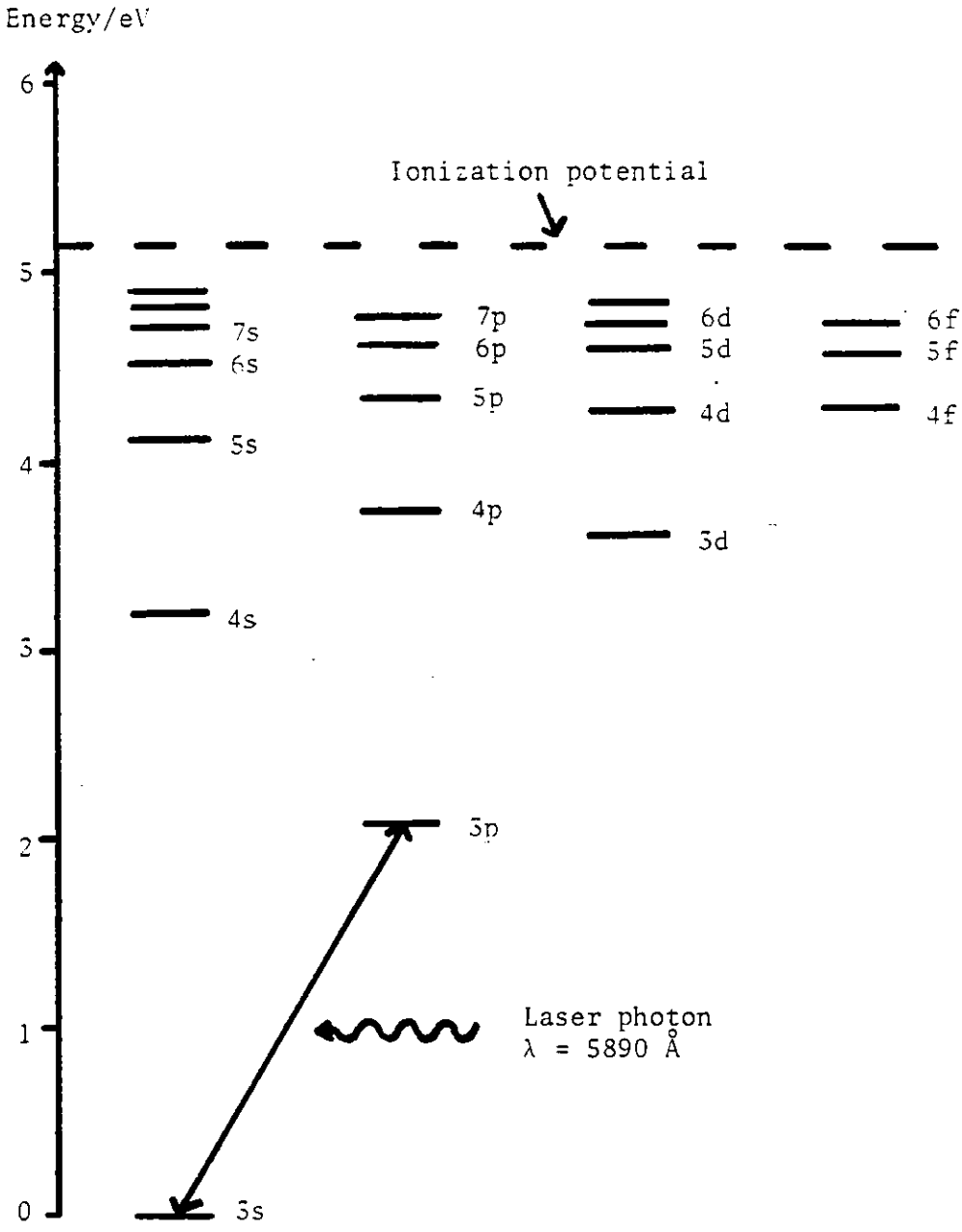


Fig. 3.1. Sodium term diagram (with resonant pumping scheme).

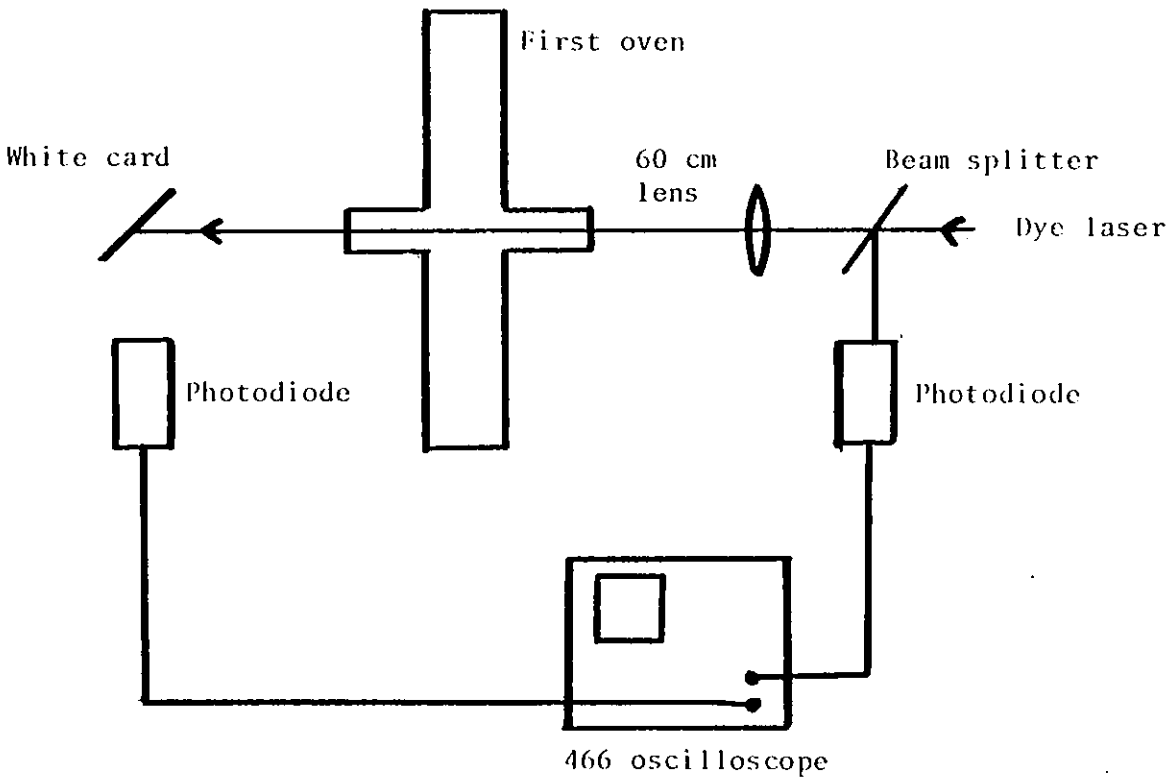


Fig. 3.2. Experimental layout for transmission experiments.

3.2.2 Experimental Details and Results

The experimental layout is shown in Fig. 3.2. The relative input and transmitted laser fluxes were monitored by two PIN photodiodes and their signals displayed on a 466 Tektronix oscilloscope via 50 Ω terminators. The laser beam was focused by a 60 cm focal length lens into the minor axis of the sodium oven and no special sodium containment was provided. The laser was then tuned to within 0.5 Å of either D line center by finding the maximum absorption (Fig. 3.3) for a laser energy of 1 mJ in 23 ns in a sodium vapor density $N_{Na} = 8 \pm 2 \times 10^{15}$ cm^{-3}. Figures 3.4 and 3.5 show plots of laser transmission versus sodium density for 1 mJ and 5 mJ laser energy respectively. The densities were deduced from vapor pressure tables (JANAF, 1971) and the transmission results corrected for laser fluctuations by ratioing the photodiode signals. The curves drawn through the experimental points are for visual aid.

3.2.3 Analysis of Transmission Results

The high density regions of Figs. 3.4 and 3.5 show a levelling in transmission towards a finite value rather than the predicted steepening. In fact, the transmitted beams at high densities were observed to be solid cones of $\sim$ 20 mrad half-angle, yielding 15 - 20 ns FWHM speckled reflections typical of coherent emission. Such off-axis emission has recently been observed by Brechignac et al. (1980) in resonantly pumped strontium vapor for similar laser fluxes and vapor densities. They attributed the speckled emission to filamentation during self-focusing of the laser beam. Skinner and Kleiber (1980) suggested the conical emission was a consequence of non-linear 4-wave mixing (see Ewart et al., 1981).

This unexpected result prompted a spectral analysis of the transmitted light cone. For this purpose, the Bentham spectrometer was interspaced between beam and photodiode. At $N_{Na} = 10^{17}$ cm^{-3}, the spectrum of transmitted light consisted of two $\sim$ 20 Å FWHM spikes centered symmetrically about the D lines and peaking at $\sim$ 5950 Å and $\sim$ 5850 Å. This self-reversed lineshape, quite apart from its coherent nature, was clear evidence of insufficient laser energy to bleach through the vapor column at $N_{Na} = 10^{17}$ cm^{-3}. Hence, only stimulated emission at wavelength detunings corresponding to optical depths $\lesssim 1$ could be expected to escape. Figure 3.6 is a Polaroid picture of the self-reversed spectrum taken with a Chelsea Instruments spectrometer.

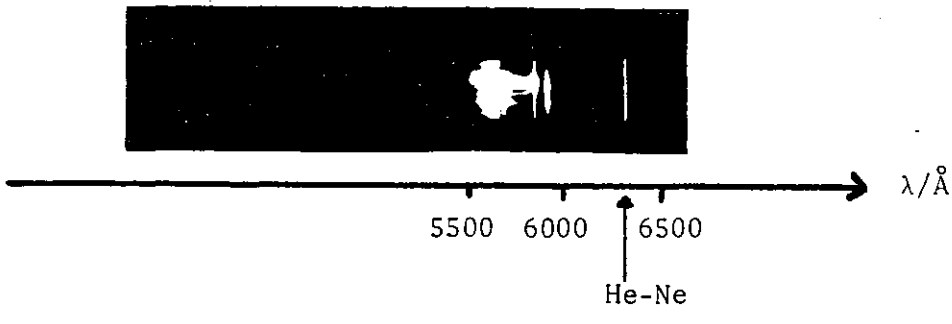


Fig. 3.6. Spectrum of transmitted laser light.

The emission between 5600 and 5700 Å is laser ASE, another factor contributing to the anomalously high transmission observed in Figs. 3.4 and 3.5. The most interesting feature, however, is the absorption line at $\lambda \sim 5685$ Å in the ASE corresponding to the 3p - 4d transition (see Fig. 3.1).

The length of unexcited vapor contributing to the self-reversal can be estimated as follows. The D lines are assumed to be resonance broadened Lorentzians (see section 3.4.2.5) for all detunings < 100 Å.

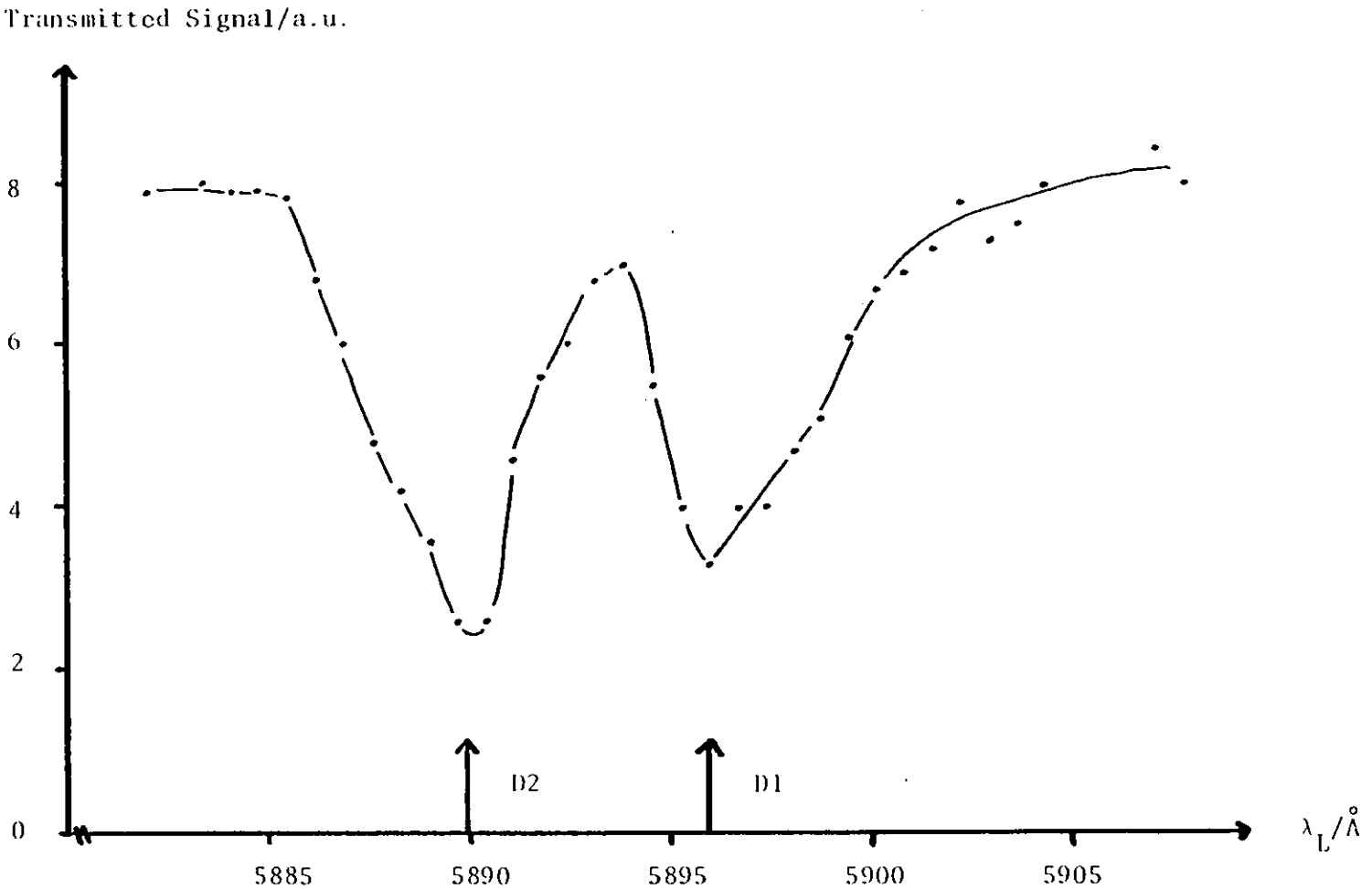


Fig. 3.3. Absorption profile of sodium D lines: $N_{Na} = 8 \times 10^{15}$ cm^{-3}.

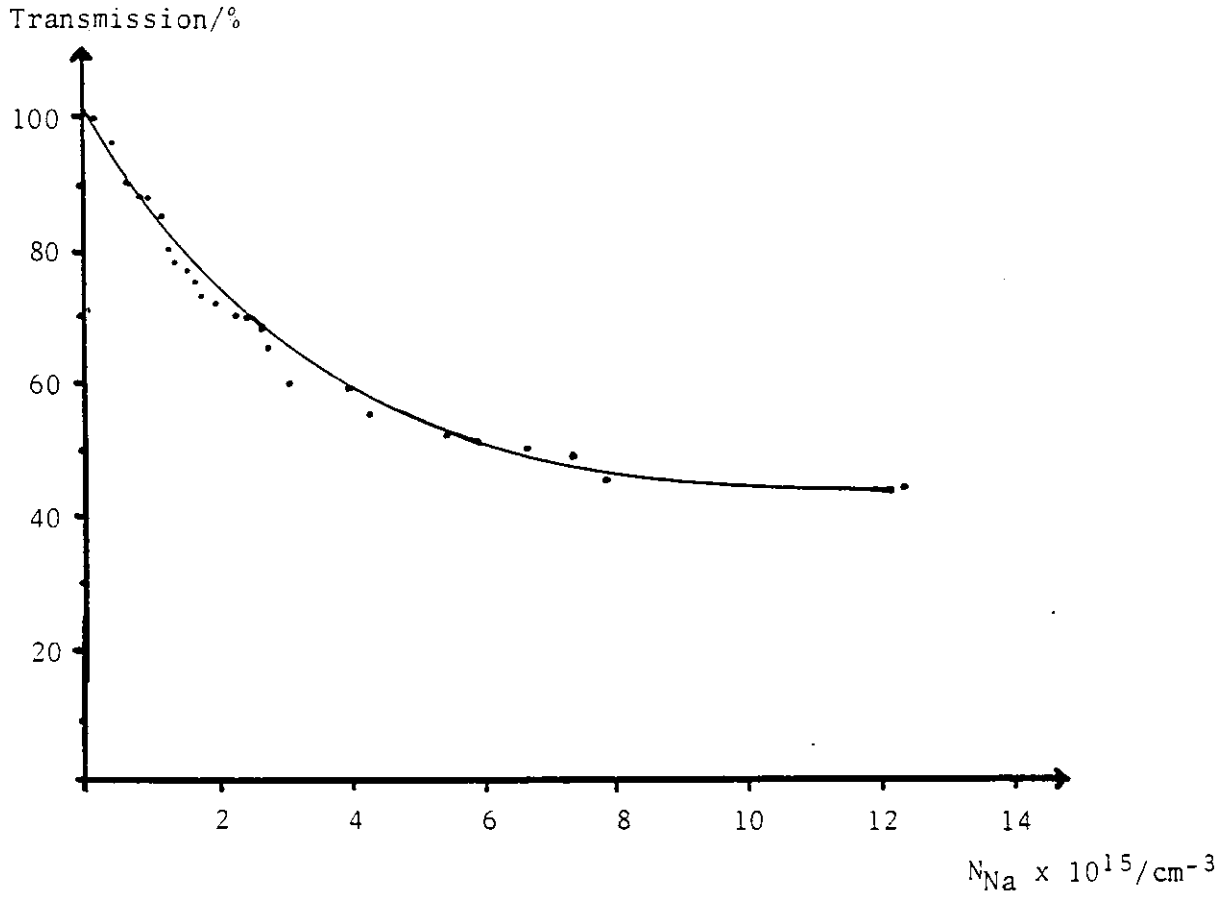


Fig. 3.4. Laser transmission at low N_{Na}.
λ_L = 5896 Å, $I_L \approx$ 4 MW cm^{-2}.

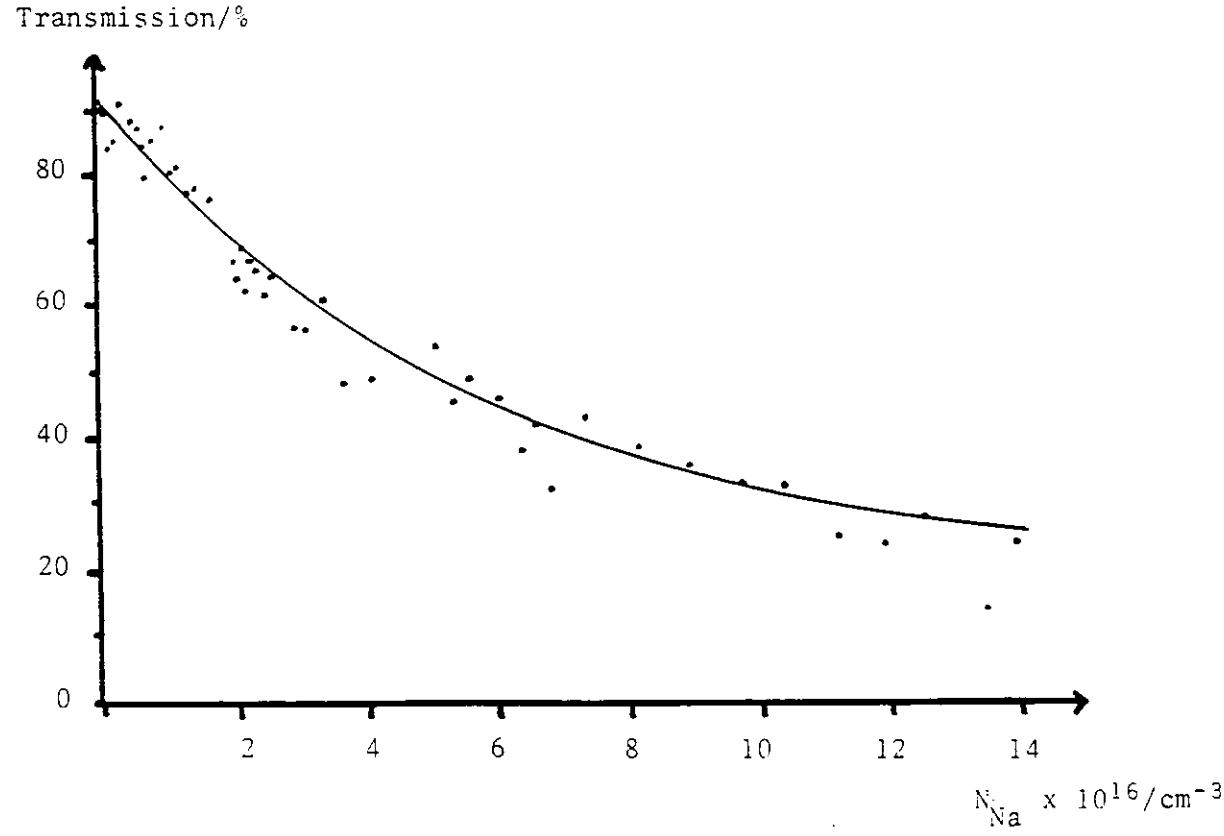


Fig. 3.5. Laser transmission at high N_{Na}.
λ_L = 5890 Å, $I_L \approx$ 20 MW cm^{-2}.

This is certainly true in the line core as $\frac{\Delta\lambda_R}{\Delta\lambda_D} = \frac{.042}{.015} \sim 3$ at $N_{Na} = 10^{17}$ cm^{-3}, where $\Delta\lambda_R$ and $\Delta\lambda_D$ are the resonance and Doppler widths respectively. Furthermore, the theoretical quasistatic correction applied by Hynne (1974) is negligible for $\Delta\lambda \gtrsim 10$ Å, as experimentally verified by Veza and Pichler (1983). The optical depth is then given by:

$$\tau(\lambda - \lambda_0) = \frac{K_0 (\Delta\lambda_R)^2 \, \ell}{(\lambda - \lambda_0)^2 + (\Delta\lambda_R)^2} \qquad (3.3)$$

where K_0 is the line center absorption coefficient and ℓ the vapor length. For $N_{Na} = 10^{17}$ cm^{-3}:

$$\tau(\lambda - \lambda_0) = \frac{1.5 \times 10^5 \times (.04)^2 \times \ell}{(\lambda - \lambda_0)^2} \quad \text{for } \lambda - \lambda_0 >> \Delta\lambda_R$$

$$\Rightarrow \quad \lambda - \lambda_0\big|_{\tau=1} = \sqrt{250\,\ell} \qquad (\lambda - \lambda_0 \text{ in Å})$$

Hence the peak emission occurring at $\lambda - \lambda_0 \sim 50$ Å corresponded to $\ell = 10$ cm. This compared favorably with the diameter of the heating elements, 6 cm.

From Fig. 3.5, 80% transmission occurred at $N_{Na} = 1.7 \times 10^{16}$ cm^{-3} for an irradiance of 3 mJ of tuned radiation within 23 ns and in $\sim$ 1 mm^2. Using equation (3.1), ℓ can be estimated at 30 cm, again consistent with oven dimensions.

3.2.4 Conclusions on Transmission Results

Good agreement at low densities ($< 2 \times 10^{16}$ cm^{-3}) between laser energy transmitted and energy absorbed in exciting the sodium D lines confirmed the presence of saturated vapor in the oven. The substantial

fraction (30%) of unabsorbed ASE and of stimulated emission in the transmitted beam at high densities ruined any chance of observing enhanced absorption due to ionization. These unexpected results demonstrated the need for spectral resolution in future diagnostics.

3.3 Fluorescence Experiments

3.3.1 Introduction

Spectroscopy as a diagnostic tool for plasmas has been used for over 40 years (Inglis and Teller, 1939) to determine level populations, ion and electron densities, and temperatures. At present, topics relevant to this thesis such as plasma line broadening in non-hydrogenic species and the conditions for validity of temperature measurements from relative line intensities show good agreement (within 10 - 20%) between theory and experiment (Griem, 1964). These have therefore become primary diagnostics for N_e, T_e and $N(n\ell)$, allowing less well researched and understood plasma effects such as ionization potential depression and the emergence of dipole forbidden components to be compared with existing theory.

However, there are few spectroscopic observations of plasmas approaching the non-Debye limit. The majority pertain to plasmas formed by laser-solid interactions relevant to fusion (Kilkenny et al., 1980) in which maximum $N_e = 3 \times 10^{23}$ cm^{-3} and minimum $T_e = 10$ eV are attained, corresponding to $N_D = 0.4$. Under such conditions, the electrons are partially Fermi degenerate (Fermi temperature $\sim$ 15 eV). The spectroscopic effects of this degeneracy (Burgess and Lee, 1982 and Davis and Blaha, 1982) are superimposed upon any non-Debye effects. However, lower N_e and T_e plasmas offer the opportunity of retaining

strongly-coupled behavior while lifting this degeneracy.

The only known research based on fluorescence diagnostics of such plasmas is listed in Table 3.1.

TABLE 3.1

Strongly-Coupled Non-Degenerate Plasmas

Reference	Plasma Device	N_e/cm^{-3}	T_e/eV	N_D	Features Observed
Ya'akobi (1968, 1969)	Exploding Li Wires	10^{19}	1	0.5	Linear Stark effect; forbidden lines; plasmon satellite
Baker (1979)	Z-pinch	$3x10^{18}$	1.5-2	2-3	Quasi-molecular satellites; asymmetries
Baldwin	Z-pinch	10^{19}	2-3	2-3	

The regime investigated has been extended in the fluorescence experiments described next by lowering the temperature to $T_e \sim 0.2 - 0.3$ eV for $N_D \sim 1-2$.

3.3.2 Experimental Layout

The experimental layout is shown schematically in Fig. 2.1. The 2 MW, 25 ns dye laser beam was tuned to the D2 line at $\lambda = 5890$ Å and focused to an ~ 2 mm^2 spot at the center of the oven where the sodium was contained by one of the three schemes mentioned earlier (section 2.5).

The fluorescence at 90° was collected by a 14 cm focal length lens and focused onto the horizontal slit of an f/4.3 Bentham spectrometer placed on its side. In this manner a 1 - 2 cm length of laser-induced fluorescence could be imaged onto the slit, yielding a measured 8-fold increase in photon numbers entering the spectrometer compared to a vertical slit geometry. Slit widths of 50 and 100 μm were used to provide 2 to 2.5 Å resolution. The spectrally dispersed light was imaged onto an RCA 7265 photomultiplier run at 2 to 2.4 kV. An S-20 photocathode was chosen for its increased sensitivity in the near infrared, allowing the important 3p - 3d sodium transition at λ = 8194 Å to be spectrally resolved. The photomultiplier signals were displayed on a 7834 or 466 Tektronix Storage oscilloscope with either 3 ns or 15 ns time resolution.

The spectra were recorded on a shot-to-shot basis using a stepping motor drive to scan through lines at 0.5 or 1 Å intervals. Since a typical run for one spectral line lasted one hour, it was important to monitor any pressure, temperature or neutral density fluctuations. Three methods used to estimate absolute densities will therefore be described next before presenting lineshape results.

3.3.3 Sodium Vapor Density

3.3.3.1 Vapor Pressure Tables. The most recent data available (Janaf Thermochemical Tables, 1971) were used to estimate N_{Na} from thermocouple temperature readings. Although this proved to be the easiest monitor of N_{Na}, systematic errors arise due to

(a) the presence of impurities in the molten sodium;

(b) the assumption of saturated vapor;

(c) the difference in temperature and hence density between the region probed by the thermocouple and the laser-vapor interaction region.

3.3.3.2 Dimer Absorption of He-Ne Laser Beam (λ_L = 6328 Å). The absorption coefficient of sodium dimers as a function of wavelength has been experimentally determined in saturated sodium vapor at 900K (de Groot and van Rooijen, 1975). At other temperatures, however, vapor pressure tables yielding the ratio N_{Na_2}/N_{Na} versus temperature are needed to translate these absorption coefficients into atom concentrations. The only advantage remaining over method (a) is the possibility of probing the interaction region.

This has been achieved with a 10 mW He-Ne laser using the layout described previously in the transmission experiment (section 3.2.2). Unfortunately, no meaningful results could be obtained when the sodium was contained in the vertical sapphire tube (Fig. 2.9c) due to scattering of the He-Ne beam from the surfaces of the tube degraded by sodium attack. For horizontal containment (Figs. 2.9a and b), $\sim$ 90% absorption of the He-Ne beam occurred at a dimer density of 10^{16} cm^{-3} as inferred from the JANAF Tables. Since the photon absorption cross-section at λ = 6328 Å is 4 x 10^{-17} cm^2 (de Groot and van Rooijen, 1975) the vapor column length can be calculated as

$$0.1 = e^{-10^{16} \times 4\times10^{-17} \times \ell} \Rightarrow \ell = 5 \text{ cm}$$

which is consistent with the tube length. It should be noted, however, that the He-Ne transmitted intensity flickered at a frequency of 0.2 to 0.3 Hz by $\sim$ 10% about a mean value. All plasmas formed by the pulsed

dye laser were thus subject to a 10% uncertainty in initial sodium density from shot-to-shot.

The He-Ne laser beam suffered strong easily visible side-scattering in sodium vapor above $N_{Na} \sim 3 \times 10^{16}$ cm^{-3}. This was attributed to molecular absorption and re-emission ($\sigma \sim 4 \times 10^{-17}$ cm^2) rather than to atomic Rayleigh scattering from the red wing of the D lines ($\sigma \sim 3 \times 10^{-23}$ cm^2) (see section 5.2.2). The transition from saturated to unsaturated vapor as the molten sodium supply disappeared by vapor diffusion from the containment tubes manifested itself in a rapid (< 1 minute) drop in this He-Ne laser beam scattering intensity and signified the end of an experimental run.

3.3.3.3 Curve of Growth of Resonance Line. The absorption line-shape of the D lines provided an independent estimate of the ground-state sodium population density. Using equation (3.3), the wavelength detuning corresponding to 50% absorption is given by:

$$\lambda - \lambda_0|_{\tau=0.7} = \sqrt{1.4 K_0 \ell}\ \Delta\lambda_R \qquad \text{for } \lambda - \lambda_0|_{\tau=0.7} >> \Delta\lambda_R$$

For the sodium D2 line blue wing:

$$\Delta\lambda_R = 4.2 \times 10^{-19}\ N(3s) \qquad \text{(Popov and Ruzov, 1980)}$$

$$K_0 = 1.5 \times 10^5\ \text{cm}^{-1}$$

$$\Rightarrow \qquad \lambda - \lambda_0|_{\tau=0.7}/\text{Å} = 2 \times 10^{-16}\ \sqrt{\ell}\ N(3s) \qquad (3.4)$$

The variation in $\lambda - \lambda_0|_{\tau=0.7}$ with sodium vapor density was monitored using a 60 W tungsten lamp as background light source focused onto the 1.6 cm diameter sapphire tube. The transmitted light flux was scanned spectrally with the Bentham spectrometer. The results are

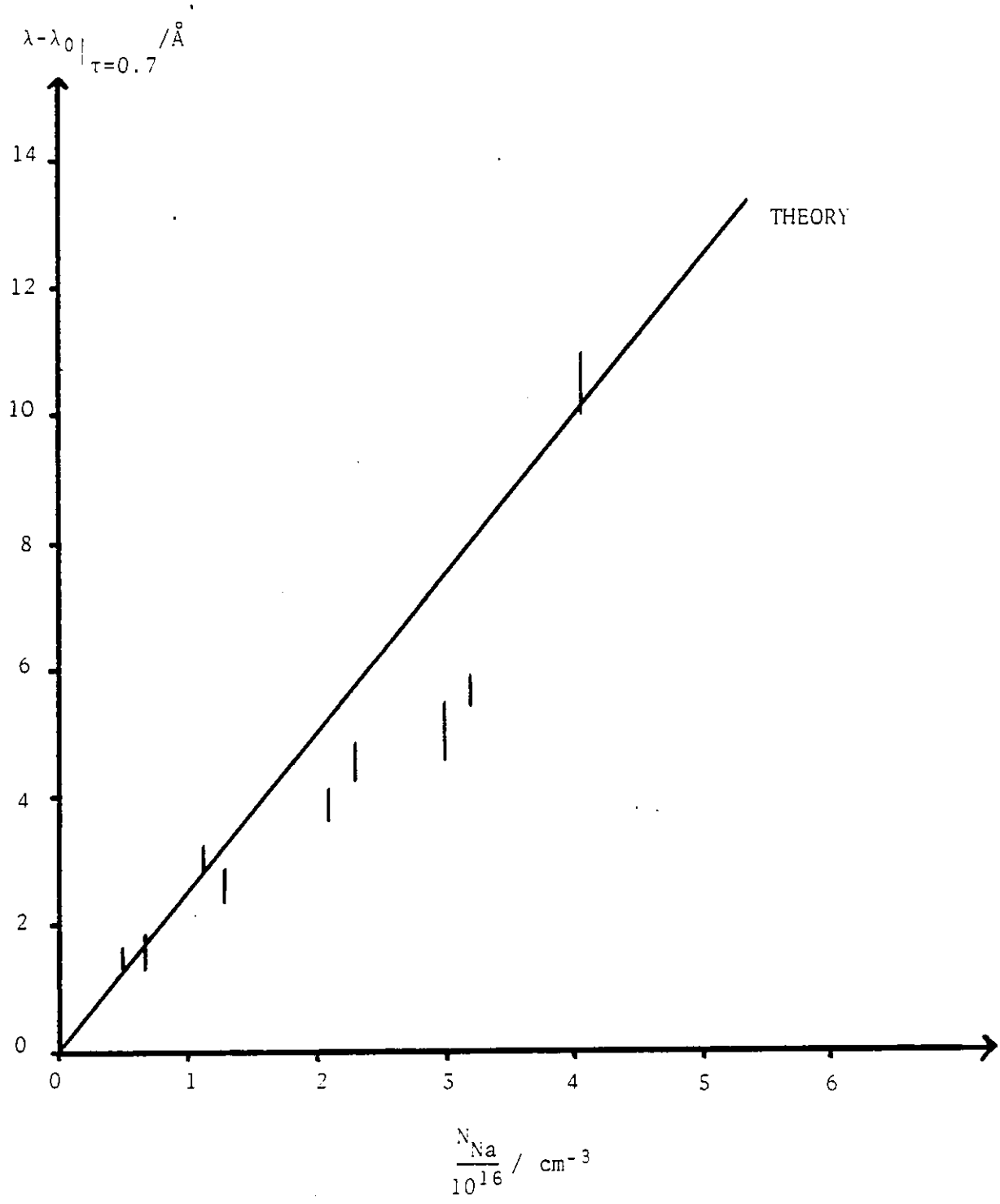


Fig. 3.7. Curve of growth.

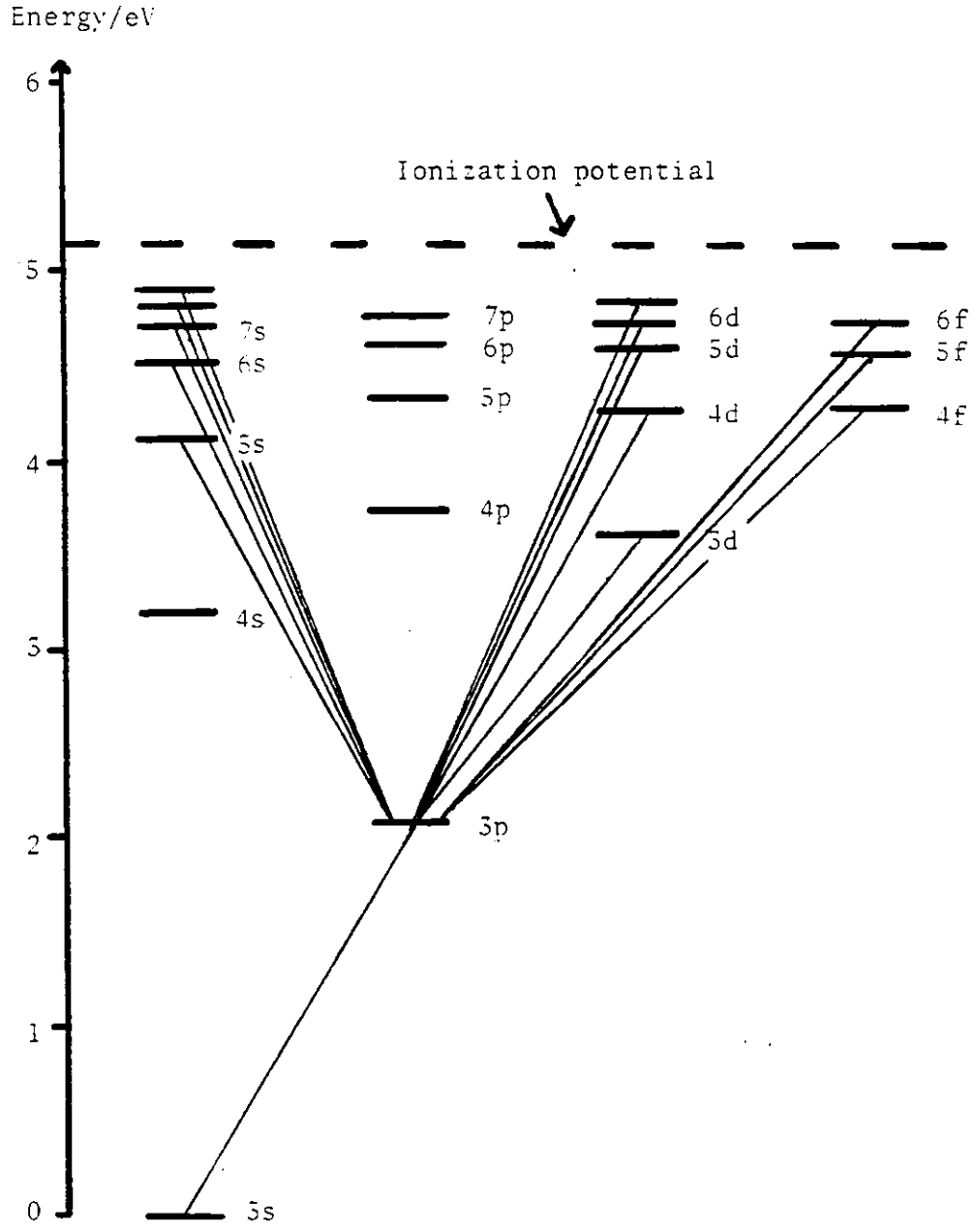


Fig. 3.8. Sodium term diagram (with emission lines).

presented in Fig. 3.7 along with the theoretical prediction of equation (3.4). The temperatures corresponding to each absorption lineshape have been converted to sodium densities using the JANAF Tables. Hence, the goodness of fit between theory and experiment in Fig. 3.7 is a direct test of the agreement between sodium densities determined spectroscopically and by thermodynamics. The results obtained show that up to 50% systematic errors in N_{Na} can be expected when relying on vapor pressure tables.

3.3.4 Fluorescence Results

The laser excited sodium vapor emitted a white glow similar to that reported in laser pumped caesium vapor (Tam and Happer, 1977). The sodium atomic doublet transitions identified in emission and shown in Fig. 3.8 were as follows: 3p - ns for n = 5 - 9, 3p - nd for n = 3 - 10, 3p - nf (dipole forbidden) for n = 4 - 6 and the D lines 3s - 3p. Temporally resolved profiles with 1.8 to 2.3 Å resolution were recorded for 3p - 3d, 3p - 4d, 3p - 5s, 3p - 5d, 3p - 6d and 3p - 6s transitions at two sodium densities $N_{Na} = 8 \times 10^{16}$ cm^{-3} and 3×10^{17} cm^{-3}. A low pressure Phillips sodium spectral lamp was used for absolute spectral calibrations at these various transitions. A selection of lineshapes is shown in Figs. 3.9 to 3.15. The features of interest are:

(a) Strong self-absorption occurred for just one line of the 3p - 3d doublet (Fig. 3.10), the one whose ground-state sublevel (either $3p_{\frac{1}{2}}$ or $3p_{\frac{3}{2}}$) was pumped by the dye laser. This signified that a cooler absorbing region of vapor outside the plasma had been produced by the low intensity regions of the resonant laser beam.

(b) The various transitions exhibited different linewidths (3 - 20 Å)

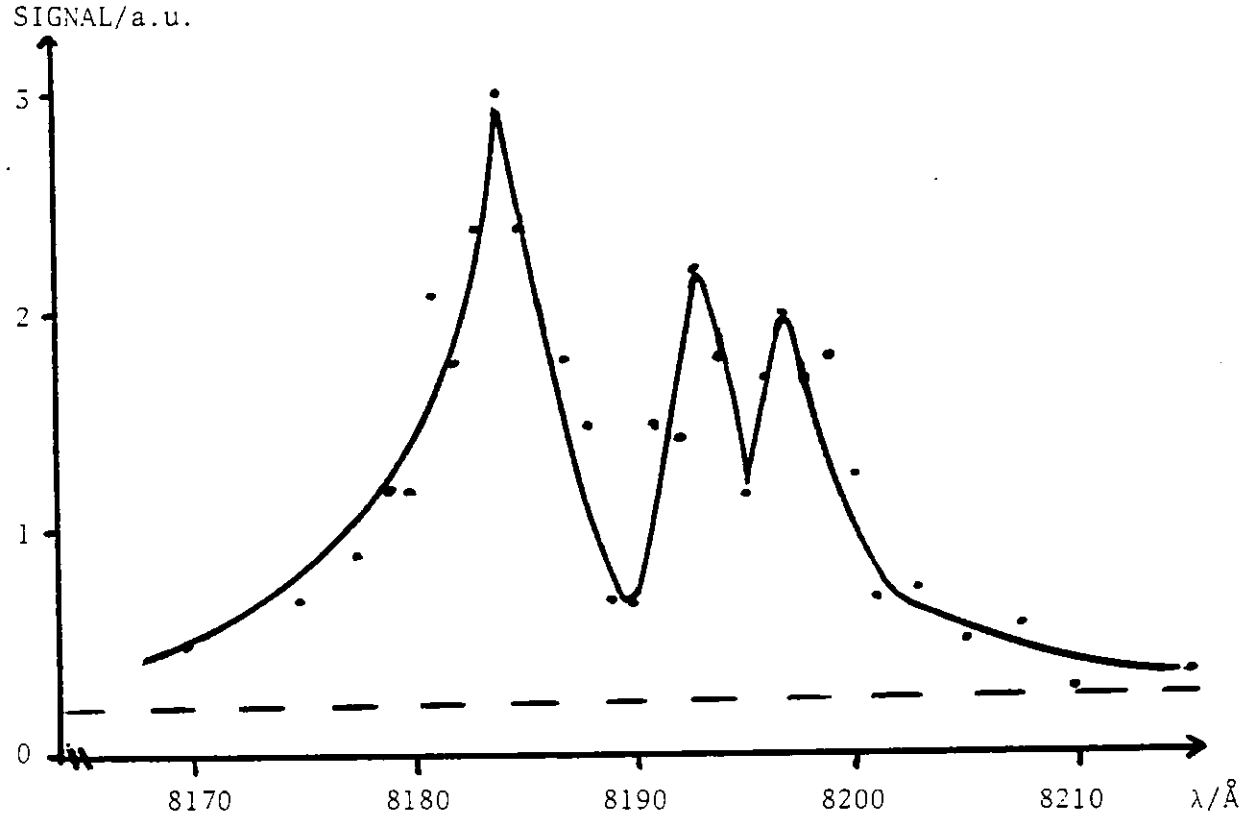


Fig. 3.9. 3p-3d lineshape: $N_{Na} = 8 \times 10^{16}$ cm^{-3}, t = 50 ns and $\lambda_L = \lambda_{3s_{\frac{1}{2}}-3p_{3/2}} = 5980$ Å (dotted line is background level).

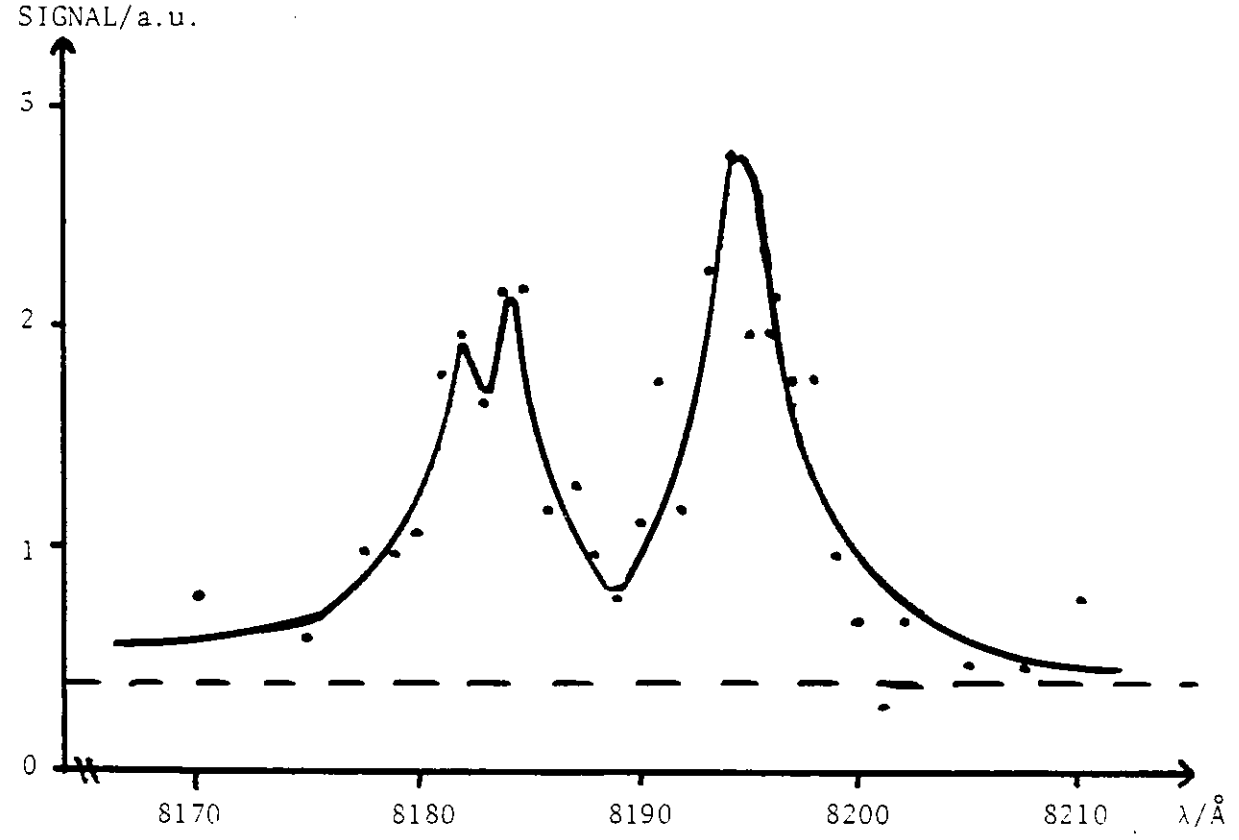


Fig. 3.10. 3p-3d lineshape: $N_{Na} = 8 \times 10^{16}$ cm^{-3}, t = 50 ns and $\lambda_L = \lambda_{3s_{\frac{1}{2}}-3p_{\frac{1}{2}}} = 5896$ Å.

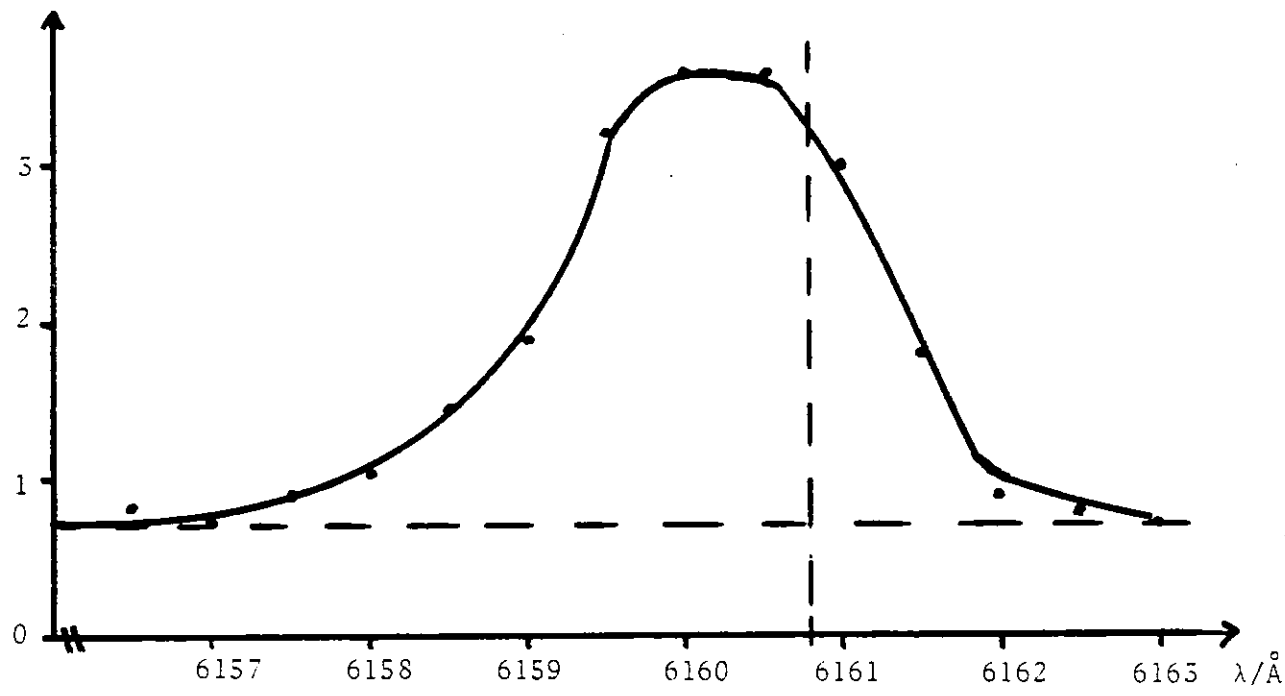


Fig. 3.11. 3p-5s lineshape: $N_{Na} = 8 \times 10^{16}$ cm^{-3} and t = 50 ns. (Vertical dotted line is unperturbed $3p_{3/2}$-$5s_{1/2}$ line center.)

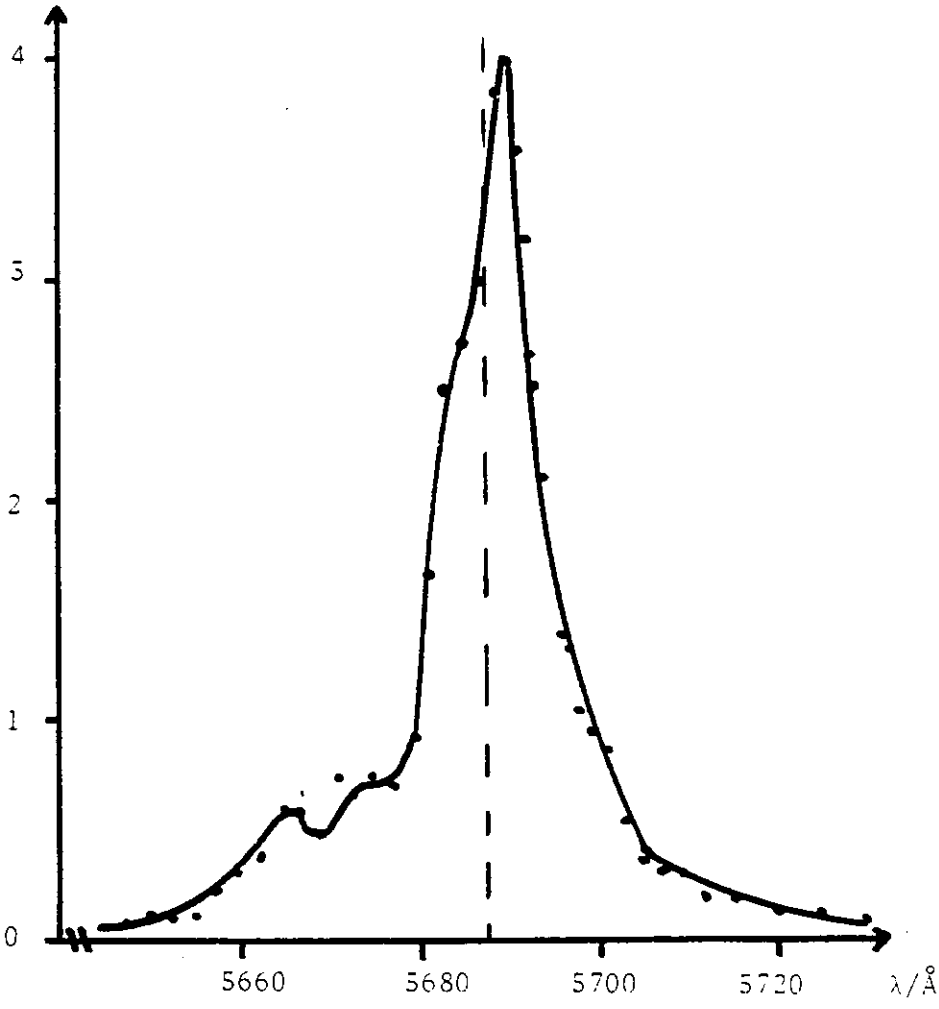


Fig. 3.12. 3p-4d lineshape: $N_{Na} = 4 \times 10^{17}$ cm^{-3} and t = 80 ns (dotted line is unperturbed line center of $3p_{3/2}$-$4d_{5/2}$).

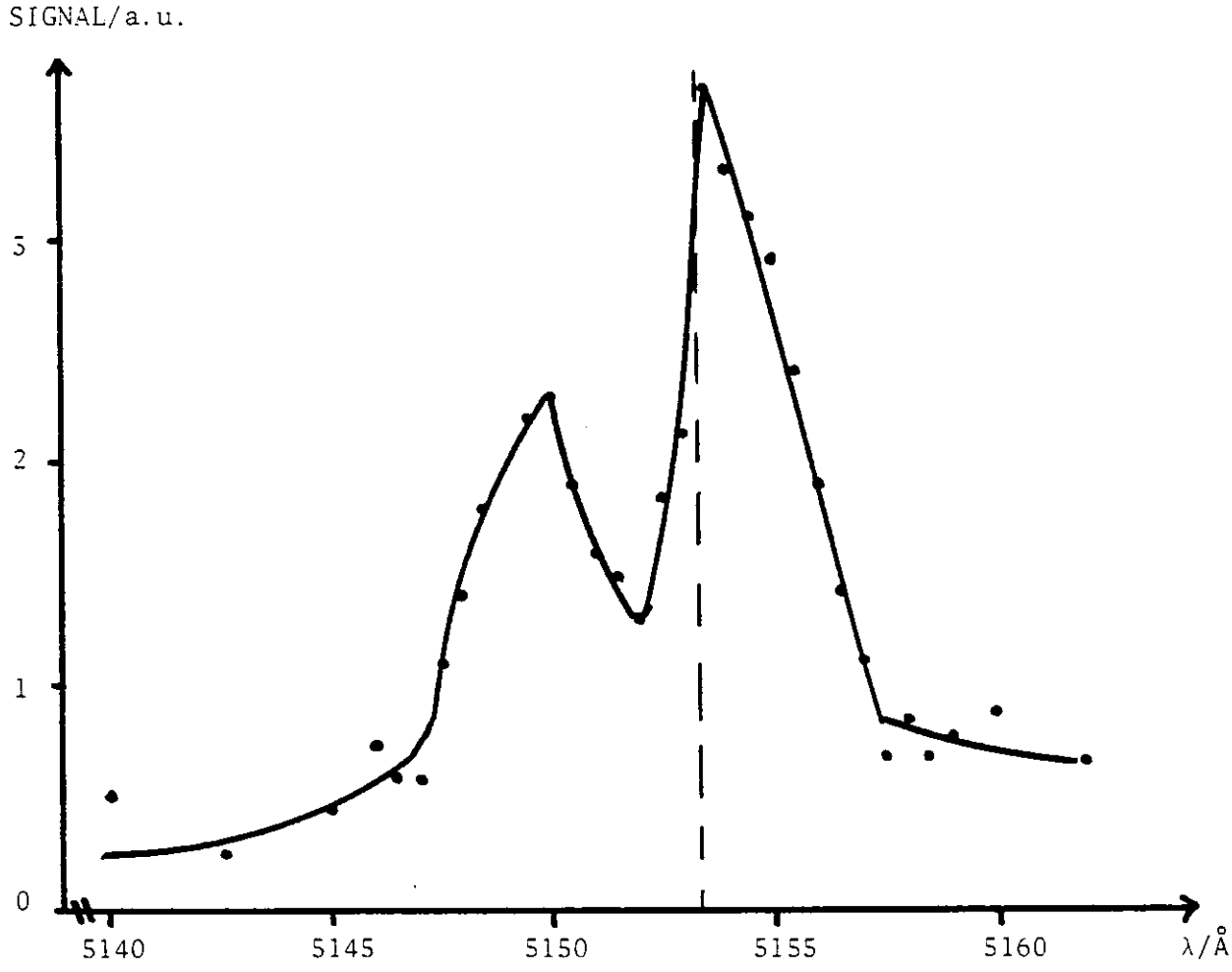


Fig. 3.13. 3p-6s lineshape: $N_{Na} = 8 \times 10^{16}$ cm^{-3} and t = 50 ns (dotted line is unperturbed $3p_{3/2}$-$6s_{1/2}$ line center).

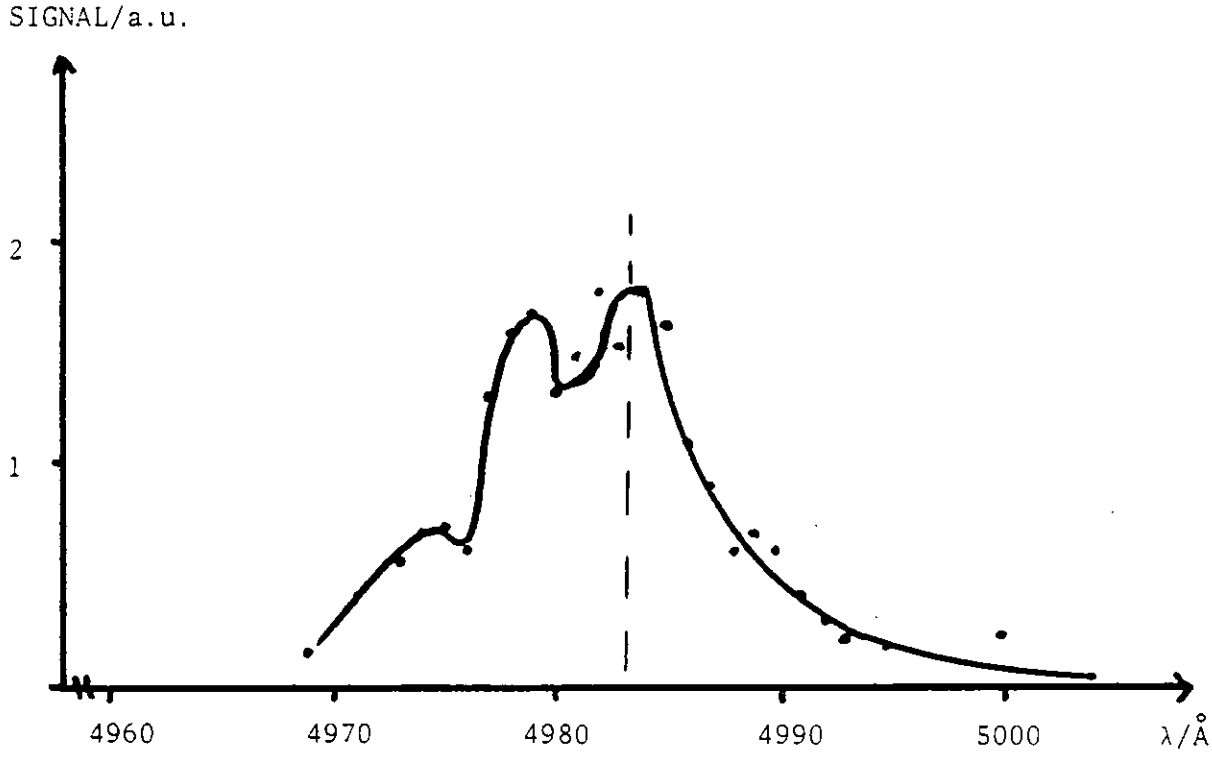


Fig. 3.14. 3p-5d lineshape: N_{Na} = 8 x 10^{16} cm^{-3} and t = 160 ns (dotted line is unperturbed $3p_{3/2}$-$5d_{5/2}$ line center).

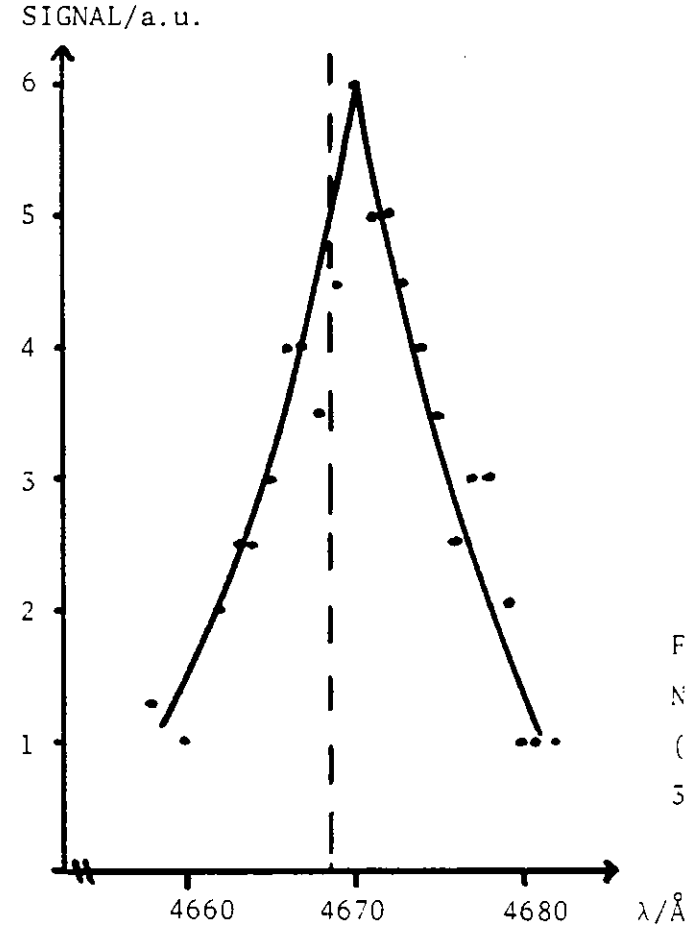


Fig. 3.15. 3p-6d lineshape: N_{Na} = 8 x 10^{16} cm^{-3}, t = 110 ns (dotted line is unperturbed $3p_{3/2}$-$6d_{5/2}$ line center).

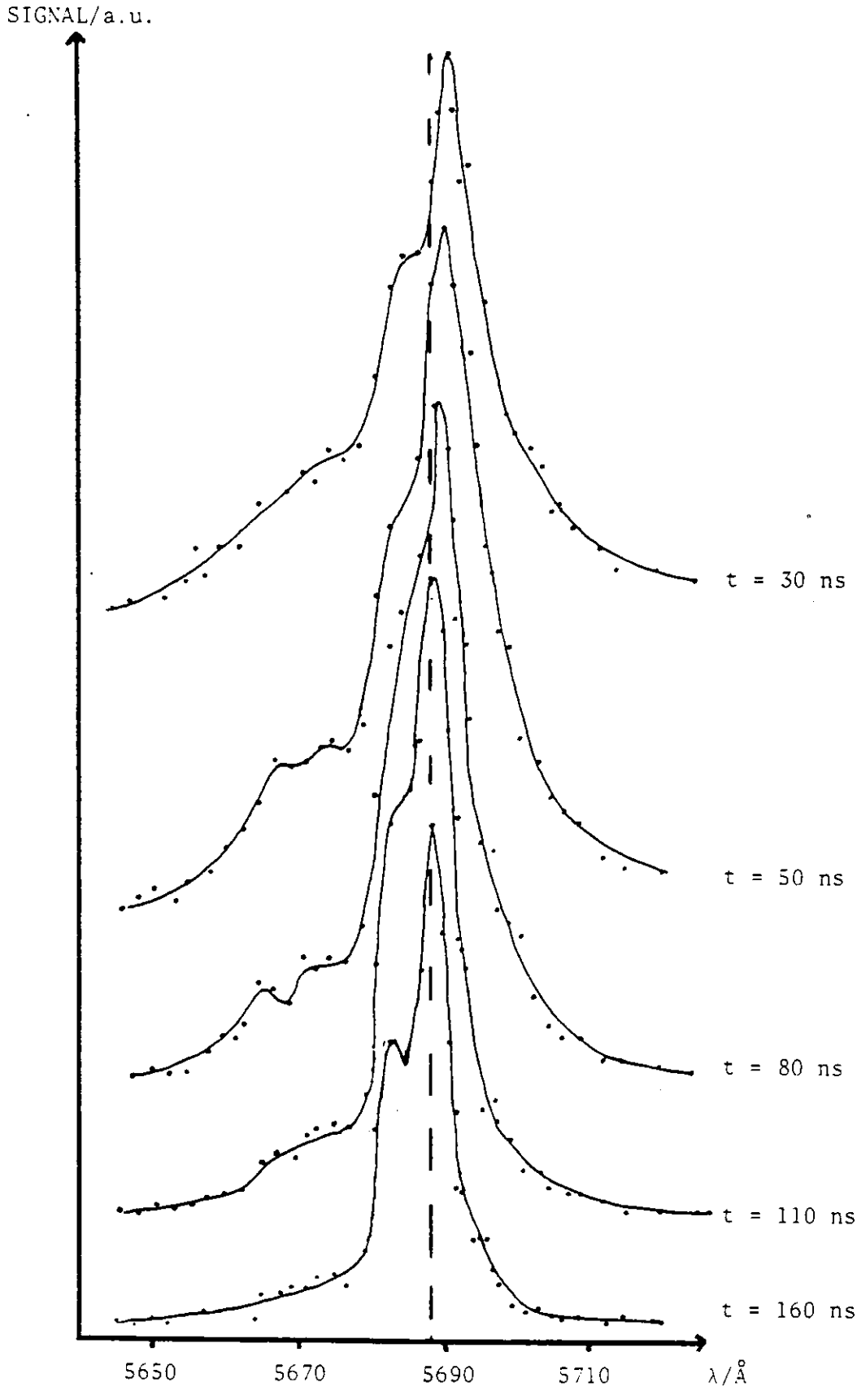


Fig. 3.16. Temporal history of 3p-4d lineshape: $N_{Na} = 4 \times 10^{17}$ cm^{-3}. Lineshapes are displaced vertically for ease of viewing.

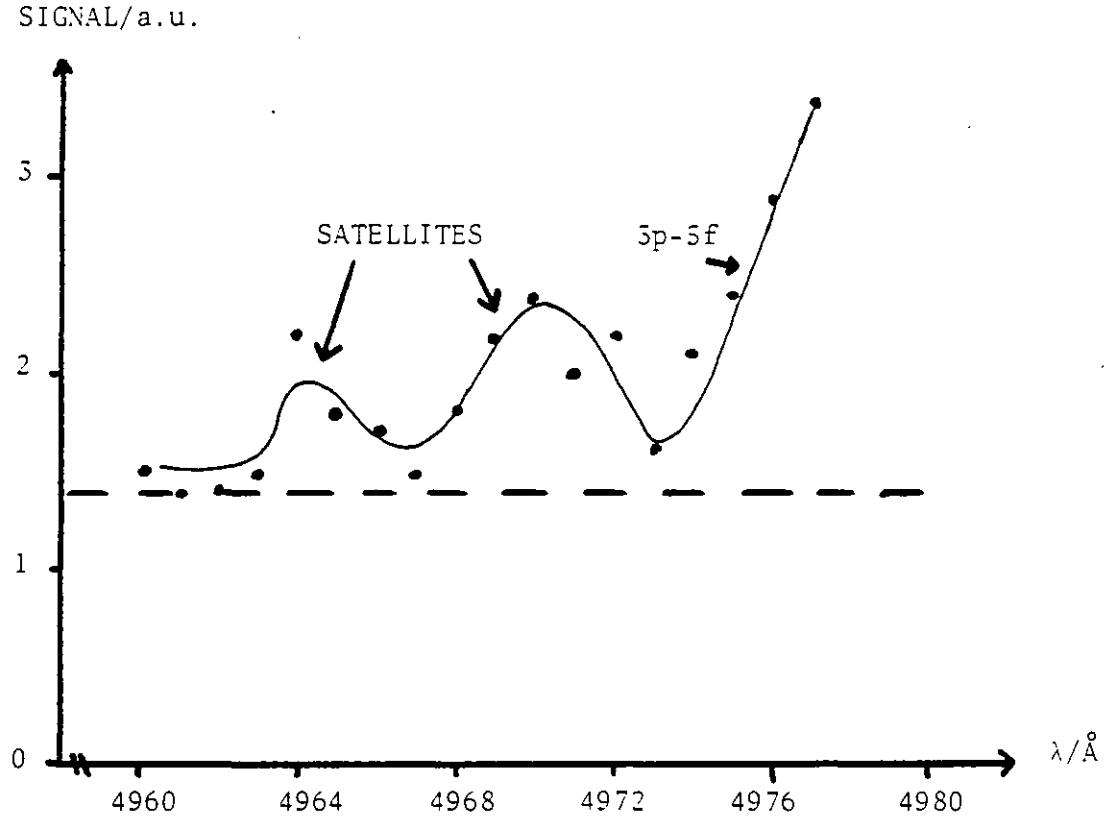


Fig. 3.17. Satellites on 3p-5f blue wing:
$N_{Na} = 8 \times 10^{16}$ cm^{-3} and t = 30 ns
(dotted line is background level).

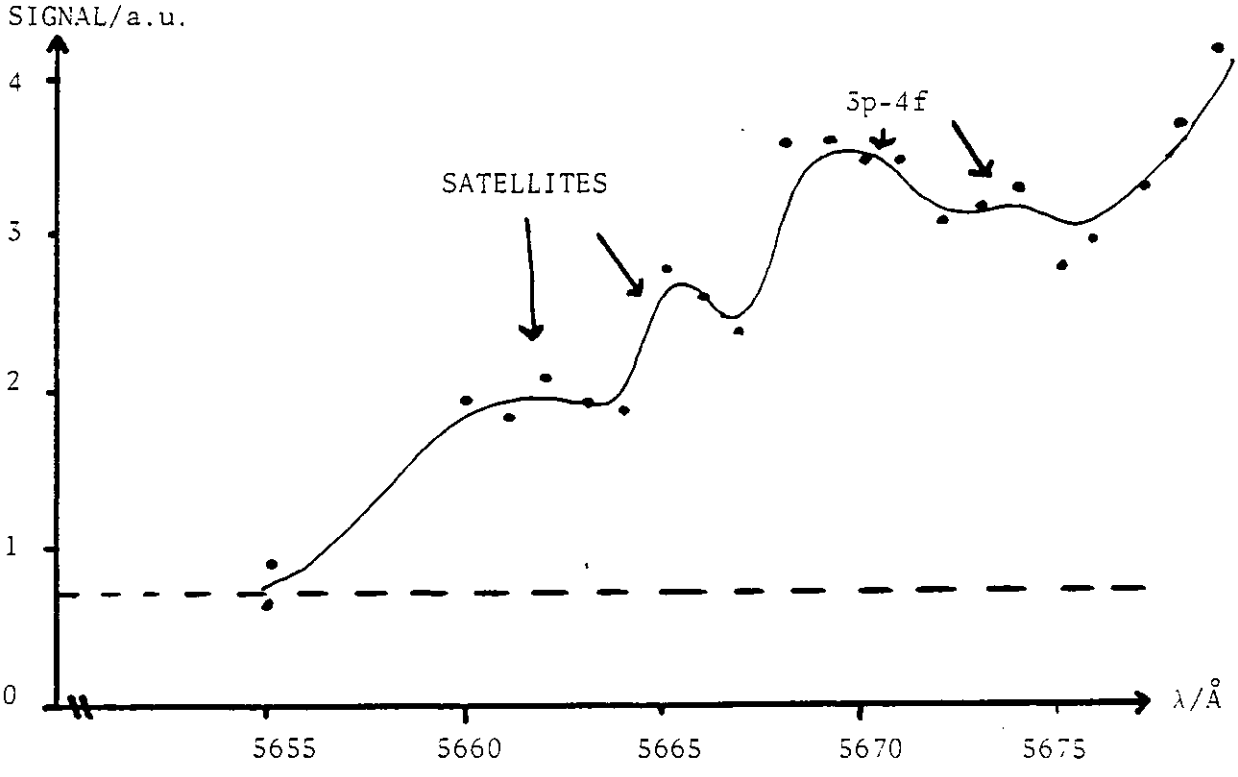


Fig. 3.18. Satellites on 3p-4f blue wing:
$N_{Na} = 10^{17}$ cm^{-3} and t = 50 ns.

at similar times in the plasma afterglow. These widths were functions of several line broadening processes considered in detail in section 3.4.2.

(c) Forbidden components appeared on the blue wings of 3p - 4d, 3p - 5d and 3p - 6d due to the presence of a perturbing plasma microfield (section 3.4.7).

(d) Spectral shifts of strongly perturbed lines were observed due to quadratic Stark effects, most noticeable for the 3p - 4d lineshape. The 3p - 4d lineshape time history illustrated in Fig. 3.16 clearly shows the decrease in width, shift and ratio of forbidden to allowed component intensity as the plasma recombines.

(e) Weak emission features appeared on the blue wing of 3p - 4f and 3p - 5f, enlarged in Figs. 3.17 and 3.18. These satellites are discussed in section 3.4.8.

These results represent, in sodium, the first temporally resolved shifts, forbidden components, plasma-induced widths of 3p - 5s, 3p - 6s, 3p - 3d and 3p - 6d and satellite features.

3.4 Electron Density

3.4.1 Introduction

The time history of N_e is calculated from linewidths after correcting for all other competing line broadening processes. These electron densities are then compared with other density diagnostics which include line shifts, forbidden component intensities and the Inglis-Teller limit.

3.4.2 Line Broadening Mechanisms

It is instructive to consider the magnitudes of all possible known

contributions to the fluorescence linewidths.

3.4.2.1 Doppler Effect. A maximum oven temperature of 0.07 eV corresponded to a FWHM of 30 mÅ in unexcited sodium vapor. If complete thermalization between electrons and atoms occurs, the Doppler width would be increased to 60 mÅ for $T_e \sim 0.3$ eV.

3.4.2.2 Helium-Sodium Collisions. For the sodium D lines, various calculations and experimental results agree on the magnitude of pressure broadening by helium, $\Delta\lambda = 10^{-20}$ Å atom^{-1} cm^3 (Lewis and McNamara, 1972; Kielkopf, 1980; McCartan and Farr, 1976). At the maximum buffer gas pressure used, 100 Torr, this corresponded to a linewidth contribution of 20 mÅ.

For ℓ changing collisions by He of the upper states of the nd - 3p transitions seen in emission, Gallagher and Cooke (1978) report cross-sections of the order of $n^4\pi a_0^2$ where a_0 is the Bohr radius. At $N_{He} = 10^{18}$ cm^{-3}, $v_{He} = 10^5$ cm s^{-1} and n = 6, this corresponds to an impact width of 10 mÅ. Cross-sections for inelastic n changing collisions by He of ns states were typically two orders of magnitude less (Gallagher and Cooke, 1978).

3.4.2.3 Dimer-Atom Collisions. Lam et al. (1978) have measured the quenching rate coefficient of the 3p level by Na_2 as 3×10^{-9} cm^3 s^{-1} at 400K. For the highest dimer densities encountered in these experiments, 3×10^{16} cm^{-3}, and assuming no dissociation or photoionization upon laser irradiation (section 3.5.5), this yielded an impact linewidth of 0.1 mÅ.

3.4.2.4 Atom-Atom Collisions. This category groups together all atom-atom collisions depopulating either ground or excited state of the spectrally resolved transitions. The relevant processes, associative ionization and energy pooling collisions (see section 1.3) have been recently reviewed by Kopystynska and Moi (1982). For a maximum $N(3p) = 3 \times 10^{17}$ cm^{-3} and a total cross-section of 10^{-14} cm^2 (section 1.3), a maximum impact linewidth of < 1 mÅ can be expected. Although substantially larger cross-sections have been attributed to energy pooling collisions between highly excited states (Rb:$\sigma = 10^{-11}$cm^2: Chéret et al. (1981)), the total inelastic rates and hence linewidth contributions will still be negligible as excited level populations will be orders of magnitude less than the 3p population (section 3.5).

3.4.2.5 Resonance Broadening. The resonance linewidth, applicable to any transition connected to the 3p state, is given theoretically (Sobel'man et al., 1981) and experimentally (Popov and Ruzov, 1980) as:

$$\begin{aligned} &\text{D2 Line:} \quad \Delta\lambda/\text{Å} = 8.4 \times 10^{-19}\, N(3s) \\ &\text{D1 Line:} \quad \Delta\lambda/\text{Å} = 5.2 \times 10^{-19}\, N(3s) \end{aligned} \qquad (3.5)$$

Hence, at the highest N_{Na} encountered, 3×10^{17} cm^{-3}, the resonance linewidth of $n\ell - 3p_{3/2}$ transitions was 300 mÅ.

3.4.2.6 AC Stark Effect. The interaction of the time varying electric field of a laser with a resonant transition has been shown theoretically and experimentally (Smith and Hogan, 1979) to produce emission sidebands at a detuning Ω_R (the Rabi frequency) from line center, where

$$\Omega_R = \sqrt{\frac{AF\lambda_0^2}{8\pi^2}}$$

and A is the spontaneous decay rate and F the photon flux. For the peak laser flux used, 10^8 W cm^{-2}, Ω_R = 6 Å for 3s - 3p. Since such laser-induced broadening was comparable to plasma broadening (section 3.4.2.10), no lineshapes recorded during laser irradiation were used to determine N_e.

3.4.2.7 Power Broadening. This term has been confused with saturation broadening in the literature (Kumar et al., 1982). The latter is a trivial source of broadening, apparent when measuring absorption profiles by tuning a non-bleaching laser through an optically thick transition ($\tau_0 > 1$). Power broadening is a consequence of the uncertainty principle. The cycling of the bound electron between upper and lower state by the laser diminishes the upper state lifetime and hence broadens the transition as follows:

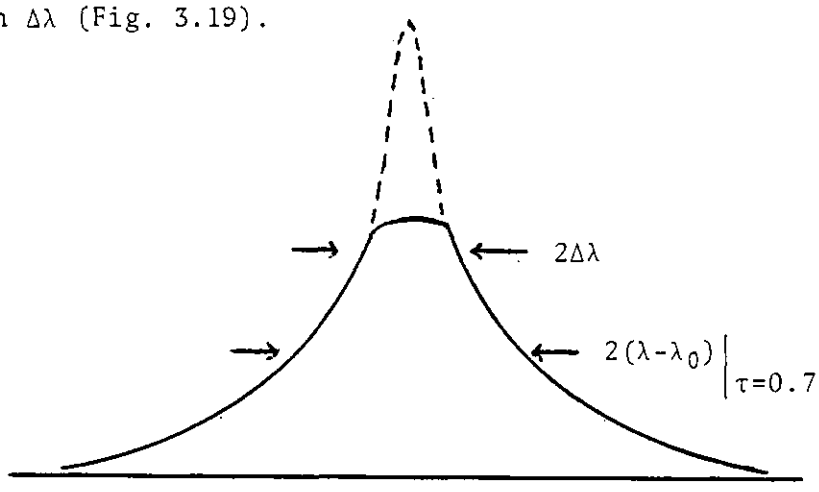
$$\Delta\nu_p = \frac{1}{2\pi} BI(\nu)$$

For the D lines:
$$\Delta\lambda_p/\text{Å} = 2 \times 10^{-7}\, I(\lambda)/\text{W cm}^{-2}\,\text{Å}^{-1} \qquad (3.6)$$

This formula is only strictly applicable for $\Delta\lambda_p < \Delta\lambda_{LASER}$ under which conditions it has been experimentally verified for the sodium D lines (van Calcar et al., 1982). Since $I(\lambda) > 10^{10}$ W cm^{-2} Å^{-1} in the present experiments, $\Delta\lambda_p \not< \Delta\lambda_{LASER}$ by equation (3.6). Furthermore it has been suggested (J. Bowen, private communication) that power broadening could never exceed the laser linewidth, making it less important than the AC Stark effect.

3.4.2.8 Instrument Function. The spectrometer resolution was frequently monitored using a low pressure Phillips sodium lamp. The instrument profiles were well approximated by Gaussian lineshapes with FWHM = 1.8 to 2.3 Å.

3.4.2.9 Opacity Effects. The apparent width of any spectral line, $|\lambda - \lambda_0|_{\tau=0.7}$, in the absence of inversion is greater than its true width $\Delta\lambda$ (Fig. 3.19).



For a homogeneously broadened line: $\lambda - \lambda_0|_{\tau=0.7} = \Delta\lambda\sqrt{\frac{\tau_0}{\ell n 2}}$ if $\tau_0 >> 1$.

Fig. 3.19. Opacity effect on lineshape.

3.4.2.10 Plasma Broadening. The plasma induced widths for isolated lines of non-hydrogenic neutral atoms such as sodium have been calculated (Griem, 1964, 1974) by convoluting the effects of elastic and inelastic electron impacts with the quasi-static microfield of the ions. The half-width is given by (Griem, 1964):

$$\Delta\lambda_W = W\left(\frac{N_e}{10^{16}}\right) + 1.75\,\alpha\, W\left(\frac{N_e}{10^{16}}\right)^{5/4}\left[1 - \tfrac{3}{4}N_D^{-1/3}\right] \qquad (3.7)$$

where the parameter W represents electron impact broadening and α

represents the contribution by the ion microfield. The term in the square brackets accounts for ion-ion correlations (Hooper, 1968) and screening by electrons, and is valid for $N_D \gtrsim 2$. For $3 > N_D > 0.1$, Weisheit and Pollock (1982) have shown that the effect of the microfield is well approximated by setting $N_D \sim 1$ in equation (3.7).

The predominant broadening mechanisms for each of the transitions observed experimentally are listed in Table 3.2, where $\Delta\lambda_W$ is for $N_e = 10^{16}$ cm^{-3}. The parameter $\frac{\Delta\lambda_W}{f}$ is a measure of the relative importance of plasma broadening over opacity effects, where f is an oscillator strength (Wiese et al., 1969).

TABLE 3.2

Parameters of Observed Transitions

Transition	Broadening	λ/Å	$\Delta\lambda_W$/Å	f	i'	$E_i - E_{i'}$/eV	$\Delta\lambda_W/f$
$3p_{3/2}$-$3s_{\frac{1}{2}}$	e^- Elastic	6160.8	0.25	0.0137	5p	0.28	18
$3p_{3/2}$-$6s_{\frac{1}{2}}$	e^- Elastic	5153.4	0.5	0.0044	6p	0.13	110
$3p_{3/2}$-$3d_{5/2}$	e^- Elastic	3194.8	0.19	0.75	4p	0.13	0.25
$3p_{3/2}$-$4d_{5/2}$	e^- Inelastic - 15% Na^-	5688.2	1.8	0.095	4f	0.005	19
$3p_{3/2}$-$5d_{5/2}$	e^- Inelastic - 20% Na^-	4982.8	5.3	0.028	5f	0.005	190
$3p_{3/2}$-$6d_{5/2}$	e^- Inelastic + 25% Na^+	4668.6	12	0.013	6f	0.005	920

The possible deviations from equation (3.7) are:

(a) The classical path approximation for elastic electron collisions, inherent to equation (3.7), becomes dubious when the energy separation between nearest perturbing level i' and energy level i of the transition of interest is more than kT_e (listed as $E_i - E_{i'}$ in Table 3.2). Since

the minimum measured T_e was 0.2 eV (section 3.5), only the 3p - 5s transition would be affected.

(b) The quadratic Stark effects converts to a linear effect as $\Delta\lambda_W$ becomes comparable to $E_i - E_{i'}$. This should be detected by a decrease in the asymmetry, shift and width of the line as predicted by equations (3.7) and (3.16).

(c) First order ion quadrupole corrections to the width are a maximum of $\frac{m_e a_0 v_e}{\hbar}$ (Griem, 1974), corresponding to 1% for an electron velocity $v_e = 2 \times 10^7$ cm s^{-1}.

(d) Debye shielding of high frequency electron impacts, important when $E_i - E_{i'} < \hbar\omega_p$, reduces the number of perturbers and hence the linewidth given by equation (3.6). For instance, the fractional reduction in the 3p - 5d electron impact linewidth W for $N_e = 2.5 \times 10^{16}$ cm^{-3}, $T_e = 0.2$ eV, $N_D = 1$ is given by, in the Debye theory:

$$\left| \frac{\Delta W}{W} \right| \sim 30\% \qquad \text{(Griem, 1974)}.$$

$$\text{or} \quad \left| \frac{\Delta W}{W} \right| \sim \frac{100}{\lambda_D} \sim 40\% \qquad \text{(Davis and Morin, 1971)} \qquad (3.8)$$

where λ_D is in Å.

However, this correction may be an overestimate for N_D tending to 1 or less as few electrons are available for screening within λ_D.

3.4.2.11 Summary. The four dominant broadening processes in the plasma afterglow were instrumental, resonance, opacity and plasma induced, all others being less than the experimental errors, ± 0.3 Å. The instrument profiles were deconvolved from the raw experimental lineshapes. The next two sections describe how plasma and opacity

effects were separated.

3.4.3 Radiation Transport

The self-reversed 3p - 3d transition (Fig. 3.10) implied that a gradient existed in the excitation temperature of the sodium atoms. Hence, the excited vapor was modelled by dividing it into two homogeneous regions, A and B (Fig. 3.20).

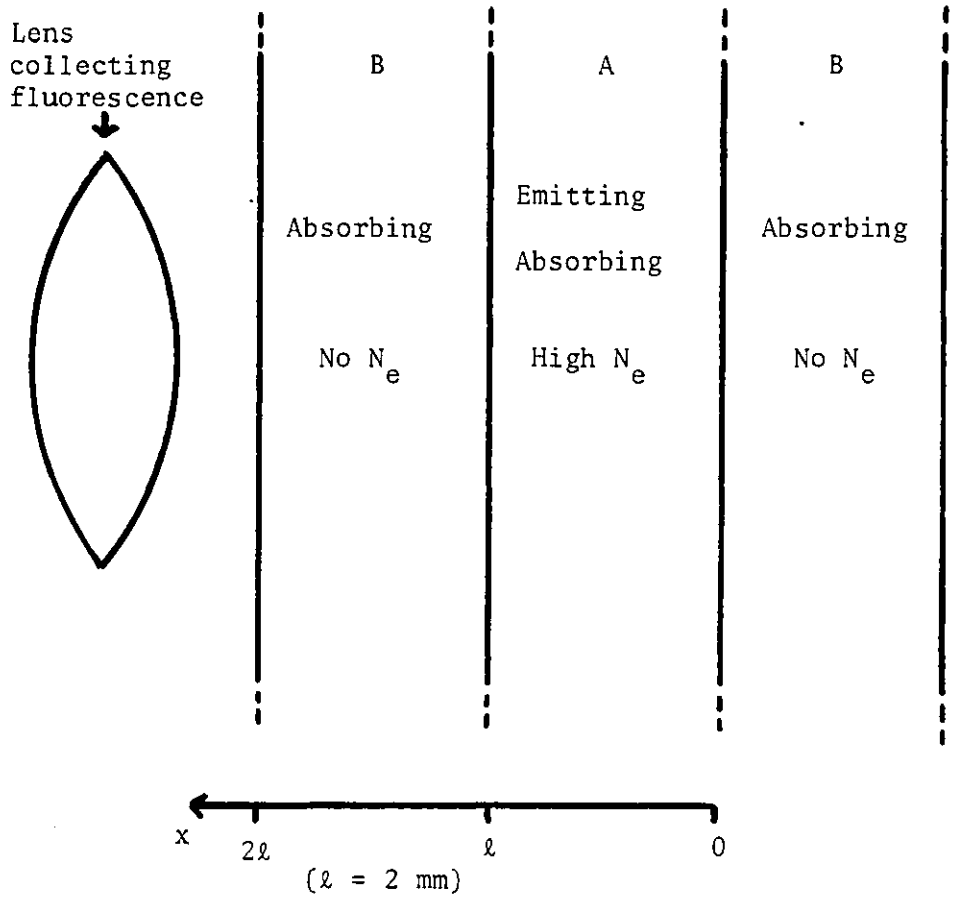


Fig. 3.20. Radiation Transport Model.

These corresponded to a high electron density emitting and absorbing region surrounded by a resonance broadened cooler absorbing region.

The expression for radiation transport in region A is then given by:

$$\frac{dI(\lambda-\lambda_0,x)}{dx} = N(n\ell)_A A h\nu_0 L_A(\lambda-\lambda_0) - I(\lambda-\lambda_0,x)k_A(\lambda-\lambda_0) \qquad (3.9)$$

where A and ν_0 are the spontaneous decay rate and frequency of the transition 3p - nℓ, k is the absorption coefficient and L the normalized lineshape profile. For complete collisional redistribution of radiation, Kirchoff's law is obeyed, so k/L = constant. Integrating equation (3.9) from x = 0 to ℓ for a slab geometry (Fig. 3.20) yields:

$$I_A(\lambda-\lambda_0)\big|_{x=\ell} = B(T_A)[1 - e^{-\tau_A(\lambda-\lambda_0)}] \qquad (3.10)$$

where $\tau_A = k_A\ell$ and $B(T_A)$ is the black-body limit at temperature T_A.

For absorbing region B, the Beer-Lambert law applies:

$$\frac{dI(\lambda-\lambda_0,x)}{dx} = - I(\lambda-\lambda_0,x)k_B(\lambda-\lambda_0)$$

$$\Rightarrow \quad I_B(\lambda-\lambda_0)\big|_{x=2\ell} = I_A(\lambda-\lambda_0)\big|_{x=\ell} e^{-\tau_B(\lambda-\lambda_0)} \qquad (3.11)$$

Combining (3.10) and (3.11), the flux incident on the spectrometer is given by:

$$I(\lambda-\lambda_0) = B(T_A)[1 - e^{-\tau_A(\lambda-\lambda_0)}]e^{-\tau_B(\lambda-\lambda_0)} \qquad (3.12)$$

For collisionally broadened Lorentzian lineshapes:

$$I(\lambda-\lambda_0) = B(T_A)\left[1-\exp-\left(\frac{\lambda_0^2 e^2 f\ell N(3p)_A \Delta\lambda_A}{4\pi\varepsilon_0 mc^2[(\lambda-\lambda_0-\Delta\lambda_S)^2+\Delta\lambda_A^2]}\right)\right]\exp-\left(\frac{\lambda_0^2 e^2 f\ell N(3p)_B \Delta\lambda_B}{4\pi\varepsilon_0 mc^2[(\lambda-\lambda_0)^2+\Delta\lambda_B^2]}\right) \qquad (3.13)$$

where $\Delta\lambda_A$ is the sum of the resonance width (equation (3.5)) and the plasma-induced width (equation (3.7)), and $\Delta\lambda_s$ is the plasma-induced shift (equation (3.16)) and $\Delta\lambda_B$ is the resonance width.

3.4.4 N_e versus N(3p) Plot

The half-width at half-maximum, $(\lambda-\lambda_0)_{\frac{1}{2}}$, for all transitions but the self-reversed 3p - 3d line, is defined by:

$$\frac{I(\lambda-\lambda_0)_{\frac{1}{2}}}{I(\lambda_0)} \equiv f(N_e, N(3p)_A, N(3p)_B) = \frac{1}{2}$$

The variable $N(3p)_B$ accounting for reabsorption could be estimated from the separation of the self-reversed peaks of 3p - 3d. The two variables remaining, N_e and $N(3p)_A$, could be deduced as follows (Kilkenny et al., 1980). Each measured linewidth represented a mixture of opacity and plasma broadening defined by the above-mentioned function $f(N_e, N(3p)_A)$. Each transition had different f and $\Delta\lambda_W$ values and hence a different function, drawn as curves on a plot of N(3p) versus N_e. The intersection of all such curves should be at just one point, yielding N_e and N(3p). A typical example of such a plot is shown in Fig. 3.21 for $N_{Na} = 8 \times 10^{16}$ cm^{-3} and t = 50 ns. The error bar on the 3p - 3d curve represents a possible systematic error due to the uncertainty in the plasma width ℓ and does not affect the relative position of the curves. The error in N_e was estimated at 20%, principally due to the quoted uncertainty in the plasma broadening parameters (Griem, 1974). In fact all transitions shown on Fig. 3.21 except 3p - 3d had $\tau_0 < 2$ at t = 50 ns. The 3p - 6d linewidth underestimated the electron density. This was attributed

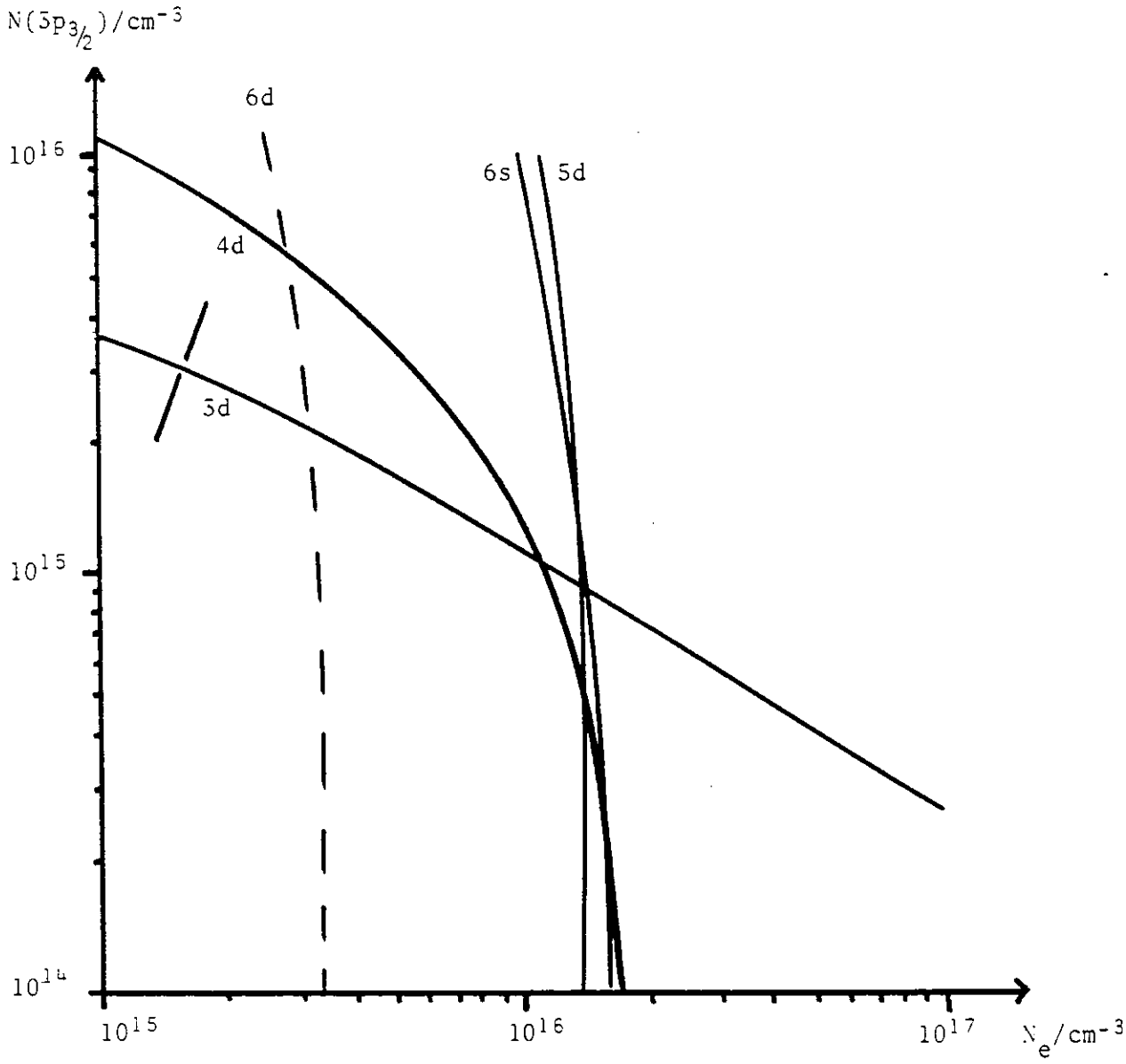


Fig. 3.21. N(3p) versus N_e plot: $N_{Na} = 8 \times 10^{16}$ cm^{-3} and t = 50 ns.

to the breakdown of the quadratic Stark effect as the 2.9 Å separation from the nearest perturbing level, 6f, was smaller than the measured HWHM, 4 Å.

3.4.5 Temporal Histories of N_e and N(3p)

The N_e versus N(3p) plots were repeated for various times in the plasma afterglow yielding the temporal behavior of N_e amd N(3p). These are shown in Figs. 3.22 and 3.23 for $N_{Na} = 8 \times 10^{16}$ cm^{-3} and 4×10^{17} cm^{-3}. A minimum $N_e = 3 \times 10^{15}$ cm^{-3} could be measured spectroscopically, corresponding to the reading error in the 3p - 4d linewidth. In principle, lower electron densities could be ascertained from linewidths of higher members of the 3p - nd series (Table 3.2) more strongly perturbed by the surrounding plasma, but the low fluorescence signals emanating from such states at late times increased fractional errors.

The dotted line on Fig. 3.23, normalized at t = 50 ns, represents the theoretical decay rate A' modified for radiation trapping of the resonance broadened 3s - 3p transition (Holstein, 1951)

$$A' = A/\sqrt{\pi\tau_0}$$

$A = 6 \times 10^7$ s^{-1}, $\tau_0 = 3 \times 10^4$

$$\Rightarrow \quad A' = 2 \times 10^5 \text{ s}^{-1} \Rightarrow \tau_{3p}' = 5 \ \mu\text{s}.$$

The experimentally measured 3p lifetime by Fig. 3.23 is initially much shorter, $\sim$ 30 ns, signifying collisional depopulation by electrons. An equilibrium 3p population is reached for t > 100 ns when electron excitation and de-excitation rates are equal:

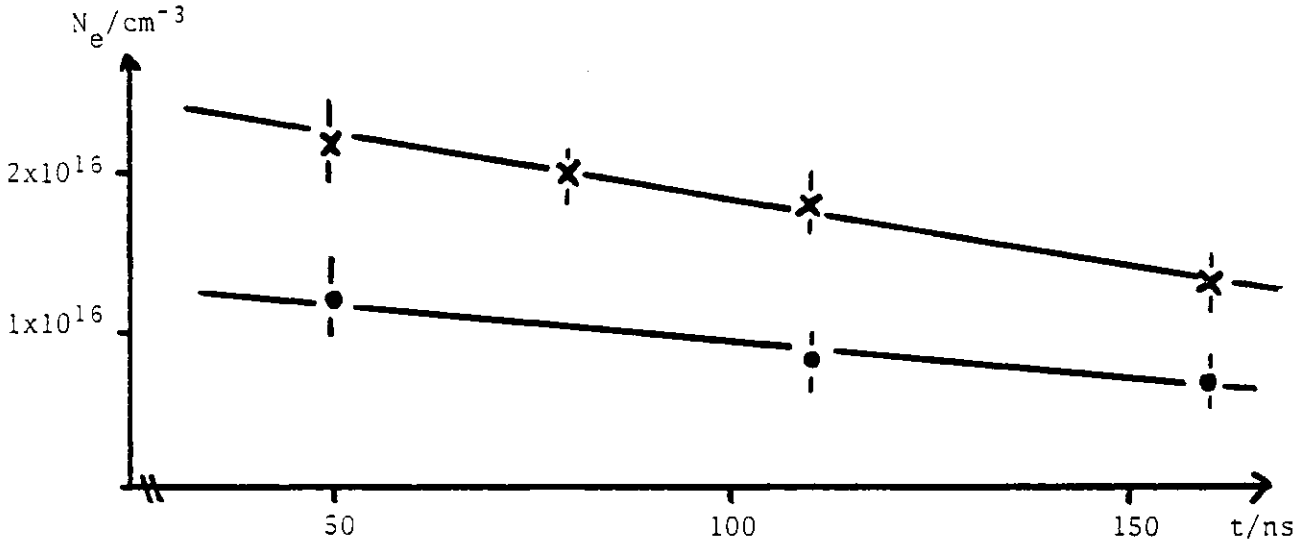


Fig. 3.22. Temporal history of N_e:
• $N_{Na} = 8 \times 10^{16}$ cm^{-3};
x $N_{Na} = 4 \times 10^{17}$ cm^{-3}.

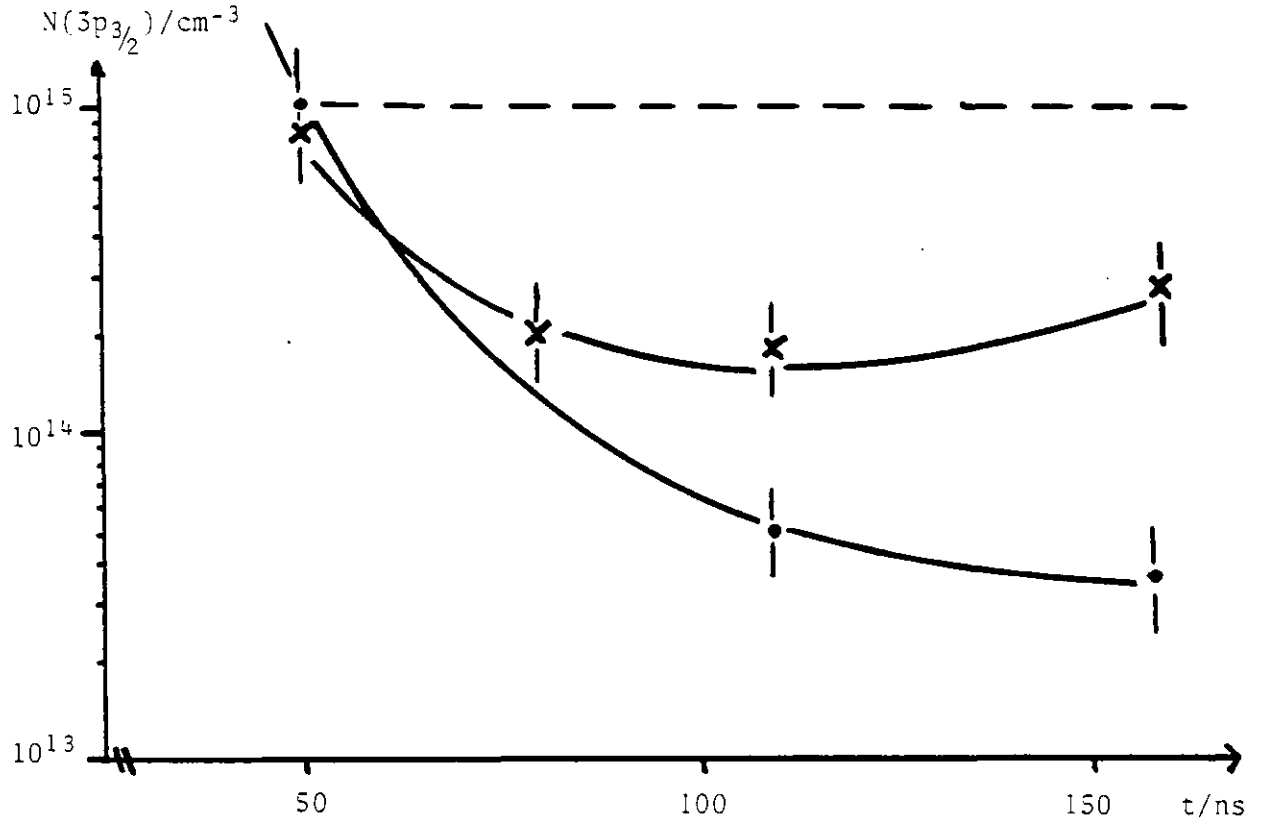


Fig. 3.23. Temporal history of $N(3p_{3/2})$.
• $N_{Na} = 8 \times 10^{16}$ cm^{-3}
× $N_{Na} = 4 \times 10^{17}$ cm^{-3}

$$\frac{dN(3p)}{dt} = N(3s)g_{3p}\,N_e\,\langle\sigma v_e\rangle\,e^{-2.1/T_e} - N(3p)g_{3s}\,N_e\,\langle\sigma v_e\rangle = 0 \qquad (3.15)$$

A Maxwell-Boltzmann distribution of free electrons is assumed in equation (3.15) and is justified in section 3.5.4. Hence, the electron temperature may be estimated by simplifying expression (3.15) to:

$$\frac{N(3p)_{3/2}}{N(3s)} = 2e^{-2.1/T_e} \quad \text{as} \quad \frac{g_{3p_{3/2}}}{g_{3s}} = 2$$

At $t = 160$ ns, $N_{Na} = 8 \times 10^{16}$ cm^{-3}: $\dfrac{N(3p)_{3/2}}{N(3s)} = \dfrac{2\pm1\times10^{13}}{8\pm2\times10^{16}}$ (Fig. 3.23)

$$\Rightarrow \quad T_e = 0.25 \pm .03 \text{ eV}$$

Similarly, for $N_{Na} = 3 \pm 1 \times 10^{17}$ cm^{-3}:

$$T_e = 0.27 \pm .02 \text{ eV} \quad \text{for } 80 \text{ ns} < t < 160 \text{ ns}.$$

These temperatures compared favorably with those calculated from line intensity ratios (see section 3.5.3) and justified the value for T_e used in calculating Griem's plasma broadening parameters, 2500K.

3.4.6 Stark Shifts

For isolated lines, plasma shifts are predominantly due to the ion quadratic Stark effect and weak, distant elastic electron collisions. The value of the shift is given by (Griem, 1964, 1974):

$$\Delta\lambda_s = d\left(\frac{N_e}{10^{16}}\right) + 2\alpha W\left(\frac{N_e}{10^{16}}\right)^{5/4}\left[1 - \tfrac{3}{4}N_D^{-1/3}\right] \qquad (3.16)$$

The validity of this equation is limited by the same assumptions as discussed for linewidths in section 3.4.2, apart from the unshifted

quadrupole effect. However, the critical dependence of the shift on distant collisions makes expression (3.16) even more prone to errors for short Debye length plasmas. For instance, the fractional reduction in the electron shift and width due to Debye shielding for the 3p - 4d transition can be calculated (Griem, 1974) as for 3p - 5d (equation (3.8)) as:

$$\frac{\Delta d}{d} = -35\% \qquad \text{versus} \qquad \frac{\Delta W}{W} = -10\%$$

for $N_e = 2 \times 10^{16}$ cm^{-3}, $T_e = 0.2$ eV. Hence the ratio of shift to width should be a sensitive measure of the applicability of Debye shielding for the present plasmas.

Table 3.3 compares experimental shifts from the emission lineshapes with theoretical calculations, with and without Debye shielding, using the electron densities determined from linewidths. All shifts were towards increasing wavelength as expected for the allowed components.

TABLE 3.3

Comparison of Experimental and Theoretical Quadratic Stark Shifts at $N_e = 10^{16}$ cm^{-3}

Transition	(± 0.25 Å) Experimental shift / Å	Theoretical shift / Å	
		Without shielding	With shielding
3p - 3d	< 0.5	0.24	0.24
3p - 5s	< 0.5	0.32	0.32
3p - 4d	1	1.4	1.1
3p - 6s	0.75	0.60	0.60
3p - 5d	1	4.4	2.7
3p - 6d	1.5	8.9	4.5

For the 3p - 3d, 3p - 5s, 3p - 4d and 3p - 6s transitions, the electron density measured by the Stark shift and width were equal within experimental error with or without Debye shielding. The transitions most prone to corrections for Debye shielding, 3p - 5d and 3p - 6d, had considerably smaller shifts than expected (see Table 3.3). However, this can be attributed to a partial conversion to the linear Stark effect as forbidden and allowed components merge leading to a reduction in the shift. Figure 3.24 compares the temporal history of N_e determined from 3p - 4d shifts (± 0.25 Å) and widths (reproduced from Fig. 3.22) for $N_{Na} = 4 \times 10^{17}$ cm^{-3}.

3.4.7 Forbidden Components

Dipole forbidden components arise from the mixing of eigenstates of two neighboring levels by the plasma microfield. The selection rules ($\Delta\ell = \pm 1$) break down and the oscillator strength of an allowed transition, in this case 3p - nd, is shared with $\Delta\ell = 0,2\ldots(n-2)$ transitions corresponding to 3p - np, 3p - nf, 3p - ng up to 3p - n,ℓ = n-1. The ratio of spectrally integrated forbidden to allowed component intensities for small ratios, hydrogenic wavefunctions and a nearest neighbor microfield distribution is (Griem, 1974):

$$\frac{I_F}{I_A} = 2^{\frac{1}{4}}\pi N_{Na^+} \left[\frac{3\ell_>}{2\ell+1} n^2(n^2 - \ell_>^2) \left(\frac{\hbar}{m\omega_{AF}} \right)^2 \right]^{\frac{3}{4}} \qquad (3.17)$$

where $\ell_>$ is the larger of the orbital angular momenta, ℓ is the allowed component angular momentum and ω_{AF} is the frequency separation between allowed and forbidden components.

Applying this formula to the hydrogenic forbidden components

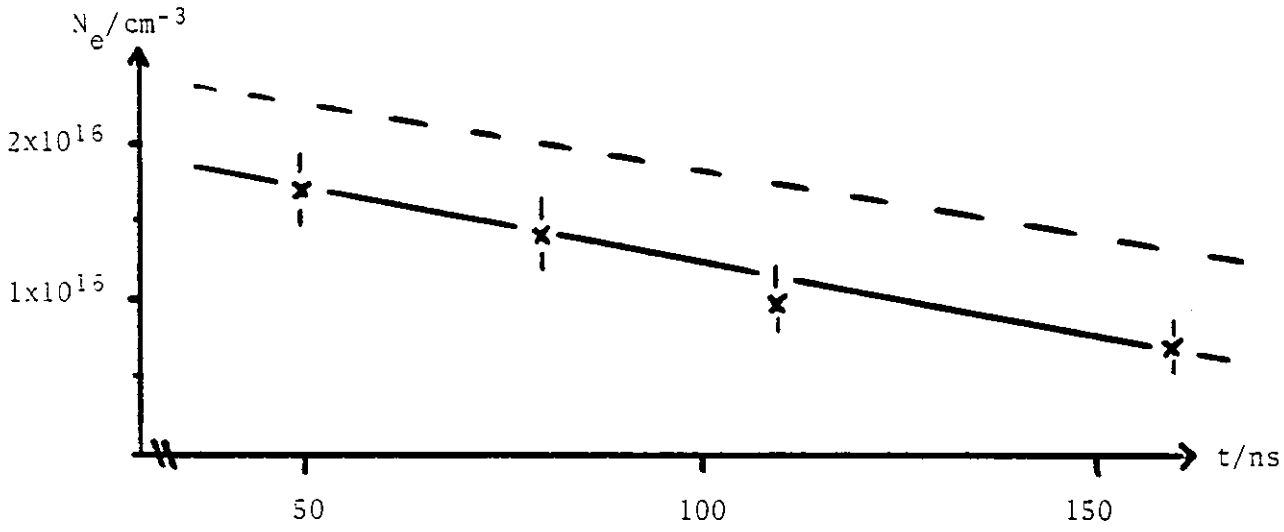


Fig. 3.24. N_e from 3p-4d Stark shift (dotted line from Fig. 3.22).

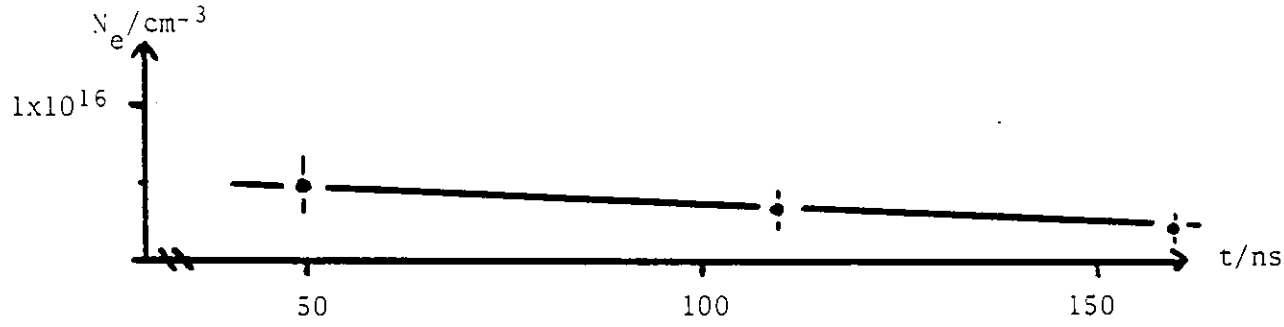


Fig. 3.25. N_e from $\frac{I_{3p-5f}}{I_{3p-5d}}$.

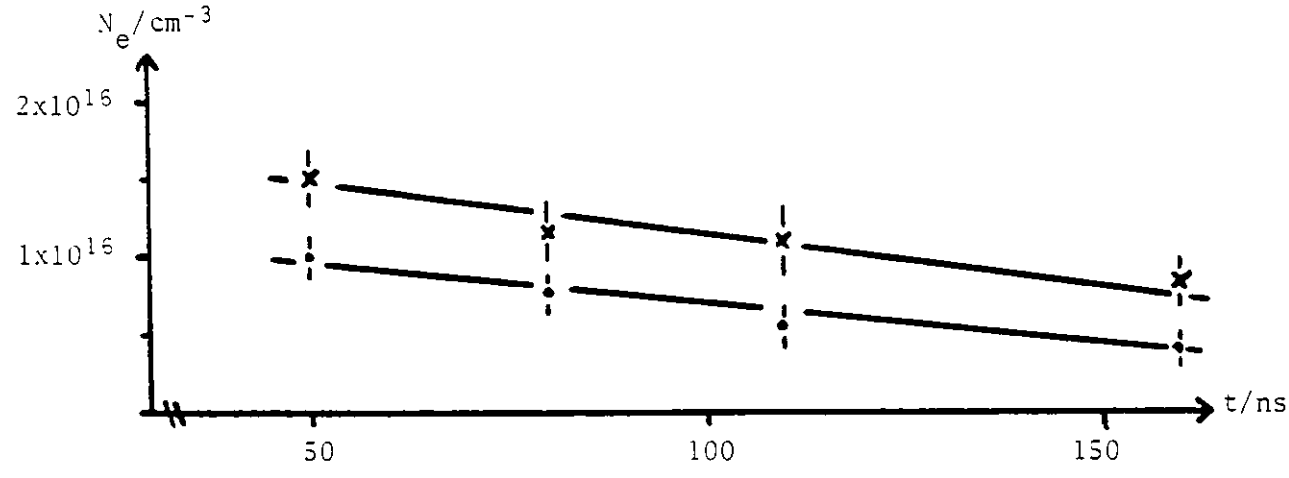


Fig. 3.26. N_e from $\frac{I_{3p-4f}}{I_{3p-4d}}$.

• $N_{Na} = 8 \times 10^{16}$ cm^{-3}

× $N_{Na} = 4 \times 10^{17}$ cm^{-3}

observed experimentally as detached features (see Figs. 3.12 and 3.13):

$$\text{For } 3p - 4d,4f: \qquad I_F/I_A = 1.3 \times 10^{-17} N_e \qquad (3.18)$$

$$\text{For } 3p - 5d,5f: \qquad I_F/I_A = 1.4 \times 10^{-16} N_e \qquad (3.19)$$

Experimental ratios have been extracted from the emission lineshapes after subtracting the allowed wing blue wing intensity in the vicinity of the forbidden component. Hence a third independent measure of the electron density temporal history has been plotted (Figs. 3.25 and 3.26) for the same conditions as Fig. 3.22. The discrepancy between N_e determined from linewidths (Fig. 3.22) and from the I_F/I_A ratio for 3p - 5d,5f (Fig. 3.25) is not surprising as the measured ratios are large, up to 75%, signifying strong mixing of the 5d and 5f levels and the breakdown of perturbation theory inherent in equation (3.17). A better test of the theory clearly lies in the I_F/I_A ratio for 3p - 4d,4f where good agreement was found comparing Figs. 3.26 and 3.22.

Since no 3p - np forbidden components for n = 5, 6 or 7 were observed experimentally in emission above background, their intensities were estimated as $\lesssim$ 0.1 of the 3p - 4d intensity. From equation (3.17), the ratio of 3p - 5p to 3p - 4f intensities is approximately given by:

$$\frac{I_{3p-5p}}{I_{3p-4f}} \sim \left(\frac{f_{4d-5p}}{f_{4d-4f}} \right)^{3/4} \left(\frac{\omega_{4d-4f}}{\omega_{4d-5p}} \right)^{3/2} \sim \frac{1}{5}$$

Using equation (3.18):

$$\Rightarrow \quad \frac{I_{3p-5p}}{I_{3p-4d}} \sim 2.5 \times 10^{-18} N_e$$

$$\lesssim 0.05 \text{ for } N_e = 2 \times 10^{16} \text{ cm}^{-3}$$

Similar ratios apply for the higher members of the 3p - np series, hence explaining their absence in emission.

3.4.8 Satellites

Several emission features were recorded and time resolved on the blue wing of the 3p - 4f and 3p - 5f forbidden doublets and are shown in Figs. 3.17 and 3.18. Possible explanations include molecular transitions, impurity lines, quasimolecular satellites and plasmon satellites.

3.4.8.1 Molecular Transitions. The 3p - 4d doublet lies on the blue wing of the Na (A→X) band and the 3p - 5d doublet lies in the center of the Na (B→X) band (see Fig. 2.7). Previous work on resonance pumping of sodium vapor (Allegrini et al., 1977) did yield molecular fluorescence superimposed upon these atomic lines. However, such Na_2 emission occurred throughout the B→X and A→X bands, and the vibrational transitions on the 3p - 5d red wing were as strong as those on the blue wing, in complete contradiction to the localized features seen at λ = 4964 Å and λ = 4970 Å. Thus, although molecular fluorescence could be a constituent of the broadband background fluorescence, it could be discounted as a satellite source.

3.4.8.2 Impurity Lines. The only likely impurity transitions accounting for at least one of the satellite features was the caesium 6p - 9d transition at λ = 5664 Å. The absence in emission, however, of much stronger caesium lines such as the second resonance doublet 6s - 7p at λ = 4555 Å and 4593 Å dismissed impurities as an explanation.

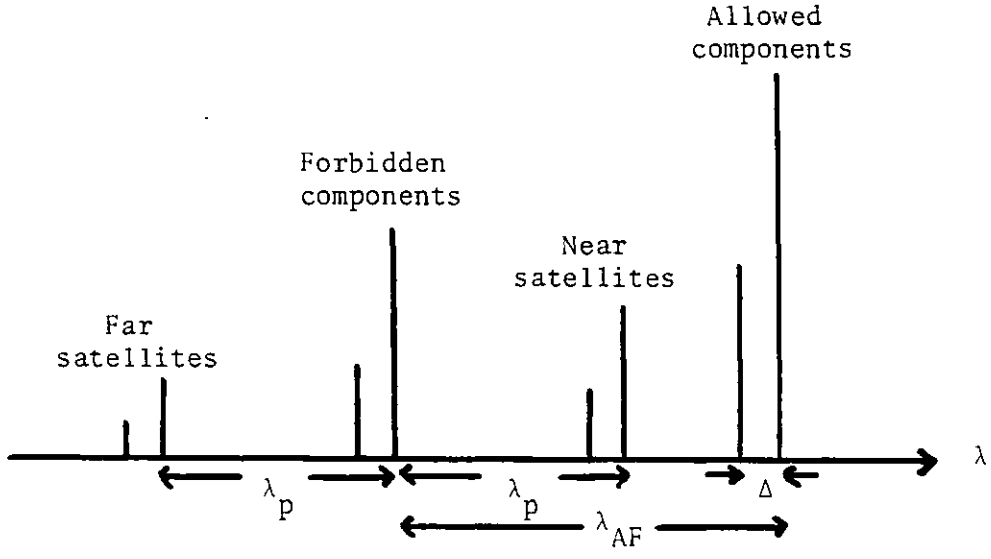
3.4.8.3 Quasimolecular Satellites. Close encounters between emitting sodium atoms and other perturbing species such as Na^+, He or Na_2 distort the potential curves of bound electrons such that maxima and minima can appear in the difference potential of two states. These maxima and minima translate in the frequency domain as satellites located on opposite sides of the unperturbed transition connecting these two states (Baker and Burgess, 1979; Preston, 1977). However, no experimental nor theoretical data were available for determining their strength and position for excited alkali transitions.

3.4.8.4 Plasma Satellites. Longitudinal plasma waves can couple with electronic transitions with the resultant emission through conservation of energy, of photons at frequencies $\pm n\omega_p$ away from the transition line center, n being odd for forbidden components, even for allowed components. The ratio of first order satellites (n=1) to forbidden component intensities for small ratios is then proportional to the ratio of plasma wave energy density to particle microfield energy density. Plasma satellites have thus been observed in emission and by laser fluorescence techniques when plasma wave activity was enhanced by hot electrons in turbulent plasmas (Hildebrandt, 1983) or when the mean thermal collective wave energy became comparable to the nearest neighbor Coulombic energy (Ya'akobi and Bekefi, 1969). In this latter case, the ratio of satellite to forbidden component intensities was shown to fit the following approximate equation for first order satellites (Griem, 1974)

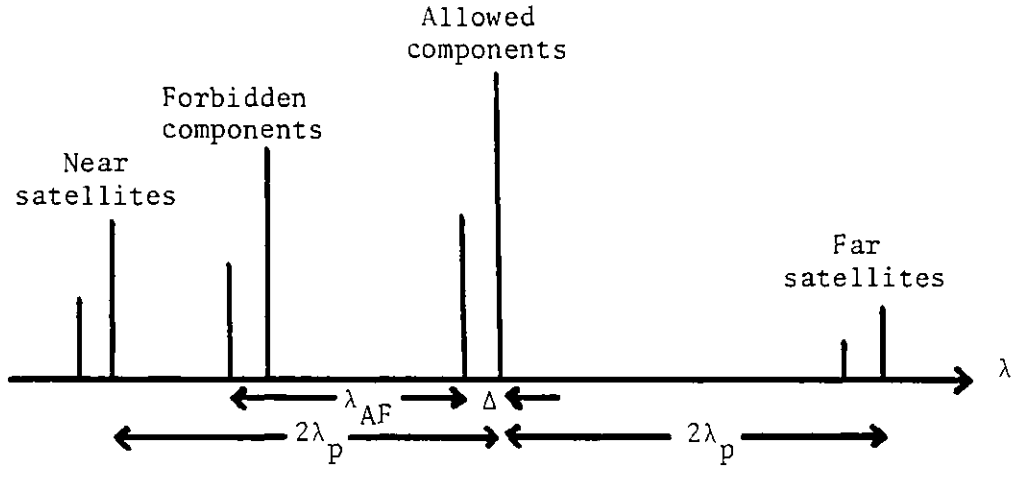
$$\frac{I_{\omega_p}}{I_F} = \frac{1}{2}\left(\frac{E_w}{E_p}\right)^2\left(\frac{\omega_{AF}}{\omega_{AF}\pm\omega_p}\right)^2 = \frac{0.5}{N_D^{1/3}}\left(\frac{\lambda_p}{\lambda_p\pm\lambda_{AF}}\right)^2 \qquad (3.20)$$

$$\lambda_p/\text{Å} = 3 \times 10^{-15} \lambda_F^2 N_e^{\frac{1}{2}} ; \quad \lambda_p = \frac{\lambda_F^2}{2\pi c} \cdot \omega_p \qquad (3.21)$$

where E_w and E_p are mean wave and particle fields respectively, I_{ω_p} is the first order satellite intensity, λ_{AF} is the wavelength separation between allowed and forbidden components and λ_F is the wavelength of the forbidden transition in Å. The ± correspond to far and near satellites respectively, schematically shown in Fig. 3.27a for the sodium doublets with separation Δ.



(a) First-order Plasmon Satellites.



(b) Fourth-order Plasmon Satellites.

Fig. 3.27.

The far satellite intensity on the 3p - 4f blue wing at $N_e = 1.5 \times 10^{16}$ cm^{-3}, $N_D = 2$ is given by, using equations (3.20) and (3.21):

$$\lambda_{AF} = 12.5 \text{ Å}, \quad \lambda_p = 12 \text{ Å} \Rightarrow \frac{I\omega_p}{I_F} = 0.1 \qquad (3.22)$$

Since $\lambda_p \sim \lambda_{AF}$, the near satellite (Fig. 3.27a) would be merged with the strong allowed component and hence difficult to detect.

The experimentally observed satellite positions and intensities are listed in Table 3.4.

TABLE 3.4

Satellite Characteristics

Allowed Transition	λ_A/Å	λ_F/Å	λ_S/Å	Δ/Å	λ_{AF}/Å	λ_{FS}/Å	I_S/I_F	λ_{AS}/Å
$3p_{3/2}$-$4d_{5/2}$	5688.2	5675.7 (4f)	5664-5667	5.6	12.5	9-12	0.5-0.7	21-24
$3p_{\frac{1}{2}}$ -$4d_{3/2}$	5682.6	5670.2	5659-5661		12.4	9-11	0-0.4	23-24
$3p_{3/2}$-$5d_{5/2}$	4982.8	4977.5 (5f)	4970	4.3	5.3	8	~0.5	13
$3p_{\frac{1}{2}}$ -$5d_{3/2}$	4978.5	4973.5	4964		5	10	~0.5	15
$3p_{3/2}$-$5d_{5/2}$	4982.8	4977.0 (3g)			5.8			
$3p_{\frac{1}{2}}$ -$5d_{3/2}$	4978.5	4972.7			5.8			

λ_S is the wavelength of the satellite transition, λ_{FS} is the forbidden component to satellite separation, λ_{AS} is the allowed component to satellite separation and I_S/I_F is the ratio of observed satellite to forbidden component intensities. Hence, there was support for identifying the wing features as plasmon satellites since a doublet

structure was observed several times on the 3p - 4f and 3p - 5f blue wings at $\sim \lambda_p$ detuning and with similar doublet separation Δ as for the allowed and forbidden components. These satellites would be expected to shift towards the forbidden component as N_e and hence λ_p (equation (3.21)) dropped. The shifts in the temporally resolved satellites proved to be irreproducible, however, even when the photomultiplier was replaced by a Hadland Instruments streak camera and the photographed spectra scanned by microdensitometer.

The two plasmon scheme shown in Fig. 3.27b producing fourth order satellites at $2\lambda_p$ away from the allowed component could also explain the observed features since $\lambda_p \sim \lambda_{AF}$. In fact, the near fourth order satellite intensity can exceed the far first order satellite intensity (Burgess, 1971) and is given by:

$$\frac{I_{2\omega_p}}{I_A} = \frac{c^2 \langle E^2_w \rangle^2}{(2\omega_p)^2 (\omega_p - \omega_{AF})^2} \tag{3.23}$$

where $$\frac{I_F}{I_A} = \frac{c \langle E^2_p \rangle}{\omega_{AF}^2} \tag{3.24}$$

and c is a constant.

Combining equations (3.20), (3.23) and (3.24):

$$\frac{I_{2\omega_p}\ (\text{Near})}{I_{\omega_p}\ (\text{Far})} = \frac{I_F}{I_A} \cdot \frac{0.5}{N_D^{1/3}} \cdot \left(\frac{\omega_{AF}}{2\omega_p} \right)^2 \cdot \frac{(\omega_{AF} + \omega_p)^2}{(\omega_p - \omega_{AF})^2} \tag{3.25}$$

For the measured values $\frac{I_{3p\text{-}4f}}{I_{3p\text{-}4d}} = 0.25$, $N_D = 2$ and $\omega_p \sim \omega_{AF}$:

$$\frac{I_{2\omega_p}}{I_{\omega_p}} \sim \frac{0.1\ \omega_{AF}^2}{(\omega_p - \omega_{AF})^2} \tag{3.26}$$

From Table 3.4, the maximum $\lambda_p - \lambda_{AF}$ is $\sim$ 3 Å which implies:

$$\left.\frac{I_{2\omega_p}}{I_{\omega_p}}\right|_{\text{MINIMUM}} \sim 1 \qquad (3.27)$$

Thus fourth order satellites at $2\lambda_p$ would dominate the blue wing spectrum of the forbidden components and, by combining equations (3.22) and (3.27), could account for the large I_S/I_F ratios observed. Moreover, by differentiating equation (3.23) with respect to N_e, the satellite intensity fluctuations observed can be explained by their strong dependence on shot-to-shot plasma density variations:

$$\frac{\Delta I_{2\omega_p}}{I_{2\omega_p}} > 4\,\frac{\Delta N_e}{N_e} \qquad \text{for } \lambda_{AF} - \lambda_p < 3 \text{ Å}$$

(cf. From equation (3.18): $\dfrac{\Delta I_{3p\text{-}4f}}{I_{3p\text{-}4f}} = 0.2\,\dfrac{\Delta N_e}{N_e}$)

Since the concept of Debye length and hence plasma frequency becomes unclear for N_D approaching 1, the Q-value of the plasma resonance could decrease implying an increase in the width of ω_p (Bekefi, 1976):

$$\frac{\Delta\omega_p}{\omega_p} \sim \frac{0.3}{N_D^{\frac{1}{2}}} \qquad (3.28)$$

The plasmon satellite spectral lineshape might then be a convolution of the plasma resonance spectrum (HWHM by equation (3.28)) with the atomic frequency response (equation (3.23)) yielding in general peaks at $-2\lambda_{AF}$ and $-2\lambda_p$ detuning from the allowed component. By inspection of Table 3.4, either or both peaks could explain the experimental features. A final point in favor of $2\lambda_p$ satellites was the absence

of a far satellite at + $2\lambda_p$ on the allowed red wing. This can be understood by comparing near and far satellite intensities (Burgess, 1971):

$$\frac{I_{2\omega_p}\ (FAR)}{I_{2\omega_p}\ (NEAR)} = \left(\frac{\omega_p - \omega_{AF}}{\omega_p + \omega_{AF}} \right)^2 < \frac{1}{50} \quad \text{for } \lambda_p - \lambda_{AF} < 3\ \text{Å}$$

Finally, it is interesting to note that another satellite observed in a non-Debye plasma (Ya'akobi and Bekefi, 1969) can also be explained by a fourth order effect since $\lambda_p = \lambda_{AF}$ to within 5% in this case.

3.4.9 Continuum Depression

The high-lying levels closest to the ionization limit are most perturbed by the plasma microfield. These states merge when quasi-static Stark shifts become greater than level separations or disappear due to the depression of the ionization potential by the influence of neighboring ions. In either case, the continuum appears to extend below the unperturbed ionization potential by an amount $\Delta\chi$ given by the Inglis-Teller limit (Inglis and Teller, 1939) for the former case and by either the Debye-Hückel (Debye and Hückel, 1923) nearest neighbor (Unsöld, 1948), quasi-crystalline (Likal'ter, 1981) or Thomas-Fermi model (Stewart and Pyatt, 1966) for the latter case.

For the sodium series most easily observed in emission in the visible region, 3p - nd, the Inglis-Teller limit is given by:

$$N_e = 10^{23.9 \pm 0.2} (n^*)^{-7.5} \qquad n^* > 3 \tag{3.29}$$

$$\Rightarrow \quad \Delta\chi/eV = 6 \times 10^{-8}\ N_e^{4/15}$$

where n^* is the first nd state to become merged with the (n^*+1)d state.

The assumptions inherent in equation (3.29) are as follows:

(a) The sodium d states are hydrogenic, correct to within < 1%.

(b) The linear Stark effect dominates over the quadratic Stark effect for n* and higher. This is justified since nd to nf, ng, etc... level separations are typically $1/50$th of nd to (n+1)d level separations. Hence all $\ell > 1$ states should be merged for n approaching n*.

(c) Both ions and electrons are treated throughout the line profile as quasistatic perturbers. This requirement is harder to satisfy for the faster electrons and, for the 3p - nd transitions, is given by (Griem, 1964):

$$N_e > \left(\frac{kT_e}{6m_e} \right)^{3/2} \left(\frac{m_e}{\hbar} \right)^3 \frac{1}{(n^2-9)^3} \qquad (3.30)$$

For T_e = 2500K and $N_e = 1.5 \times 10^{16}$ cm^{-3}, equation (3.30) is satisfied for n > 5, which is well below n* = 12 from equation (3.29).

(d) The average plasma microfield is determined by the nearest neighbor for both ions and electrons, as suggested by Weisheit and Pollock (1982) for $N_D < 3$.

The numerical values of the ionization potential depression due to the average plasma electric field are presented below for the various theories (in eV):

Debye-Hückel: $\Delta\chi = 2 \times 10^{-7}/\lambda_D$ (λ_D in cm) (3.31)

Unsöld: $\Delta\chi = 6.9 \times 10^{-7} N_e^{1/3}$ (3.32)

Likal'ter: $\Delta\chi = 10^{-7} N_e^{1/3}$ (3.33)

Stewart & Pyatt: $\Delta\chi = \frac{kT_e}{4} \left[\left(\frac{2^{3/2}}{N_D} + 1 \right)^{2/3} - 1 \right]$ (3.34)

The continuum depression was measured by recording the 3p - nd fluorescence on film using the Hadland Instruments streak camera in streak mode coupled to the Bentham spectrometer. Microdensitometer traces for $N_{Na} = 3 \times 10^{17}$ cm^{-3} are shown in Fig. 3.28 for various times in the plasma afterglow. Each trace corresponded to five shots at 20 ns, 15 Å resolution with maximum image intensifier gain. The unmerged transitions have been identified and labelled in Fig. 3.28 The continuum depressions inferred from these traces are plotted in Fig. 3.29 along with the theoretical values represented by equations (3.29) and (3.31 - 3.34), where T_e = 2500K and N_e is determined from the lower-lying transition linewidths (section 3.4.5).

The Unsöld theory overestimates the depression which appears to be determined by the Inglis-Teller limit corrected for correlations and small N_D (Hooper, 1968).

3.5 Electron Temperature

3.5.1 Introduction

The high peak electron densities ($N_e = 1.2 \times 10^{16}$ cm^{-3}) measured in the previous section coupled with the low temperature (0.25 eV) estimated from the $N(3p)/N(3s)$ ratio (section 3.4.5) suggested that relative line intensities of high-lying sodium levels would be a sensitive time resolved diagnostic for T_e, even before the 3p population reached an equilibrium level (Fig. 3.23). The experimental details and results of such measurements are presented in this section and the validity of assuming Local Thermodynamic Equilibrium (LTE) discussed for the present transient plasmas. Temperature time histories combined with excited state absolute population densities are used to

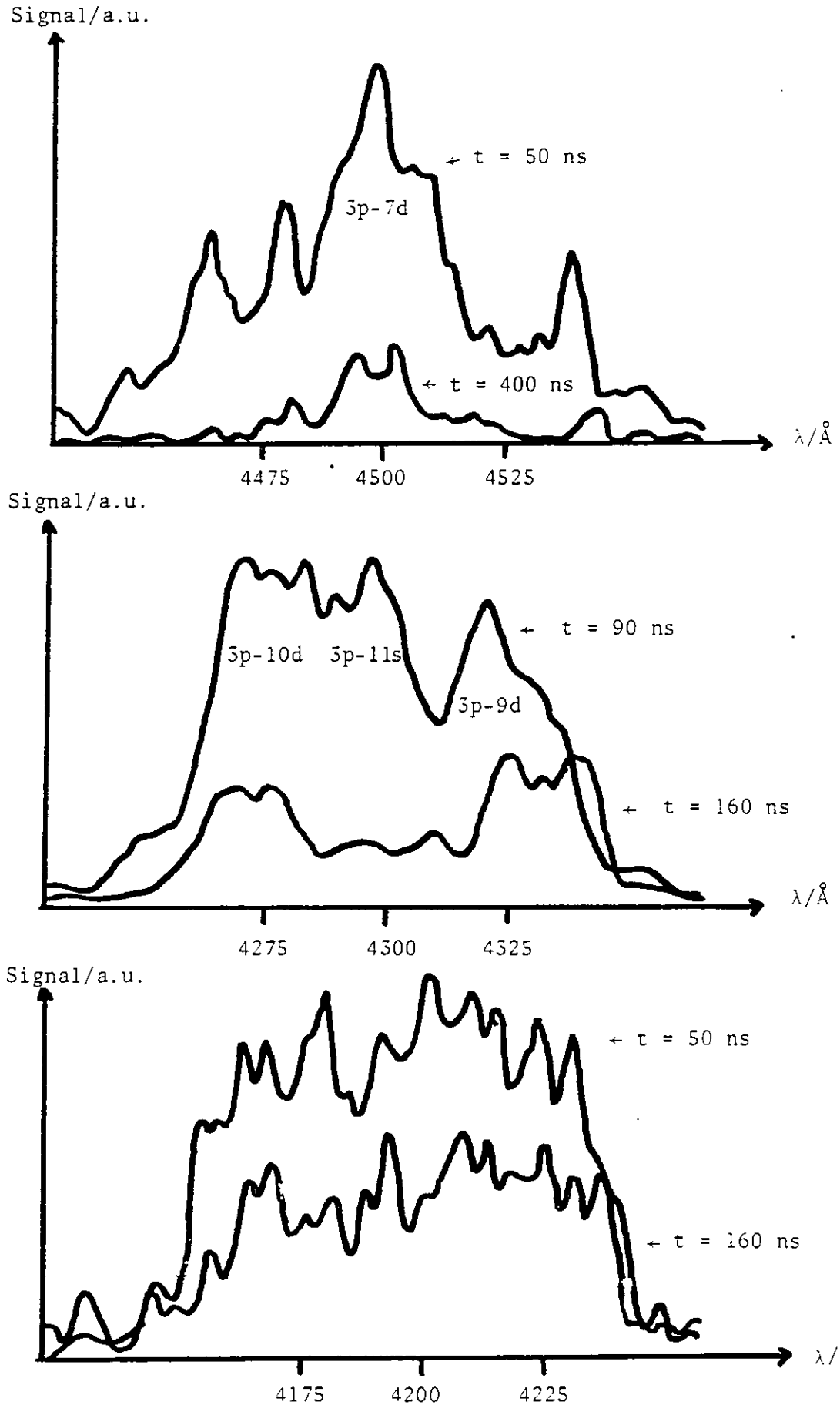


Fig. 3.28. Temporally-resolved fluorescence from levels 7d and higher.

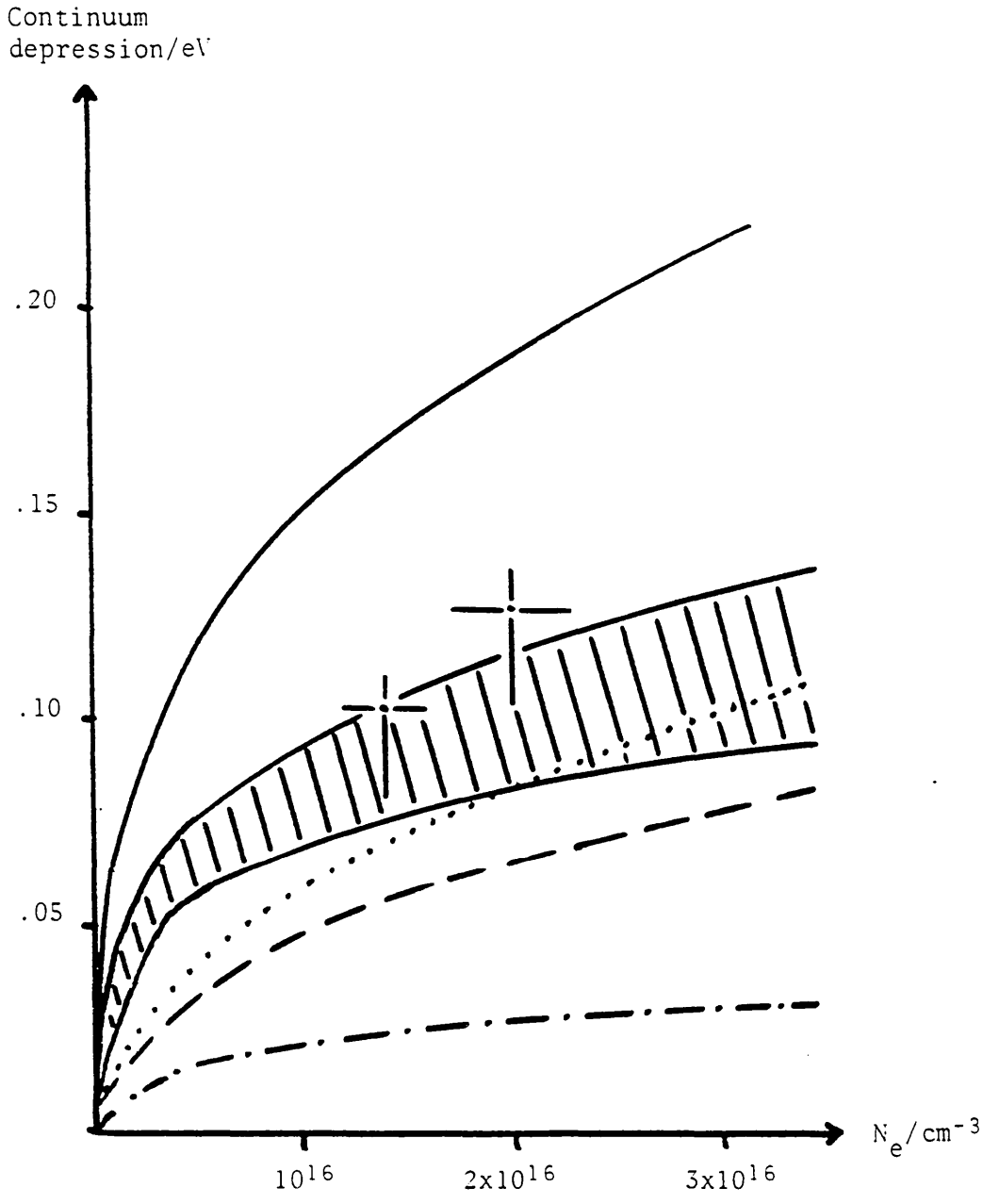


Fig. 3.29. Experimental (—•—) and theoretical values for continuum depression (T_e = 2500 K).

Inglis-Teller limit

Debye-Hückel

Unsöld

Likal'ter

Stewart and Pyatt

compare theoretical equilibrium values for N_e with those previously measured.

3.5.2 Experimental Details

The experimental layout was equivalent to that described for emission lineshapes. A standard tungsten ribbon lamp placed in the equivalent plane of the plasma was used to calibrate line emission for conversion into absolute population densities. The spectrometer slits were set at 0.2 or 0.25 mm corresponding to 5 - 7 Å FWHM. This allowed the majority of the broadened $3p_{3/2}$ - nℓ line profiles to be recorded while neglecting the line center regions of the $3p_{1/2}$ - nℓ components. This situation was favored to wider slits covering both components because of the higher line to background signals achieved.

Temporally resolved fluorescence signals were recorded on a Tektronix 466 Storage oscilloscope at 3 ns resolution for all $3p_{3/2}$ - $ns_{1/2}$ and $3p_{3/2}$ - $nd_{5/2}$ transitions, up to n = 9. These signals were then corrected for background radiation by subtracting the emission level at $\sim$ 15 Å detuning from the line centers.

3.5.3 Boltzmann Plot

The relationship between the excited state sub-level population densities and the fluorescence intensities F(nℓ) for optically thin ($\tau_0 < 0.5$) lines is given by:

$$\frac{N(n\ell)}{g(n\ell)} \propto \frac{F(n\ell)\ \lambda_{3p\text{-}n\ell}\ e^{\tau_{Na_2}(\lambda_{3p\text{-}n\ell})}}{g(n\ell)\ A_{3p\text{-}n\ell}\ \phi(\lambda_{3p\text{-}n\ell})} \qquad (3.35)$$

where $g(n\ell)$, $\lambda_{3p\text{-}n\ell}$ and $A_{3p\text{-}n\ell}$ are the upper level degeneracy, transition

wavelength and decay rate respectively and $\phi(\lambda)$ is the spectrometer and photomultiplier relative sensitivity at λ in unit current per unit incident radiation power. Molecular reabsorption at λ is accounted for by $e^{\tau_{Na_2}(\lambda)}$ for which the 5 mm vapor length between plasma and spectrometer for sapphire tube containment represented a < 25% maximum correction to the line fluorescence signals for $N_{Na} = 10^{17}$ cm^{-3}.

The Boltzmann distribution of level populations should hold for atomic levels collisionally coupled by a Maxwellian distribution of free electrons:

$$\frac{N(n\ell)}{g(n\ell)} \propto e^{-\frac{E(n\ell)}{kT_e}} \tag{3.36}$$

where $E(n\ell)$ is the energy of the $n\ell$ state above some fixed level.

The fluorescence signals were thus calibrated by the tungsten lamp, converted to densities by equation (3.35) and their logarithms plotted versus $E(n\ell)$. A typical result of such a Boltzmann plot is shown in Fig. 3.30 for t = 50 ns in the plasma afterglow and $N_{Na} = 8 \times 10^{16}$ cm^{-3}. The error bars shown reflect the random errors due to the finite slit width (30%), shot-to-shot fluctuations (10%), uncertainties in oscillator strengths and hence decay rates (20%) and uncertainty in $\phi(\lambda)$ (30%). The possible systematic error for the absolute excited state densities was estimated as a factor of two either way, principally due to the uncertainty in the plasma radius. The line of best fit was preferentially drawn through the ns densities since the 3p - ns transitions were less broad than the 3p - nd lines and hence provided better spectral overlap between the acceptance bandwidth of the spectrometer slits and the linewidths. In fact, the 4d and 5d population densities inferred from equation (3.35) tended

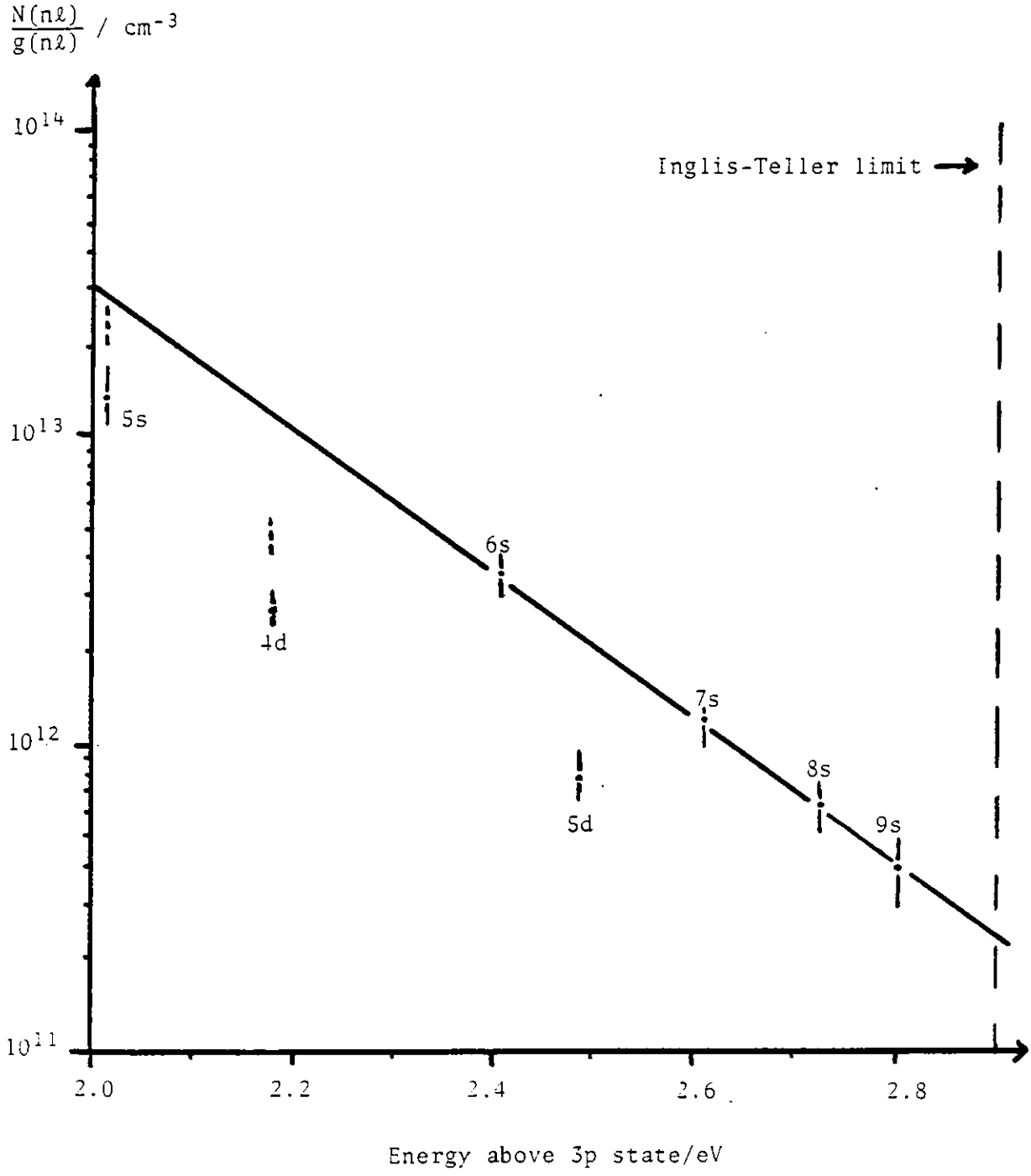


Fig. 3.30. Boltzmann plot: N_{Na} = 8 x 10^{16} cm^{-3} and t = 50 ns. (Dotted vertical lines are corrections for opacity.)

towards the line of best fit at later times as N_e and hence linewidths decreased. The 5s and 4d densities were underestimates at early times in the plasma afterglow ($t < 100$ ns) due to opacity. The corrected values using Fig. 3.23 and equation (3.14) are shown as dotted lines on Fig. 3.30.

By extrapolating the line of best fit to $E_{n\ell} = E_{3p}$, the 3p population determined from the N(3p) versus N_e plots can be compared with that expected if the first resonance state 3p were collisionally coupled with the higher excited states. For $N_{Na} = 8 \times 10^{16}$ cm^{-3}, $t = 50$ ns:

$$N(3p) \quad \text{(Extrapolation)} = 4^{+4}_{-2} \times 10^{17} \text{ cm}^{-3} \quad \text{(from Fig. 3.30)}$$

$$N(3p) \quad \text{(Linewidths)} = 1^{+2}_{-0.6} \times 10^{15} \text{ cm}^{-3} \quad \text{(from Fig. 3.23)}$$

The underpopulation of the 3p state with respect to higher states was even greater at later times ($t > 100$ ns) when the 3p level had been depleted by super-elastic electron collisions (Fig. 3.23). Hence the ground-state and resonance state were not collisionally coupled with the higher excited states implying complete thermal equilibrium was never reached.

3.5.4 Validity of LTE

In a steady-state situation, electron de-excitation rates $N_e C_{ij}$ must exceed decay rates A_{ij} between neighboring levels i and j by at least a factor of 3 if relative level populations are to be determined solely by electrons. For the minimum electron density measured, $N_e = 3 \times 10^{15}$ cm^{-3}, and for $T_e \sim 0.3$ eV (Enemark and Gallagher, 1972):

Minimum $N_e C_{ij}$ is for 3s - 3p = 3×10^8 s^{-1}

Maximum A_{ij} is for 3s - 3p = 6×10^7 s^{-1}

For the excited levels 5s and above, the conditions for collisional coupling is even more easily met:

$N_e C_{ij} = 10^{10} - 10^{11}$ s^{-1} (Shuker et al., 1980)

$A_{ij} = 10^7 - 10^6$ s^{-1} (Wiese et al., 1969)

The inelastic collision rates per electron, $N_j C_{ij}$, should be negligible compared with the electron-electron elastic collision rate, $1/\tau_{ee}$, for a Maxwellian electron distribution to exist. For the measured values

$N(4d) = 10^{13}$ cm^{-3} (Fig. 3.30), $N_e = 10^{16}$ cm^{-3} and $T_e = 0.2$ eV:

$N(4d)C_{4p-4d} = 10^7$ s^{-1}

$1/\tau_{ee} = 10^{12}$ s^{-1} (Spitzer, 1956)

For t < 100 ns, however, electron super-elastic collisions with the 3p level represented the dominant inelastic rate:

$N(3p)C_{3s-3p} = 10^8$ s^{-1}

$$1/\tau_{ee} \times \left(\frac{kT_e}{E_{3s-3p}} \right)^{3/2} = 3 \times 10^{10} \text{ s}^{-1}$$

Hence, even with the factor $\left(\frac{kT_e}{E_{3s-3p}} \right)^{3/2}$ accounting for the slower rate of thermalization for suprathermal electrons (MacDonald et al., 1957), all electrons should relax to a Maxwellian distribution within < 0.1 ns.

The collisional decoupling observed between the 3p and 5s states

and above even after 300 ns must then be attributed to the time delay τ_{3s} for establishing equilibrium, which is greatest for the ground-state 3s. From calculations for hydrogen (Drawin, 1969), suitably modified for the lower ionization potential of sodium:

$$\tau_{3s} = 10\ \mu s \text{ to } 1\ ms \text{ for } N_e = 10^{16}\ cm^{-3} \text{ and } T_e = 0.3 - 0.2\ eV$$

The excited level (3d and above) equilibriation times are much shorter, typically the inverse of the de-excitation rates $N_e C_{ij}$, which are < 0.1 ns. These fast relaxation times would not be affected by the transient behavior of the plasma as it decayed on a much longer time-scale, $\sim$ 100 ns (Fig. 3.22). Similarly, the diffusion time for atoms to enter the millimeter radius plasma, $\sim$ 1 μs, was too long for an appreciable density of atoms not in LTE to exist within the plasma.

Finally, atom-atom inelastic collision rates $N(n\ell)C_{Na\text{-}Na}$ were a maximum of $3 \times 10^6\ s^{-1}$ (section 1.3) after the end of the laser pulse, negligible compared to $N_e C_{ij} > 10^{10}\ s^{-1}$. This signified that the temperatures recorded from the Boltzmann plots did reflect the electron temperature and not the neutral atom temperature.

It should be noted that all electron collision rates would still exceed all other rates if they were a factor of 10 less, as suggested by recent experimental work (Gohil, 1982) on low T_e hydrogen plasmas.

3.5.5 Ionization Equilibrium and Plasma Chemistry

Excited states in LTE with free electrons should obey Saha's equation:

$$\frac{N_e\ N_{Na^+}}{N(n\ell)} = \frac{2U_{Na^+}}{g(n\ell)} \frac{(2\pi m\ kT_e)^{3/2}}{h^3} e^{-\left(\frac{\chi(n\ell) - \Delta\chi}{kT_e}\right)} \qquad (3.37)$$

where $\chi(n\ell)$ is the ionization potential of level $n\ell$, $\Delta\chi$ is the ionization potential depression taken to be $\sim$ 0.07 eV for N_e = 2×10^{16} cm^{-3} (Stewart and Pyatt, 1966) (see Fig. 3.29) and U_{Na^+} is the partition function of Na^+, equal to one within 1% for all T_e of interest.

Setting $N_e = N_{Na^+}$ presupposes no significant population densities of molecular or negative ions such as Na_2^+ or Na^-. These species become increasingly abundant for higher N_e, lower T_e plasmas (Sokolovskii, 1969; Griem, 1964) and should therefore be considered briefly:

Na_2^+ Should complete molecular multiphoton ionization occur, as has been recently suggested (Wu et al., 1982) but for which no rates are currently available, photodissociation would decrease the resultant Na_2^+ population at a rate of 10^9 s^{-1} (Kirby-Docken et al., 1976; Roussel et al., 1983) for $I \sim 10^7$ W cm^{-2}. The Na_2 and Na_2^+ populations would relax to LTE values determined by the electron temperature. In equilibrium:

$$\frac{N_{Na_2}}{N_{Na}} \propto e^{\frac{H}{kT_e}}$$

where H is the binding energy of the Na_2 ground-state, 0.8 eV. From the JANAF tables:

$$\frac{N_{Na_2}}{N_{Na}} = 0.1 \quad \text{for} \quad T_{OVEN} = 0.08 \text{ eV} \quad \text{at} \quad N_{Na} = 10^{17} \text{ cm}^{-3}$$

$$\Rightarrow \quad N_{Na_2} = 2 \times 10^{13} \text{ cm}^{-3} \text{ at } T_e = 0.2 \text{ eV}$$

If Saha equilibrium reached:

$$\frac{N_{Na_2^+} N_e}{N_{Na_2}} \sim 2 \frac{(2\pi mkT_e)^{3/2}}{h^3} e^{-\frac{\chi_{Na_2}}{kT_e}}$$

where χ_{Na_2} = 4.9 eV (Herrmann et al., 1978) and the Na_2 and Na_2^+ partition functions are assumed to be similar. For $N_e = 2 \times 10^{16}$ cm^{-3}, T_e = 0.2 eV:

$$\Rightarrow \quad N_{Na_2^+} = 10^7 \text{ cm}^{-3}$$

For T_e = 0.3 eV, $N_{Na_2} = 5 \times 10^{12}$ cm^{-3} and $N_{Na_2^+} = 10^{10}$ cm^{-3}

Hence, by the end of the laser pulse, the Na_2^+ population will have decreased to $<.01\ N_e$ and eventually reach an equilibrium population negligible compared to the Na^+ population.

Na$^-$ The extra electron on the negative sodium ion has a binding energy of 0.54 eV (Patterson et al., 1974). Hence all excited states of Na$^-$ should have a negligible population compared to Na$^-$(3s) since they can undergo exothermic autodetachment (Fig. 3.31).

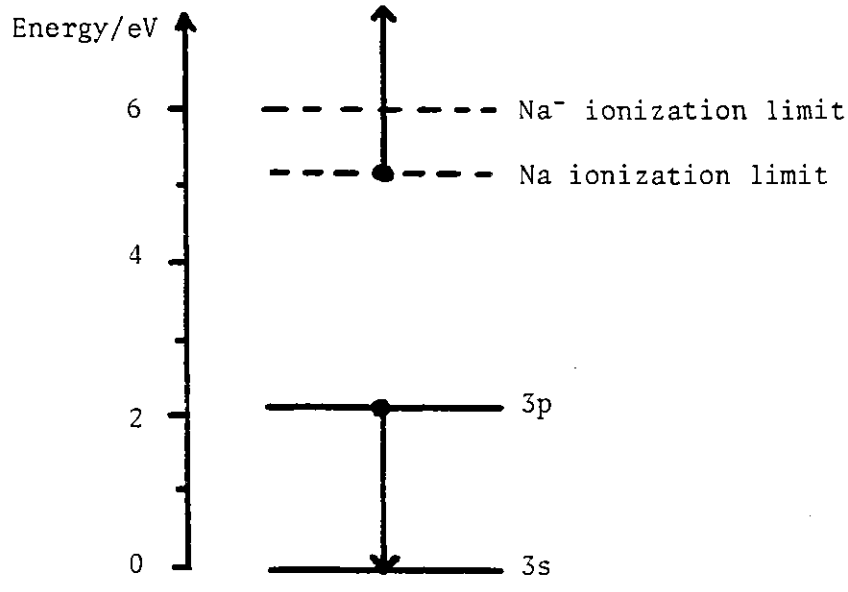


Fig. 3.31. Autodetachment for Na$^-$(3p)

The Na$^-$(3s) population can be estimated by Saha's equation:

$$\frac{N_e\, N(3s)}{N_{Na^-}} = 2\,\frac{(2\pi mkT_e)^{3/2}}{h^3}\, e^{-\frac{0.54}{kT_e}}$$

For $N(3s) = 3 \times 10^{17}$ cm^{-3}, $T_e = 0.2$ eV and $N_e = 2 \times 10^{16}$ cm^{-3};

$$\Rightarrow \quad N_{Na^-}(3s) = 2 \times 10^{14} \text{ cm}^{-3} \ll N_e, N_{Na^+}$$

These order of magnitude estimates were consistent with calculations on Cs (Sokolovskii, 1969) and Li (Kovaliov and Kulik, 1971). More exotic clusters such as Na_m, Na_m^-, Na_m^+ ($m > 1$) will be present in even smaller quantities for $N_{Na} < 10^{19}$ cm^{-3} at $T_e = 0.2$ eV (Yermohkin et al., 1975; Herrmann et al., 1978; Kovaliov and Kulik, 1971).

Hence $N_e = N_{Na^+}$ to better than 1% and equation (3.37) reduces to:

$$N_e^2 = 6 \times 10^{21}\, \frac{N(n\ell)}{g(n\ell)}\, T_e^{3/2}\, e^{-\frac{(\chi_{n\ell}-.07)}{T_e}}$$

where $\chi(n\ell)$, T_e are in eV.

For the following measured values at $t = 50$ ns:

$$N_e = 1.2 \pm 0.2 \times 10^{16} \text{ cm}^{-3}, \quad N(6s) = 3^{+3}_{-2} \times 10^{12} \text{ cm}^{-3}$$

where $\chi(6s) = 0.63$ eV and $g(6s) = 2$:

$$\Rightarrow \quad T_e \text{ (by Saha)} = 0.24 \pm .04 \text{ eV}$$

This compared favorably with $T_e = 0.2 \pm .02$ eV from the Boltzmann plot.

3.5.6 Temporal History of T_e

The time evolution of the temperature was then determined from a series of Boltzmann plots taken at 30 or 50 ns intervals in the plasma afterglow. Figures 3.32 - 3.33 show results for $N_{Na} = 4.5 \times 10^{16}$ cm^{-3},

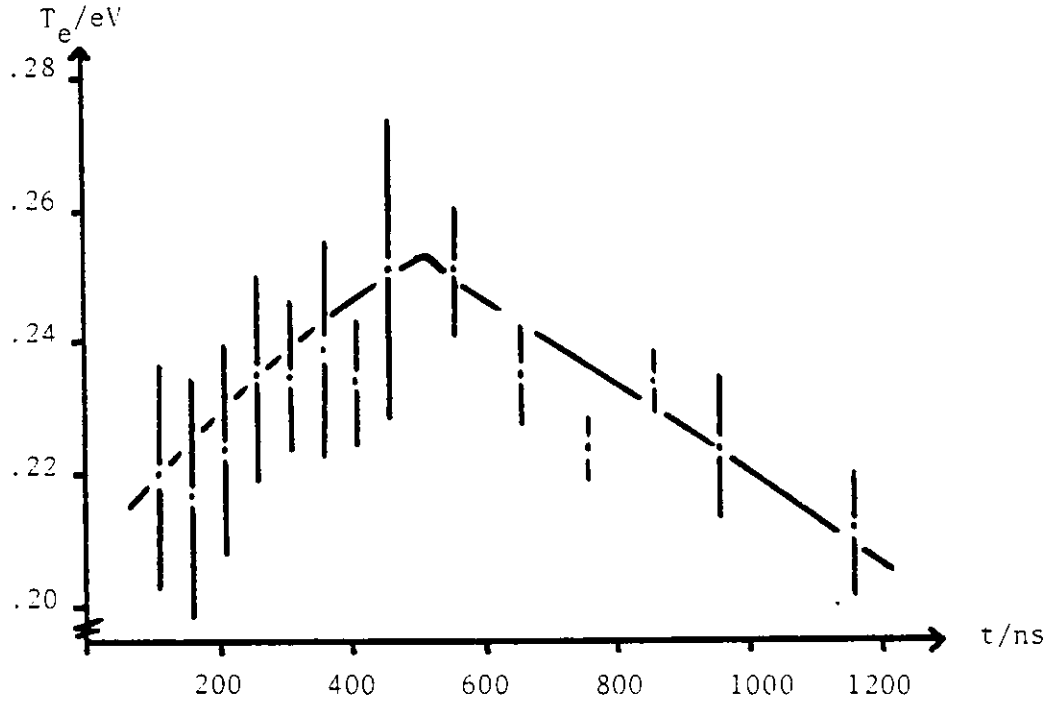


Fig. 3.32. Temporal history of T_e.
$N_{Na} = 4.5 \times 10^{16}$ cm^{-3}.

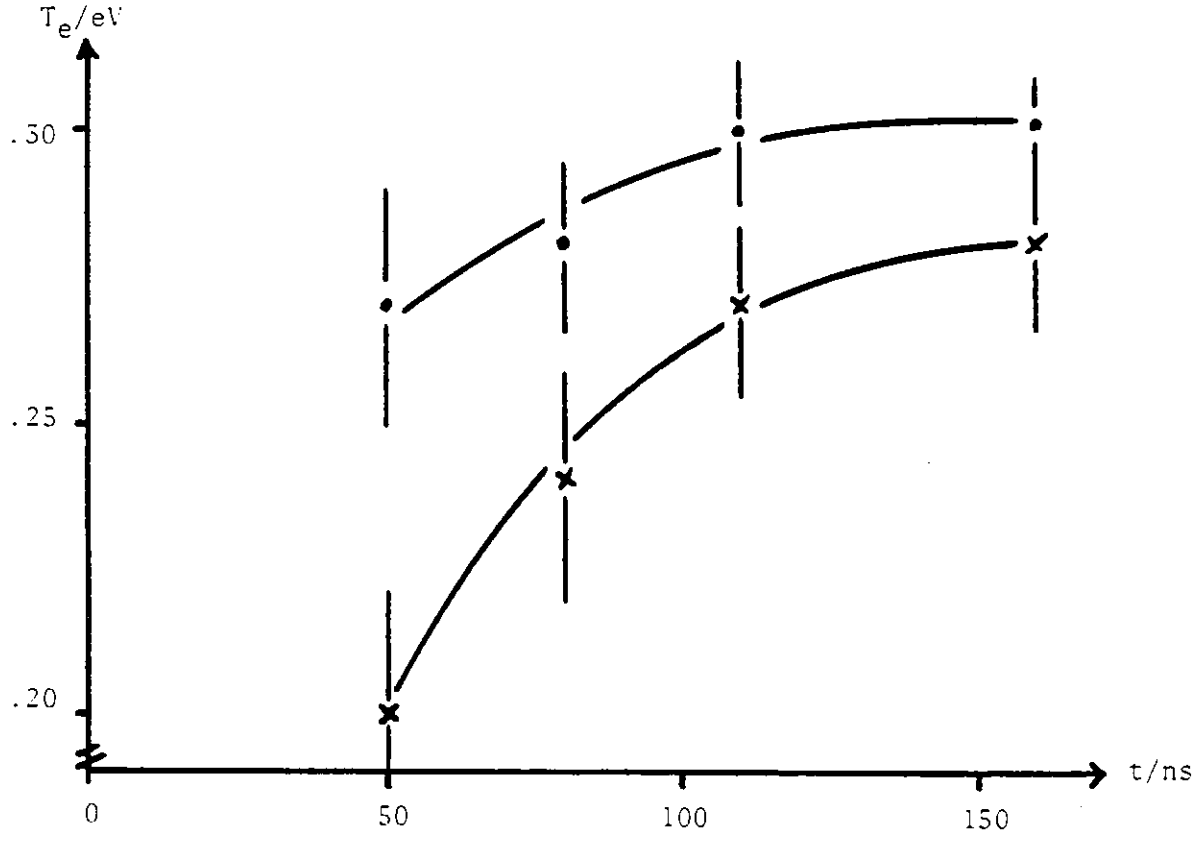


Fig. 3.33. Temporal history of T_e.
• $N_{Na} = 8 \times 10^{16}$ cm^{-3}
× $N_{Na} = 4 \times 10^{17}$ cm^{-3}

8×10^{16} cm^{-3} and 4×10^{17} cm^{-3} respectively. The initial temperature rise was attributed to:

(a) Super-elastic collisions with the 3p level:

$$e^- + N(3p) \rightarrow e^- + N(3s) + 2.1 \text{ eV}$$

$$\Rightarrow \tfrac{3}{2}\Delta T_e = \Delta N(3p)/N_e \times 2.1 \text{ eV} \qquad (3.38)$$

From Fig. 3.23, $N(3p) = 10^{15}$ cm^{-3} at $t = 50$ ns dropping to $\sim 10^{14}$ cm^{-3} within 50 ns. Hence, by equation (3.38):

$$\Rightarrow \quad \Delta T_e = 0.1 \text{ eV} \quad \text{for } N_{Na} = 4 \times 10^{17} \text{ cm}^{-3},\ N_e = 2 \times 10^{16} \text{ cm}^{-3}$$

$$\Delta T_e = 0.2 \text{ eV} \quad \text{for } N_{Na} = 8 \times 10^{16} \text{ cm}^{-3},\ N_e = 10^{16} \text{ cm}^{-3}$$

This temperature rise would be reduced by a factor of ~ 2 through electron-ion thermalization (see section 3.5.7).

(b) Heating by 3-body recombination followed by de-excitation to the 3s ground-state:

$$e^- + e^- + N_{Na^+} \rightarrow N(3s) + e^- + (\chi + \tfrac{3}{2}T_e)$$

Since collisional recombination dominated radiative recombination for $N_e > 10^{15}$ cm^{-3}, $T_e < 0.3$ eV (Bates et al., 1962):

$$\Delta T_e = -\frac{\Delta N_e}{N_e - \Delta N_e}\ (\tfrac{2}{3}\chi + T_e) \qquad (3.39)$$

For $\frac{\Delta N_e}{N_e} \ll 1$, equation (3.39) can be rearranged to give:

$$\frac{\frac{1}{N_e}\frac{dN_e}{dt}}{\frac{1}{T_e}\frac{dT_e}{dt}} = -\frac{T_e}{(\tfrac{2}{3}\chi + T_e)} \qquad (3.40)$$

The highest temperature observed experimentally, 0.3 eV, was significantly lower than predicted by Saha's equation: T_e = 0.35 - 0.38 eV for N_e/N_{Na} = 5% and N_{Na} = 5 x 10^{16} - 4 x 10^{17} cm^{-3}. Hence the plasmas never reached complete thermal equilibrium before cooling. If the only kinetic processes were 3-body recombination and collisional ionization, equation (3.40) should predict the ratio of fractional density decay to fractional temperature rise. For T_e = 0.25 eV and $\chi \sim 5$ eV, this ratio is $\sim 1/15$. The measured ratio by inspection of Figs. 3.22 and 3.33 was 1 to 2.

This discrepancy was mainly attributed to neglecting ambipolar diffusion as a density decay mechanism. The diffusion coefficient, scaled for Na^+ in Na from published experimental values for Cs^+ in Cs (Okuda et al., 1975), is $D_{Na^+,Na}$ = 100 cm^2 s^{-1} for N_{Na} = 10^{17} cm^{-3}. For a cylindrical plasma of initial radius r and initial density $N_e(0)$:

$$\frac{N_e(t)}{N_e(0)} = \frac{r^2}{(r + 2.4\sqrt{Dt})^2} \qquad (3.41)$$

Hence, for t = 200 ns, $\frac{N_e}{N_e(0)}$ = 0.8 if r = 1 mm

$\frac{N_e}{N_e(0)}$ = 0.7 if r = 0.5 mm

which is in satisfactory agreement with experimental results.

3.6 Ion and Atom Temperatures

For the present partially ionized plasmas with > 1% fractional ionization, neutral atoms gain kinetic energy from electrons via electron-ion elastic collisions during the ionized lifetime of an atom. Since the recombination rates (> 10^{10} s^{-1} by Shuker et al., 1980) are much faster than electron-ion thermalization rates (< 10^8 s^{-1} by

Spitzer, 1956), ion and atom temperatures remain equal while rising. It then follows that the effective electron-ion thermalization time, τ'_{ei}, is increased by a factor of $\frac{N_{Na}}{N_{Na^+}}$ from Spitzer's value. For $N_e = 2 \times 10^{16}$ cm^{-3}, $T_e = 0.25$ eV and $N_{Na} = 4 \times 10^{17}$ cm^{-3}, $\tau'_{ei} = 500$ ns. Hence the majority of fluorescence measurements were recorded when $T_{OVEN} < T_{Na}$, $T_{Na^+} < T_e$ and hence when the ions were more strongly coupled than the electrons, Γ_i reaching 1 when $T_{Na^+} \sim T_{OVEN}$.

3.7 Temporal History of N_D

The temporal behaviour of N_D is shown in Fig. 3.34 for $N_{Na} = 8 \times 10^{16}$ cm^{-3} and 4×10^{17} cm^{-3}. Previous published results from Table 3.1 are also plotted. The minimum N_D reached, 1.0 ± 0.2, corresponded to a ratio of potential energy to kinetic energy of 16%.

3.8 Plasma Dependence on Laser Characteristics

3.8.1 Bandwidth

By placing a nominally 100% reflecting mirror between prism and first dye amplifier (Fig. 2.1), a broadband $\sim$ 220 Å FWHM, 30 mJ 25 ns laser beam was produced in Rhodamine B, extending between 5750 and 5970 Å. The sodium vapor was pumped by this beam under the same conditions as for the narrow bandwidth laser. No differences in either fluorescence signals or electron density were detected. This somewhat surprising result is nevertheless entirely consistent with the now widely accepted view (Stacewicz, 1980; Carré et al., 1981) that the 3p state must be saturated for significant ionization to occur.

To understand this, it is instructive to calculate the minimum spectral flux necessary for saturation, defined as 10 $I_s(\lambda)$ where:

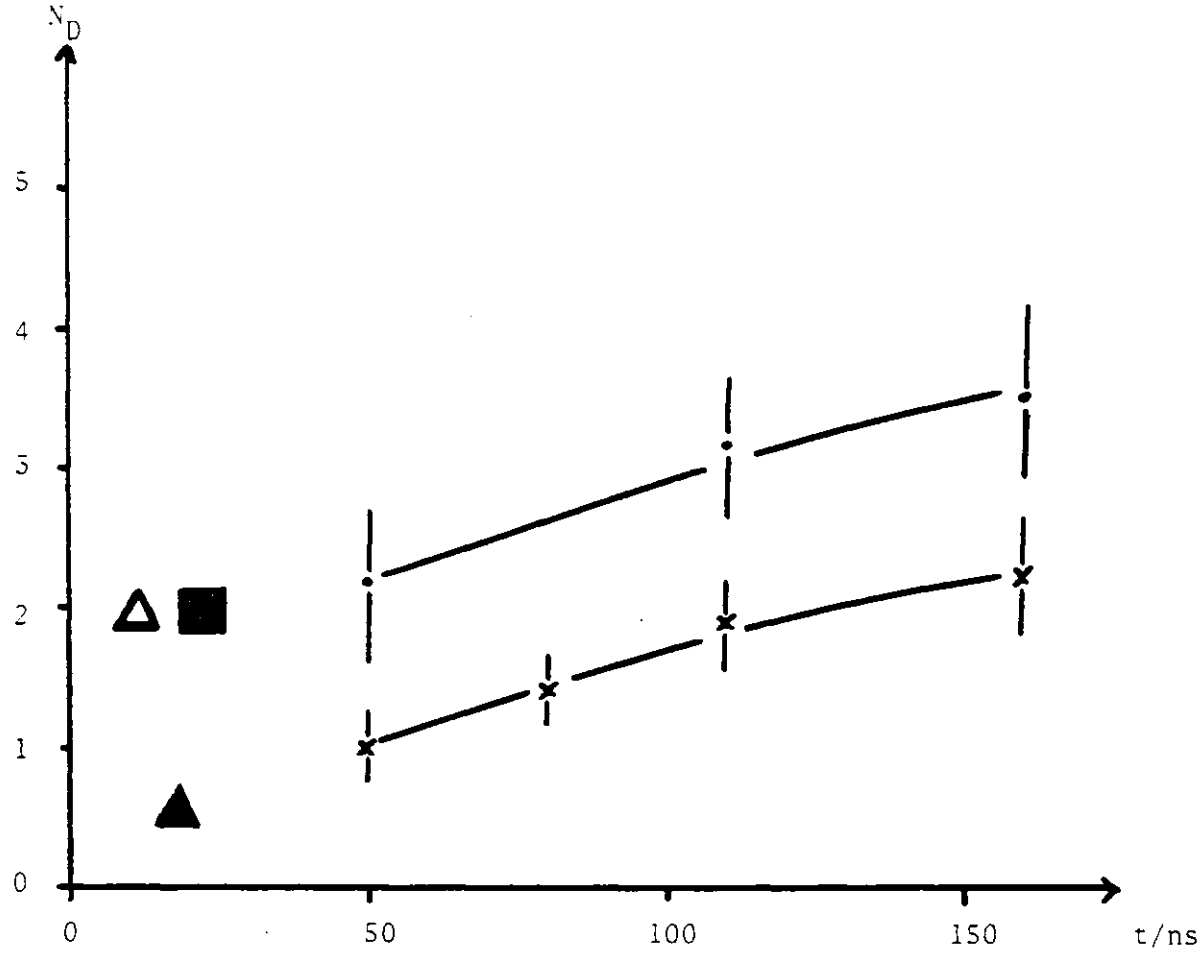


Fig. 3.34. Temporal history of number of electrons per Debye sphere.

• $N_{Na} = 8 \times 10^{16}$ cm^{-3}

× $N_{Na} = 4 \times 10^{17}$ cm^{-3}

△ Baker (1979)

■ Baldwin

▲ Ya'akobi (1968, 1969)

$$I_s(\lambda) = \frac{8\pi hc^2}{\lambda_{3s-3p}^5 \left(1 + \frac{g_{3p}}{g_{3s}}\right) A_{3p}\tau_{3p}} = \frac{10^{-6}}{\tau_{3p}} \text{ W cm}^{-2} \text{ Å}^{-1} \qquad (3.42)$$

where $1/\tau_{3p}$, the resonance state decay rate, was previously shown (section 3.5.4) to be dominated during the early plasma phase by electron super-elastic collisions, yielding $\tau_{3p} = 0.5$ ns for $N_e = 2 \times 10^{16}$ cm^{-3} and hence:

$$10\ I_s(\lambda) = 2 \times 10^4 \text{ W cm}^{-2} \text{ Å}^{-1}$$

This corresponded to an average flux for saturation of 4×10^6 W cm^{-2} for the 200 Å FWHM broadband laser, well below the estimated flux used, 3×10^7 W cm^{-2}.

The second important consideration was the percentage absorption for the broadband laser in the optically thick 3s - 3p transition. Using equation (3.4):

$$\text{Fraction} = \frac{\lambda - \lambda_0\big|_{\tau=1}}{200 \text{ Å}} \sim \frac{1}{10} \quad \text{for } \ell = 1 \text{ cm}, N(3s) = 10^{17} \text{ cm}^{-3}$$

Since the laser energy flux was $\sim$ 1 J cm^{-2}, 0.1 J cm^{-3} could be absorbed per centimeter of vapor, compared with the plasma energy density stored, $eN_e(\chi + \frac{3}{2}T_e) \sim 0.01$ J cm^{-3}. Thus, enough energy could be absorbed sufficiently quickly for broadband laser pumping to be indistinguishable from narrowband pumping.

3.8.2 Dual Wavelength Pumping (λ_L = 0.59 μm and 0.53 μm)

Since the doubled Nd:Glass laser beam was envisaged as a probe beam for future laser scattering experiments in sodium, it was necessary to estimate its perturbing influence on the plasma density

and temperature. For this purpose, a 30 mJ portion of the 0.53 μm beam was redirected to enter the oven with a maximum 4 ns delay in the opposite direction to the 0.59 μm dye laser beam, both beams being co-axial and focused in the same plane. Emission lineshapes and electron densities with and without the 0.53 μm beam were identical within the error limits, 20%. No atomic lines were visible with just 0.53 μm irradiation. Again, this supported the view that ionization occurred via the 3p state. The results also demonstrated, as predicted by theory (Bebb, 1967; Laughlin, 1978) (see section 1.3), that multiphoton ionization from either the 3s or 3p states provided a negligible electron density ($< 10^{15}$ cm^{-3}) for I $< 10^{8}$ W cm^{-2}.

3.8.3 Laser Pulse Length

The ionization mechanism suggested by Measures is strongly time-dependent, especially in the final stages of avalanche collisional ionization, for which the temporal history of N_e is given by, integrating equation (1.7):

$$N_e = Ae^{BN_{Na}t} \tag{3.43}$$

where A and B are constants. Hence it was conceivable that the laser pumping and thus saturation was of insufficient duration for full ionization to occur. To test this hypothesis, the dye laser pulse was lengthened from 25 ns to 43 ns by increasing the cavity length of the ND:glass oscillator. A second set of electron temperatures and densities was derived from emission lines at $N_{Na} = 8 \times 10^{16}$ cm^{-3} and 4×10^{17} cm^{-3} for this longer pulse length. These were identical to within 20% with the results obtained for $\tau_L = 25$ ns. This signified that equation (3.43) was inapplicable and that a steady-state had been

reached within 25 ns in which the dominant ionization mechanism balanced 3-body recombination and energy losses to sodium atoms and ions (sections 5.4 and 5.5).

3.9 Ionization Mechanism

Since photoionization could be dismissed, the two remaining strongest candidates for the ionization process were (section 1.3): (a) associative ionization in the presence of a laser field (Weiner and Polak-Dingels, 1981; Carré et al., 1981), and (b) super-elastic collisions followed by collisional ionization (Measures, 1970). Numerous tests have been devised to distinguish between these mechanisms, including measuring the dependence of the fluorescence or ionization yield on the 3p population density and on the ratio of Na_2^+ to Na^+ yield (Carré et al., 1981; Weiner and Polak-Dingels, 1981; Stacewicz, 1980; Kushawaha and Leventhal, 1982). These tests were usually found to be misleading due to the plethora of possible collisional mechanisms depleting the 3p level (Kopystynska and Moi, 1982) (section 1.3). Therefore, a less ambiguous test was necessary at high sodium densities. This was deemed to be the electron temperature at peak ionization by the following arguments.

From Measure's LIBORS code, the equilibrium T_e during ionization was predicted to be 0.9 - 1 eV (Measures and Cardinal, 1981), decreasing to 0.7 eV at > 10% fractional ionization. This is typical of an underdense plasma which cools by collisional ionization to reach Saha equilibrium. This model is also in complete contradiction with the present experimental results in which an overdense plasma is being heated by 3-body recombination from an initial $T_e \lesssim 0.2$ eV. Further refinements to the LIBORS theory by accounting for energy loss to N_2

impurities (Measures et al., 1982) predicted T_e = 0.6 eV for the measured oven leak rate of $\sim$ 2 Torr per day. Similarly, a recent theoretical model incorporating a more realistic non-Maxwellian electron energy distribution (Morgan, 1983) during the early stages of ionization and assuming collisional ionization to be the dominant process suggested T_e = 0.6 eV before electron-ion thermalization occurred. All these predictions for T_e are too high by more than a factor of 2 to explain the present experimental results.

For laser-induced associative ionization, the maximum kinetic energy imparted to the free electron is given by (see Fig. 3.35):

$$\text{Energy} \lesssim (2E_{3p} - E_{Na_2^+}(R_0)) + 2(\tfrac{3}{2}kT_{OVEN})$$

$$\lesssim -0.05 + 0.2 = 0.15 \text{ eV}$$

$$\Rightarrow \quad T_e \lesssim 0.1 \text{ eV}$$

where $E_{Na_2^+}(R_0)$ is the energy above the 3s ground-state of the crossing shown on Fig. 3.35.

This maximum temperature compared favorably with the minimum temperature recorded, 0.2 eV. The laser-induced associative ionization rate from equation (1.5) was:

$$\frac{dN_e}{dt} = 10^{-9} N(3s)N(3p)$$

Assuming laser saturation of the D lines, τ_{ION} = 10 ns for N(3s) = N(3p) = 10^{17} cm^{-3} and τ_{ION} = 30 ns for N(3s) = N(3p) = 3 x 10^{16} cm^{-3}. Hence this rate was sufficiently high to account for the 10% fractional ionization observed within $\sim$ 20 ns. It was not fast enough, however, to explain the lack of significant electron heating by super-

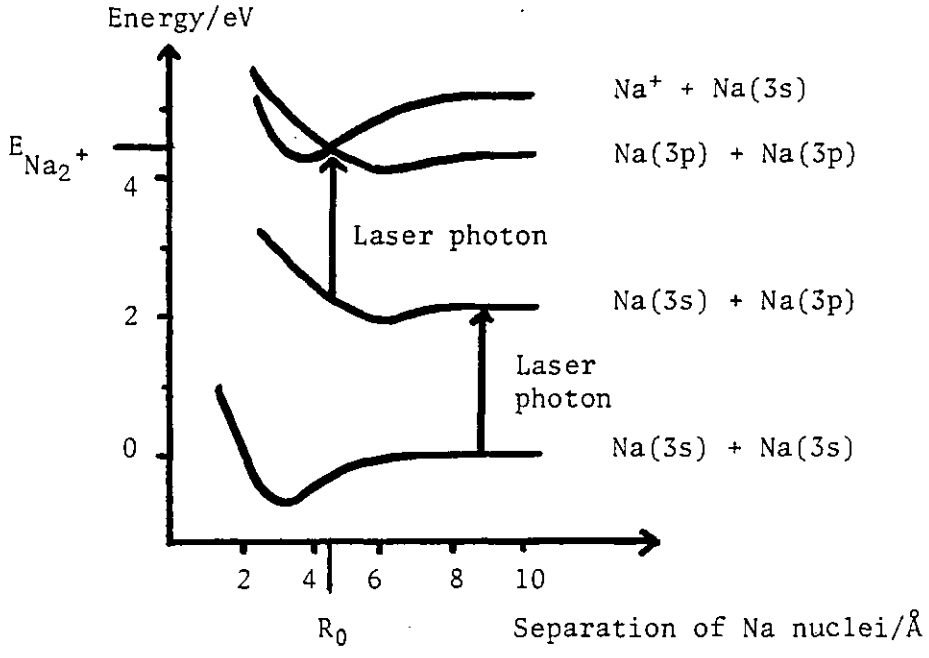


Fig. 3.35. Associative Ionization Scheme.

elastic collisions. The can be easily shown by comparing collisional depopulation rates by electrons and by atoms in the excited 3p level:

(a) Associative: $$\left.\frac{dN(3p)}{dt}\right|_{N(3p)} = - 10^{-9}\, N(3s)N(3p) \qquad (1.5)$$

(b) Electrons: $$\left.\frac{dN(3p)}{dt}\right|_{N_e} = - 10^{-7}\, N_e N(3p) \qquad (1.6)$$

For $N(3s) = 10^{17}$ cm^{-3}, $N_e = 10^{16}$ cm^{-3}:

$$\left.\frac{dN(3p)}{dt}\right|_{N_e} = 10 \left.\frac{dN(3p)}{dt}\right|_{N(3p)}$$

The low electron temperatures measured could only be explained by postulating that the vapor was <u>not</u> homogeneously saturated during laser irradiation. There were two reasons for supporting this view:

(a) The filamentation inferred from the transmission experiments (section 3.2.3) would leave unsaturated regions of vapor where the laser flux was less than the bleaching flux I_B (equation (3.2)). Such an explanation was proffered for resonantly pumped Li vapor (N_{Li} = 6 x 10^{15} cm^{-3}) (McIlrath and Lucatorto, 1977) to account for the maximum resonance state population density observed, 25% of the saturated value.

(b) The peak spatially averaged 3p population density measured from the optically thick 3p - 3d lineshape (section 3.4.5) never exceeded 2 x 10^{15} cm^{-3}, corresponding to a 2 - 5% mean degree of saturation. This could also be explained by saturated filaments occupying only $^1/_{100}$th of the vapor volume defined by the laser beam and plasma glow. Since the degree of self-focusing leading to filamentation was dependent on refractive index and hence vapor density, it was not surprising that experiments performed at lower densities (N_{Na} < 10^{15} cm^{-3}) yielded in contrast complete saturation (Salter, 1980).

Assuming complete ionization within filaments (equation 1.5) and little ionization (< 10^{16} cm^{-3}) outside, the filaments would need to comprise 0.1 of the vapor region for an average 10% ionization to be observed. Hence, the energy gained via super-elastic collisions in the filaments would be initally at least 10 times as likely to be lost by excitation collisions with ground-state atoms outside the filaments than by excitation of the 3p level inside the filaments since $\sigma_{3s-3p}(2.1\ eV) \sim \Sigma\sigma_{3p-n\ell}(2.1\ eV)$ (Shuker et al., 1980) and N(3s) ~ N(3p) for saturated conditions. Space-charge effects would be negligible since ions and electrons would diffuse together during the laser pulse over a distance $2.4\sqrt{Dt}$ (from equation (3.41)), equal to 40 μm for

T_e = 0.2 eV and 120 μm for T_e = 2 eV and hence comparable or larger than filament diameters (Brechignac et al., 1980). Therefore, by the end of the laser pulse, the plasma would be partially ionized, low temperature and homogeneous on a 100 μm scale, as observed experimentally.

CHAPTER 4

MULTIPHOTON IONIZATION (λ_L = 6854 Å)

4.1 Introduction

Laser induced multiphoton ionization of sodium atoms has recently been studied both theoretically (Zoller and Lambropoulos, 1980; Bebb, 1966, 1967; Geltman, 1980 and Manakov et al., 1977) and experimentally (Agostini et al., 1978 and Smith and Hogan, 1979) with particular emphasis on ionization enhancement when tuning close to a one or two-photon atomic resonance. The electron density yield has thus been shown to be a sensitive function of laser wavelength for near resonant conditions. The electron temperature, in the absence of collisional recombination and inverse bremsstrahlung, should just be a function of photon energy and ionization potential. Hence, a suitable laser wavelength can be found for which N_e is maximized, T_e minimized and thus N_D minimized.

Such a scheme is discussed in the following section and changes in the experimental layout are described. Fluorescence lineshapes are then presented and the electron density temporal history deduced as in the resonant pumping case. Results on the dependence of electron density yield on laser tuning are then compared with theory. The electron temperature history, measured as before, is then presented. Finally, the minimum N_D achieved is compared with that for the D line pumped sodium vapor.

4.2 Ionization Scheme

The resonantly enhanced single wavelength photoionization scheme compatible with the dyes and dye pump wavelengths available and yielding the minimum T_e in sodium proved to be the two-photon resonant (3s $\rightarrow\rightarrow$ 3d) three-photon ionization process at λ = 6854 Å. This is shown on a sodium term diagram (Fig. 4.1), producing in theory monoenergetic electrons with T_e = 0.19 eV. The two-photon transition cross-section for 3s $\rightarrow\rightarrow$ 3d has been calculated and verified experimentally for a 140 mÅ bandwidth laser tuned to line center as $\sigma_2 = 10^{-42}$ cm^4 s (van Dijk et al., 1978). The single photon ionization cross-section from the 3d state for λ= 6854 Å is $\sigma_1 = 1.5 \times 10^{-17}$ cm^2 (Aymar et al., 1976). Ignoring stimulated and spontaneous radiative decay from the 3d state and electron recombination, the relevant rate equations are:

$$\frac{dN(3d)}{dt} = N(3s)\sigma_2 F^2 - N(3d)\sigma_1 F \qquad (4.1)$$

$$\frac{dN_e}{dt} = N(3d)\sigma_1 F \qquad (4.2)$$

where F is the photon flux in cm^{-2} s^{-1} $\equiv$ 3.5 x 10^{18} I/W cm^{-2}.

Integrating equation (4.1) yields, for N(3d) << N(3s):

$$N(3d) = \frac{N(3s)\sigma_2 F}{\sigma_1} \left[1 - e^{-\sigma_1 F t}\right] \qquad (4.3)$$

Substituting for N(3d) in equation (4.2) and integrating again:

$$N_e = N(3s)\sigma_2 F^2 \left[t - \frac{1}{\sigma_1 F}\left[1 - e^{-\sigma_1 F t}\right]\right] \qquad (4.4)$$

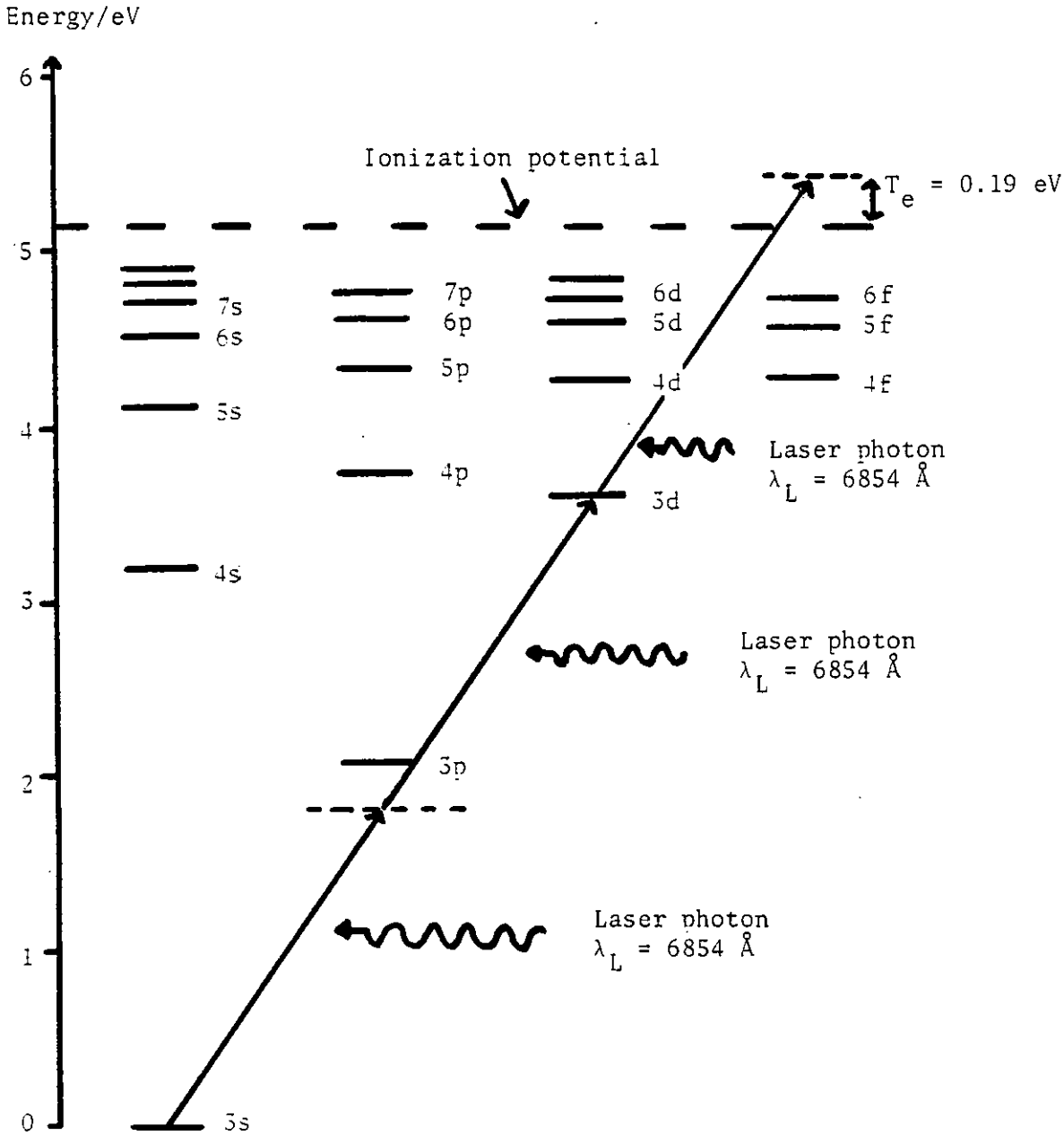


Fig. 4.1. Sodium term diagram
(with multiphoton ionization scheme).

$$\Rightarrow \quad \frac{N_e}{N(3s)} = 10^{-5} I^2 \left[t - \frac{1}{50I} \left[1 - e^{-50It} \right] \right] \qquad (4.5)$$

For small I such that 50It << 1, this equation properly reduces to $\frac{N_e}{N(3s)} \propto I^3$, which corresponds to single-step multiphoton ionization and an unsaturated 3d level.

Hence 50% ionization should occur within 10 ns for a minimum laser flux I = 3 MW cm^{-2}. This figure compares favorably with the 20% fractional ionization measured for a laser tuned to the sodium 3s $\twoheadrightarrow$ 4d two-photon transition with I = 10^7 W cm^{-2}, τ_L = 5 ns (Agostini et al., 1978) and a similar compound cross-section $\sigma_1 \times \sigma_2$ = 10^{-59} cm^6 s.

4.3 Experimental Layout

The Rhodamine dyes used for the resonant pumping experiments were replaced by the optimized 4 to 1 Rhodamine B/Oxazine 725 mixture in methanol. Figure 4.2 shows the modified arrangement for λ = 6854 Å with only two dye amplifiers in use. The 10 mJ, 22 ns laser beam was focused by a 20 cm focal length lens into the second oven. Since the multiphoton ionization rate was strongly dependent on the laser intensity by equation (4.3), a sapphire tube was not used for sodium containment as its poor surface quality would increase the focal spot size and hence decrease the laser intensity. The emission fluorescence was viewed at 90° as previously using the Bentham spectrometer and RCA 7265 photomultiplier.

4.4 Fluorescence Results

The column of excited sodium vapor exhibited an $\sim$ 3 mm diameter white glow. The same atomic transitions nd, ns - 3p were identified

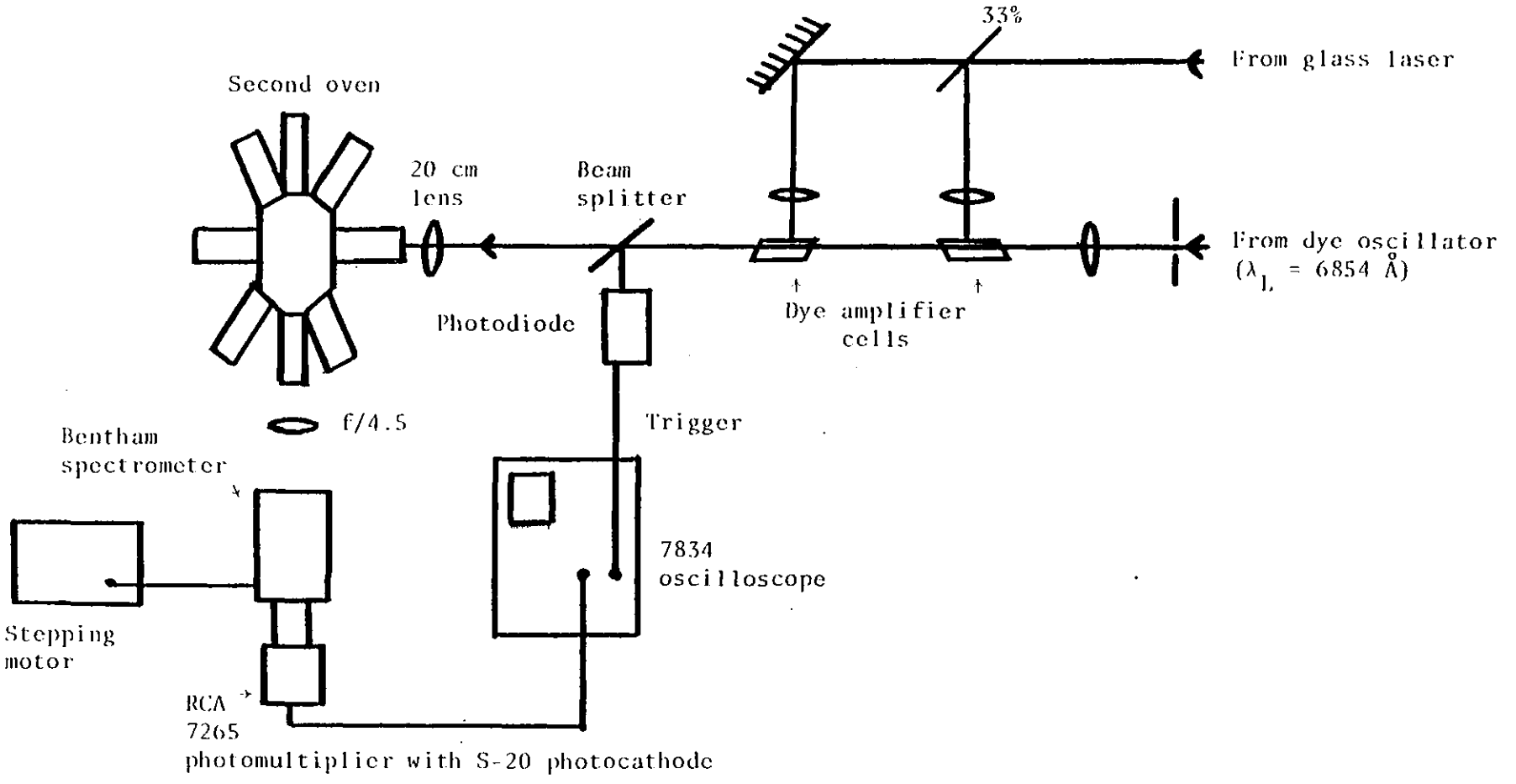


Fig. 4.2. Experimental layout for emission spectroscopy of sodium plasmas formed by multiphoton ionization.

in emission as in the resonant pumping case. The fluorescence yields and hence N_e were maximized by laser tuning in 100 mÅ steps, and this is further discussed in section 4.6. Spectrally and temporally resolved (2 Å, 15 ns) emission lineshapes were obtained for the strongest and most useful transitions for diagnosing N_e, 4d - 3p and 3d - 3p, at sodium densities $N_{Na} = 2 \times 10^{16}$ cm^{-3}, 5×10^{16} cm^{-3}, 7×10^{16} cm^{-3}, 10^{17} cm^{-3} and 2×10^{17} cm^{-3} and also for 5s - 3p at $N_{Na} = 10^{17}$ cm^{-3}. These neutral densities were inferred from the thermocouple temperatures using the JANAF vapor pressure curves as discussed in section 3.3.3, and hence assigned possible 50% systematic errors. Three of the lineshapes are presented in Figs. 4.3 - 4.5. The points of interest to note are:

(a) The 3d-3p doublets exhibited no self-reversal in the limit of 2 Å spectral resolution, in contrast with results for resonant pumping (Fig. 4.3 vs. 3.10). This signified that the vapor surrounding the plasma region and excited by the spatial wings of the laser beam had a maximum resonance state population density x annular width product $\sim 10^{13}$ cm^{-2}. Comparing the two-photon transition rate populating 3d for $\lambda = 6854$ Å (equation (4.3)) and hence populating 3p by radiative decay, with the direct one-photon transition rate to 3p for $\lambda = 5890$ Å:

$\lambda = 5890$ Å	$\lambda = 6854$ Å $\quad (\sigma_1 F \tau_L \ll 1)$
$\frac{1}{N(3s)} \frac{dN(3p)}{dt} = \sigma_{3s-3p} F$	$\frac{1}{N(3s)} \frac{dN(3d)}{dt} = \sigma_2 F^2 > \frac{1}{N(3s)} \frac{dN(3p)}{dt}$
$\frac{1}{N(3s)} \frac{dN(3p)}{dt} = 10^7 \, I$	$\frac{1}{N(3s)} \frac{dN(3p)}{dt} \lesssim 10^{-5} \, I^2$

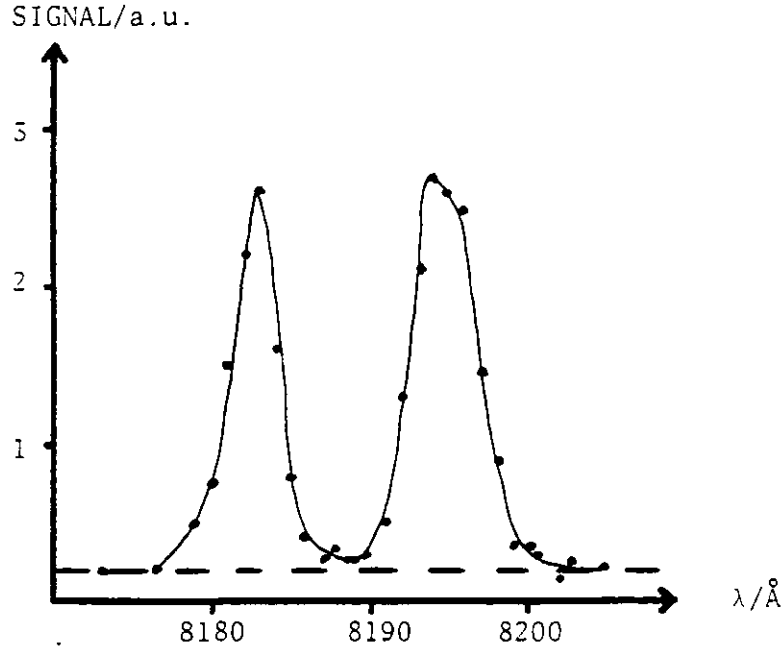


Fig. 4.3. 3p-3d lineshape:
$N_{Na} = 10^{17}$ cm^{-3} and t = 100 ns.

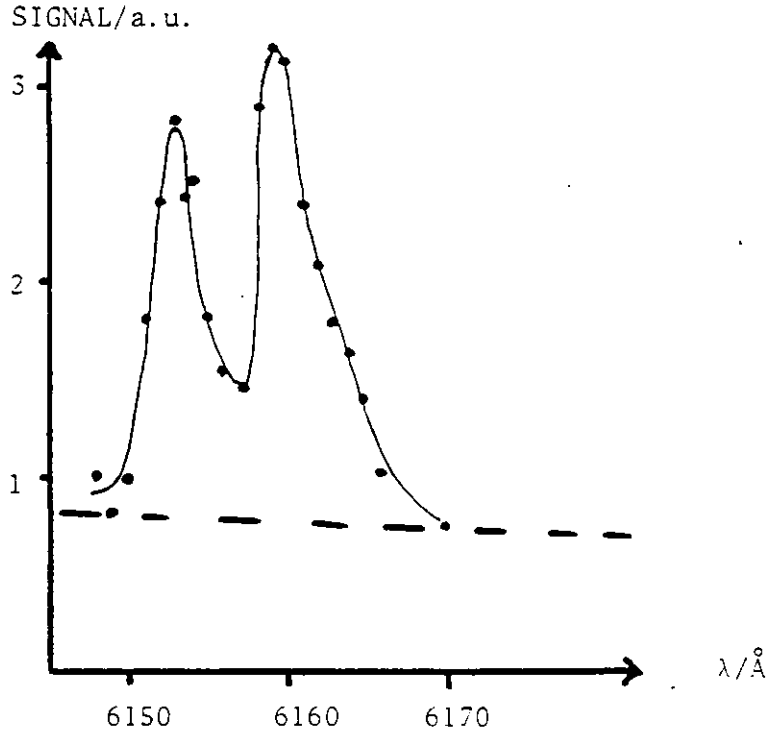


Fig. 4.4. 3p-5s lineshape:
$N_{Na} = 10^{17}$ cm^{-3} and t = 50 ns.

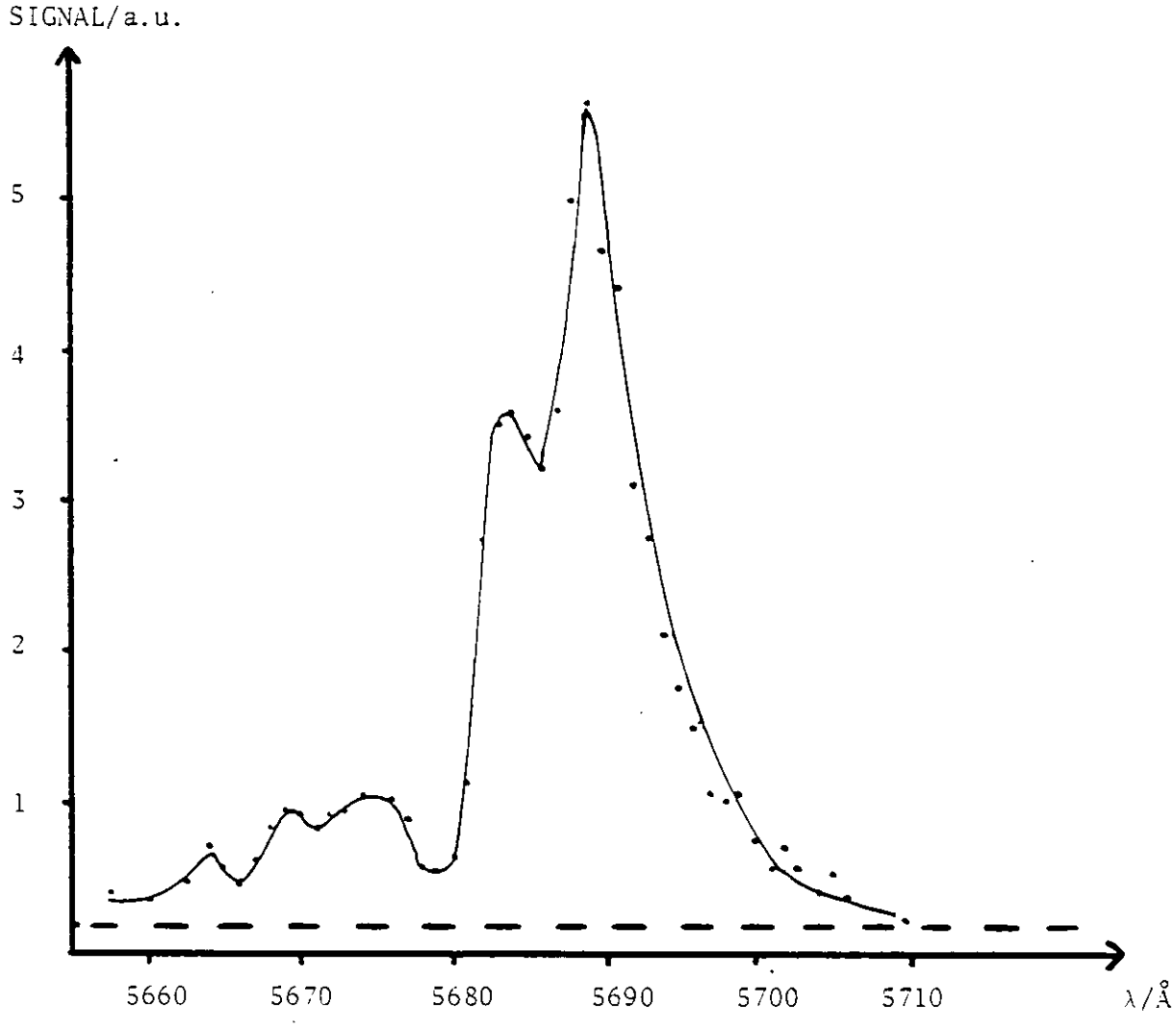


Fig. 4.5 3p-4d lineshape: $N_{Na} = 10^{17}$ cm^{-3} and t = 40 ns.

Since the resonant pumping rate was at least a factor of 10^6 greater for an estimated $I = 10^6$ W cm^{-2} at the wings of the laser beam, it was not surprising that self-reversal observed in the former case was not resolved in the latter.

(b) A progressive decrease in the line center optical depths is shown in Figs. 4.3 - 4.5 by the increase in the ratio of the peaks of the doublets, beginning at 1 and tending to 2. After deconvoluting the instrument profile, the width ratio of the optically thickest doublet, 3d - 3p, approximated to $\sqrt{g_{3d_{5/2}} - 3p_{3/2}} / g_{3d_{3/2}} - 3p_{1/2} = \sqrt{2}$, as expected for a Lorentzian profile.

(c) No meaningful lineshapes could be obtained during laser irradiation due to stimulated emission spikes occurring at line centers with a 20 ns FWHM. These were attributed to a transient population inversion between excited levels and the 3p level created by:

(i) laser pumping to the 3d level;

(ii) preferential recombination of the electrons into the higher levels at a rate approximately proportional to n^6 (Shuker et al., 1980).

(d) The 4d - 3p lineshape exhibited all the plasma effects discussed in the previous chapter: broadening, shifts, forbidden components and the emergence of blue wing satellites. These features are used to determine N_e in the next section.

4.5 Electron Density

4.5.1 Radiation Transport

In the absence of an observable absorption feature, the transport equation for fluorescence reduced to:

$$I(\lambda-\lambda_0) = B(T)\ [1 - \exp[-\frac{\lambda_0^2 e^2 f \ell N(3p)\Delta\lambda}{4\pi\varepsilon_0 mc^2[(\lambda-\lambda_0)^2 + (\Delta\lambda)^2]}]] \qquad (4.6)$$

where $\Delta\lambda$ is defined in section 3.4.3 and the plasma diameter ℓ estimated as 3 mm. From the measured linewidths, plots of N(3p) versus N_e for the 3d - 3p and 4d - 3p transitions yielded unique values of N_e and N(3p).

4.5.2 $N_e(t)$ and N(3p)(t)

The N_e and N(3p) temporal histories are shown in Figs. 4.6 and 4.7 for $N_{Na} = 5 \times 10^{16}$ cm^{-3} and 10^{17} cm^{-3}. An example of the reproducibility of the plasma density is tabulated below for t = 50 ns, $N_{Na} = 5 \times 10^{16}$ cm^{-3}.

TABLE 4.

Reproducibility of Plasma Density

Date	N_e/cm^{-3}
28/10/82	$1.4 \pm 0.2 \times 10^{16}$
5/11/82	$1.4 \pm 0.2 \times 10^{16}$
6/11/82	$1.4 \pm 0.2 \times 10^{16}$
16/11/82	$1.7 \pm 0.2 \times 10^{16}$

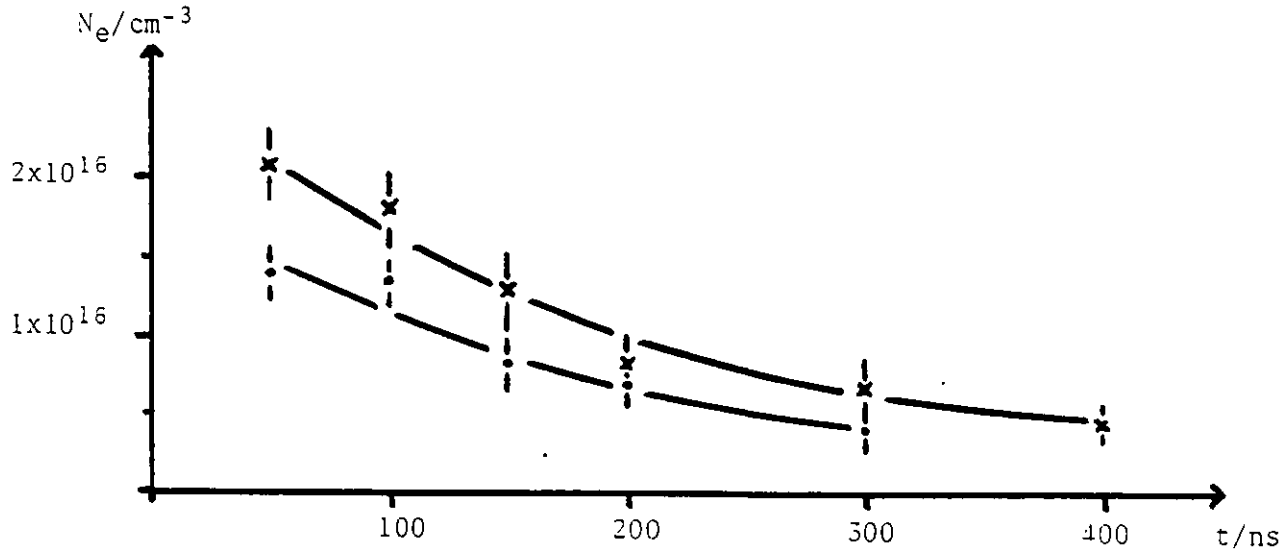


Fig. 4.6. Temporal history of N_e.
• $N_{Na} = 5 \times 10^{16}$ cm^{-3}
× $N_{Na} = 10^{17}$ cm^{-3}

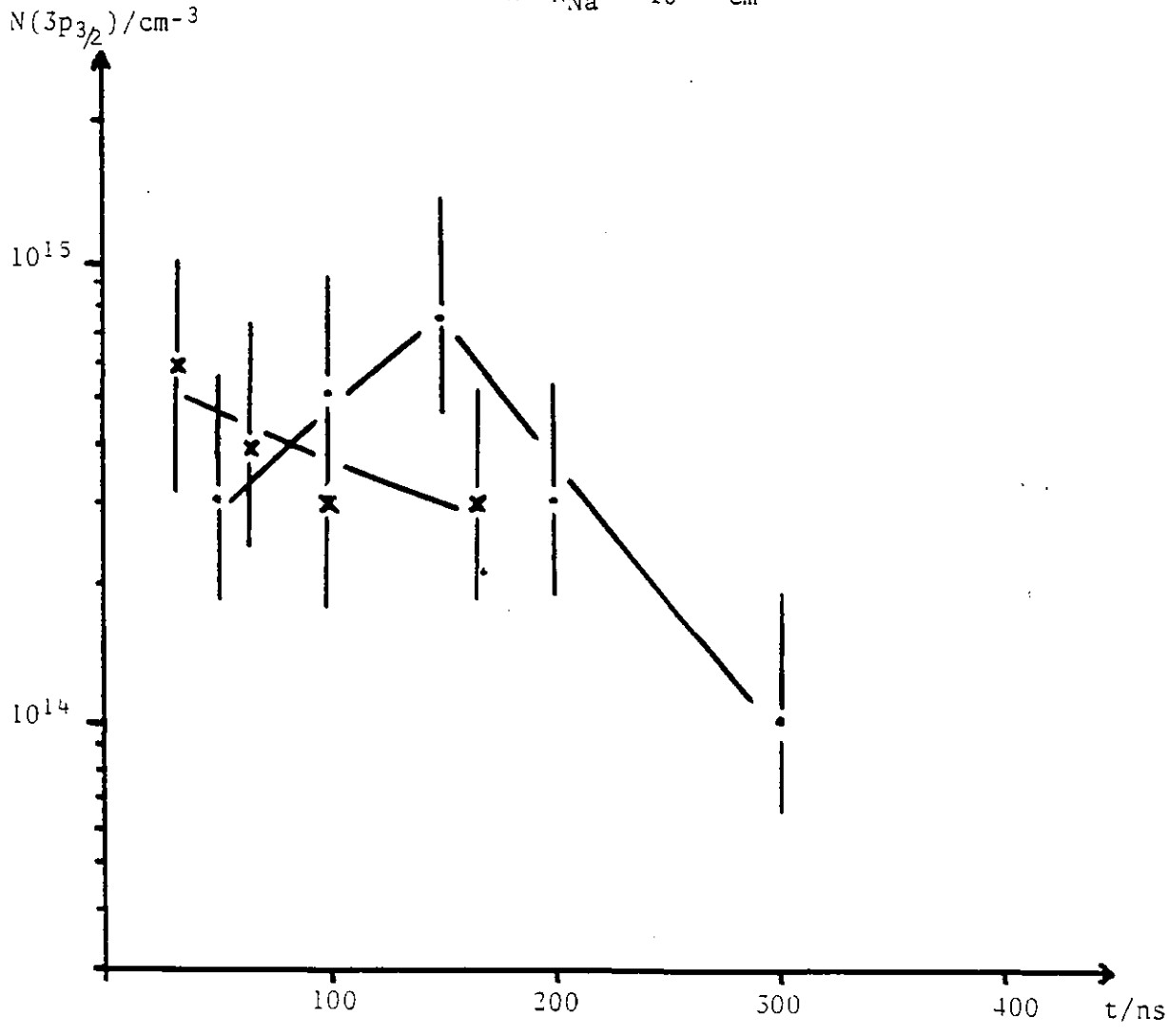


Fig. 4.7. Temporal history of $N(3p_{3/2})$
• $N_{Na} = 5 \times 10^{16}$ cm^{-3}
× $N_{Na} = 10^{17}$ cm^{-3}

A peak $N_e = 2.5 \pm 0.5 \times 10^{16}$ cm^{-3} was recorded for $N_{Na} = 2 \times 10^{17}$ cm^{-3}, equivalent to the highest N_e registered for resonant pumping.

The nearly constant 3p population density shown in Fig. 4.7 indicated a slowly varying electron temperature. Furthermore it suggested that the first excited state, 3p, had reached collisional equilibrium with the ground-state within 50 ns. For hydrogen, such an equilibriation time can be longer than the usual value taken to be the inverse of the de-excitation rate from the resonance state (Griem, 1963). This is because there is a competing excitation mechanism from the resonance state to higher excited states. For a ground-state 1, resonance state 2 and next highest excited state 3, the equilibrium time is lengthened if:

$$\frac{g_2 \sigma_{2-3} v_e(E_{23}) \exp(-E_{23}/T_e)}{\sigma_{1-2} v_e(E_{21})} > 1 \qquad (4.7)$$

where the velocities v_e correspond to threshold values and E_{12}, $E_{23} > T_e$.

Comparing H and Na plasmas with similar fractional ionization:

Hydrogen: $T_e = 0.8$ eV, equation (4.7) = 10 (Johnson, 1972)

Sodium: $T_e = 0.25$ eV, equation (4.7) = 0.03 (Shuker et al., 1980)

where excited state 3 is the 4s level for sodium, with $E_{23} = 1.09$ eV.

Hence, the large E_{23}/T_e ratio for sodium signified that, in contrast to typical hydrogen plasmas, the relaxation time for the resonance state was just the inverse of the super-elastic rate, 0.3 ns for $N_e = 10^{16}$ cm^{-3}.

A preliminary estimate of T_e can then be obtained from the N(3p)/N(3s) ratio as before. From Fig. 4.7:

$$\frac{2 \pm 1 \times 10^{14}}{5 \pm 3 \times 10^{16}} = 2e^{-2.1/T_e}$$

$$\Rightarrow \quad T_e = 0.34 \pm 0.05 \text{ eV}.$$

The average temperature deduced from excited state population ratios (section 4.8) was 0.25 eV, so an overall average of 0.3 eV was used for Griem's plasma broadening parameters.

4.5.3 Stark Shift

In Fig. 4.8, the electron densities inferred from the red shifts of the $4d_{5/2}$ - $3p_{3/2}$ transition, neglecting Debye shielding, are plotted against the electron densities measured simultaneously from the 4d - 3p linewidths. The dotted line represents the inclusion of Debye shielding. Slightly better agreement is found by including the Debye length. It should be noted that these observed shifts were less likely to be erroneous overestimates caused by unshifted reabsorption of fluorescence than in the resonant pumping case.

4.5.4 Forbidden Components and Satellites

In Fig. 4.9, the electron densities deduced using equation (3.26) from the spectrally integrated intensity ratios of $4f_{7/2}$ - $3p_{3/2}$ to $4d_{5/2}$ - $3p_{3/2}$ at $N_{Na} = 10^{17}$ cm^{-3} are compared with densities derived from 4d - 3p linewidths. As in the resonant pumping case, agreement is satisfactory and the forbidden doublet is strongly merged due to electron impact broadening (Fig. 4.10). The reappearance of the satellite feature at λ = 5661 Å — 5664 Å is also shown in Fig. 4.10.

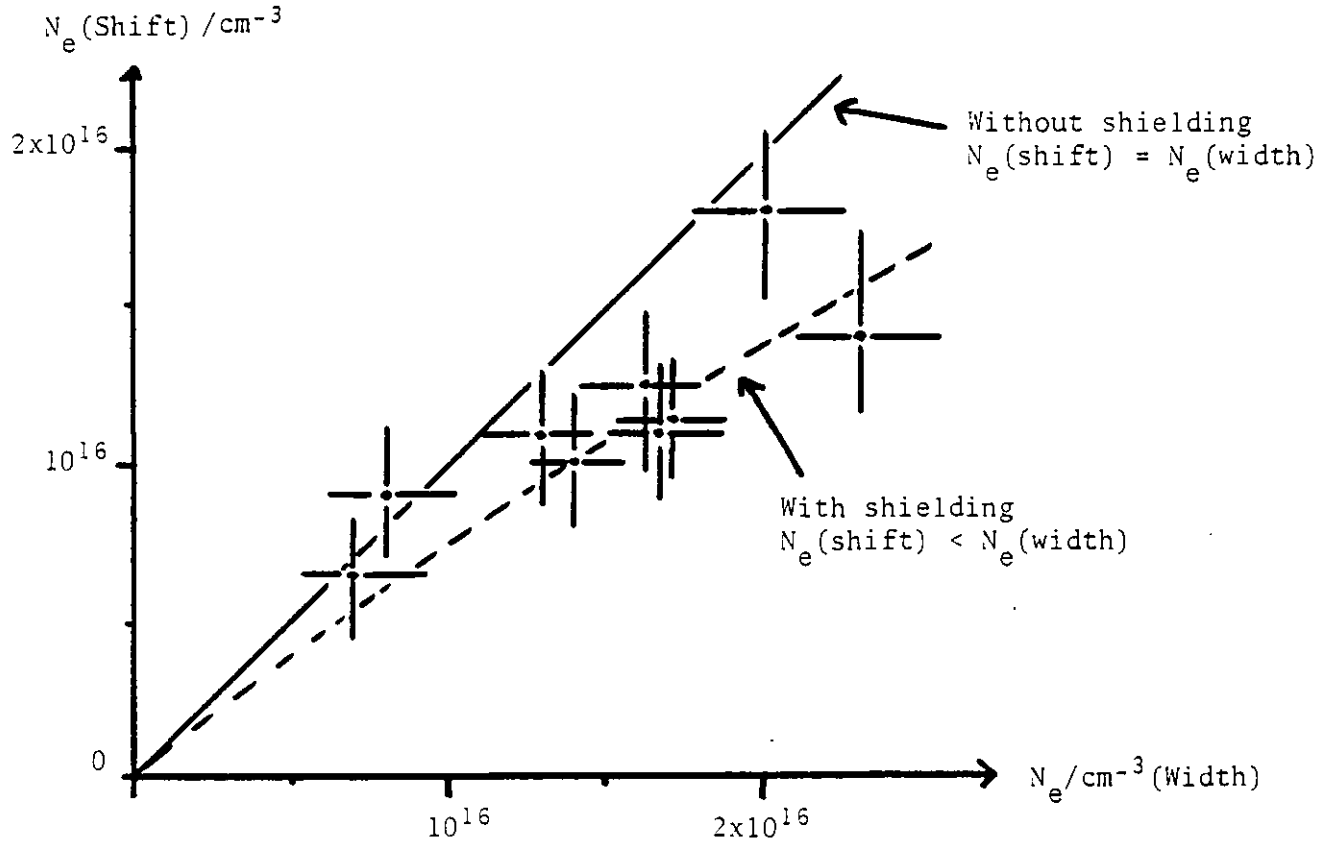


Fig. 4.8. N_e from 3p-4d shift versus N_e from 3p-4d width. Solid and dashed lines are theoretical curves without and with shielding respectively.

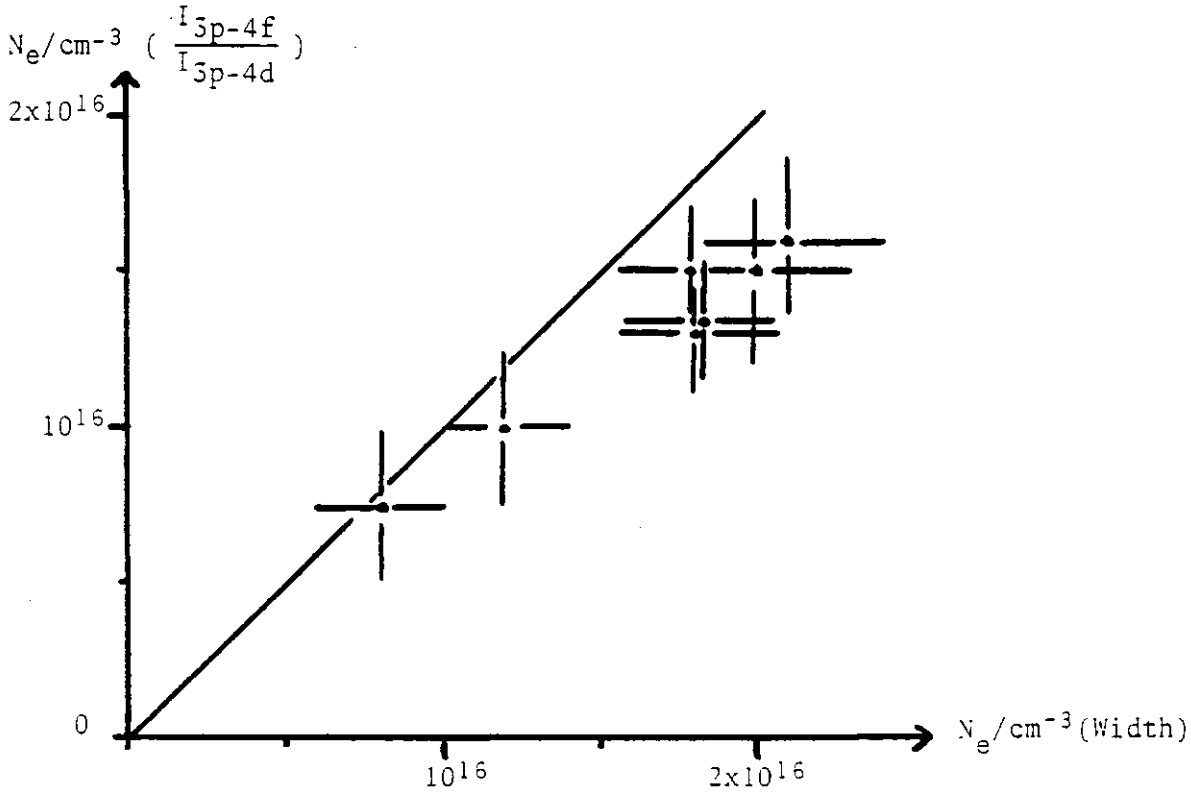


Fig. 4.9. N_e from ratio of 3p-4f to 3p-4d intensities versus N_e from 3p-4d width. Solid line represents the same N_e measured by both diagnostics.

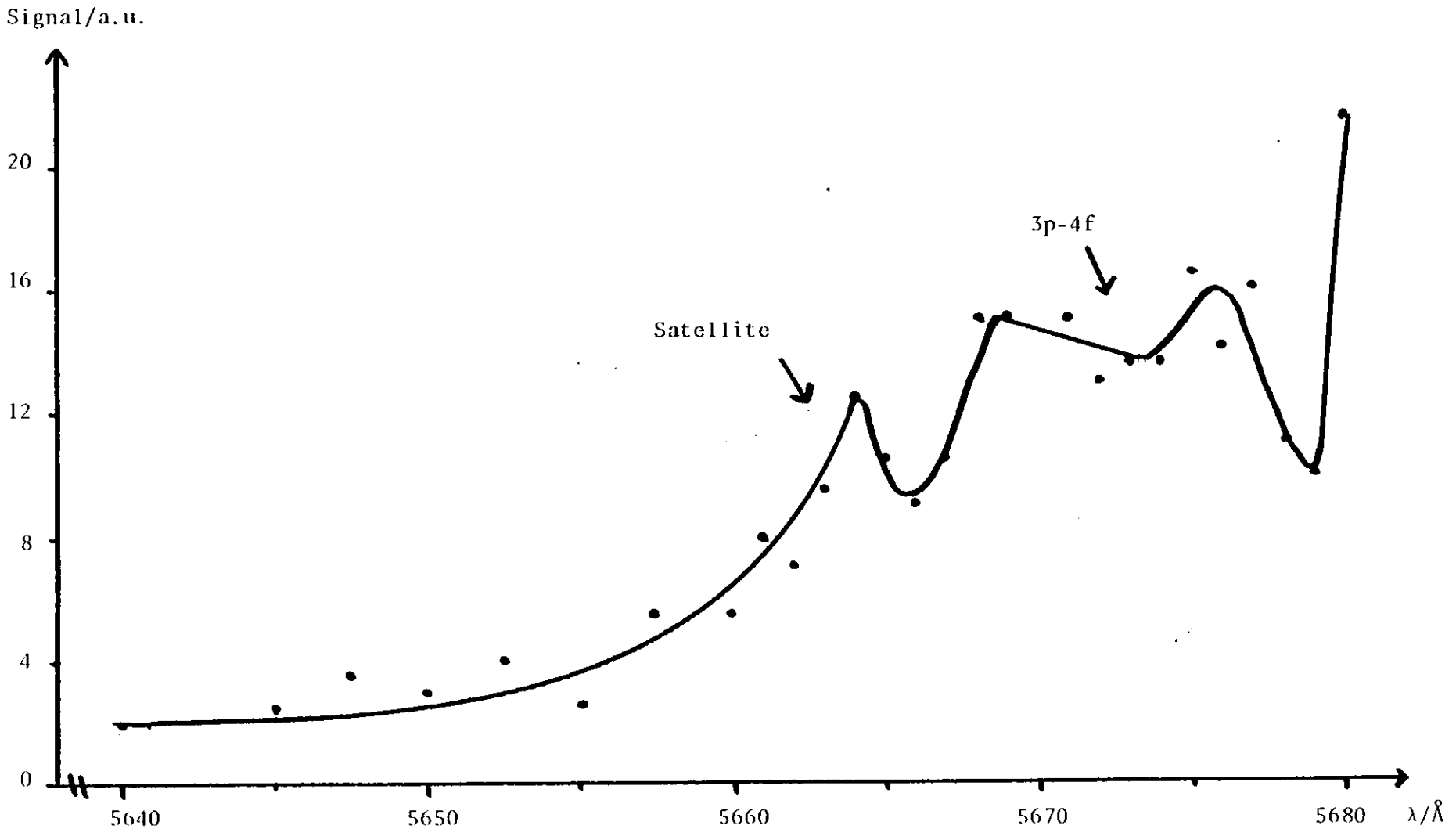


Fig. 4.10. 3p-4f and Satellite Features: $N_{Na} = 10^{17}$ cm^{-3} and t = 60 ns.

4.6 Ionization Yield vs. Laser Detuning

4.6.1 Introduction

Maximizing the fluorescence and electron density by laser tuning yielded two interesting results unconnected with the non-Debye behaviour of the sodium plasma. These are shown in Fig. 4.11 for $N_{Na} = 10^{17}$ cm^{-3}. The two features to note are the non-zero background electron density quasi-independent of laser wavelength and the asymmetry, width and shift of the ionization peak with respect to the unperturbed 3d level. Each of these are now discussed in turn.

4.6.2 Atom-Laser Interactions

The red shift observed for the maximum N_e and hence 3d level could be assigned either to a quadratic AC Stark shift due to the interaction of the detuned electric field of the laser with dipole allowed transitions from 3d, or to elastic electron collisions. To distinguish between the two, the spectrally integrated 3d - 3p fluorescence was monitored as a function of laser detuning at a lower sodium density, $N_{Na} = 3 \times 10^{14}$ cm^{-3}. The results for two laser fluxes differing by a factor of ~ 6 are shown in Figs. 4.12a and 4.12b. The similarity between Figs. 4.11 and 4.12a for which N_e differed by at least a factor of 30 while the laser flux remained constant proved the shift was not plasma induced. Moreover, Figs. 4.12a and 4.12b indicated a flux dependent shift.

For a two-photon transition, the time-averaged AC Stark shift, $\delta\omega$, is proportional to the laser flux and is given by the following equation for a non-fluctuating laser flux (Agostini et al., 1978 and Geltman, 1980):

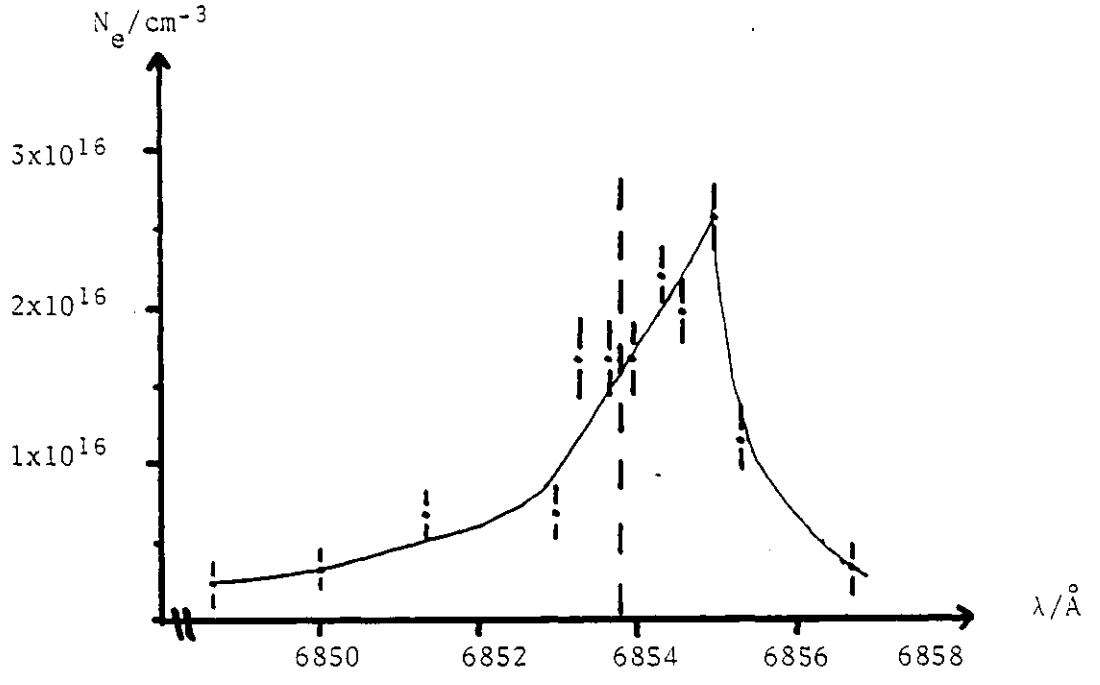


Fig. 4.11. N_e versus laser wavelength: $N_{Na} = 10^{17}$ cm^{-3}. Dotted line represents unperturbed line center for 3s →→ 3d two-photon transition.

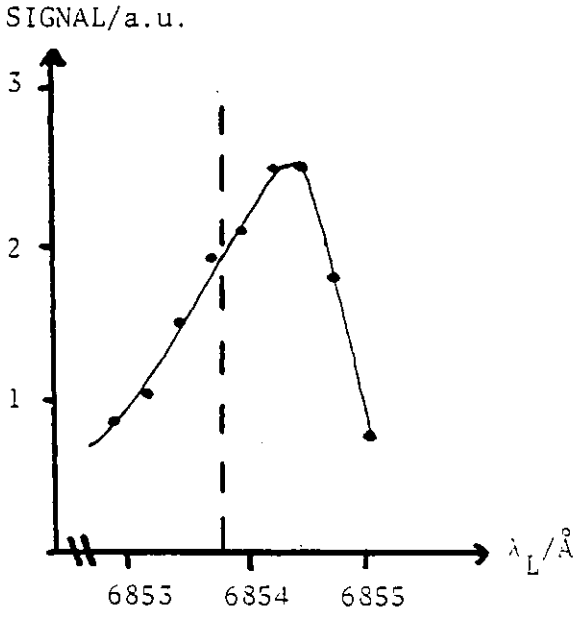


Fig. 4.12(a)

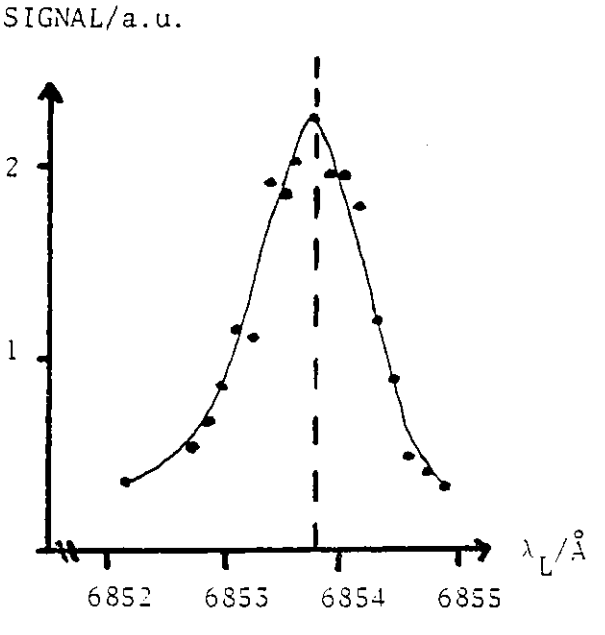


Fig. 4.12(b)

3p-3d fluorescence versus laser wavelength:
$N_{Na} = 3 \times 10^{14}$ cm^{-3}.
(a) High intensity. (b) Low intensity.

$$\delta\omega = \frac{I}{2\hbar^2}\sqrt{\frac{\mu_0}{\epsilon_0}}\left[\sum_j \frac{|\mu_{j-3s}|^2}{\omega_{j-3s}-\omega} + \frac{|\mu_{j-3s}|^2}{\omega_{j-3s}+\omega}\right.$$

$$\left. - \sum_k \frac{|\mu_{k-3d}|^2}{\omega_{k-3d}-\omega} + \frac{|\mu_{k-3d}|^2}{\omega_{k-3d}+\omega}\right] \qquad (4.8)$$

where μ_{m-n}, ω_{m-n} are the dipole matrix elements and transition frequencies between states m and n, respectively. The only important intermediate level representing j and k proved to be 3p, all others yielding a 20% correction. The shift was to the red wavelength side as the 3p - 3d dipole dominated over the 3p - 3s dipole in equation (4.8). Evaluating this shift in terms of laser wavelength:

$$\delta\lambda/\mathring{A} = 4 \times 10^{-9}\ I/W\ cm^{-2}$$

For a fluctuating field saturating a two-photon transition, an enhancement of 1.5 to 2 is expected for the shift (Zoller and Lambropoulos, 1980). Hence the measured 0.6 - 1 $\mathring{A}$ shift (Figs. 4.11 and 4.12a) corresponded to a peak flux I = 1-2 x 10^8 W cm^{-2}.

The width and asymmetry of the ionization profile can then be attributed to the spatial inhomogeneities of the laser beam. For a Lorentzian two-photon 3s $\rightarrow\rightarrow$ 3d absorption width γ, the profile can be represented by an equation of the following form:

$$N_e \propto \frac{f(I)\gamma}{(\lambda - \lambda_0 - I\delta\lambda)^2 + \gamma^2} \qquad (4.9)$$

where λ_0 = 6854 $\mathring{A}$ and f(I) represents the ionization rate for flux I, where $\frac{\partial f}{\partial I}$ is positive. Hence, the regions in the laser beam with higher flux will ionize more atoms, but only for larger detunings. Such a

profile has been observed previously in resonant multiphoton ionization of NO (Otis and Johnson, 1981) and Xe (Kruit et al., 1981).

The low flux profile (Fig. 4.12b) exhibited an absorption width $\gamma = 0.5 \pm 0.1$ Å, free of distortions from a maximum predicted AC Stark shift of 0.1 Å. This width was attributed to saturation broadening (van Dijk et al., 1978) (section 3.4.2.7), the laser linewidth being $\lesssim 10$ mÅ and Doppler broadening, self-broadening and He pressure broadening being 15 mÅ, < 0.1 mÅ and 5 mÅ respectively for $N_{Na} = 3 \times 10^{14}$ cm^{-3}, T = 800 K and $P_{He} = 20$ Torr (Stappaerts et al., 1976). The theoretical value for the half-width could not be calculated reliably due to the highly time-dependent nature of the processes competing with saturation of the 3d level, namely stimulated emission to the 3p state, photoionization and electron inelastic collisions.

4.6.3 Non-Resonant Multiphoton Ionization

The multiphoton ionization cross-section for 5 to 10 Å detunings from the two-photon 3s $\nrightarrow\nleftarrow$ 3d transition is $\sigma_3 = 10^{-74\pm1}$ cm^6 s^2 (Bebb, 1967), compared to 10^{-67} cm^6 s^2 on resonance, where:

$$\frac{dN_e}{dt} = 3!N(3s)\sigma_3 F^3 \qquad (4.10)$$

The 3! accounts for rate enhancement due to the multimode nature of the laser field (Zoller and Lambropoulos, 1980). Hence, the 2 to 3% fractional ionization observed (Fig. 4.11) corresponds to I = 10^8 W cm^{-2}, in good agreement with the peak laser flux measured by the AC Stark shift.

4.7 Plasma Inhomogeneity

Since the dye laser output was 0.5 MW, a peak I = 10^8 W cm^{-2}

corresponded to a < 700 μm diameter plasma, yet a ∿ 3 mm diameter plasma glow was recorded. In conjunction with the width of the ionization profile, this suggested there were millimetre-wide radial density gradients due to laser flux inhomogeneities. The emission lineshapes were then averages along a plasma diameter with the $N_e^2\ T_e^{-3/2} \exp(\frac{E_{n\ell}}{T_e})$ weighting of the fluorescence by Saha-Boltzmann favoring the more strongly-coupled plasma regions. Hence such averaging probably overestimated the minimum N_D achieved.

4.8 Electron Temperature

4.8.1 Boltzmann Plot

The electron temperatures were deduced from ratios of line intensities as shown in Fig. 4.13 for $N_{Na} = 2 \times 10^{16}$ cm^{-3}, t = 100 ns and 400 ns. Corrections for molecular reabsorption in the absence of sodium containment by sapphire tube were much greater than in the resonant pumping case, reaching 250% at $N_{Na} = 5 \times 10^{16}$ cm^{-3} for 5d - 3p. Such optical depths were estimated by measuring the absorption of a He-Ne laser beam traversing the oven axis used for emission diagnostics, and then normalizing to any wavelength using published absorption cross-sections (de Groot and van Rooijen, 1975). The uncertainties in these corrections are reflected in the error bars on the Boltzmann plots. Again, all levels above 3d appeared to be in LTE with the free electrons.

4.8.2 T_e Temporal History

The temporal behaviour of the electron temperature is shown in Fig. 4.14 for $N_{Na} = 2 \times 10^{16}$ cm^{-3} and 5×10^{16} cm^{-3}. There were four possible reasons why T_e exceeded the temperature expected,

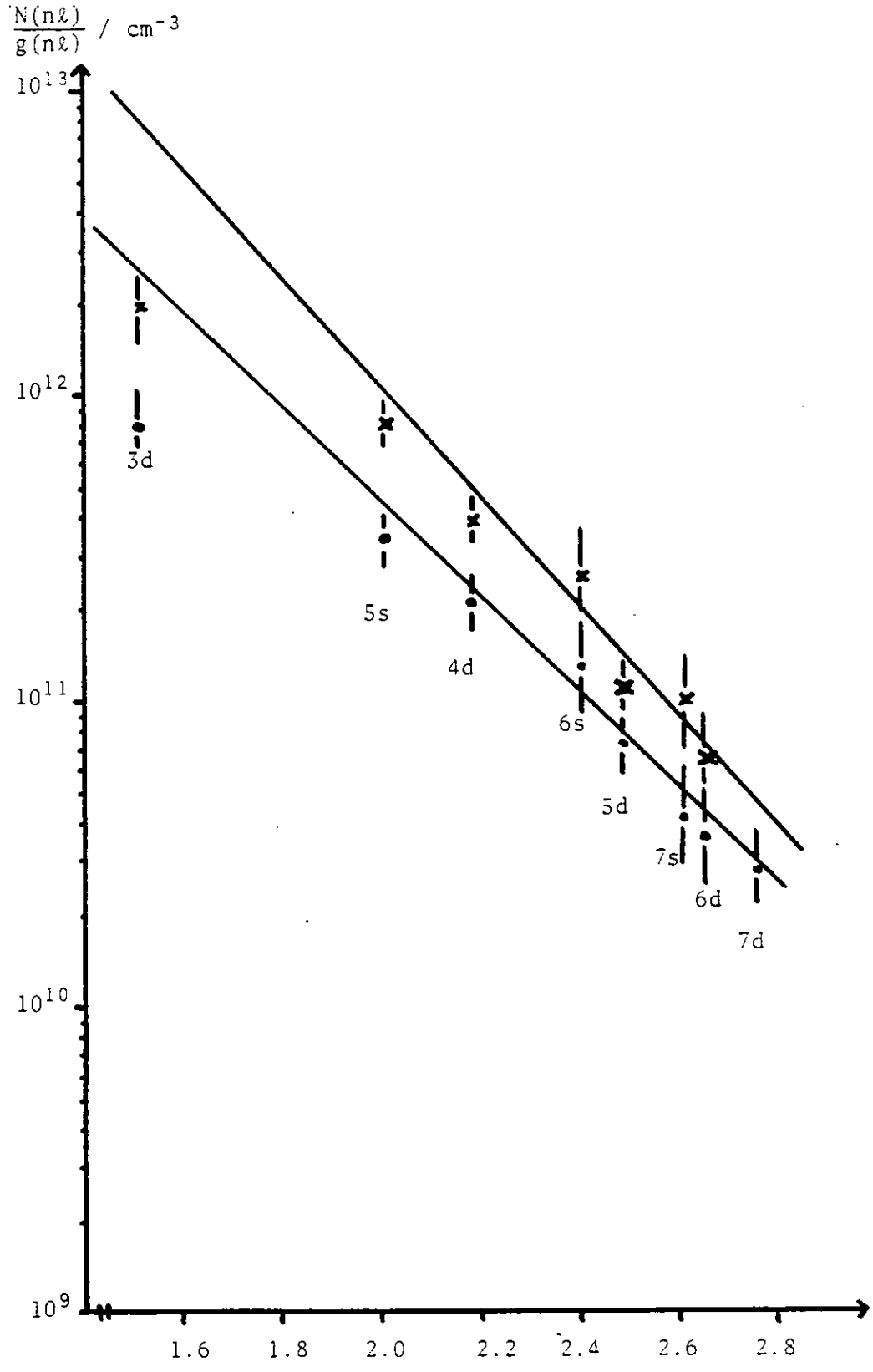


Fig. 4.13. Boltzmann plot:
$N_{Na} = 2 \times 10^{16}$ cm^{-3}
× t = 100 ns
• t = 400 ns

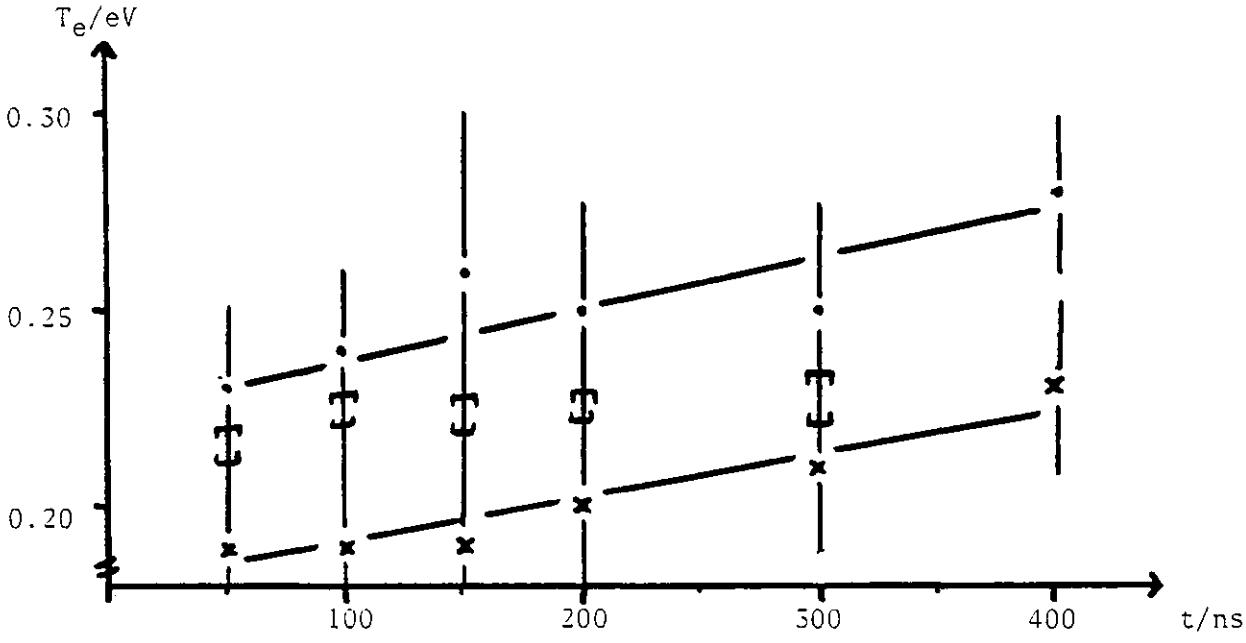


Fig. 4.14. Temporal history of T_e
- • $N_{Na} = 2 \times 10^{16}$ cm^{-3}
- × $N_{Na} = 5 \times 10^{16}$ cm^{-3}

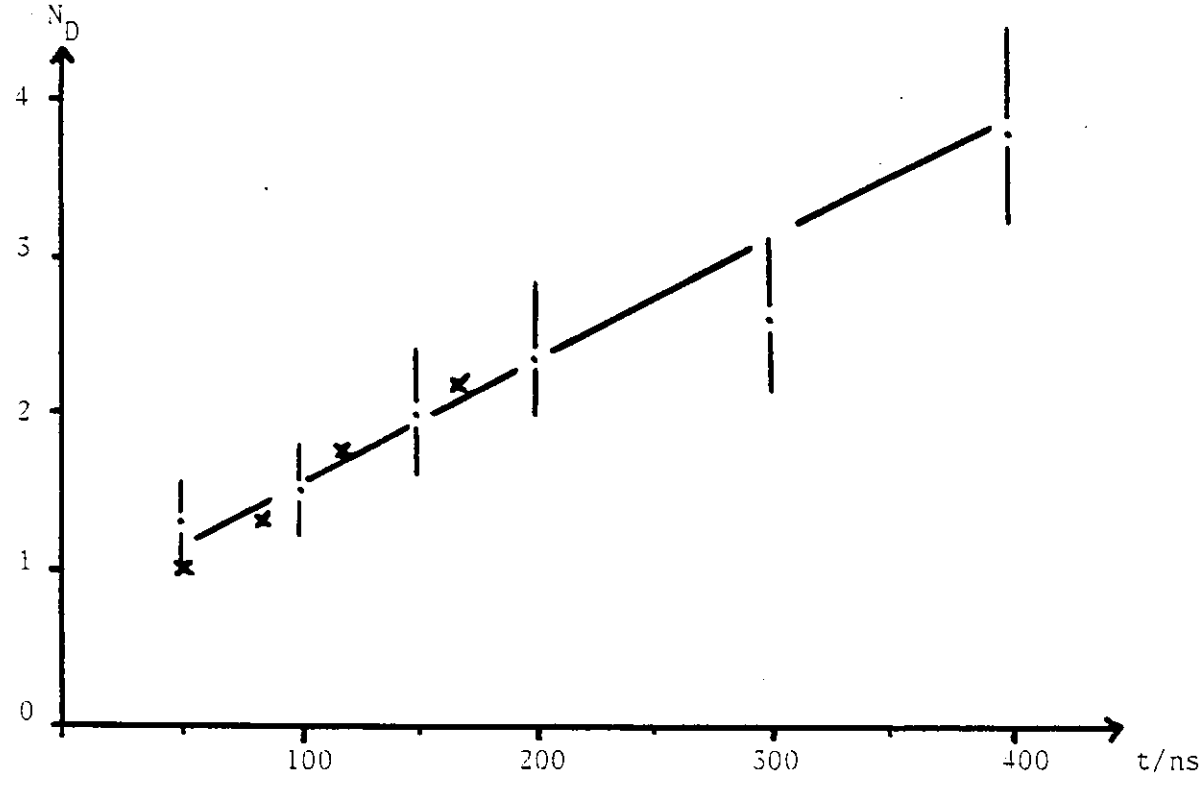


Fig. 4.15. Temporal history of number of electrons per Debye sphere.
- • $N_{Na} = 10^{17}$ cm^{-3}
- × Results of resonant pumping (from Fig. 3.34)

$\frac{2}{3}$ $(3h\nu_L - \chi) = 0.19$ eV, where ν_L is the laser frequency: ionization potential depression, inverse bremsstrahlung heating, collisional recombination and super-elastic collisions depopulating the 3d level. Only 3-body recombination could explain the gradual rise in T_e after 50 ns. The sharper rise in T_e experienced during resonant pumping (Fig. 3.33) suggested super-elastic collisions with the 3p state were a significant additional source of heating in Chapter 3.

4.9 Temporal History of N_D

The minimum N_D observed for multiphoton ionization is compared with the results for resonant pumping in Fig. 4.15. The similar minima achieved for N_D in the two schemes suggested that a mechanism common to both, 3-body recombination, dictated the degree of strong-coupling attained, and is further discussed in Chapter 5. Methods for further reducing N_D will be presented in Chapter 7.

4.10 Summary

Multiphoton ionization of sodium yielded similar N_e and T_e to resonant pumping. Plasma induced widths, shifts, forbidden components and satellites were reproduced. A 1 Å AC Stark shift was recorded for the 3d level. Hence, spectroscopic diagnostics performed during laser irradiation could be invalid (Salter, 1980) if no account is taken of fluctuating field-atom interactions (Bowen, 1982).

CHAPTER 5

PROPERTIES OF METAL VAPOR PLASMAS

5.1 Introduction

The purpose of this chapter is to discuss in conjunction with further experimental results several laser-metal vapor, plasma-vapor and laser-plasma effects relevant to both ionization schemes presented earlier. The topics covered are: molecular effects on absorption spectroscopy and laser scattering, inverse bremsstrahlung heating, plasma recombination and energy loss mechanisms.

5.2 Molecular Effects

5.2.1 Absorption Spectroscopy

An absorption experiment providing better spectral resolution by using as probe beam a < 10 mÅ bandwidth CW ring dye laser was undertaken to measure the 4d - 3p and 5s - 3p lineshapes. The experimental layout is shown in Fig. 5.1 where pump (λ_L= 6854 Å) and probe beam are co-axial and counterpropagating. The temporal history of the transmitted probe beam was recorded on a Tektronix 466 Storage Oscilloscope. The lineshape was scanned in 0.5 Å steps of the probe beam during a preliminary experiment.

A typical absorption trace for $N_{Na} = 5 \times 10^{16}$ cm^{-3}, λ = 5680 Å is shown in Fig. 5.2, and the 4d - 3p absorption lineshape at t = 120 ns

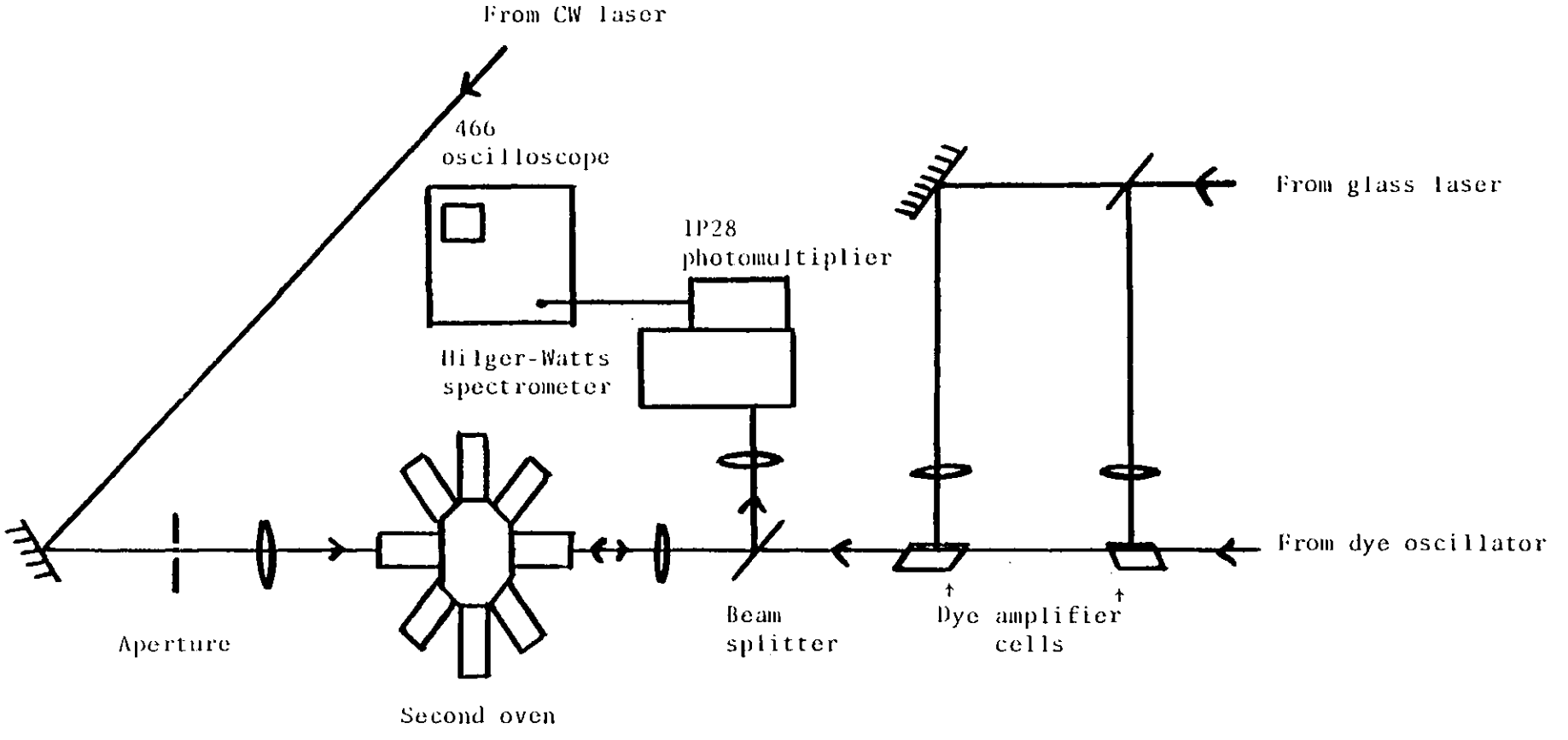


Fig. 5.1. Experimental layout for absorption spectroscopy.

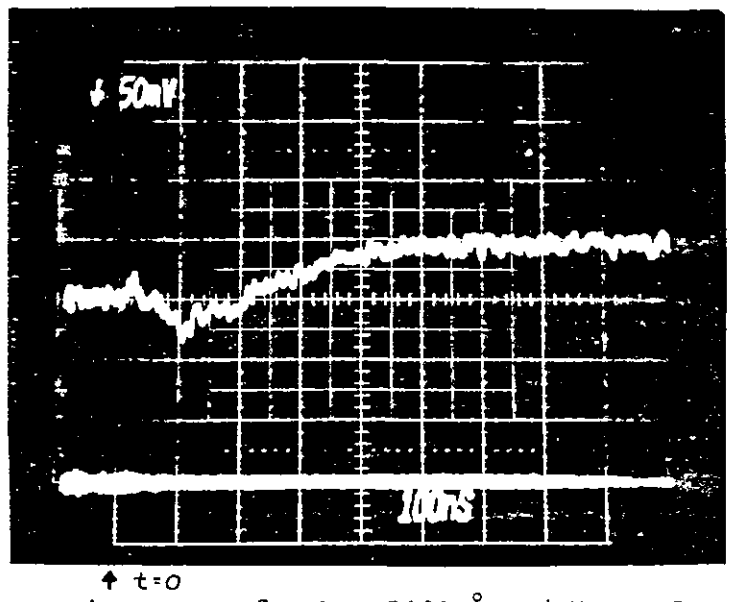


Fig. 5.2. Absorption trace for λ = 5680 Å and N_{Na} = 5 x 10^{16} cm^{-3}.

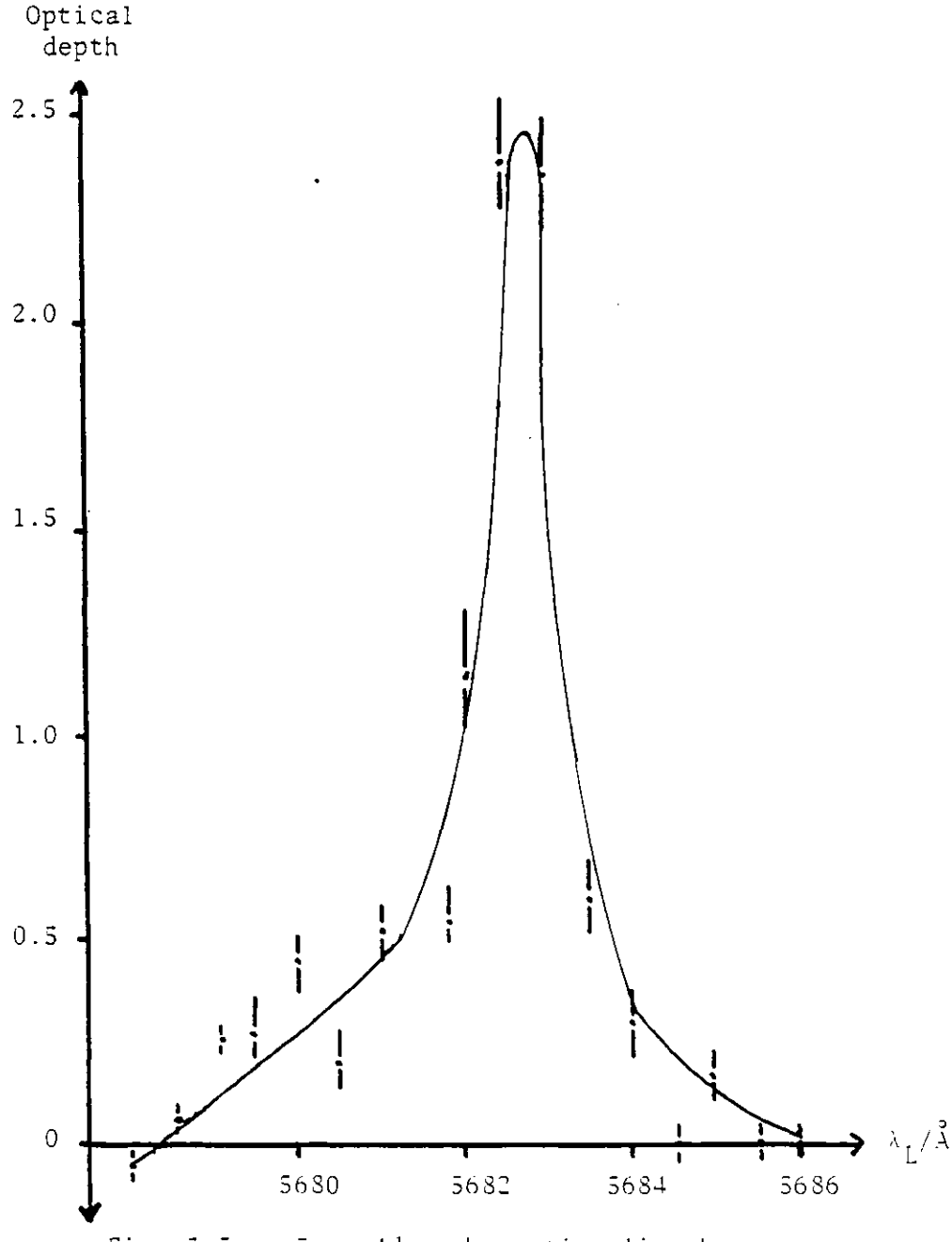


Fig. 5.3. $3p_{1/2}$-$4d_{3/2}$ absorption lineshape: N_{Na} = 5 x 10^{16} cm^{-3} and t = 120 ns.

yielding $N_e = 3 \times 10^{15}$ cm^{-3} shown in Fig. 5.3. The initial reduction in transmission, from Fig. 5.2, due to the increase in the 3p level population upon plasma formation is followed by an increase in transmission above the DC level. This last feature disappeared for small ($< 10^{13}$ cm^{-3}) sodium densities and exhibited a 10 μs lifetime. It was attributed to the reduction in the optical depth of the dimer B → X band as the ground-state Na_2 density was depleted by photodissociation, collisional dissociation and perhaps multiphoton ionization (section 3.5.5). The decay in transmission then represented dimer diffusion into the plasma of radius r occurring within a time $\tau_{Na_2} = \frac{r}{v_{Na_2}} = \frac{0.2}{2 \times 10^4} = 10$ μs, for a dimer velocity v_{Na_2} (cf. Cs_2 by Morellec and Normand, 1981). Hence the absorption profiles were subject to large inaccuracies due to molecules, especially for the weaker forbidden components, and were therefore discontinued. In fact, no absorption was detected for the 5s - 3p line as it was completely swamped by the increase in transmission. An upper limit on the percentage of ground-state dimers remaining during the plasma phase could be set at ∿ 70% from time resolved transmission traces at the He-Ne laser wavelength.

5.2.2 Thomson Scattering

Laser scattering from electrons was envisaged as an additional diagnostic for verifying N_e and T_e. For $N_e \sim 10^{16}$ cm^{-3}, $T_e \sim 0.2$ eV and using the most convenient high-power laser available, doubled Nd:glass at $\lambda = 0.53$ μm, the scattering parameter α for viewing at 90° is 1.8. This corresponds to a~flat-topped spectrum, intermediate between Thomson scattering from free electrons and collective scattering (Evans and Katzenstein, 1969), with a 12 Å half-width at half-maximum. However, even in the absence of dimers, the scattered light over the

wavelength region corresponding to the laser bandwidth, 5266 ± 1.2 Å, would be predominantly from Rayleigh scattering from the 3s - 3p blue wing. For a damped simple harmonic oscillator model of bound electrons (Dalgarno, 1963), the ratio of atomic Rayleigh scattered spectral intensity I_R to Thomson scattered spectral intensity I_T at line center is well approximated by:

$$\frac{I_R}{I_T} = \frac{\Delta_T}{\Delta_R} \times \frac{N(3s)}{N_e} \times \frac{\lambda_{3s-3p}^4}{(\lambda_L^2 - \lambda_{3s-3p}^2)^2} \sim 2500 \qquad (5.1)$$

where Δ_j are the half-widths of the scattered spectra and the values $N(3s) = 10^{17}$ cm^{-3}, $N_e = 10^{16}$ cm^{-3} were used.

The molecular contribution to the scattered flux was determined experimentally. A maximum of 15 mJ of vertically polarized 0.53 μm radiation was optically delayed by 50 ns and focused into the oven to form a ∿ 1 mm diameter beam co-axial with the λ = 6854 Å pump beam. The delay was chosen to allow the probe beam to scatter during a previously diagnosed phase of the plasma (Chapter 4). The scattered signals at 90° were spectrally resolved with 2 Å resolution and had pulse widths equal within 3 ns to the 30 ns laser pulse length. The scattered spectra for $N_{Na} = 5 \times 10^{16}$ cm^{-3} are shown in Figs. 5.4 and 5.5 with and without plasma.

The band structure observed with ∿ 30 Å spacing between peaks was clear evidence of absorption in the dimer B → X band followed by fast (6 ns by McClintock et al., 1969) radiative decay to various vibrational states of $Na_2(X)$ (Fig. 5.6). Figure 5.5 shows that a factor of ∿ 1.5 increase in molecular emission was obtained in the presence of the plasma, but only if the 0.53 μm beam was present. This signified that the increase in excited vibrational state

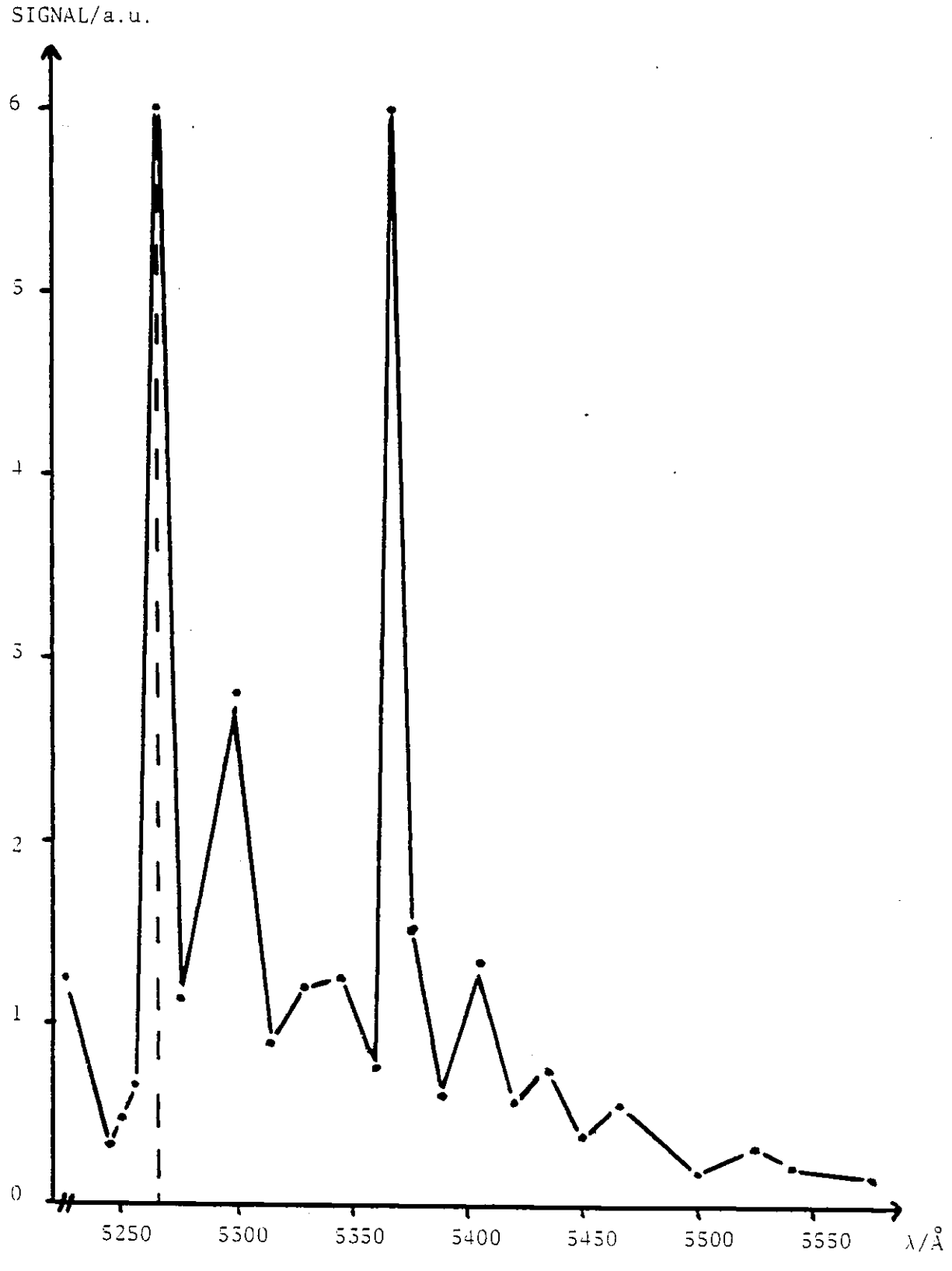


Fig. 5.4. Red wing of scattered spectrum, with plasma: $N_{Na} = 5 \times 10^{16}$ cm^{-3}. (Dotted line at $\lambda_L = 5266$ Å is laser line center.)

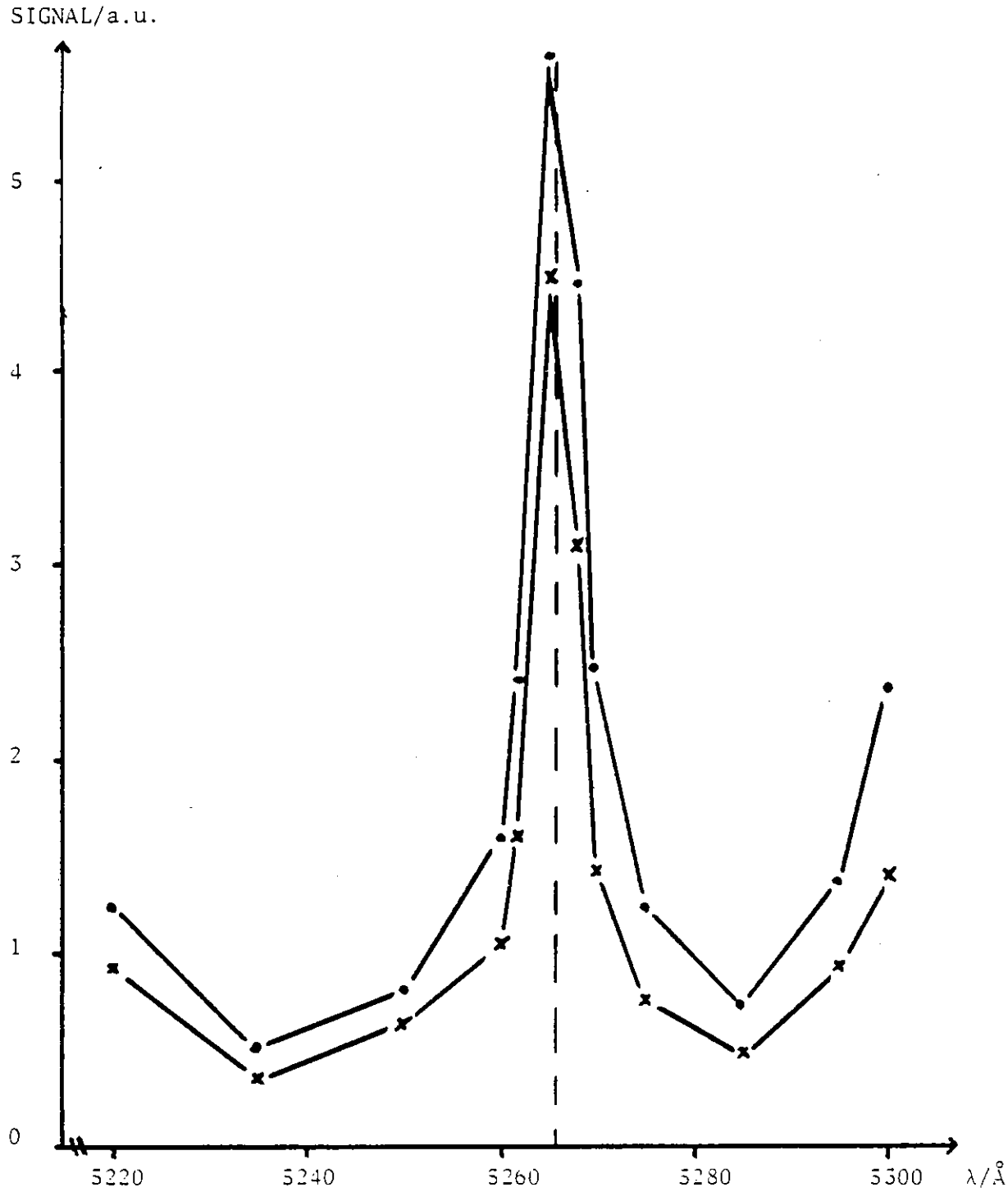


Fig. 5.5. Scattered spectrum in vicinity of laser line center (dotted line at λ = 5266 Å), N_{Na} = 5 x 10^{16} cm^{-3}.

• With plasma.

× Without plasma.

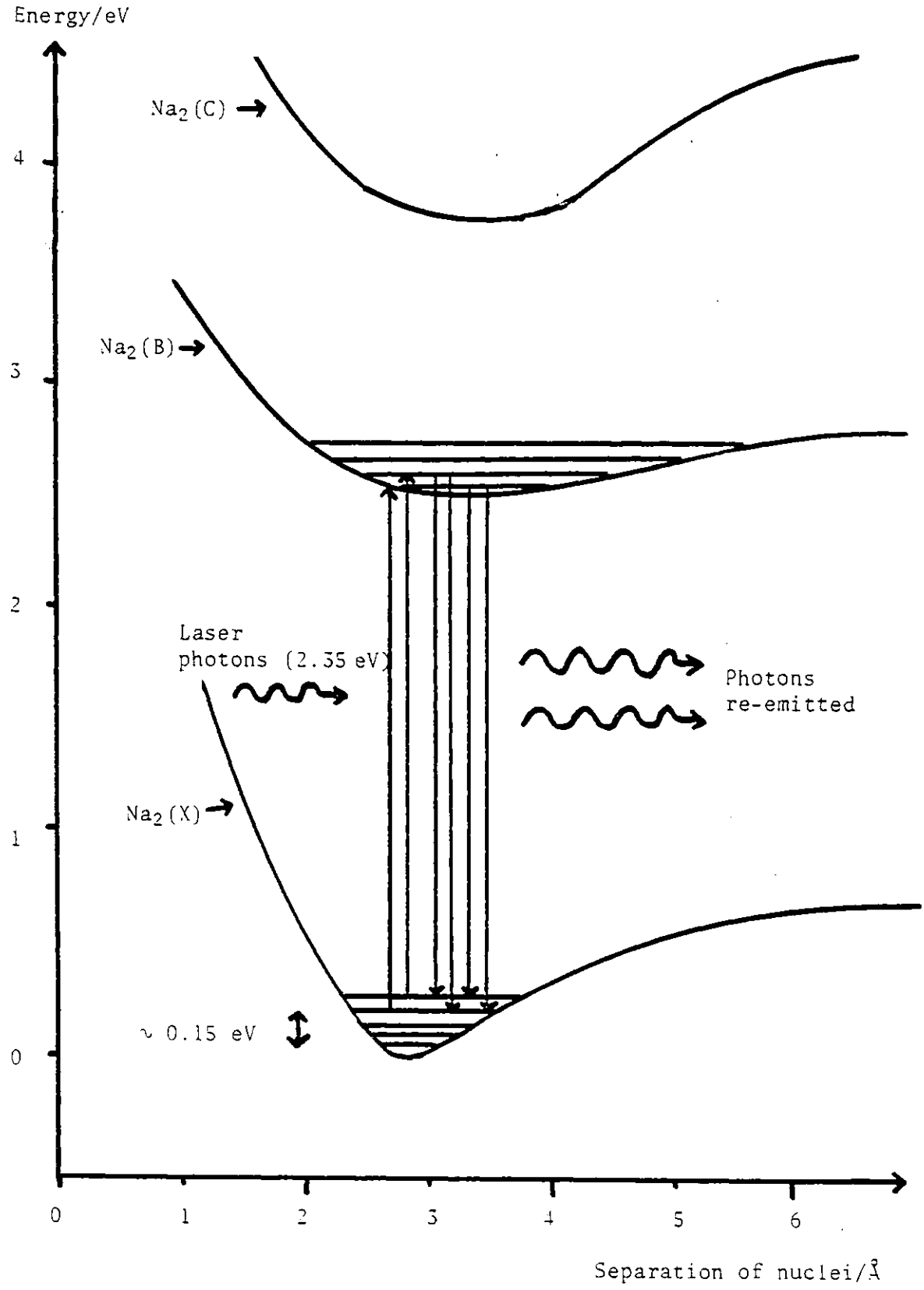


Fig. 5.6. Schematic diagram of laser scattering by dimers.

population densities of $Na_2(X)$ by inelastic electron collisions occurring within 3 ns for $N_e = 10^{16}$ cm^{-3} (Drukarev and Yurova, 1977) and from which the 0.53 μm laser could excite the $Na_2(B \leftarrow X)$ band (Fig. 5.6) outweighed by a factor of 1.5 the decrease in the molecular density 50 ns into the plasma phase. Since these vibrational states are ~ 0.15 eV and more above ground-state, their population density would increase by a factor of ~ 5 as the temperature rose from ~ 0.07 eV to $T_e \sim 0.25$ eV. Hence, it was estimated the molecular density had dropped from a saturated vapor value of 3×10^{15} cm^{-3} to $\sim 1 \times 10^{15}$ cm^{-3} within 50 ns.

After verifying the negligible contribution of stray light to the scattered signal (Fig. 5.7), the cross-section for molecular scatter over the spectral region relevant to Thomson scattering could be estimated as $3 \times 10^{-19 \pm 0.3}$ cm^2 per dimer. Therefore, even if the techniques of laser photodecomposition and vapor superheating of dimers were as successful in sodium as in caesium, for which a reduction by a factor of ~ 2000 has been recorded for the Cs_2 density (Morellec and Normand, 1981), the molecular scatter would still exceed the Thomson scatter ($\sigma \sim 10^{-24}$ cm^2) at all wavelengths by a factor of 100.

Emission spectra of sodium vapor pumped by an argon laser at $\lambda = 3512$ Å (Woerdman, 1978) demonstrated that the 2nd harmonic and 3rd harmonic of the ruby and Nd:Glass lasers at $\lambda = 3472$ Å and $\lambda = 3510$ Å respectively would also excite molecular fluorescence from the $C \rightarrow X$ band (Fig. 5.6). Similarly, the ruby laser wavelength, $\lambda = 6943$ Å, could excite the Na $(A \leftarrow X)$ band. The Nd:Glass wavelength, $\lambda = 10532$ Å, would also be inapplicable for Thomson scattering in sodium due to absorption by excited vibrational states $\sim 2T_e$ above the molecular ground-state of $Na_2(X)$. Hence the optical depth at $\lambda = 10532$ Å

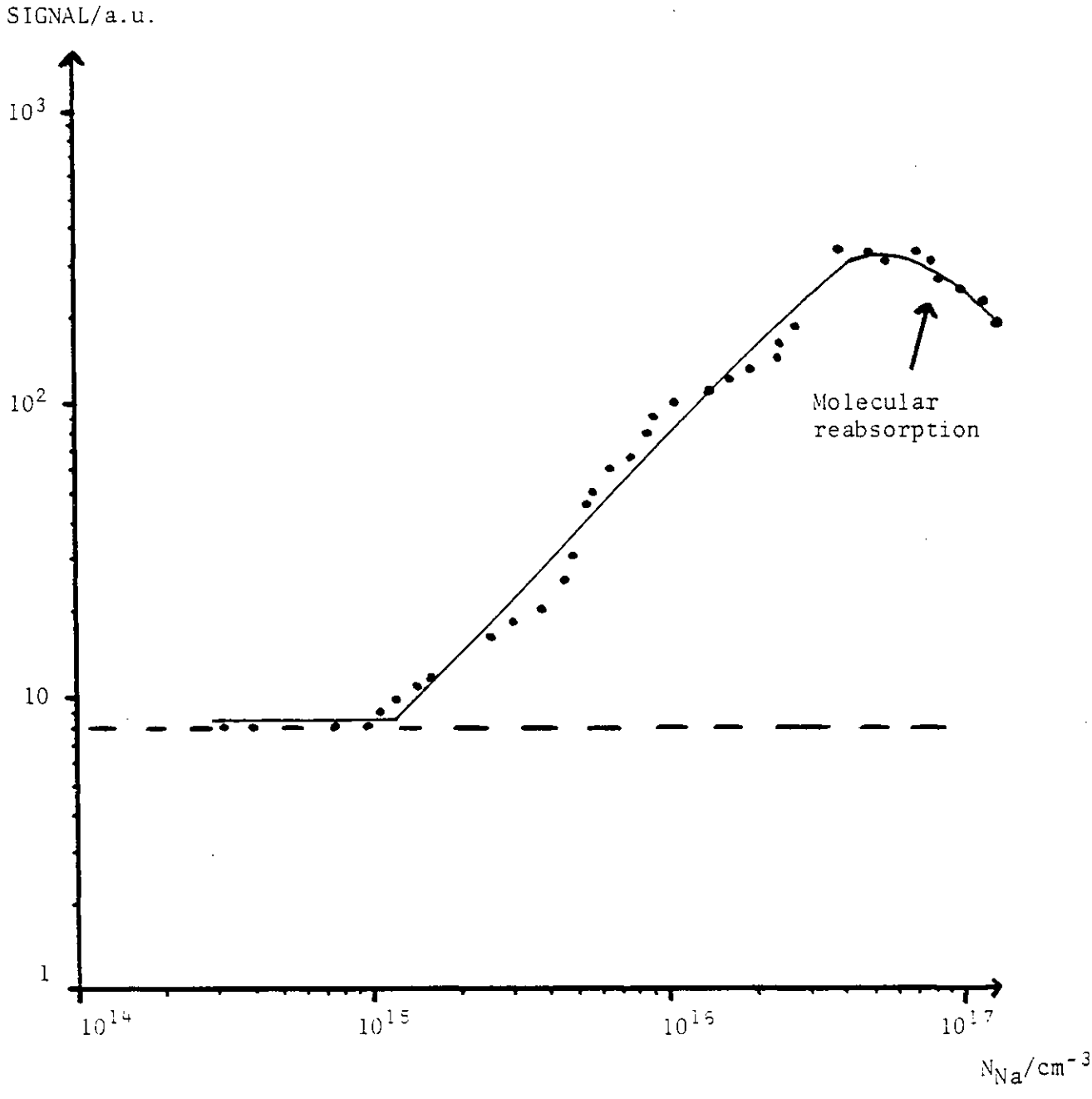


Fig. 5.7. Scattered signal at laser line center (λ = 5266 Å) versus sodium density (dotted line is stray laser light intensity).

would be at least $^1/_{e^2}$ of that experienced at the $Na_2(A \leftarrow X)$ band center, which is similar to the optical depth at $\lambda = 0.53$ μm (de Groot and van Rooijen, 1975).

Thus, molecular fluorescence prevented the diagnosis by laser scattering of the low T_e plasmas produced.

5.3 Inverse Bremsstrahlung Heating

For a plasma with $N_e = N_i$ and $\omega_L >> \omega_p$, the electron heating rate for electron-ion inverse bremsstrahlung is given by (Bekefi, 1966):

$$\frac{dT_e}{dt} = \frac{5 \times 10^{-19} \lambda_L^3 N_e I}{T_e^{\frac{1}{2}}} \left[e^{\frac{1.24}{\lambda_L T_e}} - 1 \right] g \qquad (5.2)$$

where the radiation wavelength is λ_L in microns and the free-free Gaunt factor, g, is between 1 and 1.5 for $T_e < 1$ eV, $\lambda < 1$ μm (Stallcop and Billman, 1974). Electron-atom inverse bremsstrahlung could be neglected for > 1% fractional ionization (Peach, 1967).

Using the results from multiphoton ionization of sodium (Chapter 4), $\lambda_L = 6854$ Å, $N_e = 2 \times 10^{16}$ cm^{-3}, $T_e = 0.25$ eV at $t = 50$ ns and $I = 10^8$ W cm^{-2}, the initial heating rate would be:

$$\frac{dT_e}{dt} = 10^9 \text{ eV s}^{-1} = 1 \text{ eVns}^{-1} \qquad (5.3)$$

$$= 0.5 \text{ eVns}^{-1} \text{ if ions thermalized}$$

However, a fraction of the energy gained by the free electrons is used for subsequent collisional excitation and ionization of bound electrons, hence reducing the heating efficiency. For a laser irradiated, low-fractional ionization plasma in complete thermal equilibrium, the following equations were used to obtain a numerical estimate of the modified heating rate:

$$\underline{\text{SAHA}}: \qquad N_e^2 = C\, N_0\, T_e^{3/2}\, e^{-\chi/T_e} \tag{5.4}$$

$$\underline{\text{ENERGY}}: \qquad \frac{2}{3}\frac{dE_e}{dt} = N_e \frac{dT_e}{dt} + (T_e + 2/3\chi)\frac{dN_e}{dt} \tag{5.5}$$

$E_e = N_e\chi + \frac{3}{2} N_e T_e$, C is only weakly dependent on T_e, N_0 is the ground-state atom density or neutral density and the last term in equation (5.5) represents the rate of deposition of energy into collisional ionization. By comparison, energy losses via collisional excitation could be neglected for $T_e < 0.5$ eV and $\frac{N_e}{N_0} < 0.5$ (cf. Nishida, 1982). If N_0 remains approximately constant, differentiating with respect to time equation (5.4), substituting for $\frac{dN_e}{dt}$ in equation (5.5) and equating to the right-hand side of equation (5.2) yields:

$$\frac{5\times10^{-19}\,\lambda_L^3\, N_e I}{T_e^{1/2}}\left[e^{\frac{1.24}{\lambda_L T_e}} - 1\right] g = \left[\frac{7}{4} + \frac{\chi}{T_e} + \frac{\chi^2}{3T_e^2}\right]\left[\frac{dT_e}{dt}\right] \tag{5.6}$$

Hence the heating rate by comparison with equation (5.2) has been reduced by a significant factor, $\frac{\chi^2}{3T_e^2}$ for $T_e << \chi$. Since the present plasmas were only in partial LTE, the heating rate would be larger than given by equation (5.6) by approximately a factor of $\chi/\chi_{n\ell}$ where $\chi_{n\ell}$ is the ionization potential of the lowest level in LTE with the continuum. For $\chi_{n\ell}$ estimated at 1.5 eV:

$$\frac{dT_e}{dt} = 0.03 \text{ eV ns}^{-1} \tag{5.7}$$

Hence the low electron temperatures measured in the plasma afterglow could be reconciled with the highest laser flux present, 10^8 W cm^{-2}, by considering the partitioning of energy gained through inverse bremsstrahlung.

5.4 Plasma Recombination

The temporal history of the electron density during optical pumping of the sodium vapor can be approximately represented as follows, if diffusion is ignored:

$$\frac{dN_e}{dt} = N(3s)f - \alpha(T_e)N_e^3 \tag{5.8}$$

where f is the ionization rate and $\alpha(T_e)$ is a 3-body recombination coefficient.

Specifically, for multiphoton ionization and all levels but the 3s ground-state negligibly populated:

$$\frac{dN_e}{dt} = (N_{Na} - N_e)\sigma F^n - \alpha(T_e)N_e^3 \tag{5.9}$$

The two limits of equation (5.9) for a constant flux are:

(a) The recombination rate is negligible compared to the ionization rate by the end of the laser pulse:

$$\Rightarrow \quad \frac{N_e}{N_{Na}} = \frac{N_{Na^+}}{N_{Na}} = \text{Constant} \tag{5.10}$$

(b) N_e has reached an equilibrium value $<< N_{Na}$ during the laser pulse. In addition, the recombination time $\tau_{REC} = 1/(\alpha(T_e)N_e^2)$ is longer than the laser pulse length τ_L to ensure a slowly rising T_e as dictated by experimental results:

$$\Rightarrow \quad \frac{N_{Na^+}}{N_{Na}} \propto \frac{1}{(N_{Na})^{2/3}} \text{ by setting (5.9) = 0} \tag{5.11}$$

Hence, a measure of the fractional ionization $\frac{N_{Na^+}}{N_{Na}}$ obtained at the end of the laser pulse for different initial sodium densities N_{Na} should distinguish between cases (a) and (b) (Fig. 5.8). The theoretical curve on Fig. 5.8 represents equation (5.11) normalized to the experimental point at $N_{Na} = 10^{17}$ cm^{-3}. Also shown are the peak fractional ionizations achieved for resonant pumping. Clearly, the peak electron density yields were limited by collisional recombination.

The temporal histories of N_e (Figs. 4.6 and 3.22) yielded a lower bound for the 3-body recombination time, τ_{REC}, of 100 ns for $N_e = 2 \times 10^{16}$ cm^{-3}, $T_e = 0.25$ eV. Therefore, for sodium, $\alpha(T_e = 0.25 \text{ eV}) \lesssim 3 \times 10^{-26}$ cm^6 s^{-1}. Calculations for a model alkali atom yielded a significantly higher recombination coefficient, $\alpha(T_e = 0.25 \text{ eV}) = 10^{-24}$ cm^6 s^{-1} (Bates et al., 1962) for $N_e = 2 \times 10^{16}$ cm^{-3}. This discrepancy is attributed to the inappropriate use of a hydrogenic level scheme in these calculations. In fact, the total recombination rate is well approximated by the collisional recombination rate into the highest levels, n, satisfying the condition that their electron excitation rates are less than their de-excitation rates (Hinnov and Hirschberg, 1962):

$$g_{n+1} \langle \sigma v_e \rangle_{n,n+1} e^{-\frac{E_{n,n+1}}{kT_e}} < g_{n-1} \langle \sigma v_e \rangle_{n,n-1} \qquad (5.12)$$

where n-1 and n+1 represent the lower and upper most strongly collisionally coupled neighbouring levels respectively. In sodium, the critical levels n determined from published inelastic collision cross-sections (Shuker et al., 1980) for $T_e = 0.25$ eV, were the 4s, 4p and 3d states, yielding $\alpha \gtrsim 3 \times 10^{-27}$ cm^6 s^{-1} which was consistent with experimental results.

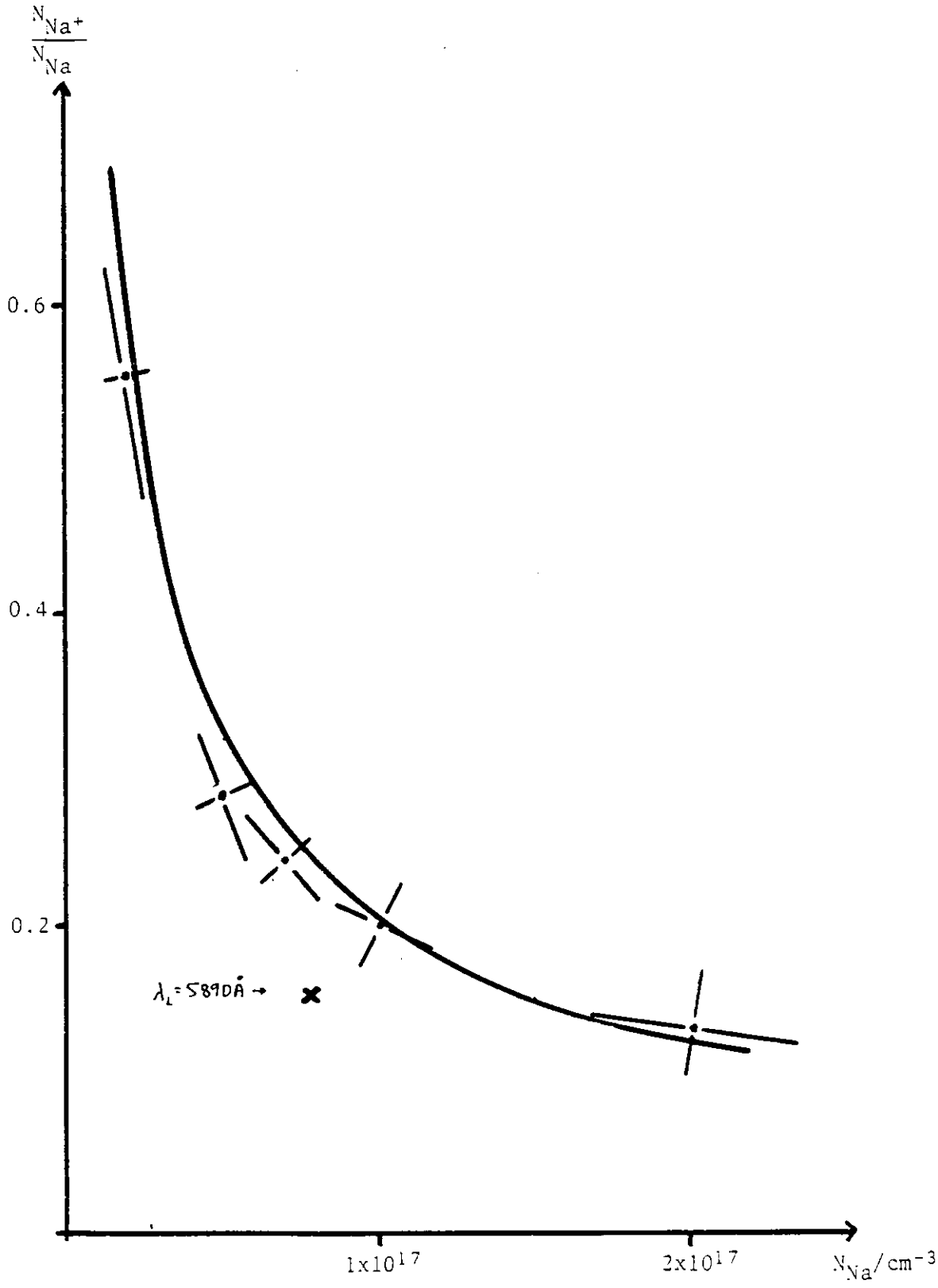


Fig. 5.8. Peak fractional ionization (λ_L = 6854 Å) versus initial sodium density. Theoretical curve represents

$$\frac{N_{Na^+}}{N_{Na}} \propto \frac{1}{N_{Na}^{2/3}}$$

5.5 Plasma Lifetime

After reviewing all atomic and molecular processes, electron-ion thermalization was determined to be the predominant energy loss mechanism for the free electrons. For $N_e = N_{Na^+} = 2 \times 10^{16}$ cm^{-3}, $T_e = 0.25$ eV, $T_{OVEN} = 0.07$ eV and $\tau_{ei} = 25$ ns (section 3.6):

$$\frac{dE_e}{dt} = -\frac{3}{2} N_e \left(\frac{T_e - T_{OVEN}}{\tau_{ei}} \right) = -4 \times 10^4 \text{ W cm}^{-3} \qquad (5.13)$$

By comparison radiative losses in such low T_e plasmas could only account for a maximum of 100 W cm^{-3}. Since the energy stored in the plasma was approximately given by:

$$E_e \sim e(\chi + \tfrac{3}{2} T_e) N_e = 0.02 \text{ J cm}^{-3} \qquad (5.14)$$

the minimum plasma lifetime could be calculated by combining (5.13) and (5.14):

$$E_e / \frac{dE_e}{dt} \sim -500 \text{ ns},$$

$$\sim -\frac{1}{N_e} \frac{dN_e}{dt} \text{ for a constant plasma volume.}$$

The lifetime based on thermalization rates would be longer than 500 ns since energy losses by thermalization terminate after $t = \tau_{ei} \left(\frac{N_{Na}}{N_{Na^+}} \right) = 250$ ns, when $T_e = T_{Na^+} = T_{Na}$ (section 3.6). Hence the shorter N_e decay times observed, $\sim$ 200 ns from Figs. 4.6 and 3.22, confirmed that diffusion governed the temporal behaviour of the electron density for millimetre radii plasmas (section 3.5.6).

CHAPTER 6

CONCLUSIONS

The 0.5 - 2 MW, 25 ns tunable dye laser assembled was of sufficient intensity and pulse length to produce up to 50% fractional ionization in dense sodium vapor. Its low divergence, $\sim$ 2 mrad, allowed peak fluxes of 10^8 W cm^{-2} to be maintained over several centimeters of vapor. Thus, a large (1 - 2 cm by 100 μm) cross-section of the plasmas formed could be imaged at 90° to the pump laser beam to provide enough photons for 2Å, 3 ns resolution of emission lineshapes. The lineshapes, barring satellite features, were reproducible within 20% due to the low (10%) shot-to-shot fluctuations of the laser beam. Since the dimer absorption coefficient reached 1 cm^{-1} for $N_{Na} > 10^{16}$ cm^{-3}, the vapor path length between plasma and diagnostic equipment had to be reduced from its value of 20 cm in the first oven. This was successfully achieved by containing sodium in a 1 cm diameter sapphire tube which remained sufficiently transparent for fluorescence measurements and by using a smaller oven.

The electron densities and temperatures measured by emission spectroscopy for the two ionization schemes represented the fewest electrons per Debye sphere, $N_D = 1$, yet recorded for laser irradiated vapors and gases. Although shock tubes (Mintsev et al., 1980) and exploding wires (Ya'akobi, 1968) have produced more strongly-coupled plasmas, the present laser ionized plasmas were more amenable to spectroscopic diagnosis. This was due to the lower N_e and T_e

encountered which increased line-to-continuum ratios in the visible region of the spectrum and decreased Doppler shifts and optical depths.

Electron impact shift-to-width ratios for the 3p - 4d transition agreed best with theory including Debye shielding for $N_D \sim 1 - 2$. The mean static ion microfield calculated from the measured upper bound for the Inglis-Teller limit and from the intensity ratio of 4f - 3p forbidden component to 4d - 3p allowed line was a factor of ~ 3 less than for a Holtsmark distribution ($N_D \to \infty$). This was consistent with a microfield distribution corrected for $N_D = 1$ and ion-ion correlations (Weisheit and Pollock, 1980; Hooper, 1966). The appearance of blue wing satellites was attributed to a two-plasmon process, with resonance enhancement occurring since $\omega_p \approx \omega_{4d-4f}$.

The low electron temperatures recorded for resonant pumping indicated that neither super-elastic collisions followed by collisional ionization nor photoionization were the dominant processes for $N_{Na} > 3 \times 10^{16}$ cm^{-3} and $I = 10^7 - 10^8$ W cm^{-2}. An alternative mechanism, laser-induced associative ionization, could explain, in the presence of filamentation, both the low T_e and short (< 20 ns) ionization times witnessed. The temporal histories of N_e and T_e in the plasma afterglows were explained by diffusion, and 3-body recombination to excited sodium states.

Several difficulties were encountered while attempting further diagnostic experiments. Transmission experiments using resonant radiation yielded unexpected filamentation and off-axis stimulated emission for $N_{Na} > 10^{16}$ cm^{-3}. Absorption lineshapes of atomic transitions were distorted by time-varying molecular absorption. Laser scattering from free electrons was masked by molecular absorption and rapid re-emission. The AC Stark shift of the sodium 3d level was

measured and compared with theory for the first time, yielding a peak flux of 10^8 W cm^{-2}. In the presence of such laser-induced shifts, no spectroscopic diagnostics were considered reliable during laser irradiation. Heating by inverse bremsstrahlung, however, was significantly reduced in these partially ionized vapors.

Hence, laser pumping of sodium vapor served as a successful exploratory experiment for producing non-Debye plasmas, allowing plasma theory to be tested for $N_D = 1$ and revealing the shortcomings associated with metallic vapor plasmas.

CHAPTER 7

PRODUCTION OF NON-DEBYE PLASMAS IN OTHER VAPORS

7.1 Introduction

Two alternative schemes for reducing N_D and circumventing the problems associated with sodium are described in this chapter. They are four-photon ionization of xenon and two-photon ionization of caesium. Preliminary results on caesium plasmas produced by multiphoton ionization are then presented.

7.2 Multiphoton Ionization of Xenon

The four-photon ionization rate for Xe can be enhanced by the fortuitous three-photon resonance $5p \rightarrow\rightarrow\rightarrow 7s_{3/2}$ at the frequency tripled Nd:glass wavelength, λ_L = 3511 Å (HWHM = 1 Å). Subsequent photoionization from the 7s state by the frequency doubled Nd:glass wavelength, λ_L = 5266 Å, would create electrons with T_e = 0.53 eV since χ_{Xe} = 12.13 eV (see Fig. 7.1). For complete ionization to occur within 10 ns, a laser flux estimated at 3 x 10^9 W cm^{-2} would be needed (Gontier and Trahin, 1978; Rothschild et al., 1981), corresponding to 200 mJ of frequency tripled radiation in 20 ns focused to a 500 μm diameter spot. At present, this would require 60% energy conversion efficiency of doubled radiation to tripled radiation. This has been achieved by mixing orthogonally polarized (Type I) fundamental and frequency doubled beams in a KD*P crystal. At 3 x 10^9 W cm^{-2}, the laser flux would be sufficiently low (< 10^{11} W cm^{-2}) such that the

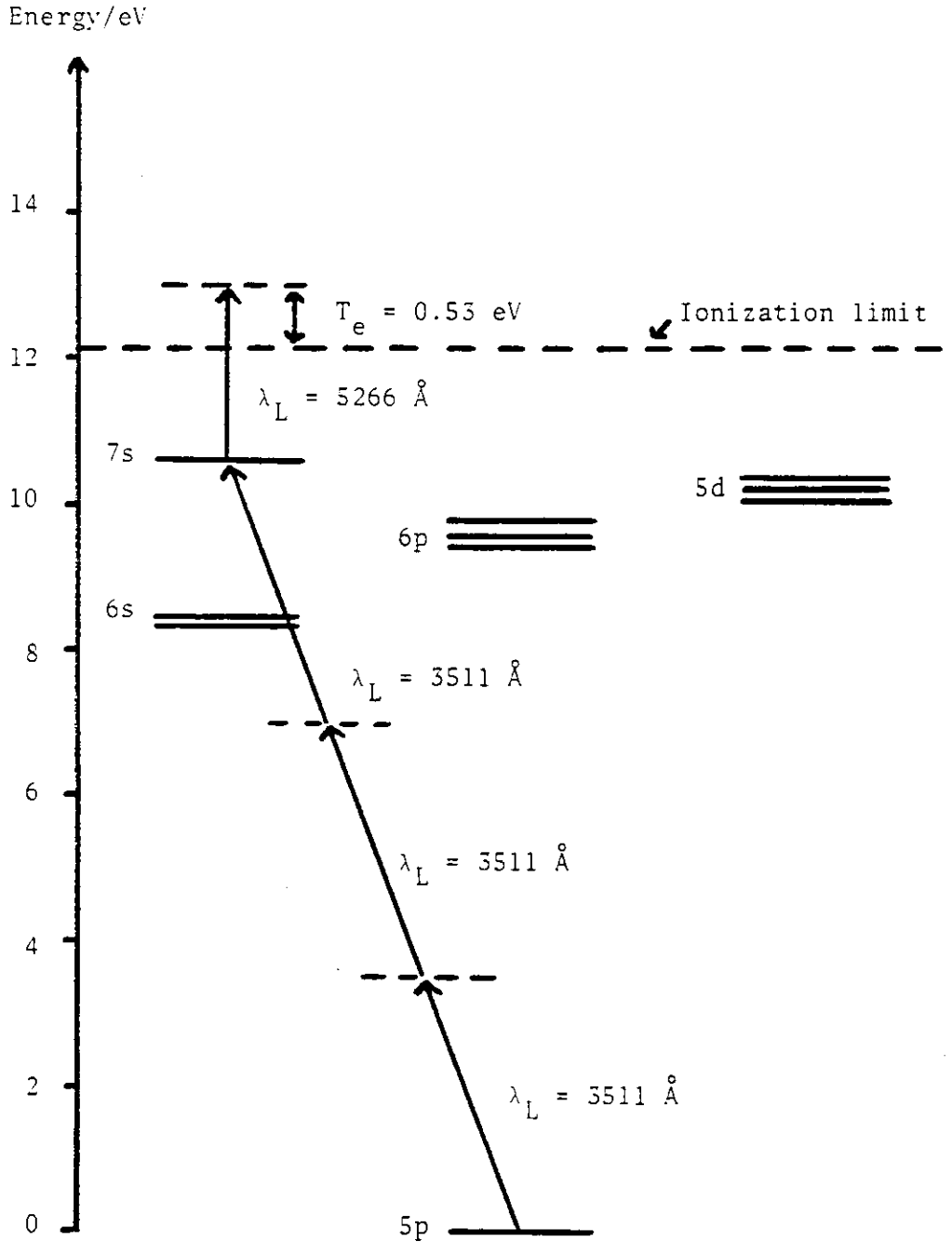


Fig. 7.1. Xenon term diagram with four-photon ionization scheme.

following effects could be ignored:

(a) The quadratic AC Stark effect shifting the $5p \rightarrow\rightarrow 7s_{3/2}$ transition outside the bandwidth of the frequency tripled beam (Kruit et al., 1981) and hence reducing the ionization rate.

(b) Absorption of additional photons during multiphoton ionization heating the plasma (Kruit et al., 1981).

Allowing for heating by inverse bremsstrahlung by equation (5.6), the following plasma parameters should be attained: $T_e = 1$ eV, $N_e = 3 \times 10^{18}$ cm^{-3}, $N_{Xe} = 3 \times 10^{19}$ cm^{-3} and hence $N_D = 1$.

Finally, since all Xe_2 bands originating from the ground-state lie in the vacuum ultraviolet, there would be no problems from molecular absorption or scattering in the visible region. This has been demonstrated by numerous laser scattering experiments performed on plasmas in other noble gases such as He and Ar (Evans and Katzenstein, 1969).

7.3 Multiphoton Ionization of Caesium

There were four reasons for choosing the element with the lowest ionization potential, caesium ($\chi = 3.893$ eV), as constituent of a non-Debye plasma:

(a) The threshold wavelengths for two-photon ionization of Cs and Cs_2 are $\lambda = 6370$ Å and 6720 Å respectively, within the tuning range of an efficient dye, DCM.

(b) For a particular electron density and neutral density, the Saha-Boltzmann equilibrium value of T_e scales linearly with χ for $T_e << \chi$ (equation (5.4)). Hence N_D is proportional to $\chi^{3/2}$, implying χ should

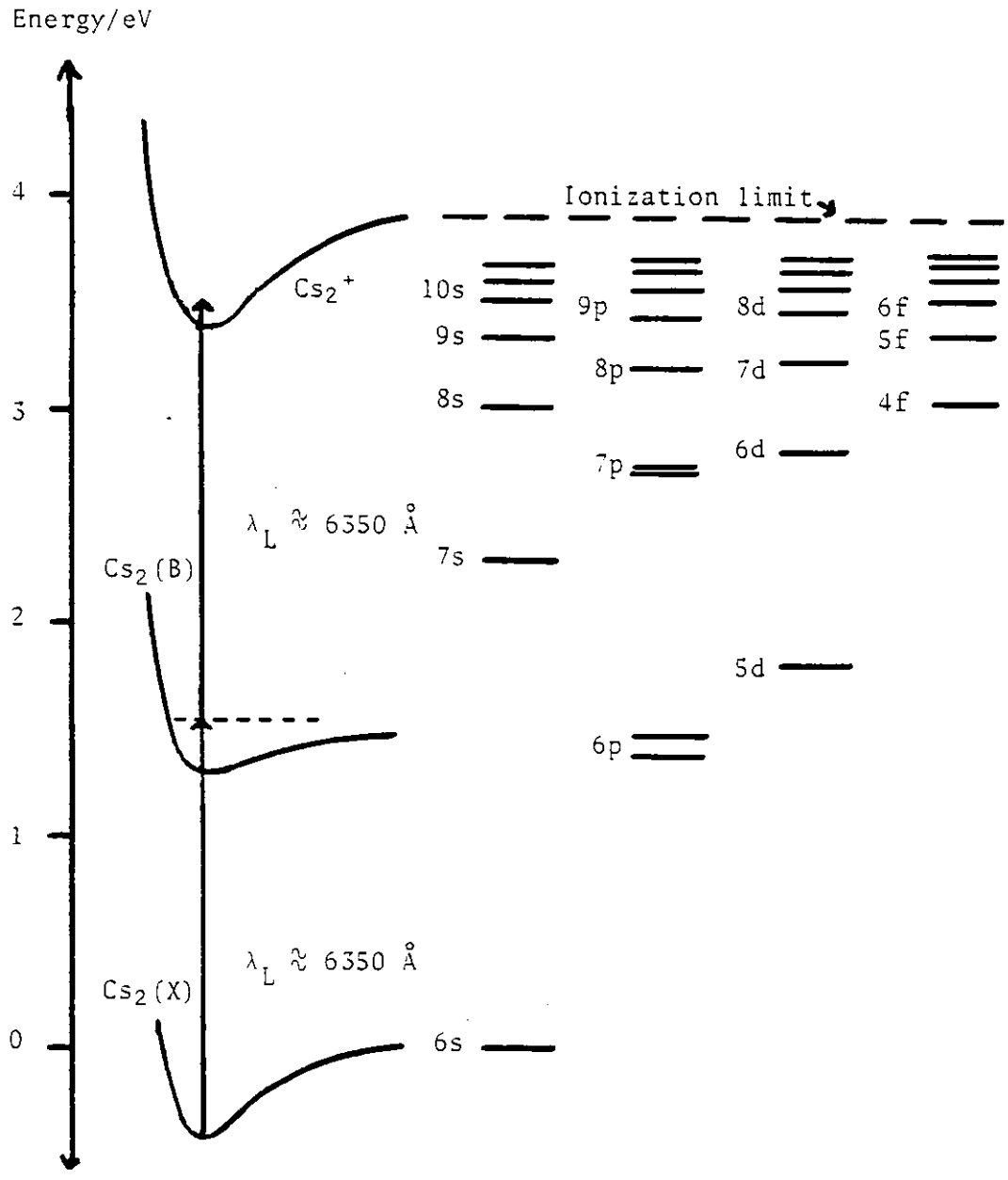


Fig. 7.2. Term diagram and ionization scheme for Caesium.

be minimized.

(c) Inverse bremsstrahlung heating scales as T_e^2/χ^2 by equation (5.6).

(d) The minimum in the absorption spectrum for Cs_2 occurs within $\sim$ 30 Å (Lapp and Harris, 1966) of the wavelength most appropriate for laser scattering, λ_L = 5266 Å. In fact, the Cs_2 absorption coefficient at λ = 5266 Å is a factor of $\sim$ 100 less than that for Na_2, for similar Na and Cs atomic densities.

To test these advantages of caesium over sodium, dense Cs vapor (N_{cs} = 7 x 10^{17} cm^{-3}) contained in Corning 1720 alkali resistant glass has been recently irradiated by a 10^7 W cm^{-2}, 25 ns dye laser beam at $\lambda_L \sim$ 6350 Å. The resultant white glow was diagnosed by emission spectroscopy using the same experimental layout and techniques as for the sodium experiments. The temporally resolved electron density was inferred from the quadratic Stark shift of the $6s_{\frac{1}{2}}$ - $7p_{\frac{1}{2}}$ transition (Fig. 7.2). A maximum shift of 10 Å was recorded 50 ns into the plasma afterglow, corresponding to a peak N_e = 5 ± 1 x 10^{17} cm^{-3}. Assuming LTE for such high electron densities, the absolute black-body spectral flux in the optically thick regions of the $6p_{3/2}$ - $7d_{5/2}$ transition (λ = 6973 Å) yielded an estimate of the electron temperature, T_e = 0.5 ± 0.1 eV at t = 50 ns. Hence the minimum N_D achieved was $0.8^{+0.4}_{-0.2}$.

The near complete ionization witnessed was attributed to two-photon ionization of caesium dimers followed by further laser absorption by excited atomic levels initially populated via inelastic electron collisions (cf. Tam and Happer, 1977). The crucial role of molecules in this scheme was demonstrated by the absence of dense plasma

production when the Cs vapor was unsaturated and the N_{Cs_2}/N_{Cs} ratio therefore diminished. More importantly, the molecular fluorescence yield at $\lambda \sim 5300$ Å when irradiating Cs vapor by the frequency doubled Nd:glass laser beam was estimated as $< 1/1000$ of that recorded for sodium.

Hence, as predicted, a reduction in both dimer interference and N_D has been accomplished by switching to caesium. This should allow laser scattering experiments to be performed for the purpose of testing the validity of collective scattering theory (Salpeter, 1960; Theimer, 1966) in strongly-coupled plasmas.

REFERENCES

Agostini, P., Georges, A. T., Wheatley, S. E., Lambropoulos, P. and Levenson, M. D. J. Phys. B. 11 (1978) 1733.

Ahlstrom, H. G. "Physics of Laser Fusion", LLNL (1982).

Allegrini, M., Alzetta, G., Kopystynska, A., Moi, L. and Orriols, G. Optics. Comm. 22 (1977) 329.

Allegrini, M., Alzetta, G., Kopystynska, A. and Moi, L. Optics. Comm. 19 (1976) 96.

Aymar, N., Luc-Koenig, F., Combet Farnoux, F. J. Phys. B. 9 (1976) 1279.

Bachor, H. A. and Kock, M. J. Phys. B. 14 (1981) 2793.

Baker, E. A. M. and Burgess, D. D. J. Phys. B. 10 (1977) L177.

Barolskii. S. G., Yermokhin, N. V., Kovaliov, B. M., Kulik, P. P. and Riabii, V. A. Proc. 12th ICPIG (1975) Eindhoven, p181.

Bates, D. R., Kingston, A. E. and McWhirter, R. W. P. Proc. Roy. Soc. A267 (1962) 297.

Bearman, G. H. and Leventhal, J. J. Phys. Rev. Lett. 41 (1978) 1227.

Bebb, H. B. Phys. Rev. A 149 (1966) 30.

Bebb, H. B. Phys. Rev. A 153 (1967) 26.

Bekefi, G. "Radiation Processes in Gases", John Wiley (1966) New York.

Bekefi, G. "Principles of Laser Plasmas", Wiley-Interscience (1976).

Berlman, I. B. Handbook of Fluorescence Spectra of Aromatic Molecules, Academic Press (1971).

Boercker, D. B., Lee, R. W. and Rogers, F. J. In press (1983).

Bowen, J. L. Ph.D. Thesis, University of London (1982).

Bréchignac, G., Cahuzac, Ph. and Debarre, A. Opt. Comm. 35 (1980) 87.

Burgess, D. D. J. Phys. B. 4 (1971) L7.

Burgess, D. D. and Lee, R. W. J. de Phys. 43 (1982) 413.

van Calcar, R. A., Heuts, M. J. G., van Uitert, B. K., Meijer, H. A. J. Hollander, T. J. and Alkemade, C. Th. J. J.Q.S.R.T. 28 (1982) 1.

Cardinal, P. G., Wizinowich, P. L. and Measures, R. M. J.Q.S.R.T. 25 (1981) 537.

Carré, B., Roussel, F., Breger, P. and Spiess, G. J. Phys. B. 14 (1981) 4271.

Carré, B., Roussel, F., Breger, P. and Spiess, G. J. Phys. B. 14 (1981) 4289.

Chéret, M., Spielfiedel, A., Durand, R. and Deloche, R. J. Phys. B. 14 (1981) 3953.

Dalgarno, A. J. of Opt. Soc. of Am. 53 (1963) 1223.

Davis, J. and Blaha, M. NRL Memorandum Report 4689 (1982).

Davis, J. and Morin, S. J.Q.S.R.T. 11 (1971) 129.

Dawson, J. M. Phys. Fluids 7 (1964) 981.

Debye, P. and Hückel, E. Phys. Z. 24 (1923) 185.

van Dijk, C. A., Zeegers, P. J. Th., Nienhuis, G. and Alkemade, C. Th. J. J.Q.S.R.T. 20 (1978) 55.

Drawin, H. W. EUR-CEA-FC-512 (1969).

Drawin, H. W. and Felenbok, P. "Data for Plasmas in Local Thermal Equilibrium", Gauthier-Villars (1965) Paris.

Drukarev, G. F. and Yurova, I. Y. J. Phys. B. 10 (1977) 3551.

Enemark, E. and Gallagher, A. Phys. Rev. A6 (1972) 192.

Evans, D. E. and Katzenstein, J. Rep. Prog. Phys. 32 (1969) 207.

Ewart, P., Ferguson, A. I. and O'Leary, S. V. Opt. Comm. 40 (1981) 147.

Freudenberg, K. Z. Physik 67 (1931) 417.

Gallagher, T. F. and Cooke, W. E. Phys. Rev. A19 (1979) 2161.

Geltman, S. J. Phys. B. 10 (1977) 3057.

Geltman, S. J. Phys. B. 13 (1980) 115.

Gohil, P. Ph.D. Thesis, University of London (1982).

Gontier, Y. and Trahin, M. J. Phys. B. 11 (1978) L131.

Granier, R., Charton, G. and Granier, J. J.Q.S.R.T. 26 (1981) 71.

Griem, H. R. Phys. Rev. 131 (1963) 1170.

Griem, H. R. "Plasma spectroscopy", McGraw-Hill Company (1964).

Griem, H. R. "Spectral line broadening by plasmas", Academic Press (1974).

de Groot, J. J. and van Rooijen, J. Proc. 12th ICPIG (1975) Eindhoven, p135.

Gross, M., Fabre, C., Pillet, P. and Haroche, S. Phys. Rev. Lett. 17 (1976) 1035.

Handbook of Lasers, CRC Press (1971) New Jersey.

Hansen, J. P. Phys. Rev. A8 (1973) 3096.

Hellmuth, T., Leuchs, G., Smith, S. J. and Walther, H. "Laser and Applications" (1981) Springer-Verlag, p194.

Herrmann, A., Schumacher, E. and Wöste, L. J. Chem. Phys. 68(5) (1978) 2327.

Hildebrandt, J. J. Phys. B. 16 (1983) 149.

Hinnov, E. and Hirschberg, J. G. Phys. Rev. 125 (1962) 795.

Holstein, T. Phys. Rev. 83 (1951) 1159.

Hooper, C. Phys. Rev. 149 (1966) 77.

Hooper, C. Phys. Rev. 169 (1968) 193.

Huennekens, J. and Gallagher, A. Phys. Rev. 27 (1983) 771.

Huennekens, J. and Gallagher, A. Phys. Rev. 27 (1983) 1851.

Hynne, F. J.Q.S.R.T. 14 (1974) 437.

Inglis, D. R. and Teller, E. Astrophys. J. 90 (1939) 439.

Ivanov, Yu. V., Mintsev, V. B., Fortov, V. E. and Dremin, A. N. Sov. Phys. JETP 44 (1976) 112.

JANAF Thermochemical Tables, 2nd Ed. NBS (1971) Washington.

Johnson, L. C. Astrophys. J. 174 (1972) 227.

de Jong, A. and van der Valk, F. J. Phys. B. 18 (1979) L561.

Kielkopf, J. F. J. Phys. B. 18 (1980) 3813.

Kilkenny, J. D., Lee, R. W., Key, M. H. and Lunney, J. G. Phys. Rev. A22 (1980) 2746.

Kirby-Docken, K., Cerjan, C. J. and Dalgarno, A. Chem. Phys. Lett. 40 (1976) 205.

Koch, M. E., Verma, K. K. and Stwalley, N. C. International Quantum Electronics Conference (1980) Boston, Paper J8.

Koechner, W. "Solid-State Laser Engineering", Springer-Verlag (1976).

Kopystynska, A. and Moi, L. Phys. Rep. 92 (1982) 137.

Kovaliov, B. M. and Kulik, P. P. Proc. 10th ICPIG (1971) Oxford, p223.

Krasinski, J., Stacewicz, T. and Stroud, C. R., Jr. Opt. Comm. 33 (1980) 158.

Krebs, D. J. and Schearer, L. D. J. Chem. Phys. 76 (1982) 2925.

Kruit, P., Kimman, J. and van der Wiel, M. J. J. Phys. B. 14 (1981) L597.

Kumar, J., Silfvast, W. T. and Wood II, O. R. J. Appl. Phys. 53 (1982) 218.

Kushawaha, V. S. and Leventhal, J. J. Phys. Rev. A22 (1980) 2468.

Kushawaha, V. S. and Leventhal, J. J. Phys. Rev. A25 (1982) 570.

Lam, L. K., Fujimoto, T. and Gallagher, A. C. J. Chem. Phys. 68(8) (1978) 3553.

Lampis, G. and Brown, S. C. Phys. Fluids 11 (1968) 1137.

Lapp, M. and Harris, L. P. J.Q.S.R.T. 6 (1966) 169.

Laughlin, C. J. Phys. B. 11 (1978) 1409.

Le Gouët, J. L., Picqué, J. L., Wuilleumier, F., Bizau, J. M., Dhez, P., Koch, P. and Ederer, D. L. Phys. Rev. Lett. 48 (1982) 600.

Lewis, E. L. and McNamara, L. F. Phys. Rev. A5 (1972) 2648.

Likal'ter, A. A. Sov. Phys. Dokl. 26 (1981) 676.

Loth, C., Meyer, Y. H. and Bos, F. Optics. Comm. 27 (1978) 310.

Loudon, R. "The Quantum Theory of Light", Clarendon Press (1973).

Lucatorto, T. B. and McIlrath, T. J. Phys. Rev. Lett. 37 (1976) 428.

Lucatorto, T. B. and McIlrath, T. J. Applied Optics 23 (1980) 3948.

Manakov, N. L., Ovsiannikov, V. D., Preobragenski, M. A. and Rapoport, L. P. J. Phys. B 11 (1978) 245.

Measures, R. M. J.Q.S.R.T. 10 (1970) 107.

Measures, R. M. J. Appl. Phys. 48 (1977) 2673.

Measures, R. M. and Cardinal, P. G. Phys. Rev. A 23 (1981) 804.

Measures, R. M., Cardinal, P. G. and Schinn, G. W. J. Appl. Phys. 52 (1981) 1269.

Measures, R. M. Drewell, N. and Cardinal, P. Applied Optics 18 (1979) 1824.

Measures, R. M., Drewell, N. and Cardinal, P. J. Appl. Phys. 50 (1979) 2662.

Measures, R. M., Wong, S. K. and Cardinal, P. G. J. Appl. Phys. 53 (1982) 5541.

Melton, L. A. and Wine, P. H. J. Appl. Phys. 51(8) (1980) 4059.

Mintsev, V. B., Fortov, V. E., Pavlov, G. A. and Gryaznov, V. K. Sov. Tech. Phys. Lett. 6 (1980) 234.

Morellec, J. and Normand, D. J. Phys. B. 14 (1981) 3919.

Morgan, W. L. Appl. Phys. Lett. 42 (1983) 790.

Morgulis, N. D., Korcevol, Yu. P. and Przhonskii, A. M. Sov. Phys. JETP 26 (1968) 279.

McCartan, D. G. and Farr, J. M. J. Phys. B. 9 (1976) 985.

McClintock, M., Demtröder, W. and Zare, R. N. J. Chem. Phys. 51 (1969) 5509.

MacDonald, W. M., Rosenbluth, M. N. and Chuck, W. Phys. Rev. 107 (1957) 131.

McIlrath, T. J. and Lucatorto, T. B. Phys. Rev. Lett. 38 (1977) 1390.

Nishida, M. J. Phys. D. 15 (1982) 1951.

Nuckolls, J., Wood, L., Thiessen, A. and Zimmerman, G. Nature 239 (1972) 139.

Oettinger, P. E. and Cooper, J. J.Q.S.R.T. 9 (1969) 591.

Okuda, T., Yamada, J., Yamauchi, T. and Asai, M. Proc. of 12th ICPIG (1975) Eindhoven, p355.

Otis, C. E. and Johnson, P. M. Chem. Phys. Lett. 83 (1981) 73.

Patterson, T. A., Hotop, H., Kasdan, A., Norcross, D. W. and Lineberger, W. C. Phys. Rev. Lett. 32 (1974) 189.

Peach, G. Mem. R. Astr. Soc. 71 (1967) 1.

Popov, K. G. and Ruzov, V. P. Opt. Spectrosc. 48(4) (1980) 372.

Pozwolski, A. E. Acta Phys. Scient. Hungaricae 52 (1982) 15.

Preston, R. C. J. Phys. B. 10 (1979) 523.

Reva, M. G., Akimov, A. I., Denisov, L. K. and Uzhinov, B. M. Zh. Prikl. Spektr. 35 (1981) 975.

Rothschild, M., Zavelovich, J., Gornik, W. and Rhodes, C. K. Opt. Comm. 39 (1981) 316.

Roussel, F., Breger, P., Spiess, G., Manus, C, and Geltmann, S. J. Phys. B. 13 (1980) L631.

Roussel, F., Carré, B., Breger, P. and Spiess, G. J. Phys. B. 16 (1983) 1749.

Salpeter, F. E. Phys. Rev. 120 (1960) 1528.

Salter, J. M. Ph.D. Thesis, University of London (1979).

Shoshan, I., Danon, N. and Oppenheim, U. J. Appl. Phys. 48 (1977) 4495.

Shuker, R., Gallagher, A. and Phelps, A. V. J. Appl. Phys. 51 (1980) 1316.

Skinner, C. H. J. Phys. B. 13 (1980) 55.

Skinner, C. H. and Kleiber, P. D. Phys. Rev. A 21 (1980) 151.

Smith, S. J. and Hogan, P. B. Laser Spectroscopy IV (1979) 360.

Sobelmann. I. I., Vainshtein, L. A. and Yukov, E. A. "Excitation of Atoms and Broadening of Spectral Lines", Springer-Verlag (1981).

Sokolovskii, I. N. High Temp. 7 (1969) 953.

Spitzer, L. "Physics of Fully Ionized Gases", Interscience Publishers Inc. (1956) New York.

Spitzer, L., Jr. and Härm, R. Phys. Rev. 89 (1952) 977.

Stacewicz, T. Optics Comm. 35 (1980) 239.

Stacewicz, T. and Krasinski, J. Optics Comm. 39 (1981) 35.

Stallcop, J. R. and Billman, K. W. Plasma Phys. 16 (1974) 1187.

Stappaerts, E. A., Bekkers, G. W., Young, J. F. and Harris, S. E. IEEE JQE 12 (1976) 330.

Stewart, J. C. and Pyatt, K. D., Jr. Ap. J. 144 (1966) 1203.

Tam, A. C. and Happer, W. Opt. Comm. 21 (1977) 403.

Theimer, O. Phys. Lett. 20 (1966) 639.

Unsöld, A. Z. Astrophys. 24 (1948) 355.

Veža, D. and Richler, G. Opt. Comm. 45 (1983) 39.

Wallenstein, R. and Zacharias, H. Opt. Comm. 32 (1980) 429.

Weiner, J. and Polak-Dingels, P. J. Chem. Phys. 74 (1981) 508.

Wiese, W. L., Smith, M. W. and Miles, B. M. "Atomic Transition Probabilities", Report #NSRDS-NBS22, Nat. Bureau of Standards (1969).

Wilhelm, H. E. Plasma Phys. 24 (1982) 1091.

Witting, H. L. and Gyftopoulos, E. P. J. Appl. Phys. 36 (1965) 1328.

Woerdman, J. P. Opt. Comm. 26 (1978) 216.

Woerdman, J. P. Opt. Comm. 28 (1979) 69.

Weisheit, J. C. and Pollock, R. L. "Spectral Line Shapes", Wende (1981) Berlin, p433.

Wu, C. Y. R., Judge, D. L., Roussel, F., Carré, B., Breger, P. and Spiess, G. "AIP Conference on Laser Techniques for Extreme UV Spectroscopy" (1982) p39.

Ya'akobi, B. Phys. Rev. 176 (1968) 227.

Ya'akobi, B. JQSRT 9 (1969) 137.

Ya'akobi, B. and Bekefi, G. Phys. Lett. 30A (1969) 539.

Yamada, J. and Okuda, T. J. Phys. Soc. Jap. 35 (1973) 881.

Yermokhin, N. V., Kovaliov, B. M. and Kulik, P. P. Proceedings of 12th ICPIG (1975) Eindhoven.

Zoller, P. and Lambropoulos, P. J. Phys. B. 13 (1980) 69.